UNIVERSITY OF CALGARY

Nonadiabatic Control for Quantum Information Processing and Biological Electron Transfer

by

Nathan S. Babcock

A DISSERTATION
SUBMITTED TO THE FACULTY OF GRADUATE STUDIES
IN PARTIAL FULFILLMENT OF THE REQUIREMENTS FOR THE
DEGREE OF DOCTOR OF PHILOSOPHY

DEPARTMENT OF PHYSICS AND ASTRONOMY

CALGARY, ALBERTA

April, 2015

Abstract

In this Thesis, I investigate two disparate topics in the fields of quantum information processing and macromolecular biochemistry, inter-related by the underlying physics of nonadiabatic electronic transitions (*i.e.*, the breakdown of the Born-Oppenheimer approximation). The main body of the Thesis is divided into two Parts.

In Part I, I describe my proposal for a two-qubit quantum logic gate to be implemented based on qubits stored using the total orbital angular momentum states of ultracold neutral atoms. I carry out numerical analyses to evaluate gate fidelity over a range of gate speeds, and I derive a simple criterion to ensure adiabatic gate operation. I propose a scheme to significantly improve the gate's fidelity without decreasing its speed. I contribute to the development of a "loophole-free" Bell inequality test based on the use of this gate by carrying out an order-of-magnitude feasibility analysis to assess whether the test is viable given realistic technological limitations.

In Part II, I investigate electron transfer reaction experiments performed on native and mutant forms of the MADH–amicyanin redox complex derived from *P. denitrificans*. I implement molecular dynamics simulations of native and mutant forms of the solvated MADH–amicyanin complex. I analyze the resulting nuclear coordinate trajectories, both geometrically and in terms of electronic redox coupling. I find that the interprotein solvent dynamics of the mutant systems differ dramatically from those of the native system, and that the stability of an electron-transfer-mediating "water bridge" is compromised in the mutant complexes. I conclude that the mutations disrupt a protective "molecular breakwater" on the surface of amicyanin that stabilizes the interprotein water bridge.

I discuss parallels between the nonadiabatic effects as they manifest themselves in the two systems, and I suggest how my findings in Part I promote technological developments to better characterize systems like that examined in Part II.

Preface

No storyteller has been able to dream up anything as fantastically unlikely as what really does happen in this mad Universe.

—Robert A. Heinlein, 1973 [1]

A decade ago, while completing my Science Baccalaureate (Honours Physics) at the University of Waterloo, I became interested in the prospect of molecular-scale engines and the question of what fundamental physical principles would enable their operation. In an effort to broach these questions, I wrote my undergraduate thesis, "Towards a Quantum Carnot Engine," under the supervision of Lucien Hardy at the Perimeter Institute. During that investigation, I analyzed the work performed by a quantum mechanical particle confined to a classical infinite square potential and subjected to a thermodynamic cycle of quantum adiabatic and isothermal expansions and compressions.

My investigation inspired more questions than it answered. What physical trait could distinguish the "engine" from the quantum "working fluid" it contained, if the engine too must be composed of quantum mechanical particles? In what limit could the engine cycle be described by a time-dependent classical potential? Finally, how could a thermodynamic cycle be generated in the absence of explicit time-depedent control of the Hamiltonian describing all of the particles comprising engine and fluid? Confounded, I turned my attention to molecular biology to see what Nature had already discovered.

This Thesis represents the outcome of my search so far.

Nathan S. Babcock
Calgary, Alberta
15 March 2015

Acknowledgement

I am immensely grateful to my Supervisor Barry Sanders and to my Co-Supervisor Dennis Salahub for their astounding patience, enthusiasm, insight, and support. I am deeply indebted to them for their wisdom and subtle guidance in all matters related to my development as a scientist and as a person.

I am grateful to the members of my Supervisory Committee, Robert Thompson and Sergei Noskov, for their thoughtful feedback and advice, and to the members of my Defence Committee, Peter Kusalik and Alán Aspuru-Guzik, for their experience and vision. I wish to express gratitude for the expertise of my scientific collaborators, Aurélien de la Lande, Bernard Lévy, Mark Raizen, Jan Řeháček, René Stock, and Nathan Wiebe, and also for past guidance from Lucien Hardy, Stefan Idziak, and Ray Laflamme.

For insightful discussions and words of encouragement, I wish to thank Ali Asadian, Ilya Balabin, Dave Bell, David Beratan, Mari Boesen, Hans Briegel, Cool Paul Carr, JJ Choquette, Victor Davidson, Paul Davies, Ivan Deutsch, David Feder, Graham Fleming, Gilad Gour, David Hayes, John Honek, Jonny Johannes, Stu Kauffman, Wolfgang Ketterle, Leah Kilvert, Judith Klinman, Ben Lavoie, Tony Leggett, Tina Chen Liu, Rebecca Lumsden, Rudy Marcus, Elliot Martin, Gerard Milburn, Rachid Ouyed, Ian Reid, Kevin Resch, Andrew Ringsmith, Marlan Scully, Michael Skotiniotis, Spiros Skourtis, Luca Turin, Vlatko Vedral, Gregor Weihs, and Ehsan Zahedinejad. I thank Robert Gennis for access to unpublished materials regarding biochemical experimental techniques. Computing facilities were provided by Westgrid and Compute Canada Calcul Canada.

This work would not have been possible without financial support from both of my primary funding agencies, the Natural Sciences and Engineering Research Council of Canada and Alberta Innovates—Technology Futures. This financial trust has afforded me enormous academic and creative freedom to explore topics related to the physics of nanotechnology at my own discretion.

To My Parents

"As above, so below."

Table of Contents

Part I

Part II

List of My Written Contributions

My peer-reviewed scientific articles, completed at the University of Calgary:

[2] Nathan S. Babcock, René Stock, Mark G. Raizen, and Barry C. Sanders, "Entangling identical bosons in optical tweezers via exchange interaction," *Canadian Journal of Physics* **86**, 549-555 (2008).

[3] René Stock, Nathan S. Babcock, Mark G. Raizen, and Barry C. Sanders, "Entanglement of group-II-like atoms with fast measurement for quantum information processing," *Physical Review A* **78**, 022301 (2008).

[4] Nathan Wiebe and Nathan S. Babcock, "Improved error-scaling for adiabatic quantum evolutions," *New Journal of Physics* **14**, 013024 (2012).

[5] Aurélien de la Lande, Nathan S. Babcock, Jan Řezáč, Barry C. Sanders, and Dennis R. Salahub, "Surface residues dynamically organize water bridges to enhance electron transfer between proteins," *Proceedings of the National Academy of Science* **107**, 11799-11804 (2010).

[6] Aurélien de la Lande, Nathan S. Babcock, Jan Řezáč, Bernard Lévy, Barry C. Sanders, and Dennis R. Salahub, "Quantum effects in biological electron transfer," *Physical Chemistry Chemical Physics* **14**, 5902-5918 (2012).

My peer-reviewed scientific articles, completed at the University of Waterloo:

[7] Marsha Kisilak, Heather Anderson, Nathan S. Babcock, MacKenzie R. Setzer, Stefan H. J. Idziak, and Eric B. Sirota, "An x-ray extensional flow cell," *Review of Scientific Instruments* **72**, 4305-4307 (2001).

[8] Brian Nieman, Xavier Commeinhes, Nathan S. Babcock, Ivan Frola, Rick Forgett, and Stefan H. J. Idziak, "An x-ray confinement cell for studies of complex fluids under shear and confinement," *Review of Scientific Instruments* **75**, 936-941 (2004).

My independently-authored articles:

[9] Nathan S. Babcock, "Towards a Quantum Carnot Engine," Undergraduate Thesis, University of Waterloo (2005).

[10] Nathan S. Babcock, "The Impact of Quantum Information Science: 45 Years Later and Still Plenty of Room," First Prize Winner, Institute for Quantum Information Science Grand Opening Essay Contest, University of Calgary (2005).

[11] Nathan S. Babcock, "Quantum Theory at Burning Man," *The Quantum Times* **3**, 1-3 (2008).

[12] Nathan S. Babcock, "Canonical Rate-Expression for Nonadiabatic Electron Transfer," manuscript in preparation.

List of Tables

List of Figures

List of Abbreviations

AADH	aromatic amine dehydrogenase
APS	American Physical Society
ASCII	American Standard Code for Information Interchange
AC	alternating current
Ala	alanine
ATP	adenosine triphosphate
BEC	Bose-Einstein condensate
CHARMM	Chemistry at HARvard Molecular Mechanics
CHSH	Clauser, Horne, Shimony, and Holt
Cl	cholorine
Cu	copper
Cys	cysteine
DC	direct current
DFT	density functional theory
DNA	deoxyribonucleic acid
ET	electron transfer
et al.	*et alia*
etc.	*et cetera*
Glu	glutamine
Gly	glycine
His	histidine
IOP	Institute of Physics
IUPAC	International Union of Pure and Applied Chemistry
K	potassium

Kr	krypton
Leu	leucine
LED	light emitting diode
LCAO	linear combination of atomic orbitals
LOCC	local operations and classical communication
Lys	lysine
M51A	methionine 51 to alanine mutant
M51K	methionine 51 to lysine mutant
M51L	methionine 51 to leucine mutant
MADH	methylamine dehydrogenase
MATLAB	matrix laboratory
Met	methionine
MD	molecular dynamics
MIT	Massachusetts Institute of Technology
N	nitrogen
N-quinol	amine-reduced
O	oxygen
O-quinol	dithionite-reduced
O-quinone	fully-oxidized
P. denitrificans	*Paracoccus denitrificans*
NAMD	Not just Another Molecular Dynamics
P52G	proline 52 to glycine mutant
PCR	polymerase chain reaction
PDB	protein data bank
Phe	phenylalanine

PHM	peptidylglycine α-hydroxylating monooxygenase
Pro	proline
QIP	quantum information processing
QKD	quantum key distribution
REMPI	resonantly enhanced multi-photon ionization
RF	radio frequency
RMSD	root-mean-square deviation
RSA	Rivest, Shamir, Adleman
Ru	ruthenium
SCF	self-consistent field
Ser	serine
Sr	strontium
TIP3P	transferable intermolecular potential, three point
TM	trade mark
transl.	translation
Trp	tryptophan
TTQ	tryptophan tryptoquinone / tryptophan tryptoquinol
USA	United States of America
Val	valine
VMD	visual molecular dynamics
Xe	xenon
Yb	ytterbium

Chapter 1

Summary of Contribution

> *The way life manages information involves a logical structure that differs fundamentally from mere complex chemistry. Therefore chemistry alone will not explain life's origin, any more than a study of silicon, copper and plastic will explain how a computer can execute a program.*
>
> —Paul Davies, 2013 [15]

James Watson and Francis Crick's discovery of the double helical structure of deoxyribose nucleic acid (DNA) in 1953 [16] set the stage for the discovery of the genetic code [17] and the application of information theory [18] to fundamental problems in biology. While quantum mechanics is known to provide the underlying physical foundation of anatomy and physiology by way of molecular biochemistry [19], the application of quantum mechanics to biological systems has heretofore been limited mostly to structural and spectroscopic studies. Recently, the role of dynamical quantum effects in biology has become a topic of intense academic interest [20]. This development opens up the possibility of a previously-unanticipated picture of microbiological systems as quantum information processing (QIP) machines [21].

In this Thesis, I investigate and characterize the dynamics of two diametrically different examples of quantum systems, drawn respectively from the areas of quantum computing and macromolecular biochemistry. Although these areas represent disparate fields of inquiry, the two systems I study both provide examples of the same underlying physical phenomenon: the controlled nonadiabatic breakdown of the Born-Oppenheimer approximation. More precisely, these systems represent physical applications of the control and

suppression of nonadiabatic quantum transitions that accompany the breakdown of the quantum adiabatic assumption of the Born-Oppenheimer approximation. I contribute solutions to existing problems in these two fields, and I discuss the physical parallels between the quantum dynamics of these physical systems.

The main body (Chapters 3 through 8) of this Thesis is divided into two Parts, respectively devoted to each of two separate investigations:

1. The first investigation concerns the generation of entanglement between ultracold neutral atoms, with application to quantum computing.

2. The second investigation concerns the efficient transfer of individual electrons between enzymes, with application to biological energy transduction.

In this introductory Chapter, I briefly summarize the nature of these two scientific contributions, with regard to their novelty, importance, limitations, and similarities.

1.1 Summary of Part I

In Part I of this Thesis, I describe my proposal for a two-qubit quantum logic gate to be implemented using qubits stored in the orbital angular momentum states of ultracold, Bosonic, neutral atoms. Part I of this Thesis comprises four chapters related to my proposal. The first of these Chapters provides necessary background material, whereas the remaining three chapters describe scientific investigations that I have carried out and reported in three corresponding peer-reviewed journal articles that I co-authored.

These scientific investigations are as follows:

- I investigate the traditional adiabatic speed limit for the linear operation of this gate by deriving a simple criterion to ensure its coherent operation and by running numerical simulations to demonstrate the validity of that criterion [2].

- I investigate the feasibility of carrying out a specific QIP application for this gate, in the form of a "loophole-free" physical test of Einstein, Podolsky, and Rosen's local-realistic model of empirical experience [3].

- I investigate a means to improve the fidelity of this gate over the limit set by Born and Fock's adiabatic approximation, and I show how a polynomial improvement in gate operation can be obtained using a coherent control technique [4].

I now briefly summarize the motivation, object, originality, impact, and limitations of these investigations in order to exhibit the merit of my contributions.

1.1.1 Motivation

In May of 1981, Richard Feynman delivered a keynote address to the assembly of the First Conference on Physics and Computation at the Massachusetts Institute of Technology (MIT). He conjectured that concepts and methods drawn from algorithmic complexity theory could be used to devise new tests of fundamental physical postulates [22]. During this lecture, he developed ideas originally proposed by Benioff, Bennett, Fredkin, Toffoli and others regarding the possibility of physically-reversible computation [23, 24]. He elucidated the concept of a quantum computer as a "universal quantum simulator," and he conceived the idea of an ordered set of quantifiably-equivalent complexity classes of quantum computing machines [22]. He expressed his belief "that with a suitable class of quantum machines you could imitate any quantum system, including the physical world."

Immense progress has been made in the field of quantum information science since Feynman gave that famous address. It is now established that some classically "hard" problems in computer science can be solved more efficiently on a quantum computer, even exponentially-so [21]. There is now a concerted, worldwide effort to develop the requisite physical components to construct both application-specific and universal QIP

machines. The physical realization of a scalable, universal quantum computer would render many present-day information security technologies obsolete, with global commercial and political ramifications [25, 26].

1.1.2 Object of Investigation

The object of this investigation is a quantum mechanical logic gate that operates on a pair of logical qubits. The qubits are respectively stored in the internal states of a pair of identical particles that are spatially-constrained to separate traps [27]. This logic gate is known as a "$\sqrt{\text{SWAP}}$ gate," and it is implemented by way of the controlled amplification of the exchange interaction between the two particles, as the tunneling barrier separating the two traps is precisely lowered and raised. This two-qubit logic gate represents an entanglement-generating class of quantum mechanical gates, analogous to the classical "exclusive-OR" gate operating on two bits of information [21]. It is known to provide a requisite physical component for a quantum computer built according to a "circuit-based" quantum computing architecture [27].

The $\sqrt{\text{SWAP}}$ gate was proposed in 1997 for quantum computing applications by Loss and DiVincenzo, based on the use of qubits realized in the Fermionic "spin states of coupled single-electron quantum dots" [27]. More recently, Hayes *et al.* adapted Loss and DiVincenzo's $\sqrt{\text{SWAP}}$ gate proposal [27] to be applied to qubits stored in nuclear spin states of Fermionic atoms constrained to the vibrational ground state of a pair of individual optical dipole traps ("laser tweezers") [28]. An experimental realization of a $\sqrt{\text{SWAP}}$ gate was concurrently demonstrated using qubits stored in the Zeeman states of an ensemble of Bosonic atoms confined to a double-well optical lattice potential [29].

In Hayes *et al.*'s conception of the gate, the tunneling barrier is effectively lowered and raised by using spatial control of the optical tweezers to combine and reseparate the traps. More specifically, gate operation is realized as a pair of initially-distant optical tweezers

are brought into proximity to the point of complete overlap, and then re-separated to their original positions. Precision control of the gate's speed allows the qubits to be put into an arbitrary superposition of "swapped" and "not-swapped" states. By definition, a $\sqrt{\text{SWAP}}$ gate puts an initially-unentangled pair of qubits into an equal superposition of "swapped" and "not-swapped" states. This gate can be used to perform universal quantum computation in concert with arbitrary single qubit rotations [27]. High-fidelity operation is ensured by performing the gate sufficiently slowly, so that the vibrational ground state of the atoms evolves quantum adiabatically with respect to the motion of the tweezers (*i.e.*, adiabatic state transfer with near-unit fidelity).

1.1.3 Originality of My Contributions

I propose, analyze, and develop a novel scientific application for a new physical realization of the $\sqrt{\text{SWAP}}$ quantum logic gate.

Following Hayes and coworkers [28], I adapt the exchange-based entanglement concept of DiVincenzo's proposal to store qubits stored in the non-magnetic total angular momentum states of the electronic configurations of Bosonic atoms [2, 3]. The novelty of my proposal is evinced in my departure from the use of magnetic spin degrees of freedom to store the logical qubit states, common to all three prior conceptions of the gate [27, 28, 29]. Responding to a practical insight made by Anderlini and coworkers [29], I propose instead to store qubits across "magnetic-field-insensitive" orbital angular momentum states of Bosonic atoms. I substantiate my proposal with a detailed quantitative analysis of its limitations. Because qubits are stored using stable and metastable electronic states of individual atoms cooled to their vibrational centre-of-mass ground state, I consider vibrational excitations during motion as the dominant source of gate decoherence. I analyze the gate's fidelity by deriving a criterion to ensure coherent adiabatic transport of the atomic vibrational states. This contribution is described in Chapter 4.

I justify the value of my proposal by elucidating a specific scientific application for it. I collaboratively develop a novel application for the gate in the form of a "loophole-free" test of Bell's inequality, and I carry out a basic analysis of the feasibility of performing this test in a single laboratory. This contribution is described in Chapter 5.

I invent a technique for improving gate fidelity beyond that implied by the standard adiabatic approximation. I show that this technique can be used to generate asymptotic improvements in gate operation. This contribution is described in Chapter 6.

1.1.4 Scientific Impact

The physical realization of a quantum computing architecture is made more efficiently-scalable if it is constructed using arrays of separate registers of qubits, wherein "several qubits can be stored for a long time and local quantum operations can be carried out with a very high fidelity" [30]. Arrays of trapped neutral atoms provide the opportunity to implement such architectures, if the realizations of the logical qubits are chosen to ensure that the qubits are encoded into a direct product space of the system [30]. Qubits stored separately in the nuclear and electronic subspaces of atoms allow for architectural constructions of this kind, and thus proffer significant advantages to quantum computing proposals by enabling single-atom quantum registers [30].

My proposed implementation of the $\sqrt{\text{SWAP}}$ gate provides an essential entanglement-generating component to atom-based QIP systems that employ hybrid registers of nuclear and electronic qubits. Hayes *et al.*'s proposal to implement the $\sqrt{\text{SWAP}}$ gate using qubits stored in nuclear spins does not exclude my proposal to implement it using non-magnetic orbital states. Rather, the specific choice of non-magnetic orbitals ensures that the state of an electronic orbital qubit can be decoupled from the states of any spin qubits stored in the atomic nuclei. The opportunity to manipulate and entangle multiple qubits that are simulatenously stored in distinct subsystems of the same atom enables a "novel approach"

to QIP with significant scalability advantages [30].

To this effect, my proposal [2, 3] has inspired the development of a hybrid proposal that combines the use of electronic orbital and nuclear spin qubits, in order to produce a quantum register of qubits stored in a single alkaline-earth atom [30]. A register of this kind can provide an essential component to a neutral-atom quantum computing implementation built according to either a circuit-based or a measurement-based architecture. It can also be extended to ionic quantum computing implementations [30]. This approach holds promise for the development of prototypes of atomistic QIP implementations, where technical issues regarding scaling efficiencies may be explored experimentally with regard to the development of optimization strategies for next generation systems.

In addition to its role in this key QIP application, my proposal for an entangling $\sqrt{\text{SWAP}}$ gate [2, 3] has also provided explicit motivation for independent investigations in a number of different areas of scientific inquiry. These areas include adiabatically-evolving optical lattice potentials [31], bounds on adiabatic quantum computing [32], low-cost multiple-trap optical-tweezer systems [33], scalable neutral atom quantum computing schemes [34], techniques for producing Bose-Einstein condensates [35], thermodynamics of magnetic materials [36], ultracold atomic collisions [37], and nuclear structures of exotic elements [38].

1.1.5 Obstacles and Limitations

Whereas an adiabatic exchange gate like the one I propose has been demonstrated *en masse* using an ensemble of qubit pairs trapped in an optical lattice [29], the implementation of this gate using a single pair of qubits "on-demand" [34] remains yet to be empirically demonstrated. The limiting factor holding back the "on-demand" realization of a two-qubit entangling gate would appear to be the difficulty associated with the preparation of pairs of individual alkaline-earth atoms in their vibrational ground states,

but experimental progress in this direction is proceeding rapidly [39, 40, 41, 42, 43, 44].

Although my proposal for the gate itself has inspired and motivated tangible scientific developments outlined above, my schemes for improving the gate's fidelity using nonadiabatic interference effects [4] and for employing the gate in a "loophole-free" Bell inequality test [3] have received less academic attention. Here, the lack of any rapid scientific follow-up may be attributed to the nascent state of the technologies involved. Naturally, a technique for optimizing the gate's performance [4] will not be of practical importance until demonstrations of the gate move beyond the proof-of-principle stage. Likewise, the gate cannot be reliably applied as part of a larger physical investigation (such as a Bell test [3]) until the technology has been refined to the point where it can be realized when required, repeatedly and robustly.

1.2 Summary of Part II

In Part II of this Thesis, I describe my quantiative analysis of data produced by molecular dynamics (MD) simulations of a metabolic redox complex, with regard to nonadiabatic electron transfer (ET) in this system. Part II of this Thesis comprises two Chapters related to my analysis. The first of these Chapters provides necessary background material, whereas the remaining chapter describes two of my scientific investigations as they relate to my independent contributions to one peer-reviewed scientific article that I co-authored on the subject. The presented contributions are as follows:

- I present statistical and geometrical analyses of classical nuclear trajectories generated by MD simulations of the solvated MADH–amicyanin complex to show that surface residues organize solvent dynamics at the complex interface [5].

- I present a categorical analysis of data generated by tunneling pathway calculations performed on the nuclear trajectories, to show that the disruption of the

infered solvent-organizing mechanism leads to reduced electronic coupling between the "donor" and "acceptor" redox states of mutant forms of the ET complex [5].

I now briefly summarize the motivation, object, originality, impact, and limitations of this scientific investigation in order to exhibit the merit of my contributions.

1.2.1 Motivation

In September of 1976, Albert Szent-Györgyi delivered a welcoming address during a workshop devoted to the topic of "Cell-Associated Water," at the First International Congress on Cell Biology in Boston [45]. He expressed his fascination with the "special place" that water occupies in biology, calling water both the "mater" and the "matrix" of life [45]. He emphasized water's integral role in life, declaring that there could be "no sharp separation between solvent and solute" in living systems. He expressed his belief that "water is not only a solvent which can separate molecules, but it is also a 'cement' which helps to hold the living machinery together" [45].

Scientific interest in water as an "active constituent" in cellular biology has grown enormously since Szent-Györgyi gave that welcoming address, and water is now recognized as "a substance that actively engages and interacts with biomolecules in complex, subtle, and essential ways" [46]. The idea that water might act as an adhesive in a metabolic complex, and even facilitate resonant charge transfer in one, gained credence in 1994 when Chen and coworkers succeeded in crystalizing the redox triad formed by the enzymes methylamine dehydrogenase (MADH), amicyanin, and cytochrome c_{551} [47]. Chen *et al.*'s crystal structure revealed a water molecule harboured at the interprotein interface between MADH and amicyanin, which might enhance donor-acceptor ET coupling if also present during biological ET.

The following year, Ermler and coworkers identified an analogous water molecule in the crystal structure of flavohemoglobin [48]. They hypothesized that [48],

> A striking feature of the region between the prosthetic groups is the high number of polar residues whose predominantly large side chains originate from all three domains. These residues may not act as electron mediator, but influence the electrochemical potential of the prosthetic groups, the dielectric constant of the intervening space, and finally the kinetics of the electron transfer process. The high electric field generated is reflected by a large number of firmly bound solvent molecules in this region. It may be speculated that the high electric field is mainly built up to fix the electron-transferring water molecule between the prosthetic groups.

Interest in solvent-mediated ET intensified in 2001 when Tezcan and coworkers [49] demonstrated that water molecules could facilitate ET in protein crystals, and again in 2004 after Klinman and coworkers [50] demonstrated that enzymatic ET in the protein peptidylglycine α-hydroxylating monooxygenase (PHM) is most likely to occur via solvent-mediated electronic coupling. In 2005, Lin and coworkers used MD simulations in conjunction with semi-empirical "extended Hückel" quantum chemistry calcuations to show that interprotein solvent organization could hypothetically play a key role in modulating biological ET rates [51].

In 2007, de la Lande and coworkers [52] carried out MD simulations of the native PHM enzyme alongside mutant forms of it. Their findings supported Lin *et al.*'s "structured water" [51] hypothesis, because they showed that experimentally-motivated mutations [53] were simulatenously correlated with decreased electronic couplings and decreased stability of a bridging water molcule in the space between the redox cofactors [52]. Thus arose a growing body of evidence indicating a key role for water as a mediator of charge and energy transfer in biomolecular systems.

1.2.2 Object of Investigation

The object of investigation is a nonadiabatic interprotein ET reaction carried out by the bacterial metabolic redox complex formed by the proteins MADH and amicyanin. Amicyanin serves as MADH's exclusive redox partner during metabolism, and therefore functions as a critical bottleneck during methylamine metabolism in the methylotrophic soil bacterium *Paracocous denitrificans* [54]. The partner exclusivity of MADH with amicyanin provides an essential empirical control that allows findings from *in vitro* site-directed mutagenesis experiments to be compared directly to their counterparts *in vivo*.

Two decades ago, Chen and coworkers showed that the interprotein interface between crystalized MADH and amicyanin held a water molecule that might enhance donor-acceptor ET coupling if it were also present in that location during biological ET [47]. The role that water might play modulating ET from MADH to amicyanin became a topic of empirical interest again in 2007, when Ma and coworkers (under the direction of Victor Davidson) carried out a set of redox experiments using native and mutant forms of amicyanin. They found that mutations performed on amicyanin's Methionine 51 ("Met51") surface residue had the effect of changing the kinetic mechanism governing ET from MADH to amicyanin—*without* significantly affecting the dissociation constant K_{d} associated with complex formation [14]. Ma *et al.* concluded [14],

> The interactions involving the Met51 side chain are entirely responsible for the change in ET parameters and conversion of the true ET reaction of native amicyanin into the conformationally gated ET reaction. Since the K_{d} for complex formation is not affected by the M51A mutation, it follows that the change in the kinetic mechanism of the reaction is to reduce the rate of a pre-existing normally rapid conformational rearrangement rather than to introduce a new slow reaction step. ... These results show that surface

> residues of redox proteins may not only dictate specificity for their redox protein partners but also be critical to optimize the orientations of the redox centers and intervening media within the protein complex for the ET event.

Methionine 51 is part of a hydrophobic patch of residues on the surface of amicyanin, not far from the location of the purported ET-enhancing water molecule in the crystal structure [55]. In light of Chen *et al.*'s findings [47]—as well as other findings indicating the importance of structured water molecules in mediating ET [48, 51]—Ma *et al.*'s results suggested that the Met51 mutation had disrupted the structure of an ET-mediating water network at the protein–protein interface.

1.2.3 Originality of My Contribution

> **I analyze data from MD simulations to demonstrate that amino acid residues at the interface of the MADH–amicyanin redox complex organize the dynamics of interprotein water molecules in order to facilitate nonadiabatic interprotein ET.**

Following the method of de la Lande and coworkers [52], I generated computer-simulated structures of the same mutant forms of amicyanin used by Ma and coworkers in their MADH–amicyanin redox experiments [14]. I implemented MD simulations of the MADH–amicyanin complex in solution using the CHARMM software package [56] with simulation parameters provided to me directly by Aurélien de la Lande. The novelty of my scientific contribution is found in my approach to analyzing the nuclear coordinate trajctories generated by these simulations.

After carrying out extensive qualitative inspections of the trajectory data using the "Visual Molecular Dynamics" (VMD) software [57], it became evident to me that the interprotein solvent dynamics of the mutant complexes bore striking differences from those

of the native complex, in terms of both the numbers of water molecules found inside the complex and the turbulence of their motion. In order to turn this qualitative, anecdotal insight into a quantitative, statistically-meaningful result, I independently conceived three quantitative figures of merit with which to compare the solvent dynamics of the native complex with those of the mutants. Specifically, I elected to measure

- the average number of water molecules trapped in the interprotein region,
- the probability of occupation of a particular doubly-hydrogen-bonded "water bridge" found linking MADH to amicyanin, and
- the number of distinct water molecules found occupying the bridge position over the course of each simulation.

Compared to the mutants, the native complex exhibited a quantitatively smaller number of trapped water molecules, a greater probability of bridge occupation, and a smaller number of different water molecules occupying the bridge position. These numbers together revealed the presence of a highly-stable solvent bridge in the native complex that was not present consistently in the mutant complexes.

In order to conclusively link the observed changes in solvent dynamics to reduced ET efficiency, I carried out "tunneling pathway" calculations on the trajectory data to estimate the strength of the electronic coupling between the "donor" and "acceptor" redox cofactors. I conceived and implemented detailed categorical analyses on the numerical results of those calculations. My analyses revealed that a water molecule in the stable "bridge" configuration afforded consistently superior ET coupling in comparison to other statistically-significant solvent configurations, confirming that the destabilization of the water bridge resulted directly in the decreased electronic coupling observed in the simulated mutant complexes.

1.2.4 Scientific Impact

My computational finding that surface residues organize the dynamics of interprotein solvent molecules in order to enhance ET between MADH and amicyanin adds strong evidence in support of a growing body of theoretical [58, 51, 59, 52, 60] and experimental [47, 50, 61] data showing that structured arrangements of water molecules play an essential role in controlling the rates of metabolic ET reactions.

My findings provide a rare example showing explicitly how a mutation performed on a surface residue that is not involved in ET coupling can nevertheless modulate the ET coupling strength of a redox complex. Previous theoretical studies have shown how protein surfaces might control the orientational structure of intervening solvent molecules to enhance or diminish the donor–acceptor electronic coupling strength [51, 52, 59]. My computationally-motivated explanation for how the mutation of nearby surface residues can control ET kinetics in a metabolic redox complex provides a unique and fundamental scientific contribution to the field of biological ET research.

My contribution is fundamentally important because it affords the opportunity for direct comparison between different realizations of the MADH–amicyanin complex, as it is expressed *in silico*, *in vitro*, and *in vivo*. Unlike the authors of studies involving metabolically-absent prosthetic systems [62], I do not need to extrapolate to interpret my findings with regard to their physiological relevance to actual living systems.

My physical interpretation of this data has been adopted by experimental biochemists in Victor Davidson's laboratory to motivate the need for novel experiments involving surface mutations performed on enzymatic proteins [63], and to interpret the results of new experiments that they have recently performed [64]. My findings have also motivated the development of new empirical techniques in microscopy [65]. With regard to long-term impact, my conclusions have helped to solidify an emerging consensus regarding the physiological role of structured water in mediating long-range ET. My findings have

had a direct and considerable impact on the opinion of the wider scientific community: ET-mediating structured water is no longer passed off as a "curiosity" [66], and it is now being seriously considered as "biochemical machinery" [67] that is "assigned a major role" [68] in facilitating "substantially enhanced rates of ET" [69] during metabolism.

1.2.5 Obstacles and Limitations

A limitation of the tunneling pathway analysis is its neglect of quantum interference effects between multiple pathways through the ET medium. Solvent-mediated ET systems have been shown to exhibit significant multi-pathway interference effects in model systems for biological ET [51], and quantum chemical calculations are necessary to rigorously incorporate the effects of these interferences. However, the emergence of an apparent "single-pathway regime" [51] in the native system suggests that the results of these semi-empirical pathway analyses will be reproduced by quantum chemical calculations when they are performed on this system.

More serious obstacles are presented by computational limitations that restrict the simulation duration to a timescale comparable to the length of the ET event itself, precluding the performance of simulations long enough to reproduce other conformational effects that may contribute to the observed changes in the reaction kinetics. Although simulations of the MADH–amicyanin system were able to partially explain the overall reduction in the experimentally observed ET rates in the mutant complexes, this explanation is only qualitative and it neglects the concomitant increase in the apparent activation free energy of the ET reaction. The loss of a single, dominant coupling pathway in the mutant complexes is consistent with a picture of the failure of ET theory due to Condon breakdown (see Section 7.3.5), and the emergence of a new kinetic mechanism identified by the experimentalists [14].

Conceptual difficulties—related to the problem of how to include the experimentally-hypothesized "previously unrecognized conformational rearrangement" into the reaction coordinate describing the reaction's activation step—arise in the event of the breakdown of the Born-Oppenheimer approximation *along* the ET reaction coordinate, as conformational motions (*i.e.*, rotational and translational motions of the nuclei) that are not accounted for by the Born-Oppenheimer approximation [70] begin to limit the reaction rate. The question of how to properly account for non-Born-Oppenheimer eigenstates that contribute to nuclear motions along the reaction coordinate of an enzymatic reactions remains an unresolved problem in biochemical physics.

1.3 Perspective

The Born-Oppenheimer treatment of a chemical reaction coordinate in terms of some electronic state(s) evolving adiabatically along with a classical ensemble of atomic centre-of-mass degrees of freedom is essentially the same, regardless of the specific electronic states involved or the number of atomic centre-of-mass degrees of freedom in the ensemble. For this reason, the system quantum logic gate examined in Part I provides a miniature analogue of the ET reaction complex examined in Part II. The total angular momentum electronic states in Part I are replaced by charge occupation states in Part II as the ensemble size scales from two atoms to many thousands of atoms.

In Chapter 2, I provide a brief review of the Born-Oppenheimer approximation and its implications because this approximation lays the physical foundation for a comparative analysis of the two systems examined in the remainder of the Thesis. In Chapter 9, I elaborate further on the intrinsic similarities shared by these two systems and I offer my perspective regarding chemical reactions as QIP algorithms.

Chapter 2

Nonadiabatic Transitions

It can be said that wave mechanics is the tool for a complete understanding, on a physical basis, of all the fundamental facts of chemistry.

—Walter Heitler, 1956 [71]

In essence, the adiabatic theorem states that a quantum mechanical system that is prepared in an instantaneous eigenstate of its time-dependent Hamiltonian will remain in a corresponding instantaneous eigenstate of the Hamiltonian to a good approximation, if the Hamiltonian evolves sufficiently slowly in time [72]. Quantum adiabatic processes are used to model systems of interest in many areas of physics and engineering [73]. The separation of timescales afforded by this approximation allows the complexity of a model describing the system to be greatly reduced, as the motions of the system's slowly-evolving degrees of freedom are evaluated in an effectively time-independent limit.

The adiabatic approximation is of particular importance to the field of theoretical chemistry, where it was implicitly employed by physicists Walter Heitler and Fritz London in order to construct the first quantum mechanical model of the covalent bond [71, 74]. They constructed their model by considering two distant hydrogen atoms in their ground electronic states, gradually and adiabatically approaching each other [71]. They found that the degeneracy of the singlet and triplet states of the electrons orbiting the distant nuclei was broken as the nuclei approached each other, resulting in an attractive potential for antiparallel electronic spins (*i.e.*, bonding), and a repulsive potential for parallel electronic spins (*i.e.*, antibonding). This adiabatic description of a molecular system continues to provide the theoretical foundation of quantum chemistry today [70, 75].

2.1 The Adiabatic Theorem

In 1928, Born and Fock developed the adiabatic theorem to rigorously describe the dynamics of a quantum mechanical system described by a time-dependent Hamiltonian $\hat{\mathcal{H}}(t)$ that evolves "very slowly" in time t [76]. Assuming the system to be initially prepared at time $t = t_0$ in an instantaneous Hamiltonian eigenstate $|\psi(t_0)\rangle = |a(t_0)\rangle$ with energy $E_a(t_0)$, Born and Fock estimated the probability that the system would make a transition from the initial eigenstate $|a(t_0)\rangle$ to some final (non-degenerate) eigenstate $|b(t)\rangle$ with energy $E_b(t)$, where $\langle a(t)|b(t)\rangle = 0$ [76]. A summary of their derivation follows.

For a Hamiltonian evolving sufficiently-slowly in time, the probability amplitude $C_b(t)$ describing the occupation of eigenstate b at time t is approximately given by the equation,

$$C_b(t) \approx \frac{1}{h} \int_{t_0}^{t} \frac{\dot{\hat{\mathcal{H}}}_{ba}(t')}{\omega_{ba}(t')} \, e^{\mathrm{i} \int_{t_0}^{t'} \omega_{ba}(t'')\mathrm{d}t''} \, \mathrm{d}t', \tag{2.1}$$

where $\dot{\hat{\mathcal{H}}}_{ba} = \langle b(t)|(\partial\hat{\mathcal{H}}(t)/\partial t)|a(t)\rangle$ by convention, $h\omega_{ba}(t) = E_b(t) - E_a(t)$, and h is Planck's constant [76]. As a crude estimate, we may assume ω_{ba} and $\partial\hat{\mathcal{H}}/\partial t$ are approximately time-independent to obtain

$$P_{ba}(t) \lesssim \frac{4|\dot{\hat{\mathcal{H}}}_{ba}|^2}{h^2\omega_{ba}^4}, \tag{2.2}$$

where $P_{ba}(t)$ is the probability of a transition occuring from the initial state $|a(t_0)\rangle$ to the final state $|b(t)\rangle$ [76]. More generally, if the time-variation of the phase factor in eq. (2.1) evolves rapidly and independently from the time-variation of the Hamiltonian, then it is reasonable to expect the integral (2.1) to sum incoherently. In this limit, the transition amplitude C_b becomes proportional to $\dot{\hat{\mathcal{H}}}_{ba}/\omega_{ba}$, so that the global condition

$$\|\dot{\hat{\mathcal{H}}}_{ba}\| \ll h\omega_{ba}^2 \tag{2.3}$$

is adequate to ensure that C_b is negligibly small. For a suitably chosen eigenbasis, the final state of the system $|\psi(t)\rangle$ at time t will be given by

$$|\psi(t)\rangle \approx e^{-\mathrm{i}\int_0^t E_0(t')\mathrm{d}t/h} \, |a(t)\rangle. \tag{2.4}$$

The criterion (2.3) and the result (2.4) are widely referred to as the "adiabatic approximation" [76]. This approximation suggests the existence of an upper bound on the probability of a transition away from an initially-prepared eigenstate of a time-depedent Hamiltonian, if the Hamiltonian evolves sufficiently slowly in time. In other words, the probability of transforming the initial state $|a(t_0)\rangle$ into the final state $|a(t)\rangle$ can be made arbitrarily close to unity, simply by configuring the Hamiltonian to evolve sufficiently slowly in time. Such a time evolution is called an *adiabatic evolution*.

2.1.1 Adiabatic Errors

In 2004, Marzlin and Sanders brought the validity of the adiabatic approximation into dispute by devising a counter-example to it [72], wherein the naïve neglect of the exponential phase factor in eq. (2.1) resulted in the generation of a non-neglible cumulative error. The Marzlin-Sanders counter-example motivated interest in the development of more rigorous derivations of the adiabatic approximation and the formulation of tight bounds to describe deviations from it (see Refs. [4, 77] and citations therein).

Strict conditions ensuring that a system will evolve approximately adiabatically are now given in terms of the total system's evolution time, the differences between its instantaneous eigenvalues, and various orders of "reduced-time" derivatives of its Hamiltonian [77]. Asymptotic expressions of the magnitudes of nonadiabatic errors are given as mathematical expansions in terms of the system size and the evolution duration [4, 77].

The discovery of asymptotically-tight expressions for the error in the adiabatic approximation creates opportunities for the application of algorithmic complexity theory to the analysis of fundamental problems in fields where the adiabatic approximation is used as a founding assumption, such as the field of quantum chemistry.

2.2 Adiabatic Description of Atoms and Molecules

The calculation of quantifiable properties of a chemical system directly from the principles of quantum statistical mechanics remains the central problem of theoretical chemstry. The number of degrees of freedom required to completely describe a chemical system using quantum mechanics grows exponentially with the number of particles (*i.e.*, electrons and nuclei) comprising the system [78], unlike the polynomial number of degrees of freedom required by classical mechanics. The exponential scaling of the quantum mechanical description of a system renders intractable the numerical treatment of sizeable quantum systems on classical computers, thus motivating the need for quantum computers to describe quantum chemical systems [78].

A common practice for reducing the number of degrees of freedom needed to describe a chemical system is to neglect the system's explicit magnetic interactions [75, 79]. When magnetic interactions are ignored, the nonrelativistic Hamiltonian describing a chemical system $\mathcal{C}$ of charged particles is reduced to the so-called Coloumb Hamiltonian $\hat{\mathcal{H}}_{\mathcal{C}}$, where

$$\hat{\mathcal{H}}_{\mathcal{C}} = \sum_{i=1}^{N} \frac{\hbar^2}{2m_i} \nabla_i^2 + \sum_{i<i'}^{N} \frac{q_i \, q_{i'}}{4\pi\varepsilon_0 \, r_{ii'}} \,, \tag{2.5}$$

and where i (i') enumerates a whole number N of charged particles, q_i ($q_{i'}$) is the charge of particle i (i'), ∇_i^2 is the Laplacian acting on the i^{th} particle, m_i is the i^{th} particle's mass, π is the ratio of a circle's circumference to its diameter, ε_0 is the permittivity of free space, and $r_{ii'}$ is the scalar quantifying the distance between particles i and i' .

Another method for reducing the requisite number of degrees of freedom needed to describe a chemical system is given in the approach initially developed by Born and Oppenheimer in 1927 [80], by treating the nuclei as stationary point charges on the timescale of the electronic motion. This semiclassical approach was conceptually essential to Heitler and London's seminal treatment of the hydrogen molecule, when they considered a system of two hydrogen nuclei adiabatically approaching one another [74].

2.2.1 The Born-Oppenheimer Approximation

The analysis of a chemical system may be greatly simplified if the nuclei contained in it may be regarded as slowly-moving point charges residing on an electrostatic potential defined by a single electronic eigenstate, such that the nonadiabatic effect of nuclear motion on the electronic state may be ignored [79, 81]. This traditional treatment is known as the "Born-Oppenheimer" method in honour of physicists Max Born and Robert Oppenheimer who elucidated it in German in 1927 [80].

The Born-Oppenheimer approximation is derived from two assumptions:

- **Assumption 1** — Nuclear positions are treated as *classical point particles*, for the purpose of evaluating the Coulomb potential terms in eq. (2.5).
- **Assumption 2** — Nuclear motions are treated *adiabatically* with respect to the electronic motions, for the purpose of evaluating the kinetic terms in eq. (2.5).

In the limit defined by these assumptions, it is convenient to express the Coulomb Hamiltonian in the form,

$$\hat{\mathcal{H}}_{\mathcal{C}} = \hat{\mathcal{K}}_{\mathrm{n}} + \hat{\mathcal{K}}_{\mathrm{e}} + \hat{\mathcal{V}}, \tag{2.6}$$

where $\vec{\mathcal{K}}_{\mathrm{n}}$ and $\vec{\mathcal{K}}_{\mathrm{e}}$ each respectively comprise the sums of the nuclear and electronic kinetic energy operators, and where $\vec{\mathcal{V}}$ is the potential energy operator representing the sum of the pairwise Coulomb interactions between all of the particles. We define the "electronic Hamiltonian" operator $\hat{\mathcal{H}}_{\mathrm{e}}(\vec{r}_{\mathrm{e}}, \vec{r}_{\mathrm{n}})$ such that $\hat{\mathcal{H}}_{\mathrm{e}} = \hat{\mathcal{K}}_{\mathrm{e}} + \hat{\mathcal{V}}$.

Conventional treatments of the Born-Oppenheimer theorem parametrically diagonalize the electronic subspace of $\hat{\mathcal{H}}_{\mathrm{e}}$ by assuming that the nuclear wavefunction is well-approximated by collection of fixed point charges, in order to define a complete set of $\vec{r}_{\mathrm{n}}(t)$-parameterized electronic eigenfunctions $\{\chi_j(\vec{r}_{\mathrm{e}}; \vec{r}_{\mathrm{n}})\}$, where $\{j\}$ is the set of whole numbers. These eigenfunctions obey the eigenvalue equation

$$\hat{\mathcal{H}}_{\mathrm{e}}(\vec{r}_{\mathrm{e}}, \vec{r}_{\mathrm{n}})\, \chi_j(\vec{r}_{\mathrm{e}}; \vec{r}_{\mathrm{n}}) \;=\; V_j(\vec{r}_{\mathrm{n}})\, \chi_j(\vec{r}_{\mathrm{e}}; \vec{r}_{\mathrm{n}}), \tag{2.7}$$

where $\vec{r}_{\rm e}$ and $\vec{r}_{\rm n}$ are vectors collectively representing the positions of all the electrons and nuclei, respectively. According to this method, the electronic Hamiltonian $\hat{\mathcal{H}}_{\rm e}$ defines a discrete manifold of potential energy hypersurfaces $\{V_j(\vec{r}_{\rm n})\}$ [79].

The Born-Oppenheimer theorem states that, to a "good approximation" [79], the potential surfaces $\{V_j(\vec{r}_{\rm n})\}$ may be used in place of the proper electronic Hamiltonian operator in eq. (2.6), in order to generate the nuclear eigenvalue equation

$$\hat{\mathcal{H}}_{\mathcal{C}}\,\phi_k(\vec{r}_{\rm n}) \;\approx\; \Big(\hat{\mathcal{K}}_{\rm n} + V_j(\vec{r}_{\rm n})\Big)\,\phi_k(\vec{r}_{\rm n}) \;=\; E_{jk}\,\phi_{jk}(\vec{r}_{\rm n}). \tag{2.8}$$

To quantify the validity of the approximaton, it is convention to insert the separable *ansatz* solution $\Psi_{jk}(\vec{r}_{\rm e},\vec{r}_{\rm n}) = \chi_j(\vec{r}_{\rm e};\vec{r}_{\rm n})\,\phi_k(\vec{r}_{\rm n})$ (where $\{k\}$ is the set of whole numbers) into the time-independent Schrödinger equation for $\hat{\mathcal{H}}_{\mathcal{C}}$. Doing so, we find that

$$\hat{\mathcal{H}}_{\mathcal{C}}\,\Psi_{jk}(\vec{r}_{\rm e},\vec{r}_{\rm n}) \;=\; E_{jk}\,\Psi_{jk}(\vec{r}_{\rm e},\vec{r}_{\rm n}) \;+\; \mathcal{E}(\vec{r}_{\rm e},\vec{r}_{\rm n})\,. \tag{2.9}$$

where the error $\mathcal{E}(\vec{r}_{\rm e},\vec{r}_{\rm n})$ in the approximation [79] is given by

$$\mathcal{E}(\vec{r}_{\rm e},\vec{r}_{\rm n}) = -\sum_{n=1}^{N_{\rm n}} \frac{\hbar^2}{2m_n^i} \sum_{i=1}^{3} \left(2\,\frac{\partial\chi}{\partial r_n^i}\,\frac{\partial\phi}{\partial r_n^i} \;+\; \frac{\partial^2\chi}{\partial {r_n^i}^2}\,\phi \right), \tag{2.10}$$

such that n enumerates the set $\{m_n\}$ of $N_{\rm n}$ nuclear masses. Likewise, n and i enumerate the set $\{r_n^i\}$ that defines the $3N_{\rm n}$ elements of $\vec{r}_{\rm n}$.

In the limit where $\mathcal{E}(\vec{r}_{\rm e},\vec{r}_{\rm n})$ is negligible, the finite sets $\{j\}$ and $\{k\}$ approximately define the quantum numbers that enumerate the $\vec{r}_{\rm n}$-parameterized eigenstates of the Coulomb Hamiltonian (2.6), such that the *parameter* $\vec{r}_{\rm n}$ in $\chi_j(\vec{r}_{\rm e};\vec{r}_{\rm n})$ effectively describes the *centroids* of the nuclear wavepackets defined by $\phi_k(\vec{r}_{\rm n})$ [70]. According to Feynman's theorem [82], we may use the derivatives of the $V_j(\vec{r}_{\rm n})$ with respect to the elements of $\vec{r}_{\rm n}$ in order to determine the net of electrostatic forces on the nuclei, and thus the classical equations of motion of the nuclear centroids. If the error $\mathcal{E}(\vec{r}_{\rm e},\vec{r}_{\rm n})$ were to be exactly zero, then in that case no force calculation would be necessary, as the eigenstates $\phi_{jk}(\vec{r}_{\rm n})$ would be exact and $\Psi_{jk}(\vec{r}_{\rm e},\vec{r}_{\rm n})$ would truly define a stationary eigenstate of the system.

However, in general $\mathcal{E}(\vec{r}_{\rm e}, \vec{r}_{\rm n})$ is not zero, and the positions of the nuclear centroids will evolve in time under the influence of the potential $V_j(\vec{r}_{\rm n})$.

The atomic nuclei are three orders of magnitude more massive than the electrons, and move sluggishly in comparison; electronic velocities can approach 10^8 cm/s, whereas nuclear velocities rarely exceed 10^5 cm/s in chemical systems of interest [70]. The relatively large masses and low velocities of the nuclei found in chemical systems of interest help to ensure the validity of both assumptions of the Born-Oppenheimer approximation, so that the system dynamics may be described by the quantum adiabatic evolution of an electronic eigenstate $\chi_j(\vec{r}_{\rm e}; \vec{r}_{\rm n})$ (typically the ground state χ_0) as it follows the classical trajectory defined by the dynamics of the slowly-moving nuclear centroids.

Thus, the central result of the Born-Oppenheimer theorem is that the nuclear and electronic components of the wavefunction describing a chemical system are approximately *separable* and that the time-evolution of the electronic component of the wavefunction will follow the centroids defined by the nuclear component *quantum adiabatically*. In this manner, the time-dependent dynamics of the entire system may be described in terms of the classical trajectories of the nuclear centres. This *adiabatic description* [70] of a system of atoms provides the theoretical starting point for the analysis of many systems of interest in both physics and chemistry, including the ones examined in this Thesis.

2.3 Born-Oppenheimer Breakdown

The adiabatic description defined in Section 2.2.1 will break down when the quantum mechanical character of the nuclear position distribution cannot be neglected when evaluating the Coulomb interactions, or when the coupling between the electronic eigenstates by the nuclear momentum operator cannot be neglected. Let us consider the conditions for the validity of each of these assumptions in order.

2.3.1 Validity of Assumption 1 (Nuclear Classicality)

The first assumption of the Born-Oppenheimer approximation is to treat the nuclei as a set of classical point charges—each located at the centroid of the probability distribution describing the location of an individual nucleus [70]. The assumption is meaningful and valid when the degree of overlap between wavefunctions describing individual nuclei are negligible, and when the nuclear wavefunctions are tightly-localized in space compared to the electronic wavefunction(s).

The validity of this assumption is based upon the quantum mechanical property of *cluster separability* (see Section 5-4 of Ref. [83]). Strictly-speaking, the wavefunction describing a collection of particles must be correctly symmetrized with respect to any identical bosonic or fermionic nuclei it describes, in accordance with the Pauli exclusion principle. This general symmetrization requirement implies that identical particles are always entangled and cannot in general be represented separably. However, entanglement of this kind has "no observable effect" for distantly-separated particles [83], because the matrix elements of an operator representing a local observable vanish with respect to the states of a remote particle. As a result, the wavefunctions describing local clusters of particles may be treated as being separable from the wavefunctions of distant particles with which they do not overlap. Spatially-separated identical particles are effectively distinguishable.

Assumption 1 may be taken to be exactly fulfilled for many quantum chemical systems of interest. Examples of its breakdown include hydrogen-tunneling and Bose-Einstein condensation.

2.3.2 Validity of Assumption 2 (Adiabaticity)

The second assumption of the Born-Oppenheimer approximation is to assume that the nuclei move infinitessimally slowly and thus adiabatically with respect to the motions of

the electrons. Under this assumption, the electronic subsystem—having been prepared in an eigenstate of the electronic Hamiltonian—will evolve quantum adiabatically along with the nuclear dynamics. The failure of this assumption corresponds to a *nonadiabatic* transition from one electronic state of the system to another.

The probability of a nonadiabatic transition remains negligible, where the energy spacing of the electronic potential surfaces is much larger than the corresponding electronic matrix elements of the nuclear kinetic energy operator. Born-Oppenheimer breakdown tends to occur near "avoided crossings" of the potential surfaces, where electronic eigenstates with different symmetries approach degeneracy. Evidently, the $\frac{\partial^2 \chi}{\partial {r_{\mathrm{n}}^i}^2}\phi$ terms in eq. (2.10) couple different electronic states of the system without affecting the nuclear configuration. Nonadiabatic transitions that arise from the $\frac{\partial^2 \chi}{\partial {r_{\mathrm{n}}^i}^2}\phi$ terms are of particular interest in chemistry because these "vertical transitions" obey the Franck-Condon principle [84].

2.3.3 Statistical Mechanical Considerations

It is of value to reiterate that that the $\vec{r}_{\mathrm{n}}(t)$-parameterization used to define the electronic eigenstates assumes that the nuclear probability density is described by a set of distinct wavepackets that are much more compact than the probability density of the electronic eigenstate(s). This assumption allows the nuclei to be treated as an arrangement of effectively-classical point charges [70, 75, 81]. The assumption of nuclear locality is of little consequence to the traditional study of molecules and solids with rigid, well-defined chemical structures. As we have discussed, this assumption is also appropriate for the description of the dynamics of systems that do not involve nonadiabatic transitions.

In principle, however, this semiclassical assumption poses a severe complication to the statistical mechanical analysis of molecules with significant conformational motions [70], such as biological molecules. This is because the eigenstates $\chi_j(\vec{r}_{\mathrm{e}}; \vec{r}_{\mathrm{n}})$ and $\phi_k(\vec{r}_{\mathrm{n}})$ do not

correspond to the canonical eigenstates of a statistical mechanical ensemble, and therefore cannot generally be used to generate the Boltzmann or Gibbs entropy functions needed to define the free energies of the system. This *caveat* has fundamental implications related to the meaningful definition of the reaction coordinate(s) used to describe nonadiabatic physical processes, including nonadiabatic chemical reactions with large activation energies that are expected to contain contributions from higher-order non-Born-Oppenheimer eigenstates, such as ET from MADH to amicyanin (see Section 7.5).

2.4 Controlled Nonadiabatic Dynamics

The couplings between the "external" centre-of-mass degrees of freedom and the "internal" electronic degrees of freedom that are introduced by the "error" terms in eq. (2.10) provide effective means for controlling the dynamics of a variety of quantum mechanical systems in the limit as a pair of degenerate "diabatic" (i.e., uncoupled) internal basis states are subject to a nonadiabatic degeneracy-splitting effect when the coupling between the diabatic states is "turned on."

The use of adiabatic control of one degree of freedom in order to generate *coherent* nonadiabatic dynamics along another degree of freedom has been implicitly proposed, as a means of implementing an entangling gate between atomistic qubits [2, 3, 85]. Meanwhile, controlled *incoherent* nonadiabatic transitions are already essential to the operation of the biochemical systems that carry out cellular metabolism, where they enable efficient, site-specific electron transfer between redox enzymes [86]. The remainder of this Thesis provides a study revealing how the individual models used to describe the coherent exchange-based entangling gate examined in Part I and the incoherent biological electron transfer system examined in Part II are related by a single underlying quantum information theoretic resource—entanglement.

Part I

When we get to the very, very small world—say circuits of seven atoms—we have a lot of new things that would happen that represent completely new opportunities for design. Atoms on a small scale behave like nothing *on a large scale, for they satisfy the laws of quantum mechanics. So, as we go down and fiddle around with the atoms down there, we are working with different laws, and we can expect to do different things. We can manufacture in different ways. We can use, not just circuits, but some system involving the quantized energy levels, or the interactions of quantized spins, etc.*

—Richard P. Feynman, 1959 [87]

Chapter 3

Quantum Information Processing

> *When two systems, of which we know the states by their respective representatives, enter into temporary physical interaction due to known forces between them, and when after a time of mutual influence the systems separate again, then they can no longer be described in the same way as before, viz. by endowing each of them with a representative of its own. I would not call that* one *but rather* the *characteristic trait of quantum mechanics, the one that enforces its entire departure from classical lines of thought. By the interaction the two representatives (or ψ-functions) have become entangled.*
>
> —Erwin Schrödinger, 1935 [88]

In 1935, Albert Einstein, Boris Podolsky, and Nathan Rosen wrote to the Physical Review asking, "Can Quantum-Mechanical Description of Physical Reality Be Considered Complete?" They proposed that [89],

> In a complete theory there is an element corresponding to each element of reality. A sufficient condition for the reality of a physical quantity is the possibility of predicting it with certainty, without disturbing the system. In quantum mechanics in the case of two physical quantities described by non-commuting operators, the knowledge of one precludes the knowledge of the other. Then either (1) the description of reality given by the wave function in quantum mechanics is not complete or (2) these two quantities cannot have simultaneous reality.

According to their chosen definition of a "complete theory," Einstein, Podolsky, and Rosen demonstrated that "the wave function does not provide a complete description of the physical reality" [89]. They did not answer questions of whether such a complete description could be possible, or what specifically it would entail. Later the same year, Erwin Schrödinger coined the term "entanglement" to measure the degree to which a pair of spatially-separated quantum systems cannot be described by a separable pair of wavefunctions [88]. He identified entanglement as "*the* characteristic trait of quantum mechanics, the one that enforces its entire departure from classical lines of thought" [88].

According to quantum mechanics, the appropriate set of entanglement measurements performed on a pair of entangled particles will be perfectly correlated with each other, yet individually random and undetermined until the time of measurement. The indeterministic aspect of the measurement outcome presents philosophical difficulties, because quantum mechanics does not specify any local mechanism to enforce the correlation of spatially-separated measurements in the absence of a predetermined outcome.

Following the publication of Einstein, Podolsky, and Rosen's paper, considerable effort was directed towards the discovery a deeper theory containing "hidden variables" to account for the "elements of reality" missing from quantum mechanics [90]. David Bohm proposed a hidden variable interpretation of quantum mechanics to rationalize the existence of nonlocal quantum correlations using nonlocal hidden variables [91, 92], but this construction recovers Einstein, Podolksy and Rosen's realism at the cost of locality.

The search for a local *and* realistic hidden variable theory came to its apparent end in 1964, with the publication of an article by John Bell "On the Einstein Podolsky Rosen Paradox" [90]. Bell proved that no Lorentz-invariant local hidden-variable theory could reproduce the statistical correlations of quantum mechanics [90]. In other words, any hidden-variable interpretation of quantum mechanics must be inherently nonlocal (such as Bohmian mechanics [91, 92]).

3.1 Quantum Information Theory

In the early 1930s, Paul Dirac [93] and John von Neumann [94] formalized the mathematical foundations of quantum mechanics in terms of operators acting on a Hilbert space. Alan Turing defined a universal computing machine in 1936 [95], and Claude Shannon derived the *noisy channel coding theorem* in his seminal work, "The Mathematical Theory of Communication," in 1948 [18]. These key developments laid the information theoretic foundation for the computational implications of Bell's theorem to be recognized over the ensuing decades.

Academic interest in quantum information theory evolved rather quietly until 1982, when Richard Feynman proposed his concept of a "quantum computer"—a computer that would be uniquely capable of efficiently simulating a quantum mechanical system [22]. In 1983, Stephen Weisner proposed quantum mechanical protocols for "transmitting two messages either but not both of which may be received" and for producing currency that is "physically impossible to counterfeit" [96]. In 1984, Charles Bennett and Gilles Brassard devised a scheme for using quantum entanglement to securely communicate (*i.e.*, distribute) a private cryptographic key from one party to another [21]. In 1985, David Deutsch formalized Feynman's concept of a universal quantum computer by defining the quantum analogue of a Turing Machine [97]. In 1989, Deutsch gave tangible significance to this abstract result by showing that univeral quantum computation could be practically achieved on an array of quantum bits ("qubits") by implementing three-qubit Toffoli gates in conjuction with single-qubit operations and measurements [98, 99].

In 1994, Peter Shor devised an algorithm to factor large integers on a quantum computer exponentially faster than the fastest known classical algorithm [100]. Shor's algorithm presented a tractable scheme for factoring arbitrarily large integers, enabling it to be used to break public key cryptosystems such as the established Rivest-Shamir-

Adleman (RSA) encryption algorithm [100]. At that time, the construction of a practical quantum computer was considered intractable, because of the prevalent belief that the decoherence of a single qubit would corrupt the computer's entire memory due to entanglement [101, 102]. The following year, Shor showed that if qubits could be assumed to decohere independently, that the multi-qubit entanglement could be exploited as a quantum error-correcting resource, in order to restore the integrity of the computer memory [101]. This suggested the possibility of a "quantum analog" to Shannon's noisy channel coding theorem [21], which Seth Lloyd derived in 1997 to prove that quantum computing could be made physically tractable [102].

Quantum computers gained strategic military importance [25] with the discovery of Shor's algorithm and fault-tolerant schemes to implement it. Enormous public and private resources have since been allocated for the development of QIP technologies, and research institutes have opened worldwide for the dedicated study of quantum information science. Governmental and corporate investments in quantum key distribution schemes (to enable "private-key" encryption schemes that are invulnerable to a quantum attack) have blossomed [26]. Today, major corporate entities such as Microsoft, Google, and Lockheed-Martin have dedicated quantum computing initiatives [103]. Programs to develop of QIP technologies have become critical components in the economic and political strategies of industrialized nations.

3.2 Quantum Computing Architectures

In 1994, DiVincenzo proved that combinations of two-qubit gates (along with arbitrary one-qubit gates) could be used instead of three-qubit Toffoli gates to achieve universal quantum computation [99]. This revelation established that quantum computations could be efficiently performed in an operational paradigm defined by a set of one- and two-qubit

gates acting on a separable array of qubits—analogous to the semiconductor gates that operate on circuits of electrostatically-encoded bits in conventional computers.

This picture of a quantum computation in terms of a program of unitary one- and two-qubit operations has come to be known as the "circuit model" of quantum computing because quantum algorithms formulated under it can be visually represented a linear circuits where the "wires" depict individual qubits progressing along a time axis through an ordered sequence of quantum gates. Today, the circuit model represents one of three dominant approaches to designing QIP architectures, discussed as follows.

3.2.1 Circuit Model Quantum Computing

According to the circuit model of quantum computing [21], quantum information is encoded into a separable ensemble of binary quantum mechanical elements called "qubits." A qubit is a mathematical object described by a unit-normalized, two-dimensional, complex vector in an inner product space called a *Hilbert space* [21]. The two basis states of each qubit are typically represented using Dirac notation in the logical basis $\{|0\rangle, |1\rangle\}$, where $|0\rangle$ and $|1\rangle$ represent complex, two-dimensional column vectors such that

$$|0\rangle = \begin{bmatrix} 1 \\ 0 \end{bmatrix} \qquad \text{and} \qquad |1\rangle = \begin{bmatrix} 0 \\ 1 \end{bmatrix}. \tag{3.1}$$

The circuit model assumes that an arbitrarily large number of qubits can be initialized in the $|0\rangle$ state and ultimately measured in the logical basis with arbitrarily-high fidelity. It also assumes that unitary single-qubit and two-qubit operations can be performed on specified selections of qubits with arbitrarily-high precision. The model is readily generalized to account for imperfect qubit initializations and operations by way of quantum error-correcting algorithms [21].

A quantum computer designed using the circuit-model architecture is said to perform "universal" quantum computation if it can reproduce the effect of any specified unitary

operation in the Hilbert space defined by an arbitrarily large number of initial qubits, to an arbitrarily-specified precision. In practice, any actual implementation of a circuit-model quantum computer will be built out of a finite set of pre-defined unitary operations called "gates." A set of gates is said to be universal if a selection of those gates can be used to implement any overall unitary operation on a finite number of qubits to arbitrary precision in finite time [21]. A prototypical set of univeral quantum gates are defined using the single-qubit Pauli spin matrices [104],

$$\hat{\sigma}_{\mathrm{x}} = \begin{bmatrix} 0 & 1 \\ 1 & 0 \end{bmatrix}, \qquad \hat{\sigma}_{\mathrm{y}} = \begin{bmatrix} 0 & -\mathrm{i} \\ \mathrm{i} & 0 \end{bmatrix}, \qquad \hat{\sigma}_{\mathrm{z}} = \begin{bmatrix} 1 & 0 \\ 0 & -1 \end{bmatrix}, \tag{3.2}$$

and the two-qubit "controlled-phase" (matrix) operator

$$\mathrm{c}\hat{\mathrm{Z}} = \begin{bmatrix} 1 & 0 & 0 & 0 \\ 0 & 1 & 0 & 0 \\ 0 & 0 & 1 & 0 \\ 0 & 0 & 0 & -1 \end{bmatrix}. \tag{3.3}$$

Universal quantum computation can be achieved using an ensemble of initialized qubits when two-qubit controlled-phase operations can be implemented in conjunction with unitary single-qubit "rotations" of the form $\hat{R}_{\vec{n}}(\theta)$ such that

$$\hat{R}_{\vec{n}}(\theta) = \exp(-\mathrm{i}\theta\, \vec{n} \cdot \hat{\vec{\sigma}}), \tag{3.4}$$

where $\vec{n}$ is a real, arbitrarily-chosen unit vector, and where $\hat{\vec{\sigma}} = (\hat{\sigma}_{\mathrm{x}}, \hat{\sigma}_{\mathrm{y}}, \hat{\sigma}_{\mathrm{z}})$ [21].

A *quantum algorithm* is an algorithm that is to be carried out on a quantum computer. The *computational complexity* of a quantum algorithm is quantified by the asymptotic scaling of the number of gates required to carry out the algorithm with respect to the number of input qubits [21]. Because gates are peformed with imperfect precision, and the fidelity of the quantum information stored using the qubits decays spontaneously over time, quantum error correction is necessary to preserve quantum information against loss. The additional overhead, quantified in terms of the number of ancilliary qubits and

quantum gates needed to carry out the error-corrected algorithm, can signifcantly increase the actual complexity of an algorithm as it is carried out on a specific implementation of a quantum computer. The *threshold theorem of quantum mechanics* determines whether or not faulty implementations of quantum gates can be made robust through the recursive application of additional gates to implement quantum error correcting codes throughout a quantum computing circuit [21].

3.2.2 One-Way Quantum Computing

Two-qubit quantum gates are used to generate entanglement between the qubits in the memory of a quantum computer. The interactions required to generate this entanglement temporarily violate the assumption that the qubits are stored separably in the quantum memory, as the entangling gate is carried out. "Nonlocal" operations of this kind are notoriously hard to generate in practice, especially on an arbitrary pair of qubits exactly when required ("on demand") during a quantum computation.

In order to circumvent this practical difficulty, Robert Raußendorf and Hans Briegel invented a new architectural modality for quantum computing which they called "one-way" quantum computing [105, 106]. A "one-way" computation is carried out on an entangled substrate of qubits using single-qubit measurements along with the classical post-processing of those measurements [105]. For this reason, one-way quantum computing is also called "measurement-based" quantum computing [107]. Whereas the initial memory state of a circuit-based quantum computer consists of an unentangled array of qubits (each prepared in the logical $|0\rangle$ state by convention), the initial state of the memory of a measurement-based quantum computer is a highly-entangled multi-qubit state called a "cluster state" [106]. One-way quantum computation proceeds without the need for multi-qubit entangling gates, because the necessary entanglement has already been generated in the initial state, before the beginning of the computation proper.

During a one-way quantum computation, the circuit diagram of a circuit-based algorithm is "imprinted" onto the cluster state through a sequence of single-qubit measurements [105]. Under this architecture, it is assumed that one-qubit measurement can be performed in an any arbitrary one-qubit measurement basis. In practice, this can be accomplished using unitary single-qubit operations and measurements in the logical basis. In this manner, a one-way quantum computer simulates the operation of a circuit-based quantum computer. Because a one-way quantum computer simulates each gate of a circuit-based quantum computer with a fixed number of measurements, a one-way quantum computer can efficiently simulate the operation of a circuit-based quantum computer, and *vice versa*. Standard circuit-based error-correction techniques may likewise be applied to make a faulty implementation of a measurement-based quantum computer fault-tolerant [107].

3.2.3 Adiabatic Quantum Computing

In 2000, Farhi, Goldstone, Gutmann, and Sipser proposed a new computational method that they called "Quantum Computation by Adiabatic Evolution," after they observed that "many computationally interesting problems can be recast into an equivalent problem of finding a variable assignment that minimizes an 'energy' function" [108]. Based on this observation, they conceived a computer that would operate by means of the evolution of a quantum state "governed by a time-dependent Hamiltonian that interpolates between an initial Hamiltonian, whose ground state is easy to construct, and a final Hamiltonian, whose ground state encodes the satisfying assignment" [108].

During an adiabatic quantum computation, the computer memory is cooled to the ground state of a "simple" Hamiltonian. The initial Hamiltonian is "simple" in the sense that its ground state is "easy to construct" [108], such as an array of non-interacting qubits, each prepared in its ground state. The ground state of an array of non-interacting

qubits is "easy" to construct because each qubit can be *individually* cooled to its ground state. According to the quantum "adiabatic approximation" [76], the initial Hamiltonian is then slowly and adiabatically evolved into the final Hamiltonian. The final Hamiltonian is assumed to have a ground state that is hard to construct, such as the entangled ground state of a Hamiltonian describing an array of interacting qubits.

An adiabatic quantum computer can be used to compute functions that can be expressed as the ground state of a particular Hamiltonian. Universal quantum computation can be achieved, for example, using an adiabatic quantum computer that is built from a two-dimensional array of locally-interacting spin qubits [109].

3.3 Atomistic Implementations of Quantum Memory

One year after DiVincenzo reported his proof that "two-bit gates are universal for quantum computation" [99], Monroe and coworkers at the National Institute of Standards and Technology (Boulder, Colorado) reported "the first demonstration of a fundamental quantum logic gate that operates on prepared quantum states" [110]. The two qubits were respectively stored across a pair of hyperfine spin states and a pair of nuclear vibrational states of a single trapped ion, and the two-qubit gate was carried out by way of a stimulated Raman transition [110]. Since then, a host of physical systems have been proposed for the practical implementation of a quantum computer, including cavity quantum electrodynamic systems, electromagnetically trapped atoms, solid-state quantum dots, nuclear spins of molecules, photons with linear optical elements and efficient detectors, and superconducting circuits in magnetic fields [111].

Electromagnetically trapped atoms make a natural choice for the fundamental building blocks of a quantum computer, because they are also the fundamental building blocks of terrestrial matter. An individual qubit can be stored using the internal states states of

an atom, such as the nuclear vibrational [112] or spin [28] states, or the electronic orbital angular momentum [3] or spin [27] states. Atoms ejected at high velocities from a hot oven can be slowed and trapped using electromagnetic fields [113]. Individual atoms can then be prepared in optical microtraps with near-deterministic efficiency [114]. There are currently three prominent schemes for constructing quantum memories out of trapped atoms, those being ions stored in linear Paul traps, neutral atoms stored in optical lattices, and neutral atoms stored in optical tweezers [34, 115].

Ions have very long trapping times and can be stored for months using radio-frequency (RF) fields in a linear Paul trap [115]. Their net charge allows for independent control of their nuclear motions, freeing up electronic degrees of freedom for qubit storage and manipulation. The repulsion between ions enables the creation of a "linear crystal of qubits, with the Coulomb repulsion balancing the external confinement force" [115]. Entangling operations can also be generated by means of the ionic Coulomb repulsion by way of the controlled generation of state-dependent phonons in the qubit crystal [116]. The same Coulombic interaction that enables this entanglement scheme also results in decoherence due to quartic electric-field noise [115, 117] which may hinder the asymptotic scaling of the practical size of ionic quantum memories.

Neutral atoms are not subject to this field noise and can be stored in optical dipole traps created using lasers by means of the alternating-current (AC) Stark shift [118]. The AC Stark shift describes the shift in the energies of the electronic states of an atom that occurs as it is placed in the presence of an off-resonant electromagnetic field. Red-detuned fields produce down-shifted energies in the perturbative rotating-wave frame [104], resulting in a net attraction towards regions of higher field intensity. Blue-detuned fields produce up-shifted energies resulting in net repulsion. Spatial variations in laser intensity can be created using individually-focused laser beams (optical "tweezers" [119]), counter-propagating beams (optical "lattices" [120]), or combinations thereof [121].

Individually-trapped atoms make excellent candidates for the implementation of quantum memories, because they are prepared under vacuum (reducing exposure to environmental noise) and they can be chilled to their vibrational ground states using lasers (*e.g.*, via Raman sideband cooling [42, 122]). Until recently, QIP implementations using optically-trapped neutral atoms have been unable to rival the control afforded by RF-trapped ions [118]. AC Stark shifts are generally state-dependent, and this state-dependence results in the emergence of different trapping potentials with respect to different electronic states of the atom. Superpositions of different qubit-encoding states that evolve in space according to different trapping potentials are subject to decoherence due to the state-dependent nuclear heating.

A technique was developed to generate "state-independent" optical dipole traps by chosing detuning frequencies that exploit intercombinations of virtual transitions to produce the same AC Stark shift for two different electronic energy levels of an atom [118]. This technique allows an optically-trapped atom to reside in approximately the same confining potential, regardless of which of the two states it occupies [118]. In this manner, the internal qubit state is decoupled from the external motional state of the neutral atom. This development obviates one of the traditional advantages that ions have had over neutral atoms, without introducing ionic drawbacks [117]. If neutral atom storage lifetimes can be improved and/or preparation schemes can be deteriministically automated, neutral atoms will become competitive long-term candidates for the implementation of quantum memory.

3.4 Exchanged-Based Entanglement of Neutral Atoms

Qubits stored using neutral atoms are preserved against Coulombic sources of decoherence because these atoms lack net charge. Electrostatic interactions cannot be used to entan-

gle qubits stored in neutral atoms. This presents a subtle technological challenge for QIP schemes implemented using neutral atoms. Atomistic entangling gates have been proposed based on dipole-dipole interactions of excited electronic states [123, 124, 125, 126], cold collisions using state-dependent traps [85, 127, 128], and particle exchange [2, 28, 29].

Gates based on indistinguishable particle exchange generate entanglement due to the innate symmetrization requirements of the qubit-carrying particles, rather than explicit Hamiltonian interactions. The absense of an explicit interaction imparts an exchange-based atomic gate with a fundamental stability advantage over other gates that use explicit interactions and therefore introduce decoherence mechanisms [29].

The exchange-based quantum logic gate was originally introduced by Loss and DiVincenzo as a $\sqrt{\text{SWAP}}$ gate [27]. Hayes *et al.* adapted Loss and DiVincenzo's proposal [27] to use qubits stored in nuclear spin states of neutral atoms trapped in optical tweezers [28]. Meanwhile, Anderlini *et al.* demonstrated the gate using qubits encoded in the Zeeman states of an ensemble of atoms stored in a double-well optical lattice [29]. In Hayes *et al.*'s model of the exchange gate, the strength of the exchange interaction is modulated using spatial control of the degree of overlap between the centre-of-mass wavefunctions describing the pair of trapped atoms. A phase difference arises between the symmetric and antisymmetric states of the qubit pair as the trapping potentials combine and re-separate [28]. High fidelity operation is ensured by performing the gate sufficiently slowly, so vibrational states evolve quantum adiabatically with respect to tweezer motion.

The protocol proposed by Hayes *et al.* remains open to elaboration and improvement. Hayes *et al.* focused primarily on nuclear spin-$1/2$ encoded qubits stored using Fermionic atoms for the purposes of their analysis. Their result "generalizes for an arbitrary spin, qubits or qudits, Bose or Fermi, and is not restricted to elements with electron and nuclear spin decoupled" [28]. Given the important advantages afforded to neutral atom QIP architectures by the recent development of state-insensitive trapping technologies [118],

it is natural and essential to extend Hayes *et al.*'s protocol to a system of electronically-encoded qubits stored using state-independent traps. Chapters 4 through 6 provide such a detailed elaboration of Hayes *et al.*'s protocol, including adiabatic gate-speed limits, QIP applications, and nonadiabatic error correction methods.

Chapter 4

Entangling Identical Bosons via Exchange

> *I found myself wondering about the dispersive nature of the "dipole force." The force is attractive when the frequency of light is tuned below the resonance, repulsive when tuned above the resonance, and vanishes when tuned directly on the atomic resonance.*
>
> —Steven Chu, 1997 [129]

My six main contributions to the work described in Chapter 4 are summarized as follows:

1. *I define the Hamiltonian for a two-particle system, describing a pair of identical atoms in one dimension and translated along that dimension by a time-dependent potential comprising a pair of mobile Gaussian-shaped traps (Section 4.2).*

2. *I construct a computational representation of the two-particle Hamiltonian using MATLAB^{TM} and I use it to solve the time-independent Schrödinger equation for different trap-separation distances and particle interaction strengths (Section 4.3).*

3. *I show how time-dependent control of the two-particle Hamiltonian can be used to perform an entangling operation on qubits stored in the internal states of the atoms, via the exchange interaction (Section 4.4).*

4. *I investigate how two conserved quantities of the Hamiltonian, namely the spatial symmetry and parity, may be exploited to enhance operation fidelity (Section 4.5).*

5. *I derive an "adiabaticity criterion," mathematically expressing the limit in which operation times are sufficiently slow to ensure operation fidelity, and I perform numerical simulations to verify the accuracy of that limit (Section 4.6).*

6. *I numerically solve the time-dependent Schrödinger equation for several relevant Hamiltonian parameters and initial conditions, verifying the accuracy of the adiabaticity criterion for operation fidelity (Section 4.7).*

4.1 Introduction: Coherent Control of Neutral Atoms

Techniques for trapping and cooling neutral atoms to their vibrational ground states have afforded experimentalists with new opportunities "to place atoms and photons into a well-defined set of quantum states and to manipulate these states coherently" [130]. Techniques for coherently controlling ensembles of neutral atoms have important applications in QIP, including precision time-keeping [131], quantum computation [121], and simulations of chemical systems [132]. Experiments that are being performed in this area are currently focused on the development of the individual "building blocks" that will be needed to construct sophisticated QIP systems.

The ability to coherently prepare and manipulate a quantum system relies on the power to control the numbers of particles contained in the system, their internal and positional states, and the character of their interactions [41]. The functional building blocks needed to realize coherently controlled atomic systems will include such technologies as those for deterministically preparing small [41, 43] and large numbers [133] of atoms, efficiently cooling individual atoms [42], coherently manipulating the nuclear [134] and electronic [135, 136] states of atoms, entangling pairs of atoms both individually [137] and collectively [29], and transporting atoms both individually [119] and collectively [138]. Practical QIP systems will rely on varying combinations of different building blocks in order to maximize their advantages. For example, the electronic or nuclear subsystems of divalent (*e.g.*, alkaline earth) atoms offer different advantages related to the differing physical characteristics of these subsystems [139].

Divalent atoms such as strontium (Sr) and ytterbium (Yb) have ground state electronic configurations of $[\mathrm{Kr}]\,5s^2$ and $[\mathrm{Xe}]\,4f^{14}\,6s^2$ respectively. Alkaline earth elements carry advantages over the alkali atoms used traditionally in neutral atoms experiments [122, 123, 138, 140, 141], because they exhibit an especially narrow "clock transition" coupling their $^1\mathrm{S}_0$ and $^3\mathrm{P}_0$ valence states [139]. This narrowness is due to the restrictive set of momentum selection rules that govern the transition.

The transfer of angular momentum to the electronic subsystem of a divalent atom during the $^1\mathrm{S}_0 \rightarrow {}^3\mathrm{P}_0$ transition along a non-azimuthal direction, *without* the transfer of complementary information about its non-azimuthal direction, marks a unique curiosity of quantum theory. One quantum of angular momentum can be added probablistically to ($^1\mathrm{S}_0 \rightarrow {}^3\mathrm{P}_0$) or removed from ($^3\mathrm{P}_0 \rightarrow {}^1\mathrm{S}_0$) the total angular momentum of the electronic subsystem of the atom, according to the directions of the circular polarizations of the absorbed and emitted photons that mediate the virtual transitions. The transfered momentum is known *not* to be transfered along the azimuthal direction defined by the $^3\mathrm{P}_0$ state, but complementary information about the direction of the angular momentum remains absent (because the laser beams stimulating the transition are unpolarized). Coherent rotations of this kind are possible because the entropy change in the (bosonic) laser beam due to angular momentum transfer is negligibly small compared to the energy transfer, so virtually no heat is transfered between the atom and the spectral bath of the laser, making the operation practically reversible. The correct choice of laser geometry assures that no quanta of linear momenta are imparted to the system, coherently or as heat. As Benioff [23] and Feynman [24] have critically identified, the physical reversibility of the operation corresponds to its quantum mechanical unitarity.

Fermionic (odd) isotopes of alkaline earths have non-zero nuclear spins, and these spin magnetic states can be decoupled from the non-magnetic $^1\mathrm{S}_0 \leftrightarrow {}^3\mathrm{P}_0$ clock transition, allowing them to be separately exploited for distinct applications within the same atomic

system [139]. The "ultranarrow" $^1S_0 \leftrightarrow {}^3P_0$ transition of bosonic (even) isotopes of alkaline earths make them "metrologically superior" [136] to fermionic isotopes, due to complications that arise from Zeeman shifts in the clock transitions of the fermionic species [142].

Entanglement provides a resource for applications in quantum metrology [131], computation [121], and simulation [132]. Schemes for entangling neutral atoms have been proposed based on qubit-qubit interactions via high-finesse cavity radiation [143], nonlocal state-dependent qubit transport [127], dipole coupling of alkali atoms [123, 124, 141], the Rydberg blockade [144], cold collisions [85, 112, 145], and identical particle exchange [2, 28]. Forms of the proposals given in Ref. [127] and Refs. [2, 28] have been experimentally realized using ensembles of neutral atoms trapped in optical lattices [29, 146]. The entanglement of an individual pair of neutral atoms has been experimentally realized using Rubidium atoms trapped in optical tweezers [137].

Although entanglement schemes based on Rydberg interactions [144] appear promising [137], they can suffer from decoherence effects due to momentum transfer from the Rydberg-excited electrons to the nuclei [147]. Entanglement schemes based on nonlocal, state-dependent transport [127, 146] suffer from innate decoherence due to the presence of inhomogeneous magnetic field noise [29]. On the other hand, entanglement schemes that rely on adiabatic exchange [2, 28] are not subject to these decoherence effects [3, 29] and can even have nonadiabatic errors corrected [4], making exchange-based schemes especially promising candidates for the realization of precision entangling gates for neutral atoms. Technologies developed to enable exchange-based entanglement schemes are also directly applicable to quantum simulations of chemical interactions [132] that relate to fundamental problems in materials physics, magnetism, and thermodynamics [148].

By employing a QIP architecture based on exchange-based two-qubit gates and ultranarrow one-qubit clock state transitions of alkaline earth atoms, one enjoys the advantage

of a fundamentally decoherence-resistant design. This design describes an exceptional candidate for long-term scalability, with an eye toward the realization of a full-scale quantum computer containing many millions of qubits.

The one-dimensional model Hamiltonian that I employ here describes a pair of identical particles confined by moveable traps. It captures the essential physics of a pair of qubits that are stored in the non-magnetic states of neutral atoms and are entangled using the adiabatic exchange mechanism. I examine the dynamics of this model Hamiltonian, and I develop a criterion to ensure the adiabaticity of the entangling operation.

4.2 Two-Particle Tweezer Hamiltonian

In this Section, I define the Hamiltonian describing a pair of identical composite particles in one dimension and translated along that dimension by a time-dependent potential comprising a pair of spatially-symmetric, Gaussian-shaped traps.

The Hamiltonian represents a pair of identical atoms confined to one dimension by a trapping laser beam, and translated along that dimension by a pair of focused laser tweezers. It is accurately modeled using a two-particle Hamiltonian of the form,

$$\hat{H} = \sum_{i,j=0,1} \left\{ \frac{\hat{p}_{\rm a}^2}{2m} + V(x_{\rm a}, d) + \frac{\hat{p}_{\rm b}^2}{2m} + V(x_{\rm b}, d) + 2a_{ij}\hbar\omega_{\perp}\delta(x_{\rm a} - x_{\rm b}) \right\} \otimes |ij\rangle\langle ij|, \quad (4.1)$$

where $x_{\rm a}$ and $x_{\rm b}$ are the respective positions of particles labeled "a" and "b," $p_{\rm a}$ and $p_{\rm b}$ are their momentum operators, a_{ij} is the state-dependent scattering length that depends on internal atomic states $|i\rangle_{\rm a}$ and $|j\rangle_{\rm b}$ (using $|ij\rangle \equiv |i\rangle_{\rm a} \otimes |j\rangle_{\rm b}$), $\omega_{\perp}$ is the harmonic oscillation frequency due to transverse confinement [128], and d is the time-dependent centre-to-centre distance between the traps.

When the traps are independent of the internal states of the particles, each particle experiences a spatially-symmetric double-well potential with a Gaussian profile,

$$V(x,d) = -V_0 \exp\left[\frac{-(x-d/2)^2}{2\sigma^2}\right] - V_0 \exp\left[\frac{-(x+d/2)^2}{2\sigma^2}\right], \tag{4.2}$$

where $V_0 > 0$ is the depth of each Gaussian trap and σ^2 is its variance. The Gaussian shape of each trap reflects the profile of a focused laser beam [149].

4.3 Adiabatic Eigenstates

In this Section, I use MATLAB^{TM} to solve the time-independent Schrödinger equation for a system containing one or two particles trapped by the potential (4.2)*, over a range of trap-separation distances, for both positive and negative scattering lengths. I generalize these results to describe the states of the composite particle Hamiltonian given by eq.* (4.1)*.*

The ground state (*i.e.*, lowest-energy eigenstate) of a particle in one dimension confined to a single potential well, such as $V(x,d)|_{d=0}$, is an approximately Gaussian wavefunction centred at the trap centre. As such a potential well is adiabatically and symmetrically split into two twin wells, the ground state wavefunction likewise splits into a pair of approximately Gaussian wavefunctions, each reproducing the shape of the original well's wavefunction as the well-separation distance becomes large compared to the diameter σ of each trap. Thus, the ground state of particle confined to a pair of distantly-separated potential wells is closely-approximated as the normalized, symmetric (*i.e.* even parity), superposition of the individual ground states of the wells in isolation (Fig. 4.1).

The first excited eigenstate of a particle in a single well is an antisymmetric state. Although this state has a significantly larger energy than that of the ground state of a single well, these first two eigenstates approach degeneracy as the original well is adiabatically split into two separate wells, and the shape of the first nonlocal excited state

evolves into an antisymmetric "mirror image" of the ground state (Fig. 4.1). In the limit of distantly-separated wells, the energies of these two lowest states differ only because the wavefunction describing the spatially-antisymmetric excited state is exactly zero at the position equidistant between the two wells, whereas the spatially-symmetric wavefunction approaches a value arbitrarily close to zero at that location. A particle initialized locally in one of the two distant wells is described by an equal superposition of both states, and the energy difference between the states produces a phase evolution that leads to tunneling back and forth between the two wells.

The first three bound eigenstates of a single particle confined by the double-well potential (4.2) are shown in Fig. 4.1 for varying d. In general, the single-particle eigenstates are nonlocal and may be defined by the adiabatic eigenbasis $\{|\psi^{\mathrm{A}}(d)\rangle, |\psi^{\mathrm{B}}(d)\rangle, |\psi^{\mathrm{C}}(d)\rangle, \ldots\}$. To simplify our notation, we shall consider the d-dependence of these states to be implicit (e.g., $|\psi^{\mathrm{A}}\rangle \equiv |\psi^{\mathrm{A}}(d)\rangle$). Take note that as d increases, the ground state $|\psi^{\mathrm{A}}\rangle$ and the excited state $|\psi^{\mathrm{B}}\rangle$ become spatially delocalized and energetically degenerate, such that $||\psi^{\mathrm{B}}\rangle| \to |\psi^{\mathrm{A}}\rangle$. When $|d| \gg \sigma$ we can write $|\psi^{\mathrm{L}}\rangle \equiv (|\psi^{\mathrm{A}}\rangle - |\psi^{\mathrm{B}}\rangle)/\sqrt{2}$ to represent a single particle localized in the ground state of the left well, and likewise $|\psi^{\mathrm{R}}\rangle \equiv (|\psi^{\mathrm{A}}\rangle + |\psi^{\mathrm{B}}\rangle)/\sqrt{2}$ for the right well. The local states $|\psi^{\mathrm{L}}\rangle$ and $|\psi^{\mathrm{R}}\rangle$ allow for an intuitive description of the one-particle system in the limit as $\sigma/d \to \infty$.

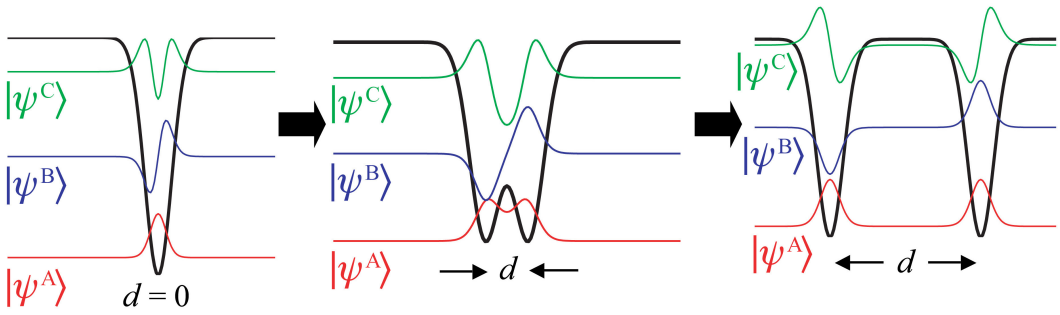

Figure 4.1: The first three eigenstates of a single particle in a double-well potential for different trap separation distances d, reproduced from Ref. [2] with permission.

The situation becomes more complicated when a second particle is added to the system. In the limit where $d = 0$ and $a_{ij} = 0$ for all i and j, the first six eigenstates are, in order of increasing energy, $|\psi^{\mathrm{A}}\psi^{\mathrm{A}}\rangle$, $\frac{1}{\sqrt{2}}\big(|\psi^{\mathrm{A}}\psi^{\mathrm{B}}\rangle - |\psi^{\mathrm{B}}\psi^{\mathrm{A}}\rangle\big)$, $\frac{1}{\sqrt{2}}\big(|\psi^{\mathrm{A}}\psi^{\mathrm{B}}\rangle + |\psi^{\mathrm{B}}\psi^{\mathrm{A}}\rangle\big)$, $\frac{1}{\sqrt{2}}\big(|\psi^{\mathrm{A}}\psi^{\mathrm{B}}\rangle - |\psi^{\mathrm{B}}\psi^{\mathrm{A}}\rangle\big)$, $\frac{1}{\sqrt{2}}\big(|\psi^{\mathrm{A}}\psi^{\mathrm{C}}\rangle - |\psi^{\mathrm{C}}\psi^{\mathrm{A}}\rangle\big)$, $\frac{1}{\sqrt{2}}\big(|\psi^{\mathrm{A}}\psi^{\mathrm{C}}\rangle + |\psi^{\mathrm{C}}\psi^{\mathrm{A}}\rangle\big)$, and $|\psi^{\mathrm{B}}\psi^{\mathrm{B}}\rangle$.

When the interaction term is "turned on" ($a_{ij} \neq 0$), it may be treated as a perturbation to the interactionless two-particle states. Accordingly, the new two-particle eigenstates may be written as a sum of "perturbed" tensor products of one-particle states. Let us use a tilde to denote the perturbation to the terms composing the new symmetrized eigenstates. States that are antisymmetric under particle exchange are not affected by the interaction at any separation and the tildes have been accordingly omitted from these states.

For a repulsive interaction between atoms ($a_{ij} > 0$) the first six two-particle eigenstates are as follows:

$d = 0$		$d \gg \sigma$	
$\widetilde{\lvert\psi^{\mathrm{B}}\psi^{\mathrm{B}}\rangle}$	$\longleftrightarrow$	$\frac{1}{2}(\widetilde{\lvert\psi^{\mathrm{A}}\psi^{\mathrm{C}}\rangle} + \widetilde{\lvert\psi^{\mathrm{C}}\psi^{\mathrm{A}}\rangle} - \widetilde{\lvert\psi^{\mathrm{B}}\psi^{\mathrm{D}}\rangle} - \widetilde{\lvert\psi^{\mathrm{D}}\psi^{\mathrm{B}}\rangle})$	(4.3a)
$\frac{1}{\sqrt{2}}(\lvert\psi^{\mathrm{A}}\psi^{\mathrm{C}}\rangle - \lvert\psi^{\mathrm{C}}\psi^{\mathrm{A}}\rangle)$	$\longleftrightarrow$	$\frac{1}{\sqrt{2}}(\lvert\psi^{\mathrm{A}}\psi^{\mathrm{C}}\rangle - \lvert\psi^{\mathrm{C}}\psi^{\mathrm{A}}\rangle)$	(4.3b)
$\frac{1}{\sqrt{2}}(\widetilde{\lvert\psi^{\mathrm{A}}\psi^{\mathrm{C}}\rangle} + \widetilde{\lvert\psi^{\mathrm{C}}\psi^{\mathrm{A}}\rangle})$	$\longleftrightarrow$	$\frac{1}{\sqrt{2}}(\widetilde{\lvert\psi^{\mathrm{L}}\psi^{\mathrm{L}}\rangle} + \widetilde{\lvert\psi^{\mathrm{R}}\psi^{\mathrm{R}}\rangle})$	(4.3c)
$\frac{1}{\sqrt{2}}(\widetilde{\lvert\psi^{\mathrm{A}}\psi^{\mathrm{B}}\rangle} + \widetilde{\lvert\psi^{\mathrm{B}}\psi^{\mathrm{A}}\rangle})$	$\longleftrightarrow$	$\frac{1}{\sqrt{2}}(\widetilde{\lvert\psi^{\mathrm{L}}\psi^{\mathrm{L}}\rangle} - \widetilde{\lvert\psi^{\mathrm{R}}\psi^{\mathrm{R}}\rangle})$	(4.3d)
$\frac{1}{\sqrt{2}}(\lvert\psi^{\mathrm{A}}\psi^{\mathrm{B}}\rangle - \lvert\psi^{\mathrm{B}}\psi^{\mathrm{A}}\rangle)$	$\longleftrightarrow$	$\frac{1}{\sqrt{2}}(\lvert\psi^{\mathrm{L}}\psi^{\mathrm{R}}\rangle - \lvert\psi^{\mathrm{R}}\psi^{\mathrm{L}}\rangle)$	(4.3e)
$\widetilde{\lvert\psi^{\mathrm{A}}\psi^{\mathrm{A}}\rangle}$	$\longleftrightarrow$	$\frac{1}{\sqrt{2}}(\widetilde{\lvert\psi^{\mathrm{L}}\psi^{\mathrm{R}}\rangle} + \widetilde{\lvert\psi^{\mathrm{R}}\psi^{\mathrm{L}}\rangle})$.	(4.3f)

In case of attractive interaction ($a_{ij} < 0$), the eigenstates are as follows:

$$
\begin{array}{ccc}
d = 0 & & d \gg \sigma \\
\frac{1}{\sqrt{2}}(|\psi^{\mathrm{A}}\psi^{\mathrm{C}}\rangle - |\psi^{\mathrm{C}}\psi^{\mathrm{A}}\rangle) & \longleftrightarrow & \frac{1}{\sqrt{2}}(|\psi^{\mathrm{A}}\psi^{\mathrm{C}}\rangle - |\psi^{\mathrm{C}}\psi^{\mathrm{A}}\rangle) \quad (4.4a) \\
\widetilde{|\psi^{\mathrm{B}}\psi^{\mathrm{B}}\rangle} & \longleftrightarrow & \frac{1}{2}(\widetilde{|\psi^{\mathrm{A}}\psi^{\mathrm{C}}\rangle} + \widetilde{|\psi^{\mathrm{C}}\psi^{\mathrm{A}}\rangle} + \widetilde{|\psi^{\mathrm{B}}\psi^{\mathrm{D}}\rangle} + \widetilde{|\psi^{\mathrm{D}}\psi^{\mathrm{B}}\rangle}) \quad (4.4b) \\
\frac{1}{\sqrt{2}}(\widetilde{|\psi^{\mathrm{A}}\psi^{\mathrm{C}}\rangle} + \widetilde{|\psi^{\mathrm{C}}\psi^{\mathrm{A}}\rangle}) & \longleftrightarrow & \frac{1}{\sqrt{2}}(\widetilde{|\psi^{\mathrm{L}}\psi^{\mathrm{R}}\rangle} + \widetilde{|\psi^{\mathrm{R}}\psi^{\mathrm{L}}\rangle}) \quad (4.4c) \\
\frac{1}{\sqrt{2}}(|\psi^{\mathrm{A}}\psi^{\mathrm{B}}\rangle - |\psi^{\mathrm{B}}\psi^{\mathrm{A}}\rangle) & \longleftrightarrow & \frac{1}{\sqrt{2}}(|\psi^{\mathrm{L}}\psi^{\mathrm{R}}\rangle - |\psi^{\mathrm{R}}\psi^{\mathrm{L}}\rangle) \quad (4.4d) \\
\frac{1}{\sqrt{2}}(\widetilde{|\psi^{\mathrm{A}}\psi^{\mathrm{B}}\rangle} + \widetilde{|\psi^{\mathrm{B}}\psi^{\mathrm{A}}\rangle}) & \longleftrightarrow & \frac{1}{\sqrt{2}}(\widetilde{|\psi^{\mathrm{L}}\psi^{\mathrm{L}}\rangle} - \widetilde{|\psi^{\mathrm{R}}\psi^{\mathrm{R}}\rangle}) \quad (4.4e) \\
\widetilde{|\psi^{\mathrm{A}}\psi^{\mathrm{A}}\rangle} & \longleftrightarrow & \frac{1}{\sqrt{2}}(\widetilde{|\psi^{\mathrm{L}}\psi^{\mathrm{L}}\rangle} + \widetilde{|\psi^{\mathrm{R}}\psi^{\mathrm{R}}\rangle}). \quad (4.4f)
\end{array}
$$

The eigenstates of the full Hamiltonian (4.1) are described by tensor products of the vibrational wavefunctions and the symmetrized qubit states. For bosonic particles, permissible eigenstates are tensor products of external (i.e., vibrational) and internal (i.e., qubit) states of the same symmetry. Thus, antisymmetrized spatial wavefunctions are permitted for a pair of composite bosons, so long as their internal structure is also antisymmetric, resulting in an overall symmetric wavefunction.

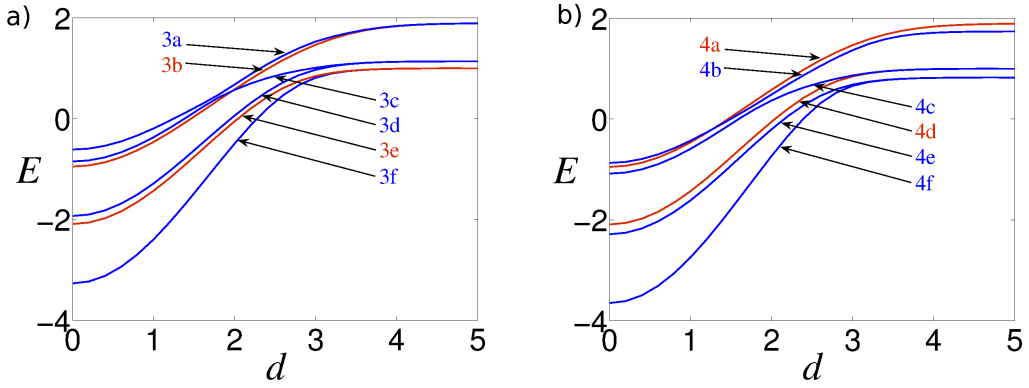

Figure 4.2: Adiabatic energy levels as a function of well separation d for (a) eqs. (4.3) with $a_{ij} = 0.1\sigma$ and (b) eqs. (4.4) with $a_{ij} = -0.1\sigma$, reproduced from Ref. [2] with permission. Well separation is in units of σ. Energies are in units of $\hbar\omega_\circ$, where $\omega_\circ$ is the harmonic oscillation frequency of one atom in the ground state of a single well. The energies of symmetric vibrational eigenstates are shown in blue, whereas those of antisymmetric states are shown in red. The crossings between oppositely symmetrized states are unavoided because the Hamiltonian does not couple these states.

4.4 Gate Operation

In this Section, I describe a two-qubit entangling gate carried out on a pair of qubits, each stored in the internal states of a neutral boson confined to one-dimension and controlled using optical tweezers.

Each of the two particles is assumed to be initialized in the ground state of one of the two spatially-separated tweezers. Gate operation occurs as the two tweezers are adiabatically approached until they completely overlap, and then are reseparated.

When the qubits are separate, the logical states of this quantum memory identify the states of the qubits on the left and the right, and are defined by the basis $\{|0_{\rm L}0_{\rm R}\rangle, |0_{\rm L}1_{\rm R}\rangle, |1_{\rm L}0_{\rm R}\rangle, |1_{\rm L}1_{\rm R}\rangle\}$. Analoguous to the fermionic case described by Hayes *et al.* [28], these logical states represent the bosonic eigenstates of the Hamiltonian,

$$|0_{\rm L}0_{\rm R}\rangle = |\Psi^+\rangle \otimes |00\rangle, \tag{4.5a}$$

$$|0_{\rm L}1_{\rm R}\rangle = \tfrac{1}{\sqrt{2}} \left(|\Psi^+\rangle \otimes |\chi^+\rangle + |\Psi^-\rangle \otimes |\chi^-\rangle\right), \tag{4.5b}$$

$$|1_{\rm L}0_{\rm R}\rangle = \tfrac{1}{\sqrt{2}} \left(|\Psi^+\rangle \otimes |\chi^+\rangle - |\Psi^-\rangle \otimes |\chi^-\rangle\right), \tag{4.5c}$$

$$|1_{\rm L}1_{\rm R}\rangle = |\Psi^+\rangle \otimes |11\rangle, \tag{4.5d}$$

where $|\Psi^\pm\rangle = \frac{1}{\sqrt{2}}(|\psi^{\rm L}\psi^{\rm R}\rangle \pm |\psi^{\rm R}\psi^{\rm L}\rangle)$ and $|\chi^\pm\rangle = \frac{1}{\sqrt{2}}(|01\rangle \pm |10\rangle)$. Evidently, "swapping" the logical qubits, such that $|0_{\rm L}1_{\rm R}\rangle \Leftrightarrow |1_{\rm L}0_{\rm R}\rangle$, amounts to a 180° phase shift between the symmetric and antisymmetric components of the odd logical states (3.5b) and (3.5c). A maximally-entangled state can be prepared from either odd logical state, by performing a 90° rotation in this subspace. Such a 90° rotation is widely referred to as a $\sqrt{\rm SWAP}$ gate [28]. For example, a 90° rotation applied around the symmetry axis of the state represented by eq. (4.5) generates $\frac{1}{\sqrt{2}} \left(|\Psi^+\rangle \otimes |\chi^+\rangle + i\,|\Psi^-\rangle \otimes |\chi^-\rangle\right) = \frac{1+i}{2} \left(|0_{\rm L}1_{\rm R}\rangle - i\,|1_{\rm L}0_{\rm R}\rangle\right)$.

For two particles that are in stationary, spatially-separated traps, all four logical states are degenerate and acquire the same (global) phase. If these logical states are re-expressed

in the Hamiltonian eigenbasis $\{|\Psi^+\rangle \otimes |00\rangle, |\Psi^+\rangle \otimes |\chi^+\rangle, |\Psi^-\rangle \otimes |\chi^-\rangle, |\Psi^+\rangle \otimes |11\rangle\}$, then an adiabatic evolution of the system becomes straightforward to describe. As the traps are adiabatically combined, each eigenstate will acquire a local phase consistent with the evolution of its energy. Entangling operation is achieved by setting the trap-separation profile to ensure that the phase acquired by the $|\Psi^+\rangle \otimes |\chi^+\rangle$ state differs from that of the $|\Psi^-\rangle \otimes |\chi^-\rangle$ state by 90°. Entangling operation can always be achieved because the singlet state $|\Psi^-\rangle \otimes |\chi^-\rangle$ always picks up a different phase than the triplet states, except in the extreme ("Tonks" [150]) limit as $a_{ij} \to \pm\infty$.

During adiabatic gate operation, particles that begin in opposite wells will end up in opposite wells. This is true even when the interaction is "turned-off" ($a_{ij} = 0$) and the $\frac{1}{\sqrt{2}}(|\psi^{\mathrm{L}}\psi^{\mathrm{R}}\rangle \pm |\psi^{\mathrm{R}}\psi^{\mathrm{L}}\rangle$ states become degenerate with the $\frac{1}{\sqrt{2}}(|\psi^{\mathrm{L}}\psi^{\mathrm{L}}\rangle \pm |\psi^{\mathrm{R}}\psi^{\mathrm{R}}\rangle$ states, because the first four eigenstates of the Hamiltonian (4.1) all have distinct symmetries and parities, leading to selection rules that forbid several nonadiabatic transitions.

4.5 Excitations to Non-Logical States

In this Section, I discuss how the innate symmetries of the Hamiltonian (exchange symmetry and spatial parity) forbid certain nonadiabatic excitations, enhancing gate fidelity.

The two-particle eigenstates may be visualized as a contour map in three dimensions by plotting the amplitudes of particle "a" on one horizontal axis against the amplitude of particle "b" along the other horizontal axis, so the amplitude of the (real) joint two-particle eigenfunction is expressed vertically (see Fig. 4.9a). Equivalently, two-dimensional plots can use colour-coding to depict the joint amplitude; these visualizations are plotted in Figs. 4.3 to 4.8. Each state has its own distinct set of symmetries. These symmetries must be preserved as the value of d is adiabatically varied, because the Hamiltonian (4.2) conserves both the particles' exchange symmetry and spatial parity.

Eigenstate	Symmetry	Parity
$\|\psi^{\mathrm{A}}\psi^{\mathrm{A}}\rangle$	even	even
$\frac{1}{\sqrt{2}}(\|\psi^{\mathrm{A}}\psi^{\mathrm{B}}\rangle - \|\psi^{\mathrm{B}}\psi^{\mathrm{A}}\rangle)$	odd	odd
$\frac{1}{\sqrt{2}}(\|\psi^{\mathrm{A}}\psi^{\mathrm{B}}\rangle + \|\psi^{\mathrm{B}}\psi^{\mathrm{A}}\rangle)$	even	odd
$\frac{1}{\sqrt{2}}(\|\psi^{\mathrm{A}}\psi^{\mathrm{C}}\rangle - \|\psi^{\mathrm{C}}\psi^{\mathrm{A}}\rangle)$	odd	even
$\frac{1}{\sqrt{2}}(\|\psi^{\mathrm{A}}\psi^{\mathrm{C}}\rangle + \|\psi^{\mathrm{C}}\psi^{\mathrm{A}}\rangle)$	even	even
$\|\psi^{\mathrm{B}}\psi^{\mathrm{B}}\rangle$	even	even

Table 4.1: Symmetries and parities of the first six eigenstates of the Hamiltonian (4.1).

When d becomes a function $d(t)$ of time t such that time-dependent changes in $d(t)$ are not perfectly adiabatic, some nonadiabatic vibrational transitions are still suppressed because the symmetry and parity conservation properties of the Hamiltonian result in selection rules that forbid transitions between states that do not share *both* the same symmetry and parity. This property of the Hamiltonian promotes gate fidelity, because it automatically prevents the occurence of some undesirable nonadiabatic transitions during realistic gate operation.

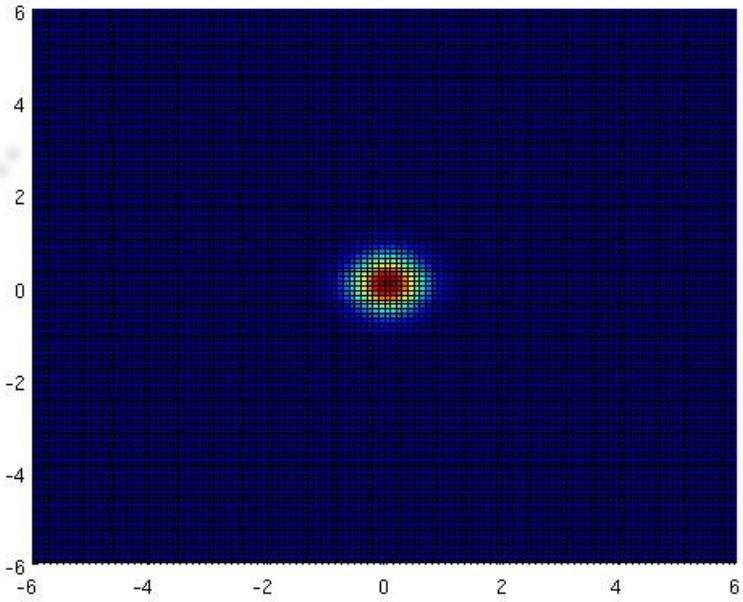

Figure 4.3: Two-dimensional contour visualization of the state $|\psi^{\mathrm{A}}\psi^{\mathrm{A}}\rangle$ for non-interacting particles for $d = 0$. This state has even symmetry and even parity. The conditional amplitude of each particle is plotted along each axis. Red is positive and blue is zero. Axes are measured in units of σ.

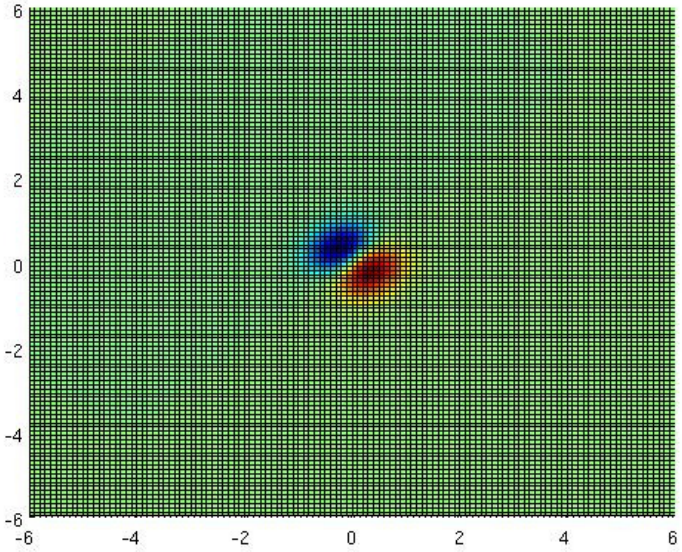

Figure 4.4: Two-dimensional contour visualization of the state $\frac{1}{\sqrt{2}}\big(|\psi^{\mathrm{A}}\psi^{\mathrm{B}}\rangle - |\psi^{\mathrm{B}}\psi^{\mathrm{A}}\rangle\big)$ for non-interacting particles for $d = 0$. This state has odd symmetry and odd parity. The conditional amplitude of each particle is plotted along each axis. Red is positive and blue is negative. Axes are in units of σ.

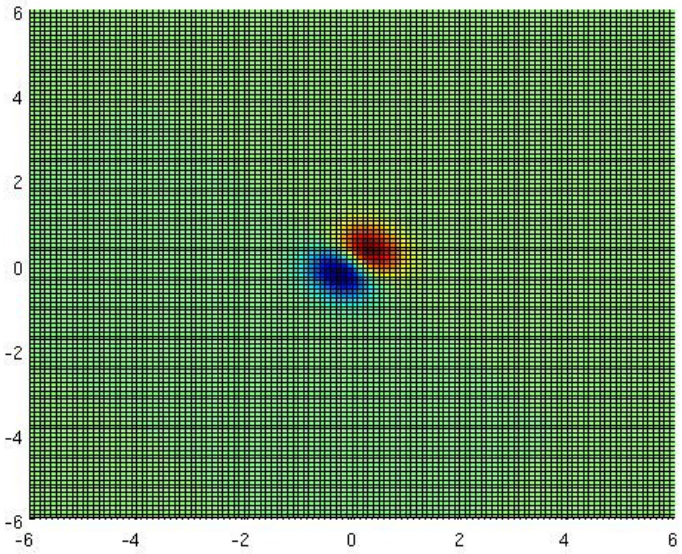

Figure 4.5: Two-dimensional contour visualization of the state $\frac{1}{\sqrt{2}}\big(|\psi^{\mathrm{A}}\psi^{\mathrm{B}}\rangle + |\psi^{\mathrm{B}}\psi^{\mathrm{A}}\rangle\big)$ for non-interacting particles for $d = 0$. This state has even symmetry and odd parity. The conditional amplitude of each particle is plotted along each axis. Red is positive and blue is negative. Axes are in units of σ.

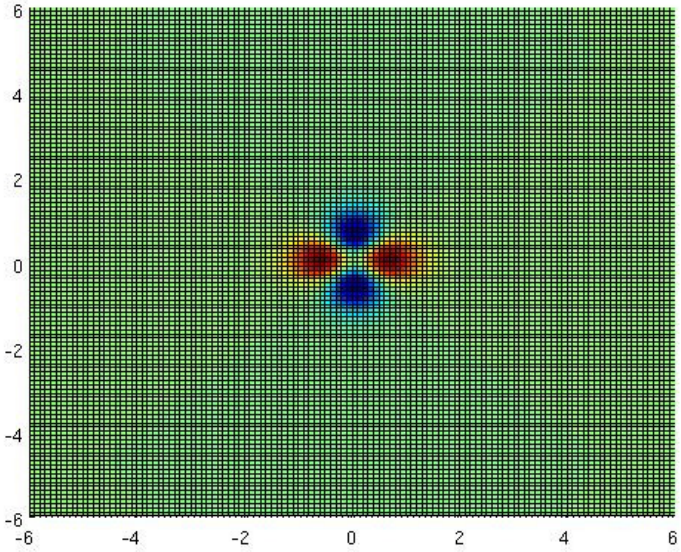

Figure 4.6: Two-dimensional contour visualization of the state $\frac{1}{\sqrt{2}}\big(|\psi^{\mathrm{A}}\psi^{\mathrm{C}}\rangle - |\psi^{\mathrm{C}}\psi^{\mathrm{A}}\rangle\big)$ for non-interacting particles for $d = 0$. This state has odd symmetry and even parity. The conditional amplitude of each particle is plotted along each axis. Red is positive and blue is negative. Axes are in units of σ.

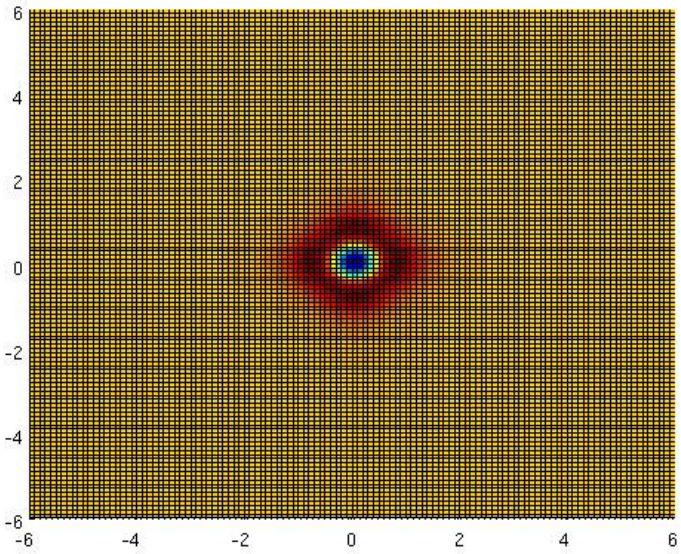

Figure 4.7: Two-dimensional contour visualization of the state $\frac{1}{\sqrt{2}}\big(|\psi^{\mathrm{A}}\psi^{\mathrm{C}}\rangle + |\psi^{\mathrm{C}}\psi^{\mathrm{A}}\rangle\big)$ for non-interacting particles for $d = 0$. This state has even symmetry and even parity. The conditional amplitude of each particle is plotted along each axis. Red is positive and blue is negative. Axes are in units of σ.

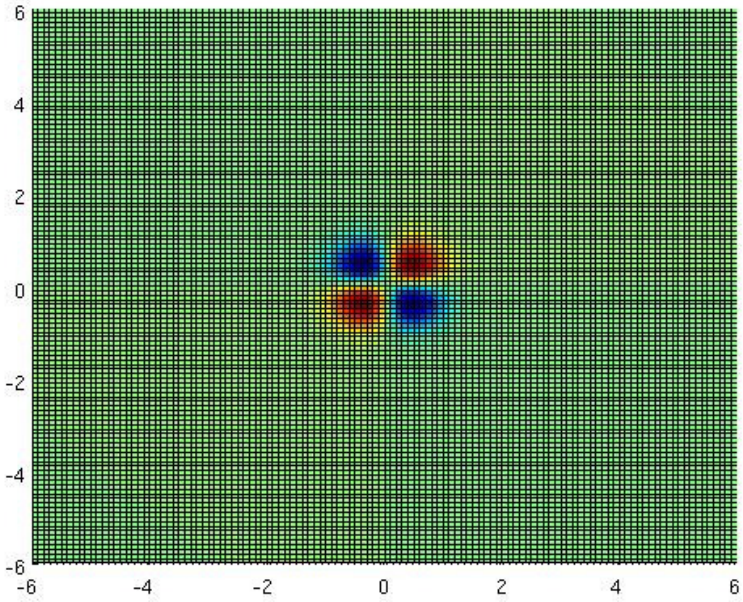

Figure 4.8: Two-dimensional contour visualization of the state $|\psi^{\mathrm{B}}\psi^{\mathrm{B}}\rangle$ for non-interacting particles for $d = 0$. The conditional amplitude of each particle is plotted along each axis. This state has even symmetry and even parity. Red is positive and blue is negative. Axes are in units of σ.

4.6 Derivation of Adiabaticity Criterion

In this Section, I derive a simple criterion to ensure the adiabaticity and thus the high-fidelity operation of the entangling gate defined in the previous section.

The general criterion for ensuring the validity of the adiabatic approximation with respect to a particular nonadiabatic transition $|a\rangle \to |b\rangle$ is given in Ref. [76] to be

$$\max_t \left| \langle a| \frac{\partial \hat{H}}{\partial t} |b\rangle \right| \ll \hbar\omega_{ab}^2 \quad \forall \ |a\rangle \neq |b\rangle \,, \tag{4.6}$$

where $\omega_{ab} = \min_t(|E_b(t) - E_a(t)|/\hbar)$ and where $|a\rangle$ and $|b\rangle$ are instantaneous eigenstates of the Hamiltonian. Since the Hamiltonian in question is invariant under exchanges of both symmetry and parity, transitions between vibrational states of different symmetry or parity are suppressed. Thus, in our case ω_{ab} is determined by the energy gap of the

two closest states having both equal symmetry and parity. This restriction contributes significantly to the robustness of this gate.

The left side of eq. (4.6) reduces to $\max_t |\langle a|\frac{dV(x,d(t))}{dt}|b\rangle|$ because only the double-well potential is time-dependent. In general, we may replace $|\langle a|\frac{dV(x,d(t))}{dt}|b\rangle|$ in eq. (4.6) with the term $\max_x |dV(x,d(t))/dt|$, because

$$\left|\langle a|\frac{dV(x,d(t))}{dt}|b\rangle\right| \;\leq\; \max_x \left|\frac{dV(x,d(t))}{dt}\right| . \tag{4.7}$$

Let us consider the simple case of gate operation carried out via the linear translation of the wells at constant velocity v, such that $d(t) = vt$. We may once again exploit the symmetries of the Hamiltonian to maximize $|dV(x,d(t))/dt|$ simultaneously with respect to both x and t, identifying the maximum at $x = 0$ by inspection, because time-dependent changes in the potential occur at the front "crest" and rear "tail" of each trap as the two traps approach each other. The maximum rate of change occuring at $x = 0$ as the two crests collide. Solving $dV(x,t)/dt|_{x=0}$, and using differential calculus to maximize the result for t, we obtain

$$\max_{x,\,t}\left|\frac{dV(x,t)}{dt}\right| \;=\; \frac{V_0 v}{\sigma}\, e^{-1/2} \;\approx\; \frac{V_0 v}{\sigma}\,. \tag{4.8}$$

Inserting this result into eq. (4.6), we obtain an adiabaticity criterion to limit the overall gate speed,

$$v \ll \frac{\hbar\sigma\omega_{ab}^2}{V_0}\,. \tag{4.9}$$

Adherence to this criterion ensures that gate operation is carried out within the adiabatic limit. Errors due to nonadiabatic transitions can be further reduced (within the adiabatic limit) by using the techniques discussed in Chapter 6. Gate tolerances, with respect to experimental imprecision, are discussed in detail in Ref. [4].

4.7 Time-Dependent Simulations of Gate Operation

In this Section, I present computer simulations of the two-qubit entangling gate carried out on a pair of qubits, each stored in the internal states of a neutral boson confined to one-dimension and controlled using optical tweezers, to show that the gate operates as expected in the adiabatic limit.

I used MATLAB$^{\text{TM}}$ to numerically express each spatial subsystem of the Hamiltonian (4.1) (one for each joint two-qubit state), using a 128×128 dimensional Hilbert space. I solved these Hamiltonians over a range of separation distances spanning $0 \leq d \leq 5\sigma$, for a variety of trap depths and scattering lengths. Representative plots chosen to highlight essential features of Hamiltonian's adiabatic energy curves are shown in Fig. 4.2.

To test the validity of eq. (4.9), I simulated evolutions of the time-dependent Schrödinger equation for the separation profile $d(t) = vt$ over a wide variety of gate speeds and values of V_0 and a_{ij} (including $a_{ij} < 0$), using each of the degenerate ground-state eigenstates as the initial state of the simulation. I performed these simulations in MATLAB$^{\text{TM}}$ using a "split-operator" formalism to iteratively propagate the position and momentum components of the Schrödinger equation describing the time-evolution of the system [151]. Defining $v_0 = \hbar\sigma\omega_{ab}^2/V_0$ according to eq. (4.9), I found that the average gate fidelity decreased steadily as gate speed was increased from $0.01v_0$ to v_0.

Representative figures showing the change-over from adiabatic to nonadiabatic gate operation are shown in Fig. 4.9. These figures depict two-dimensional visualizations of the two-particle wavefunction, in order to compare adiabatic and nonadiabatic evolutions. Under adiabatic conditions, both atoms are recovered in separate wells. Under nonadiabatic conditions both atoms may end up in the same well or escape entirely, resulting in an erroneous gate. As the gate speed increases, the average probability that the particle escapes also increases.

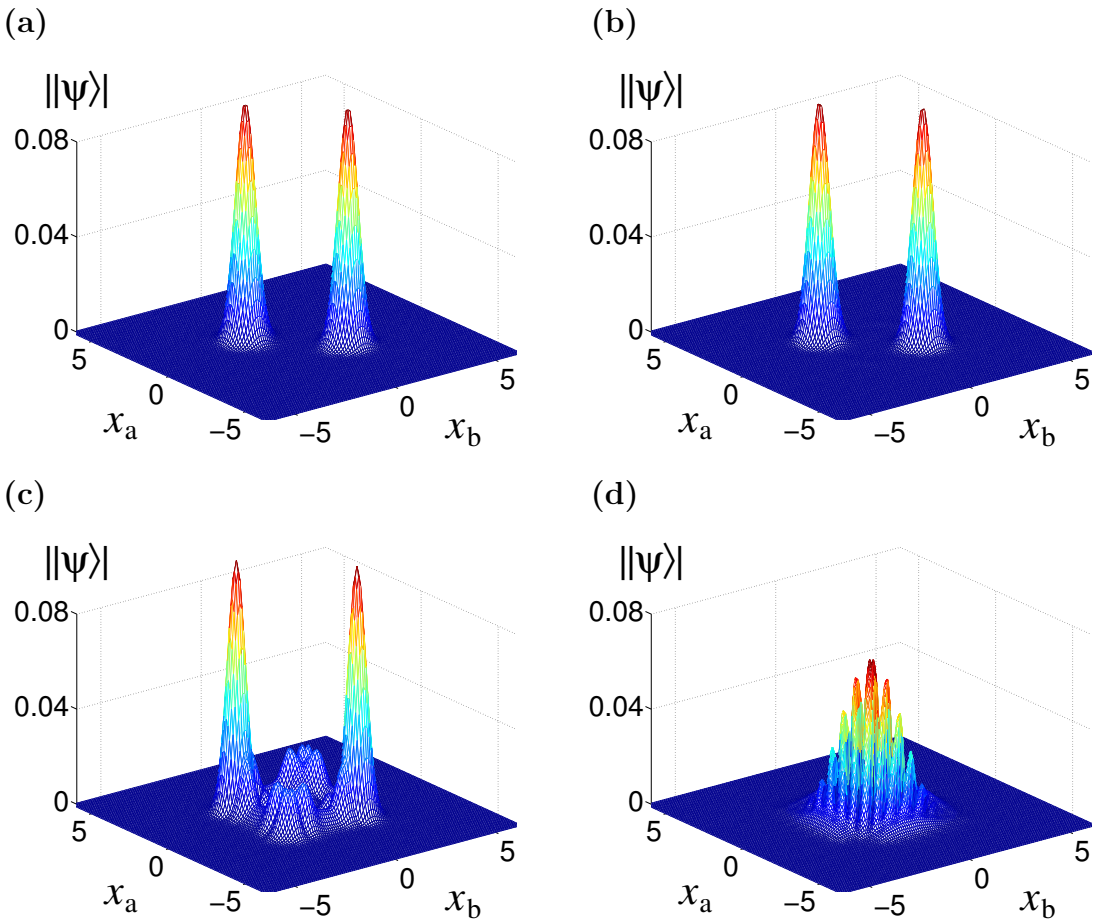

Figure 4.9: Representative figures of the magnitude of the two-atom vibrational wavefunction ($||\psi\rangle| \equiv ||\psi(x_a, x_b, t)\rangle|$) as a two-dimensional function of the position of each particle, reproduced with permission from Ref. [2] with permission. Plot (a) shows the initial wavefunction, $|\psi_{\text{init}}\rangle = (|\widetilde{\psi^{\text{L}}\psi^{\text{R}}}\rangle + |\widetilde{\psi^{\text{R}}\psi^{\text{L}}}\rangle)/\sqrt{2}$. Plots (b-d) show the wavefunction after the wells have been brought together and separated. Initial conditions are the same for all figures, and only the speed is varied (in units of $v_0 = \hbar\sigma\omega_{ab}^2/V_0$). The resulting vibrational state fidelities $f = |\langle\psi_{\text{init}}|\psi\rangle|^2$ are as follows: (b) $v \approx 0.01v_0$, $f = 0.9997$. (c) $v \approx 0.1v_0$, $f = 0.491$. (d) $v \approx v_0$, $f = 0.002$.

The local phase acquired by each eigenstate during gate operation is proportional to the time-integral of the energy of that state and is predetermined by the separation profile $d(t)$. Although the phases are acquired due to the distinct energies of the different vibrational states of the system, upon reseparation these phases are effectively "kicked

back" onto the qubit states. The phases acquired by the $|00\rangle$, $|\chi^+\rangle$, $|\chi^-\rangle$, and $|11\rangle$ states may be respectively denoted as ϕ_{00}, ϕ_+, ϕ_-, and ϕ_{11}. Using this notation, the entangling gate may be written as a unitary operation $\hat{U}$ of the form,

$$\hat{U} = e^{-i\phi_{00}}|00\rangle\langle 00| + e^{-i\phi_+}|\chi^+\rangle\langle\chi^+| + e^{-i\phi_-}|\chi^-\rangle\langle\chi^-| + e^{-i\phi_{11}}|11\rangle\langle 11|. \tag{4.10}$$

The separation profile $d(t)$ may be suitably tuned to produce phase values that are optimized to a given application. To generate a maximally entangling gate, it is only required that $\phi_+ - \phi_- = 2\pi n \pm \frac{\pi}{2}$ for arbitrary integer n.

4.8 Concluding Remarks

In conclusion, I have presented computer simulations of a time-dependent Hamiltonian representing a pair of identical composite atoms, confined by a pair of optical dipole traps ("laser tweezers") and translated along one dimension representing an additional confining beamline. I showed how the control of the physical system represented by this Hamiltonian may be used to carry out an entangling operation on the qubits stored in the internal states of the atoms by way of the exchange interaction. I showed how the spatial symmetry and parity of the system may be exploited to achieve operation fidelities better than those anticipated using the standard adiabatic criterion [76]. I used this finding to derive an operation-specific adiabatic criterion for this system under constant-velocity conditions, and I performed simulations to verify the accuracy of this criterion.

This work provides a preliminary analysis of an entangling two-qubit gate, and an example of an essential component for neutral atom-based quantum information processing technologies. While the collisional exchange-gate modeled here is based on a design employing optical tweezers and tight-confinement along one dimension, my findings regarding the symmetries of the Hamiltonian (Section 4.5) and the adiabaticity criterion (4.6) are generalizable to other implementations of exchange-based gates. Furthermore,

my anecdotal finding that certain gate speeds produced better-than-expected gate fidelities (ground state "revivals") suggests that gate quality may be enhanced by strategies to optimize gate timing, as I examine in Chapter 6.

This gate provides a conceptually simple example of a nonadiabatic transition between two degenerate electronic states defined by the logical qubit basis states $|0_{\rm L}1_{\rm R}\rangle$ and $|1_{\rm L}0_{\rm R}\rangle$. At large well separations, the concept of cluster separability [83] allows the neglect of the identical character of the two systems, so that the atoms (and the qubits they store) become effectively distinguishable. The separability of the two atoms implies that the underlying symmetric and antisymmetric states of the joint two-particle wavefunction are degenerate, as shown in Fig. 4.2. Qubit distinguishability is essential to the design and characterization of a quantum computing architecture, because it allows the quantification of the complexity of an algorithm in terms of classical input bits.

The breakdown of atomic separability (see Section 2.3.1) provides the mechanism for gate operation, as the degeneracy is broken between the adiabatic (symmetric and antisymmetric) vibrational eigenstates of the system. The phase evolution that arises between the *adiabatic* vibrational eigenstates presents itself in the form of time-dependent *nonadiabatic* dynamics of the "diabatic" electronic potential surfaces, effectively swapping them to exchange $|0_{\rm L}1_{\rm R}\rangle$ with $|1_{\rm L}0_{\rm R}\rangle$. The coherent nonadiabatic transition from $|0_{\rm L}1_{\rm R}\rangle$ to $|1_{\rm L}0_{\rm R}\rangle$ defines the logical operation of the gate. In this manner, it also provides a prototype system for investigations into the complex interplay between adiabatic and nonadiabatic dynamics of approximatately-adiabatic evolutions.

My results were published in the article, "Entangling identical bosons in optical tweezers via exchange interaction," in the *Canadian Journal of Physics* and have been cited in six (6) distinct peer-reviewed scientific articles [31, 3, 32, 34, 4, 33] since the time of the article's publication. The article is reproduced in the Appendix with written permission from the publisher.

Chapter 5

Atomistic Bell Test Without Loopholes

> *It is the requirement of locality, or more precisely that the result of a measurement on one system be unaffected by operations on a distant system with which it has interacted in the past, that creates the essential difficulty.*
>
> —John Bell, 1964 [90]

My three main contributions to the work described in Chapter 5 are summarized as follows:

1. *I present the design, on which I collaborated, for an experimental scheme to perform a loophole-free Bell-inequality test in a single laboratory (Section 5.2).*

2. *I analyze criteria necessary to ensure the feasibility of the spatial separation of an atomic Bell pair in a single laboratory using optical tweezers (Section 5.3).*

3. *I identify conditions to ensure that the selection of the measurement basis and the measurement of the Bell pair can be performed both rapidly and efficiently enough to violate Bell's inequality under spacelike-separated conditions (Section 5.4).*

5.1 Introduction: Completeness of Quantum Mechanics

The question of whether quantum mechanics can provide a "complete" description of reality has provided a steady topic of debate for eight decades [89]. Upon the publication of Bell's inequality in 1964 [90], it became possible, at least in principle, to quantitatively test the validity of the "nonlocal" quantum mechanical description of physical experience [91]. Clauser, Horn, Shimony, and Holt (CHSH) later distilled Bell's essential result

into a form that remains widely used today [152, 153], and emphasized the concepts of "signalling" and "detection" loopholes that might render the results of these experiments invalid.

Clauser *et al.* showed [152, 153] that if the states of a pair of spacelike-separated spin qubits labeled "a" and "b" are observed along axes respectively identified by the measurement operators $Q_{\rm a}$, $R_{\rm a}$, $S_{\rm b}$, $T_{\rm b}$, that the expectation values of these observables are bounded from above and below by the relationship

$$-2 \leq \langle Q_{\rm a} S_b \rangle + \langle R_{\rm a} S_{\rm b} \rangle + \langle R_{\rm a} T_{\rm b} \rangle - \langle Q_{\rm a} T_{\rm b} \rangle \leq 2 \tag{5.1}$$

for any local and realistic theory of empirical experience. This result is in contrast with the quantum mechanical result given by Cirel'son [154],

$$| \langle Q_{\rm a} S_{\rm b} \rangle + \langle R_{\rm a} S_{\rm b} \rangle + \langle R_{\rm a} T_{\rm b} \rangle - \langle Q_{\rm a} T_{\rm b} \rangle | \leq 2\sqrt{2}. \tag{5.2}$$

Cirel'son's quantum upper bound (5.2) is saturated by pairs of entangled qubits that are prepared in the $\frac{1}{\sqrt{2}}(|00\rangle + |11\rangle)$ state and observed using the measurement operators $Q_{\rm a} = \sigma_z$, $R_{\rm a} = \sigma_z$, $S_{\rm b} = (\sigma_x - \sigma_z)/\sqrt{2}$, and $T_{\rm b} = (\sigma_x + \sigma_z)/\sqrt{2}$, where $\{\sigma_x, \sigma_y, \sigma_z\}$, are the Pauli operators [3]. Quantum mechanics can be shown to be an experientially reproducable (if not "complete") description of reality by any Bell-inequality experiment that generates a statistical outcome between 2 and $2\sqrt{2}$ for eq. (5.1) using the set-up described above, granted that it is unimpinged by either the signalling or detection loopholes, described as follows.

To close the "signalling" loophole, it is required that the selection of the measurement axes and the measurements performed on each qubit be spacelike-separated from each other, in order to ensure that the result of one measurement cannot be signalled to the other measurement apparatus in time to affect the measurement outcome of that apparatus. To close the "detection" loophole, it is required that all pairs of entangled qubits that are prepared be measured, and the results of those measurements included

in the statistical average, in order to ensure that an apparently quantum mechanical result is not artificially fabricated by "pathological detectors" [152]. Although both the signalling [155] and detection [156] loopholes have each been separately closed during independent experiments, no single Bell inequality experiment has yet been carried out to close both loopholes simultaneously [26].

Regardless of the outcome of the experiment, the execution of a "loophole-free" test of local realism would mark an important milestone in the history of science, definitively answering a fundamental question about the nature of experience. Recently, loophole-free tests of quantum mechanics have also gained commercial and military importance, because the security of quantum cryptography depends on the validity of quantum mechanics. A quantum key distribution scheme might be compromised by an attacker exploiting an open loophole, even if it is possible to close the loophole in principle [26].

While experts have claimed that a loophole-free Bell-inequality test may be just a few years away using photonic entanglement-distribution schemes [26], these predictions may not anticipate all the technical obstructions hindering such an endeavor, either for a specific implementation or in general. According to Emilio Santos [157], "the validity of local realism may be either refuted by a single loophole-free experiment or increasingly confirmed by the passage of time without such an experiment." As-of-yet undiscovered physical laws may prohit the closure of both loopholes during a single experiment. For example, the loopholes themselves could obey a kind of complementary principle—akin to the uncertainty principle itself [158]—fundamentally preventing their simultaneous closure. For this reason, it is valuable to explore multiple avenues of attacking the problem, until both loopholes have been simultaneously closed. If both loopholes *cannot* be simultaneously closed, an exhaustive exploration of the problem will be necessary to determine why not [157], because the simultaneous closure of both loopholes is not presently understood to be prohibited by any laws of physics [26].

The atomic Bell test scheme that my collaborators and I propose elucidates how the entanglement and coherent long-range transport of a single-qubit may in principle be combined with existing technologies in order to perform a "loophole-free" Bell inequality test in a single laboratory. I worked closely with my collaborators René Stock, Mark Raizen, and Barry Sanders on all aspects of the conceptual design of this experiment. In addition to my design and analysis of the entangling gate (discussed in Chapter 4), my independent and essential contribution to this work was the analysis of reasonable conditions that will be necessary to achieve spacelike-separated measurements of entangled particles in a single laboratory. In addition to presenting a novel challenge to laboratory equipment that is intended to demonstrate high-precision quantum control, we offer an important alternative route to performing such a Bell test, should current approaches based on photonic entanglement distribution schemes prove insufficient.

5.2 Design of Test Scheme

In this Section, I describe a proposal for a scheme to perform a "loophole-free" test of local realism in a single laboratory that I developed in collaboration with René Stock, Barry Sanders, and Mark Raizen.

The scheme consists of multiple iterations of cycles of atomic Bell-pair preparations and measurements, in order to generate reliable statistics. Each iteration of the cycle consists of six distinct components:

- *Atomic Qubit Preparation* by the deterministic extraction of individual atoms from a Bose-Einstein condensate,
- *Qubit Encoding* as atoms are cooled into encoded logical states,
- *Single Qubit Operations* to prepare the atomic qubits in superposition states,

- *Entangling Operation* to create the Bell pair from two qubits,
- *Qubit Transport* to opposite ends of the laboratory, and
- *Rapid Measurement* of the qubits in randomly-selected measurement bases.

Detailed descriptions of each of these components follow.

5.2.1 Atomic Qubit Preparation

We propose to prepare atomic qubits using a scheme developed by Diener *et al.* [159] to deterministically extract individual bosonic atoms from Bose-Einstein condensate (BEC). Although experimental investigations into this atom-extraction scheme [159] and some others [39, 40] have been delayed [160], these proposals remain in principle viable. The development of high-fidelity methods for preparing individual continues to advance rapidly [114, 41, 43, 44].

Once each individual atom has been prepared, residual nuclear vibrations may be eliminated by cooling the atom down to its quantum ground state using Raman ("resolved") sideband cooling techniques [42].

5.2.2 Qubit Encoding

We propose to encode qubits in long-lived, spin-0 electronic states of divalent ("group-II-like") atoms. These "optical clock states" correspond to very narrow transitions to long-lived (metastable) electronic states. For example, group-II atoms such as strontium (Sr) exhibit a long-lived $^3\mathrm{P}_0$ state with a lifetime of approximately 30 s, while the lifetime of the $^3\mathrm{P}_2$ state is "longer still" [139]. To preserve coherence, it is crucial to store each atom in a state-independent trap via the use of a "magic wavelength," at which the AC Stark shifts of the encoded states become equal.

5.2.3 Single Qubit Operations

We propose to employ multiphoton stimulated absorption and emission processes using virtual states in order to encode qubits across metastable "forbidden" transitions, such as the $^3S_0 \leftrightarrow {}^3P_0$ transition that is common to group-II atoms. One- and two-photon transitions between $^3S_0$ and $^3P_0$ are respectively dipole- and parity-forbidden. Thus, state transfer from $^3S_0$ to $^3P_0$ requires at least two intermediary (virtual) states, such as $^3P_1$ and $^3S_1$. We propose to carry out single qubit rotations between $^3S_0$ and $^3P_0$ based on the three-photon sequence,

$$^3S_0 \rightarrow {}^3P_1 \rightarrow {}^3S_1 \rightarrow {}^3P_0. \tag{5.3}$$

A "Raman" type transition between $^3S_0$ and $^3P_0$ can be achieved using off-resonant "virtual" transitions through the $^3P_1$ and $^3S_1$ states [118]. Because this is a three-photon stimulated transition, the lasers involved can be arranged geometrically to ensure that no net momentum is imparted to the atom. This enhances the fidelity of the single-qubit gate by making it recoil-free [161]. Gate fidelities of 99.99% can in principle be achieved using laser intensities on the order of $10^6\,\mathrm{W/cm^2}$ [3].

5.2.4 Entangling Operation

We propose to use the exchange-based gate described in the last chapter in order to entangle pairs of trapped atomic qubits. This gate is inherently robust because the entangling phase is acquired in the nonlocal ("Bell") basis and thus is not prone to spatially-inhomogeneous field effects. The gate speed can be made as slow as is necessary to ensure high-fidelity adiabatic operation, because the milliseconds-timescale of the gate is orders of magnitude shorter than the seconds-timescale of the qubit lifetime.

5.2.5 Qubit Transport

We propose to transport each qubit a distance on the order of a few metres in order to ensure that the ensuing Bell-test measurements are spacelike-separated. Researchers in Paris have demonstrated two-dimensional spatial transport of a single atomic qubit a distance of a few hundred microns using a micron-scale optical tweezer [119]. Transport of the tweezer (*i.e.*, the focal point of the laser) was accomplished by way of a piezo-electrically actuated mirror. The researchers used spin-echo techniques to preserve qubit coherence during transport. They detected no noticable coherence-loss [119], suggesting that their method may be scaled up to much longer distances.

Using comparable technology, researchers at MIT used optical tweezers to successfully transport a BEC approximately half a meter, a distance which was limited by the size of their vacuum chamber [138]. Tweezer transport was accomplished by directing the collimated laser beam through a lens mounted on a linear translation stage running parallel to the beam, allowing for translation of the beam's 24 μm-radius focal point. The MIT researchers found that a maximum acceleration of 200 mm/s and a maximum speed of 80 mm/s were possible, given the limitations of their apparatus [138]. They expected that signficant improvements could still be made to further increase transport rates by addressing known sources of error [138].

The use of optimal control techniques [73, 162] and other commercial advances [163] promise further enhancements to transport speeds and fidelities. The strategic combination of the technologies developed both in Paris and at MIT will enable coherent transport of qubits to a separation distance of several meters with present-day or near-future technologies.

5.2.6 Rapid Measurement

We propose to measure the qubits using resonant multiphoton ionization and detection. Separation distances on the order of a few meters require that the Bell test measurement (including random basis selection) be performed on a timescale on the order of 10 ns. This time-window includes the time necessary to randomly select the measurement basis (*i.e.*, the angle of rotation, as represented on the Bloch sphere) and to perform the measurement itself. Random measurement basis selection can be achieved on a nanosecond timescale using a light-emitting diode (LED) in conjunction with a photomultiplier array as described in Ref. [164], coupled to an electro-optical modulator controlling the lasers that comprise the single-qubit gating mechanism. The measurements need to be tightly synchronized to guarantee they occur simultaneously in the laboratory reference frame.

We define the measurement to span the time necessary to perform the random basis selection, single qubit rotation, and ionization. Measurement is initiated with the initialization of the random basis selection and is completed with the irreversible transfer of the electron from a bound atomic state to an unbound state of the continuum. The result of the observation, namely the detection of an ion or the lack thereof, is then amplified and recorded using ionization spectroscopy.

5.3 Spacelike-Separated Qubits

In this Section, I describe my independent analysis of the feasibility of transporting the qubits to a separation distance sufficient to ensure that the qubit measurements are spacelike separated.

Simulations performed by Stock indicate that the one-qubit gates can be performed with near-unit fidelity [3]. Simulations performed independently by myself [2] and by Hayes *et al.* [28] indicate that the two qubit entangling gate can be peformed with near-

unit fidelity. Timescales for qubit preparation and entanglement are fractions of a second, and qubit lifetimes are on the order of at least seconds. Transport techniques discussed in Section 5.2.5 indicate that high-fidelity transport of qubits over a distance of several meters can itself be achieved, so the main hurdle to overcome is the transport of the qubits to a sufficiently-large separation distance within their coherence time.

Given a coherence time of 10 s [3], and a translation speed of about 0.1 m/s for each qubit, a separation distance of 2 m may be achieved—affording about 7 ns in which to perform the measurements. Lifetimes of the $^3P_0$ states in isotopes of ytterbium have been recorded at 20 s, and lifetimes of the $^3P_0$ states in isotopes of strontium around 30 s, suggesting that substantially-larger distances and longer measurement windows may be achieved by the optimal choice of atomic species. Much longer lifetimes may become available, as research in this field continues to develop. For example, the $^3P_2$ state of magnesium has recently been attributed a lifetime of more than half an hour [165]. These numbers suggest that it is feasible to separate entangled pairs of qubits by distances of several meters, ensuring tens of nanoseconds (or longer) in which to complete synchronous Bell test measurements once they have been initiated.

5.4 Rapid Bell Measurements

In this Section, I describe my independent analysis of the feasibility of performing random Bell test measurements with sufficient speed to ensure that they are spacelike separated.

Once adequate spatial separation of the qubits has been achieved, the observation is carried out via ultra-fast basis selection, single-qubit rotations, and measurement via "resonantly enhanced multiphoton ionization" (REMPI) and detection [166, 167]. The analysis that I performed in the preceding section indicates that a measurement window on the order of 10 ns will be adequate to ensure spacelike separation of the measurements.

The random binary decision necessary to select the measurement basis for each qubit can be implemented using a dimly-lit LED attached to a photomultiplier, the output of which is channelled to an electro-optical modulator controlling the degree of rotation performed on each qubit. Experimenters found that random numbers could be generated in this way on a 2 ns timescale [164]. The lengths of the signaling pathways between the random number generators and their corresponding single-qubit-rotation lasers will need to be minimized in order to reduce the total observation time. The necessary single qubit rotations can be carried out in about 2 ns or less with high fidelity [3].

REMPI techniques can then be used to selectively ionize the atom, depending on its logical state. For example, if logical $|0\rangle$ corresponds to the $^1S_0$ state and logical $|1\rangle$ corresponds to the $^3P_0$ state, then the atom might be selectively ionized exclusively from the $^3P_0$ state. This can be accomplished by performing a rapid on-resonant transition from $^3P_0$ to $^3S_1$ followed by the ionization step, ejecting the electron. These on-resonant transitions can be extremely fast, occuring on timescales of nanoseconds or even picoseconds [3]. The ejected ion and/or electron may then be detected using standard ionization spectroscopy techniques [166, 167]. Assuming electron velocities on the order of 10^9 mm/s [70] and detector distance scales on the order of 1 mm [167], nanosecond electron detection timescales are easily achieved.

I have assumed the irreversible dephasing of the qubit state that occurs upon ionization to demarcate the end of the observation. A purist's demand for the complete resolution of the measurement into a macroscopic electric current in the electron multiplier would necessitate the use of spatially-compact detectors with nanosecond-scale latencies, further increasing the minimum required separation distance. Even under these more exacting conditions, measurement timescales on the order of tens of nanoseconds may be achieved.

5.5 Concluding Remarks

In conclusion, I have presented my feasibility analysis of a loophole-free test of local realism based on the CHSH inequality. I collaborated on the design of the test and provided the design for the entangling gate it employs (see Chapter 4). I provided an order-of-magnitude assessment of the feasibility of achieving spacelike-separated conditions for the measurements employed in the test, based on reasonable hardware specifications.

There are two essential physical variables relevant to my feasibility assessment, the qubit separation distance and the measurement time. I found the separation distance to be limited by the lifetimes of the logical states employed and the precision of the transport apparatus. The measurement time is limited by the basis-selection time, measurement time, and measurement fidelity. I found that all of the limiting criteria related to the fundamental requirement of spacelike separation can be satisfied under realistic conditions, given known or expected technical specifications of the corresponding apparatus.

The atomic Bell test experiment proposed here represents an essential contribution to the investigation of fundamental limits determined by scientific methods, because the leading photonic proposals may yet encounter insurmountable hurdles [157]. Furthermore, the implementation of successful Bell tests using various different forms of entangled media would provide fundamental verification that the underlying physical principles that generate expressions like Bell's inequality and Tsirelson's bound are uniform across nature. These kinds of tests also provide hard benchmarks for assessing the development of emerging quantum technologies.

John Bell has stated that, "it is hard for me to believe that quantum mechanics works so nicely for inefficient practical set-ups and is yet going to fail badly when sufficient refinements are made" [164]. This statement relies on the implicit assumption that "sufficient refinements" *can* fundamentally be made. The simultaneous closure of both

loopholes defines a significant and unprecedented technical hurdle, in terms of precision quantum state transport, synchronization, and measurement. It is conceivable that as-of-yet undiscovered physical laws limit the collective precision of these operations, so to fundamentally prohibit the simultaneous closure of both loopholes. Uncertainty relations, akin to those already innate to quantum mechanics, may collectively govern fundamental limits on the simultaneous precision of these laboratory operations.

This work was published in the article, "Entanglement of group-II-like atoms with fast measurement for quantum information processing," in the *Physical Review A*. It has been cited in ten (10) different peer-reviewed scientific articles [4, 30, 34, 35, 36, 37, 38, 168, 169, 170] since the time of its publication. The article is reproduced in the Appendix with written permission from the publisher.

Chapter 6

Improved Error-Scaling for Two-Qubit Entanglement

> *A physical system remains in its instantaneous eigenstate when a given perturbation is acting on it slowly enough and if there is a gap between the eigenvalue and the rest of the Hamiltonian's spectrum.*
>
> —Max Born and Vladimir Fock (transl.), 1928 [171]

My four main contributions to the work described in Chapter 6 are summarized as follows:

1. *I develop a first-order numerical technique to efficiently simulate approximately-adiabatic quantum evolution (Section 6.2).*

2. *I adapt Nathan Wiebe's zeroth-order boundary cancellation technique to enhance the operation of the adiabatic gate beyond the limit set by the standard adiabatic approximation (Section 6.3).*

3. *I show that this technique can be used to asymptotically suppress error amplitudes, by performing extensive numerical simulations (Section 6.4).*

4. *I show that gate fidelity can be improved by about two orders of magnitude by synchronizing the suppression of multiple errors (Section 6.5).*

6.1 Introduction: Enhanced Adiabatic Evolutions

Adiabatic processes are essential to several components of atomic quantum computing schemes, including adiabatic transport, cooling, state preparation and manipulation. For example, adiabatic quantum computation gained prominence as a promising quantum

computing architecture, following the discovery that a "local adiabatic evolution" could be used to reduce the complexity of an adiabatic quantum search of an unstructured N-element database from order $\mathcal{O}(N)$ to order $\mathcal{O}(\sqrt{N})$ [172]—the same computational speedup achieved by Grover's quantum algorithm over an optimal classical algorithm to search an unstructured database [21].

Because processes that are based on adiabatic control are inherently slow, it is advantageous to employ schemes to increase adiabatic process speeds without loss of fidelity in time-sensitive applications. Methods for enhancing the speed or fidelity of an adiabatic quantum evolution beyond the limit set by eq. (2.2) represent a key area of research toward the development of practical QIP technologies, because adiabatic processes are "ubiquitous" to technological applications across physical disciplines ranging from atomic physics to semiconductor physics and spintronics [171].

Several atomic entanglement generation schemes rely on the adiabatic control of the motional state of trapped atoms [2, 28, 29, 112, 127]. For example, small differences in gate fidelities can determine whether a scalable quantum computing scheme can achieve its threshold for fault tolerance [173]. In the case of a scheme that is already fault tolerant, improvements to tolerable gate fidelities will still reduce the required amount of error correction resources. For this reason, methods to optimize entangling gates for fidelity and speed will be critical for their practical application of these gates to problems in computing [121] and metrology [131]. Yet, very few schemes to optimize these gates have so far been proposed [4, 174, 175].

Collision-based entangling gates rely on adiabatic state transfer to ensure that atoms are not excited to non-logical states during transport as they are brought together to interact. In this respect, these two-qubit entangling gates represent elementary examples of adiabatic quantum algorithms, because they carry out the adiabatic transformation of an "easy to construct" (unentangled) initial quantum state into a hard to construct

(entangled) final quantum state [108]. Thus, existing techniques for optimizing adiabatic quantum algorithms can in principle be applied to optimize the operation of adiabatic entangling gates. I provide a prototype example showing how to apply one such technique to improve the atomic two-qubit gate that was presented in Chapter 4.

6.2 Efficient Simulation of Approximately Adiabatic Evolutions

In this Section, I described simulation techniques that I developed in order to perform a statistically comprehensive set of simulations needed to demonstrate an asymptotic improvement in the operation of a two-qubit entangling gate.

Over the course of performing simulations of the two-qubit exchange gate described in Chapter 4, I noticed that some "magic" simulation speeds generated significant ground state revivals [2], opening the possibility of enhancing gate operation beyond the standard limit set by the adiabatic approximation [76]. This interference effect was previously noted by Charron and coworkers [174], in regard to a two-qubit gate wherein qubits were encoded in the motional states of neutral atoms. In that Letter [174], the authors provided a proof-of-principle example showing that fidelity of gate operation could be improved by more than two orders of magnitude under certain circumstances, but they did not provide a general equation to predict these fidelity enhancements or to estimate any asymptotic limits governing their result.

Inspired by discussions with Nathan Wiebe, I hypothesized that it would be possible to produce a general fidelity enhancement for gates of this kind. I realized that I would need to perform large numbers of simulations in order to carry out the comprehensive statistical sampling necessary for an asymtotic analysis. However, the simulations I developed previously in MATLAB$^{\mathrm{TM}}$ using the "split operator" method required several hours to perform on a typical desktop computer (precluding the completion of several

hundreds of simulations in a reasonable time), and efforts to transfer them onto a supercomputing platform proved fiscally intractable (due to licensing restrictions). I ultimately overcame this difficulty by transforming the representation of the Hamiltonian describing the system from the local position basis to its nonlocal instantaneous eigenstate basis.

Informed by insight I gained while considering the orbital contributions to "Franck-Condon" overlap factors during my study of nonadiabatic chemical reactions, I realized that the computational cost of a single simulation could be dramatically reduced by carrying out the simulation in the system's instantaneous eigenbasis (rather than iterations of the position and momentum bases), by calculating the instantaneous "overlap" factors coupling different eigenstates for each step of the simulation, and then by propagating the wavefunction in time according to the corrsponding nonadiabatic transition amplitudes. Specifically, I found that the computational cost-per-timestep could be reduced from $128^2 \times \log(128^2) \approx 70\,000$ operations to about $40^2 = 1600$ operations.

The simulation method that I developed relied upon the use of an index file storing the instantaneous eigenenergies and inter-eigenstate transition amplitudes for a discrete set of trap-separation distances, and the use of a spline fitting in order to interpolate between elements of that set. Although the initial diagonalization of the Hamiltonian for 1200 separation distances was numerically costly, it was nevertheless a *one-time* (*i.e.*, constant order) cost to generate a resource that could be reused indefinitely to greatly reduce the durations of hundreds of simulations. Each simulation time-step consisted of the propagation of each instantaneous eigenstate's time-dependent phase, followed by the transformation of the wavefunction expression from one instantaneous eigenbasis to the next. In essence, this method is like the "split operator" method in which the system is transformed between position and momentum bases at each computational step, but the tranformation between conjugate bases [158] is inherently more computationally costly than the transformation between nearly-identical eigenbases. Because each simulation

differed from the next only by the time-dependent profile of the separation distance, a single set of eigenenergies and (trivially-rescaled) transition matrix elements could be reused for every simulation.

The "adiabatic-overlap" simulation technique that I devised may be readily applied to more complex systems in higher dimensions (e.g., collisional gates modeled in three dimensions), with the possibility for even greater numerical speedups. This simulation technique therefore has particular value when applied to more sophisticated simulations of quantum gates, modeled in three dimensions with nonlinear separation profiles.

6.3 Boundary Cancellation Technique

In this Section, I describe the "boundary cancellation technique" developed by Nathan Wiebe in order to use quantum interferences to deterministically predict and suppress nonadiabatic transitions during the approximately-adiabatic quantum evolution.

The standard adiabatic approximation (originally derived by Born and Fock in 1928) states that, during an approximately adiabatic evolution of a quantum system initialized in the state $|a\rangle$, the maximum probability of a nonadiabatic transition between non-degenerate states $|a(t)\rangle = |a\rangle$ and $|b(t)\rangle = |b\rangle$ is $P_{ba} \approx |\mathcal{E}_{ba}|^2$, where

$$\mathcal{E}_{ba} = \max_t \frac{2\hbar \langle b|\dot{\hat{\mathcal{H}}}(t)|a\rangle}{\left(E_b(t) - E_a(t)\right)^2} \tag{6.1}$$

and where the dot denotes the time-derivative, and where $E_b(t)$ and $E_a(t)$ are the energies of the time-dependent eigenstates $|b\rangle$ and $|a\rangle$, respectively [76]. Introducing the change of variables $t \to s$ to the "reduced time" s such that $s = t/T$, where $0 \leq s \leq 1$ and T is the total duration of the adiabatic evolution, we may reformulate (6.3) as

$$\mathcal{E}_{ba} = \frac{1}{T} \max_s \frac{2\hbar \langle b|\dot{\hat{\mathcal{H}}}(s)|a\rangle}{\left(E_b(s) - E_a(s)\right)^2} \,. \tag{6.2}$$

As a general estimate, the overall adiabatic error $|\mathcal{E}|$ may be estimated as roughly no more than the "worst" individual error, such that

$$|\mathcal{E}| \lesssim \frac{1}{T} \max_{s} \frac{2\hbar \langle b|\hat{\dot{\mathcal{H}}}(s)|a\rangle}{\min_b |E_b(s) - E_a(s)|^2} \,. \tag{6.3}$$

Evidently, the overall error $|\mathcal{E}|$ scales with order $\mathcal{O}(T^{-1})$ in the asymptotic limit. While "local adiabatic" methods of enhancing adiabatic algorithms have generated improvements in asymptotic error-scalings with respect to the Hilbert space dimension 2^N (reflected by the size N of the quantum memory), these methods do not improve the error-scaling with respect to the evolution duration [4]. For individual adiabatically-operating components of a QIP system, such as an adiabatic two-qubit gate, it is neither necessary nor desirable to improve operation fidelity with respect to the scale of the operation. Instead, it is important to improve the operation fidelity with respect to the characteristics limiting its efficient operation, such as its duration.

A number of "boundary cancellation methods" [176, 177] have been developed to enhance the fidelity of quantum adiabatic algorithms. These methods have relied on the capacity to set one or more of the time-derivatives of the Hamiltonian to zero at the temporal boundaries of the algorithm (*i.e.*, $s = 0, 1$). Wiebe has shown that even in the limit where none of the Hamiltonian's derivatives are zero at the simulation boundaries, that another criterion can be used to perform an asymptotic fidelity-enhancement on the algorithm with respect to its duration T [4].

Specifically, Wiebe found that the error due to a particular transition $|0\rangle \leftrightarrow |\nu\rangle$ could be reduced from order $\mathcal{O}(T^{-1})$ to order $\mathcal{O}(T^{-2})$ by chosing the reduced Hamiltonian $\hat{\mathcal{H}}(s)$ to obey the criterion,

$$\left.\frac{\langle \nu(s)|\hat{\dot{\mathcal{H}}}(s)|0(s)\rangle}{\left(E_\nu(s) - E_0(s)\right)^2}\right|_{s=1} = e^{\mathrm{i}\theta} \left.\frac{\langle \nu(s)|\hat{\dot{\mathcal{H}}}(s)|0(s)\rangle}{\left(E_\nu(s) - E_0(s)\right)^2}\right|_{s=0} , \tag{6.4}$$

where (for completeness) θ is an arbitrary phase factor. This condition is automatically met for time-symmetric Hamiltonians like the two-qubit exchange gate in question. Given

that eq. (6.5) is met, transitions from $|0(s)\rangle|_{s=0} \rightarrow |\nu(s)\rangle|_{s=1}$ can be reduced from order $\mathcal{O}(T^{-1})$ to order $\mathcal{O}(T^{-2})$ by chosing the total duration of the gate to obey,

$$T_{n,\nu} = \frac{n\pi - \theta}{\int_0^1 [E_\nu(s) - E_0(s)]\,\mathrm{d}s}\,, \tag{6.5}$$

for *even* positive integers n. Errors due to nonadiabatic transitions are exacerbated for odd positive integers.

6.4 Fidelity-Enhanced Adiabatic Exchange Gate

In this Section, I describe the results of my simulations of the adiabatic exchange gate described in the last chapter, and demonstrate how the fidelity of the gate can be substantially improved without increasing its duration.

In order to integrate eq. (6.5), I diagonalized the two-particle Hamiltonian (4.1) over a set range of distances (as described in Section 6.2), and used a spline fitting to produce a smooth, integrable curve. The values predicted by eq. (6.5) for $T_{n,\nu}$ using this method did not produce consistent improvements in the simulated gate fidelity, and instead produced predictable periodic improvements. I was able to eliminate these beat frequencies by refining the estimate for $T_{n,\nu}$ according to the relationship $|T_{n,\nu} - T| \approx T/\Delta n$, where Δn counts the number of beats between the inverse of the actual duration of the simuation T^{-1} and the optimal inverse-duration $T_{n,\nu}^{-1}$. This calibration method reveals that the nonadiabatic error correcting technique can be applied to realistic experimental apparatus with systematic imperfections.

Figure 6.1 shows the results of the the simulations that were performed based on the refined estimates of $T_{n,5}^{-1}$. The set of durations $\{T_{n,5}^{-1}\}$ were chosen to suppress because the fifth excited state of the Hamiltonian is actually the first excited state to couple strongly to the ground state. The inset of Fig. 6.1 was chosen to show the beat frequency between

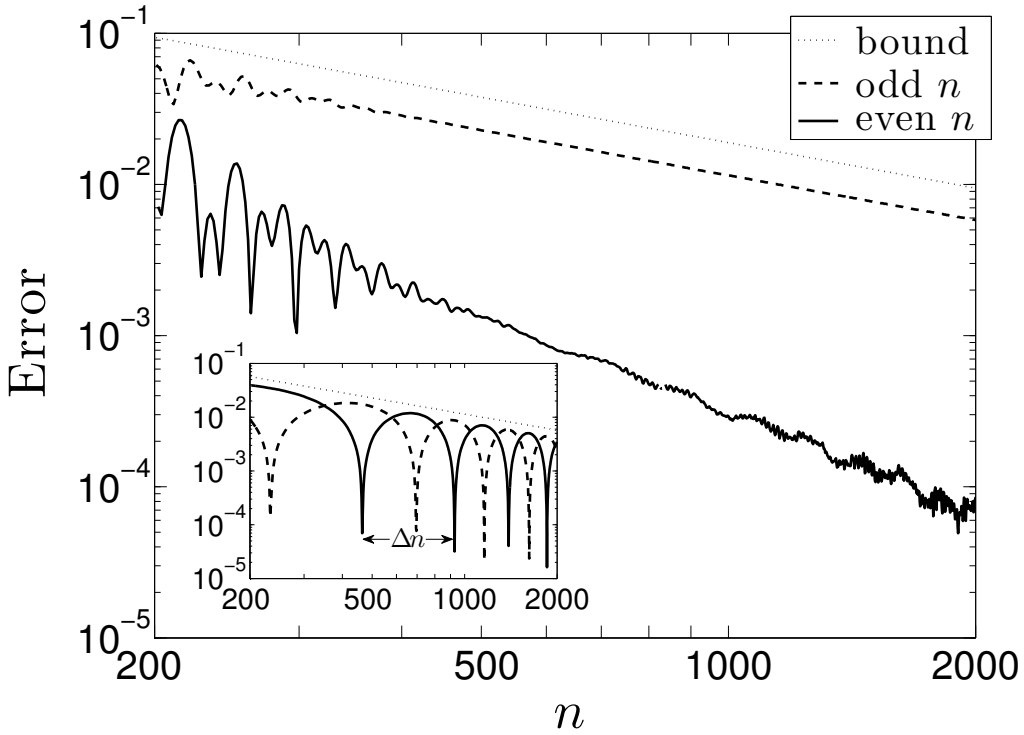

Figure 6.1: Transition amplitudes and bounds for $T = T_{n,5}$ over the range $200 \leq n \leq 2000$, reproduced from Ref. [4] with permission. The main figure shows $|\langle\psi_n^+|5\rangle| \approx |\mathcal{E}_{5\,0}|$ for even n (solid) and odd n (dashed). Odd simulations are are closely bounded by $\max_s[2\left\|\frac{\mathrm{d}}{\mathrm{d}s}H(x,p,s)\right\|/(E_5(s)-E_0(s))^2]$ (dotted), as expected. The inset shows $|\langle\psi_n^-|6\rangle|$ bounded by $\max_s[2\left\|\frac{\mathrm{d}}{\mathrm{d}s}H(x,p,s)\right\|/(E_7(s)-E_1(s))^2]$.

the simulation durations that suppress the symmetric $|0\rangle \rightarrow |5\rangle$ transition and those that suppress the antisymmetric $|1\rangle \rightarrow |6\rangle$ transition.

6.5 Suppresion of Multiple Transitions

In this Section, I show how the judicious choice of gate duration can be used to suppress multiple nonadiabatic transitions simultaneously, substantially improving gate fidelity.

As Fig. 6.1 shows, certain gate durations satisfy eq. (6.5) for multiple values of n. By carefully chosing gate times that simultaneously suppress nonadiabatic transitions in both the symmetric and antisymmetric subspaces of the Hamiltonian, the overall fidelity of the gate can be dramatically improved. Table 6.1 shows the nonadiabatic

transition *probabilities*, for simulation durations that approximately suppress the three most deleterious transitions. Specifically, these are the three nonadibatic vibrational transitions that couple most strongly to the logical subspace of the Hamiltonian during the overall operation of the gate. These findings indicate that the overall probability of an error occuring can be suppressed by two orders of magnitude using the boundary cancellation technique.

Int.	Error Probabilities ($\times 10^{-4}$)					Phase
n	$\lvert\langle 0\rvert 5\rangle\rvert^2$	$\lvert\langle 1\rvert 6\rangle\rvert^2$	$\lvert\langle 1\rvert 7\rangle\rvert^2$	$\lvert\mathcal{E}^+\rvert^2$	$\lvert\mathcal{E}^-\rvert^2$	α
456	0.024	0.012	0.245	0.988	0.535	1.645
458	0.022	0.007	0.180	0.771	0.433	−0.186
460	0.021	0.003	0.124	0.648	0.316	4.266
462	0.021	0.001	0.078	0.764	0.275	−3.849
464	0.023	<0.0001	0.043	0.980	0.249	0.603
466	0.023	<0.0003	0.018	1.010	1.201	−1.228
468	0.023	0.002	0.003	0.925	0.292	−3.059
470	0.023	0.004	<0.0001	0.763	0.452	1.392
472	0.022	0.007	0.006	0.721	0.502	−0.438
474	0.021	0.012	0.021	0.803	0.654	4.014

Table 6.1: Error probabilities and the phase gap α (radians) that is generated between symmetric and antisymmetric states, obtained from simulations of durations $\{T_{n,5}\}$ for $456 \leq n \leq 474$. The $|0\rangle \rightarrow |5\rangle$, $|1\rangle \rightarrow |6\rangle$, and $|1\rangle \rightarrow |7\rangle$ transitions are all suppressed for simulations of these durations. The total error probability for the symmetric ground state $|0\rangle$ is $|\mathcal{E}^+|^2$, whereas the total error probability for the antisymmetric metastable state $|1\rangle$ is denoted as $|\mathcal{E}^-|^2$. These values are to be compared with those predicted by eq. (6.3), which are $|\mathcal{E}^+|^2 \leq 0.46 \times 10^{-1}$ and $|\mathcal{E}^-|^2 \leq 0.62 \times 10^{-3}$ at $n = 460$.

6.6 Concluding Remarks

In conclusion, I have presented my contributions to the development of a method to polynomially improve the fidelity of the exchange-based two-qubit gate discussed in Chapter 4, beyond the limit set by the standard adiabatic approximation (6.3). I developed an algorithm to improve the computational efficiency of the simulations of the gate by carrying out simulations in the time-dependent eigenbasis of the system Hamiltonian

rather than the position (or momentum) basis used initially to define the Hamiltonian. I adapted Wiebe's zeroth-order boundary cancellation technique to predict maximally optimal (and non-optimal) gate times, and I performed extensive simulations to demonstrate an asymptotic reduction in the error-rate for a particular nonadiabatic transition. I showed that multiple transitions could be suppressed simultaneously, resulting in an overall improvement in gate fidelity of two orders of magnitude.

These results demonstrate that it is feasible to use interference effects to optimize the two-qubit entangling gate examined here, by dynamically correcting nonadiabatic errors. Although I considered a simple one-dimensional model of the gate using a linear translation profile, the optimization technique itself may be applied to more sophisticated model systems, and may readily be combined with other adiabatic optimization techniques including "local adiabatic" evolutions and higher-order "boundary cancellation" techniques. The development and characterization of these optimization techniques will provide fundamental engineering principles to guide the design and optimization of practical QIP schemes using ultracold neutral atoms and other related implementations.

My results were published in an article I co-wrote with Nathan Wiebe, titled "Improved error-scaling for adiabatic quantum evolutions," in the *New Journal of Physics* [4]. This article has been cited in nine (9) different peer-reviewed scientific articles [77, 178, 179, 180, 181, 182, 183, 184, 185] since the time of its publication. The most notable and exciting take-up of my work in this area has been by Kieferová and Wiebe, who were inspired by my findings with Wiebe [4] to invent a new type of quantum computing architecture, "*directly equivalent neither to the circuit model of quantum computing nor to adiabatic quantum computing*" [77].

Inspired by the use of interference effects due to Hamiltonian symmetries and precision timing in order to correct nonadiabatic errors [4], Kieferová and Wiebe conceived that it would be possible to correct nonadiabatic errors by instead using interferences

between superpositions of multiple time-depedent adiabatic evolutions [77]. Curiously, their generalization of the adiabatic approximation to allow the adiabatic subsystem to "evolve under a superposition of different adiabatic evolutions" [77] is equivalent to the relaxation of the first assumption of the Born-Oppenheimer approximation (*i.e.*, nuclear classicality) to allow the nuclei to follow multiple superpositions of time-dependent paths through phase space. Evidently, the introduction of nonadiabatic effects into a computing system alters the algorithmic complexity of that system. The discovery that the computational power of a quantum mechanical system can in principle be increased by the controlled relaxation of the Born-Oppenehimer approximation has fundamental implications for the quantitative bounds limiting the efficiency and specificity of a molecular recognition system.

My article with Wiebe [4] is reproduced in the Appendix with written permission from the publisher.

Part II

It is one of the most remarkable things that in all of the biological sciences there is no clue as to the necessity of death. If you say we want to make perpetual motion, we have discovered enough laws as we studied physics to see that it is either absolutely impossible or else the laws are wrong. But there is nothing in biology yet found that indicates the inevitability of death. This suggests to me that it is not at all inevitable, and that it is only a matter of time before the biologists discover what is the trouble and that that terrible universal disease or temporariness of the human's body will be cured. Anyhow, you can see that there will be problems of a fantastic magnitude coming from biology.

—Richard P. Feynman, 1964 [186]

Chapter 7

Biological Electron Transfer

> *The study of electron transfer processes has thus increased very greatly in scope and taken on an entirely new emphasis since the Faraday Society last considered this subject at the Discussion on Oxidation in 1945.*
>
> —J. Halpern and L. E. Orgel, 1960 [187]

In 1941, Albert Szent-Györgyi suggested that a model of delocalized "common energy levels" might explain the unique and mysterious catalytic properties of biological molecules [188]. In particular, he suggested that such an energetic band structure might explain the specificity and efficiency of biological electron transfer systems. He compared his hypothetical model to the one already in use to explain the conductive and semiconductive properties of crystals and metals, in which "a great number of atoms is arranged with regularity in close proximity, as for instance in a crystal lattice," so that "the terms of the single valency electrons may fuse into common bands" [188].

In 1949, Evans and Gergely followed up on Szent-Györgyi's considerations by analyzing the band-structures of a number of prototypical polypepide molecules with regard to their conductive aspects. They concluded that in general a protein structure "possesses 'semiconductive' properties, but these could never be realized by thermal excitation" [189]. Among their concluding remarks, Evans and Gergely noted that [189],

> Judging from the width of the energy bands in a protein structure the electrons are much more localized than in a metal or a graphite structure. The narrowness of these bands suggests that in order to transfer electrons to or

> from [an] empty or full level of another system the energy levels of the structures must be closely matched. This may indeed have a bearing on specificity of reactions between coupled resonating systems.

In 1956, Chance and Williams [190] examined and compared a number of then-competing conjectures about electron transport mechanisms, but did not consider tunneling among those possibilities. Ten years later, De Vault and Chance [191] found that the oxidation of cytochrome was essentially temperature-independent below 100 K, inferring that

> The slowness of the temperature-independent part of the light-induced cytochrome oxidation in *Chromatium* observed in the present work indicates that some kind of barrier to electron transfer is present, but the lack of activation energy indicates that the electron does not jump over the barrier. Tunneling is surely the simplest explanation.

De Vault and Chance's electron tunneling hypothesis remained untested for nearly two decades. In 1982, Winkler *et al.* observed rapid intramolecular charge transfer over a distance of 15 Å in horse heart *cytochrome c*, conclusively identifying tunneling-mediated electron transfer as a viable biological charge transport mechanism. Academic interest in biological electron transfer kinetics dramatically intensified in the wake of this discovery [192]. In 1982, Winkler *et al.* [193] provided more conclusive evidence of this sort, finding the rate of electron transfer across 15 Å to be temperature-independent between 0°C and 37°C in prosthetically-ruthenated horse heart cytochrome *c*. They concluded that redox enzymes could conceivably transport electrons via site-to-site tunneling, and that "the most significant aspect of this type of intramolecular fixed-site experiment is that as more data are gathered it will provide a means of critically assessing the factors that control the rates of biological electron-transfer processes" [193].

Several of the most rigorous empirical confirmations of biological electron transfer theory have come from the study of ruthenium-modified redox proteins [62, 192, 194]. These experiments have provided essential characterizations of the exponential decay factors that describe nonadiabatic electron transfer [62, 192], providing consistent empirical verification of the original studies [62]. Controlled measurements of the exponential decay factors are carried out by artificially attaching a ruthenium (Ru) atom at a specified location on a metalloprotein (such as azurin [194]), and then measuring the rate of electron transfer from the metalloprotein's native metal centre to the artificial Ru-cofactor over a range of attachment locations.

7.1 The Electron Transfer Integral

In biological ET systems, the tunneling rate is determined not by the direct donor-acceptor coupling element $\mathcal{H}_{\mathrm{DA}}$ *per se*, but rather by the transfer integral $\mathcal{T}_{\mathrm{DA}}$. The integral $\mathcal{T}_{\mathrm{DA}}$ describes a phase-weighted sum of all possible transition amplitudes that couple the donor state into the acceptor state. The instantaneous value of $\mathcal{T}_{\mathrm{DA}}$ may be formulated using molecular orbital theory as a composite of various orbital interactions mediated by virtual exchange through intervening "bridge" orbitals.

Until the late 1950s, investigations of oxidation-reduction reactions were limited almost exclusively to "considerations of stoichiometry and thermodynamics" [187], with little attention paid to the intrinsic ET mechanisms. In 1960, Harden McConnell developed a model of resonantly-coupled charge transfer between a pair of aromatic rings linked by an alkane bridge, after noticing that the rate of spin-magnetization transfer in aromatic free radicals was "essentially identical" to the rate of intramolecular charge transfer. He used the energy splitting between the symmetric and antisymmetric spatial eigenfunctions of the transient electron in order to calculate the charge transfer rate,

finding that it decayed exponentially with the charge transfer distance. He did not relate his finding to studies of electron transfer in biological molecules.

In 1974, J. J. Hopfield addressed de Vault and Chance's biological electron-tunneling hypothesis explicitly, calculating the electron transfer "tunneling matrix element" $\mathcal{T}_{\mathrm{DA}}$ between a pair of atomic "sites" by assuming that the intervening medium could be treated as a square dielectric barrier [195]. Naturally, the early models of McConnell [196] and Hopfield [195] have proliferated into a variety of treatments. Nowadays, two semi-empirical models of superexchange-mediated ET dominate the relevant literature [197], the atomically-detailed "pathway" model [198, 199, 200, 201] and the coarse-grained "packing density" model [202, 203].

7.1.1 McConnell's Model

Harden McConnell originally treated tunneling-mediated charge transfer through alkane bridges in 1961 [196]. He showed that if a pair of degenerate, spatially-separated electronic spin-orbitals ($|\chi^{\mathrm{D}}\rangle$, $|\chi^{\mathrm{A}}\rangle$) are connected through a series of N_{B} identical, tightly-bound bridging orbitals ($|\chi^{\mathrm{B}}_j\rangle$, $j = 1 \ldots N_{\mathrm{B}}$) then the degeneracy will be lifted with a corresponding energy gap g of approximate magnitude

$$g = |\mathcal{H}_{\mathrm{DB}_1}| \frac{|\mathcal{H}_{\mathrm{BB}}|^{N-1}}{|\Delta E_{\mathrm{DB}}|^{N_{\mathrm{B}}}} |\mathcal{H}_{\mathrm{B}_N\mathrm{A}}|, \tag{7.1}$$

where $\mathcal{H}_{\mathrm{DB}_1} = \langle \chi^{\mathrm{D}} | \mathcal{H} | \chi^{\mathrm{B}}_1 \rangle$, $\mathcal{H}_{\mathrm{B}_N\mathrm{A}} = \langle \chi^{\mathrm{B}}_N | \mathcal{H} | \chi^{\mathrm{A}} \rangle$, and $\mathcal{H}_{\mathrm{BB}} \ll \Delta E_{\mathrm{DB}}$. Also, for all j,

$$\mathcal{H}_{\mathrm{BB}} = \mathcal{H}_{\mathrm{B}_j\mathrm{B}_{j+1}} = \langle \chi^{\mathrm{B}}_j | \mathcal{H} | \chi^{\mathrm{B}}_{j+1} \rangle \text{ and}$$

$$\Delta E_{\mathrm{DB}} = \Delta E_{\mathrm{DB}_j} = \langle \chi^{\mathrm{D}} | \mathcal{H} | \chi^{\mathrm{D}} \rangle - \langle \chi^{\mathrm{B}}_j | \mathcal{H} | \chi^{\mathrm{B}}_j \rangle.$$

McConnell's result emerges as the highest-order approximation to the donor-acceptor coupling after carrying out the recursive perturbation of the donor orbital by each of the bridging orbitals in sequence. For a sequence of N_{B} non-identical bridging orbitals (*i.e.*,

$|\mathcal{H}_{\mathrm{B}_j\mathrm{B}_{j+1}}| \neq |\mathcal{H}_{\mathrm{B}_k\mathrm{B}_{k+1}}|$ and $|\Delta E_{\mathrm{DB}_j}| \neq |\Delta E_{\mathrm{DB}_k}|$ for all j, k), McConnell's result naturally generalizes to the form that decays exponentially with the donor-acceptor separation distance via the number of intervening bridge orbitals,

$$|\mathcal{T}_{\mathrm{DA}}| = \frac{|\mathcal{H}_{\mathrm{DB}_1}||\mathcal{H}_{\mathrm{B}_N\mathrm{A}}|}{|\Delta E_{\mathrm{DB}_1}|} \prod_{j}^{N_{\mathrm{B}}-1} \frac{|\mathcal{H}_{\mathrm{B}_j\mathrm{B}_{j+1}}|}{|\Delta E_{\mathrm{DB}_j}|}. \tag{7.2}$$

7.1.2 Hopfield's Model

In 1974, J. J. Hopfield treated electron transfer as a tunneling event across a square barrier in one-dimension. This homogenous dielectric model implies that the electronic coupling strength should decay exponentially with increasing donor-to-acceptor separation r [195]. The distance-dependent transfer function $\mathcal{T}_{\mathrm{DA}}(r)$ thus takes the generic form

$$\mathcal{T}_{\mathrm{DA}}(r) = \mathcal{T}_{\mathrm{DA}}(r_\circ) \cdot e^{-\beta(r-r_\circ)/2}, \tag{7.3}$$

where $\mathcal{T}_{\mathrm{DA}}(r_\circ)$ is the donor-acceptor coupling at the van der Waals contact distance $r_\circ$, and β is a decay factor parameterized by the barrier height. By construction, Hopfield's simplistic model is inadequate to account for electron tunneling through inhomogeneous (*i.e.*, topologically-detailed) media.

The similarity between Hopfield's model (7.3) and McConnell's model (7.1) model is evident. Both formulae consist of a close-contact coupling energy $\mathcal{T}^0_{\mathrm{DA}}$ multiplied by a unitless decay term ε, *i.e.*,

$$\mathcal{T}_{\mathrm{DA}} = \mathcal{T}^0_{\mathrm{DA}} \cdot \varepsilon_{\mathrm{DA}}. \tag{7.4}$$

The generic form of $\mathcal{T}_{\mathrm{DA}}$ given by eq. (7.4) is valid so long as the donor, acceptor, and intermediary "bridge" orbitals are distinct (*i.e.*, approximately orthonormal). Because the close-contact term $\mathcal{T}^0_{\mathrm{DA}}$ is independent of the medium structure by definition, the modeling of long-distance electron transfer through inhomogeneous media essentially reduces to the description of the tunneling wavefuction through the transfer medium and the corresponding analysis of the medium-dependent decay factor $\varepsilon_{\mathrm{DA}}$.

7.1.3 The Pathway Model

Throughout the 1980s, David Beratan, J. J. Hopfield, José Onuchic, and coworkers developed a semi-empirical model to account for the inhomogeneity of biological media. At the suggestion of Rudolf Marcus, they performed extensive investigations to determine how electronic coupling terms might arise from a combination of (covalent) "through-bond" interactions and non-bonded "through-space" interactions [198, 199, 200, 201].

Following McConnell's original treatment, Beratan *et al.* defined a "tunneling pathway" linking the donor and acceptor as a sequence of N non-identical, coupled molecular orbitals [204, 205, 206, 207]. The net tunneling amplitude (7.4) is proportional to the product of the decay factors ϵ_i connecting the orbitals in the sequence, such that $\mathcal{E}_{\mathrm{DA}} = \prod_i \epsilon_i$. In the tunneling pathway model, the decay factors are individually categorized as covalently-bonded (ϵ^{C}), hydrogen-bonded (ϵ^{H}), and through-space (ϵ^{S}) decay factors, such that

$$\varepsilon_{\mathrm{DA}} = \prod_{i=1}^{N_{\mathrm{C}}} \epsilon_i^{\mathrm{C}} \prod_{i=1}^{N_{\mathrm{S}}} \epsilon_j^{\mathrm{S}} \prod_{k=1}^{N_{\mathrm{H}}} \epsilon_k^{\mathrm{H}} \tag{7.5}$$

where N_{C}, N_{H}, and N_{S} are respectively the numbers of covalently-bonded, hydrogen-bonded, and through-space links making up a particular pathway. The individual decay factors ϵ^{C}, ϵ^{H}, and ϵ^{S} are parametrized in the following way [206]:

$$\epsilon_i^{\mathrm{C}} = 0.6, \tag{7.6}$$

$$\epsilon_j^{\mathrm{H}}(r_j) = 0.36\, e^{-1.7(r_j - 2.8\text{Å})/\text{Å}}, \tag{7.7}$$

$$\epsilon_k^{\mathrm{S}}(r_k) = 0.6\, e^{-1.7(r_k - 1.4\text{Å})/\text{Å}}. \tag{7.8}$$

This parameterization was developed semi-empirically, after Beratan and Hopfield noticed that the through-bond decay across covalent bonds was approximately 0.6/bond in the protein backbone [198]. Hydrogen-bonds contribute a decay factor of that of approximately two covalent bonds at an atom-to-atom distance of $r_j = 2.8$Å [208]. Through

space jumps fall off exponentially from the covalent value ϵ_i^{C} with an exponential decay factor of -1.7Å^{-1} in vacuum [208].

Multiple tunneling pathways may be constructed through the structurally-complex protein environment. The task of finding the optimal "donor to acceptor" pathway is mathematically equivalent to solving the graph-theoretic "shortest path" problem on a weighted, complete graph. For system comprising a configuration of bridging orbitals, there will be a combinatorial number N_ε of possible decay factors forming the set $\{\varepsilon_n\}$ where $n = 1 \ldots N_\varepsilon$. In the tunneling-pathway model, the largest term in the set is taken as the decay factor representing the entire configuration (*i.e.*, $\varepsilon_{\mathrm{DA}} = \max\{\varepsilon_n\}$). According to the pathway model, the single strongest pathway determines the magnitude of the coupling and all other pathways are neglected.

The pathway model achieves simplicity at the cost of ignoring possible interference effects between multiple pathways. Thus, the model can be expected to provide an accurate measure of the coupling strength when a single pathway (or a collection of equally-strong, constructively-interfering pathways) dominates over all of the other possible pathways in terms of the magnitude of its coupling strength. The model fails to describe the coupling for molecular configurations with multiple interfering pathways of comparable amplitude and non-uniform phase. Despite this limitation, the tunneling-pathway model has accurately predicted coupling decay factors for a variety of ruthenated proteins [208].

7.1.4 The Packing Density Model

During the 1990s, Christopher Moser, Leslie Dutton and coworkers suggested that the Beratan and coworkers' pathway formulation might be further simplified [202, 203]. Noting that the logarithms of ET rates decay roughly linearly with respect to donor-acceptor separation across a wide variety of biological and semi-synthetic systems, Dutton *et al.* hypothesized that biological ET couplings might be modeled entirely in terms of the distance

between the donor and acceptor cofactors [202]. Dutton *et al.* later expanded this model to include as a variable the overall structural density of the intervening medium [203].

The packing density model assumes that the transfer medium may be treated as an inhomogeneous dielectric medium, taking a density-weighted average between the (optimal) coupling amplitude of a covalently-bridged ET ($\beta \approx 0.9$Å) with that of vacuum-mediated transfer ($\beta \approx 2.8$Å). Thus, the decay constant in eq. (7.4) is taken as

$$\varepsilon_{\mathrm{DA}}(r) = e^{-[0.45\rho+1.4(1-\rho)](r_{\mathrm{DA}}-3.8\text{Å})/\text{Å}}, \tag{7.9}$$

where r_{DA} is the donor-acceptor distance, and the density $0 \leq \rho \leq 1$ is explicitly defined as "the fraction of the volume between redox cofactors that is within the united van der Waals radius of intervening atoms" [203]. The packing density model gives good agreement with experimentally measured electron transfer rates for numerous physiologically significant reactions [203], but is known to fail for certain specific ET systems [209].

7.1.5 *Ab Initio* Models

Ab initio calculations of the transfer integral $\mathcal{T}_{\mathrm{DA}}$ can be used to verify the accuracy of semi-empirical estimates, and can help clarify the cause of anomalous results in cases where experiment is not in agreement with the semi-empirical prediction. Empirical disagreement with the packing density model may be expected when the heterogeneity of the ET medium promotes virtual charge transfer along a non-geodesic pathway connecting the donor to the acceptor cofactor [209]. Empirical disagreements with the pathway model are expected when the magnitude of $\mathcal{T}_{\mathrm{DA}}$ depends strongly on multi-pathway interference effects [51]. In cases where multi-pathway interferences play a role and the nuclear configuration is static on the timescale of ET, the transfer integral $\mathcal{T}_{\mathrm{DA}}$ can be calculated using a *self-consistent field* (SCF) theory, such as Hartree-Fock theory [75], extended Hückel theory [210, 211], or density functional theory (DFT) [212].

Models of $\mathcal{T}_{\mathrm{DA}}$ that use a static treatment for the nuclei will fail when non-Condon effects couple electronic degrees of freedom to nuclear degrees of freedom during the ET event [84, 213, 211]. When the Condon approximation breaks down, $\mathcal{T}_{\mathrm{DA}}$ can still be calculated using time-dependent operator techniques that take vibronic resonances and dephasing into account. For example, non-Condon models of ET are crucial to models of olfaction based on phonon-assisted tunneling [214, 215]. When inelastic electronic tunneling becomes a significant factor determining $\mathcal{T}_{\mathrm{DA}}$, the primary ET mechanism can change from superexchange to resonant tunneling to sequential thermal hopping [51].

7.2 The Marcus Equation

The rate k_{ET} of a nonadiabatic electron transfer reaction is derived as the transition rate for a thermal ensemble using "Fermi's Golden Rule" such that it takes on the familiar form [76, 216],

$$k_{\mathrm{ET}} = \frac{2\pi}{\hbar} \left|\mathcal{T}_{\mathrm{DA}}\right|^2 \varrho_{\mathrm{FC}}, \tag{7.10}$$

where the Franck-Condon weighted-density of states ϱ_{FC} describes the probability that the ET system is "activated" to achieve degeneracy between the reactant and product states. Rudolph Marcus has derived a formal expression for the factor ϱ_{FC}, as it applies to nonadiabatic ET reactions, and the "Marcus equation" is now commonly used to predict nonadiabatic ET reaction rate-constants [86, 217],

$$k_{\mathrm{ET}} = \frac{2\pi}{\hbar} \left|\mathcal{T}_{\mathrm{DA}}\right|^2 \frac{1}{\sqrt{4\pi\lambda k_{\mathrm{B}} T}}\, e^{-(\Delta G^{\circ}+\lambda)^2/4\lambda k_{\mathrm{B}} T}. \tag{7.11}$$

In eq. (7.11), k_{ET} denotes the molecular electron transfer rate, $\hbar$ is the reduced Planck constant, k_{B} is Boltzmann's constant, T is the reaction temperature, $\mathcal{T}_{\mathrm{DA}}$ is the superexchange-mediated electronic transition integral [211], ΔG° is the standard Gibbs free energy of product formation [218], and λ is the so-called "reorganization free en-

ergy" [86]. Corresponding with eq. (7.10), the factors following after $|\mathcal{T}_{\mathrm{DA}}|^2$ in eq. (7.11) are collectively called the "Franck-Condon factor."

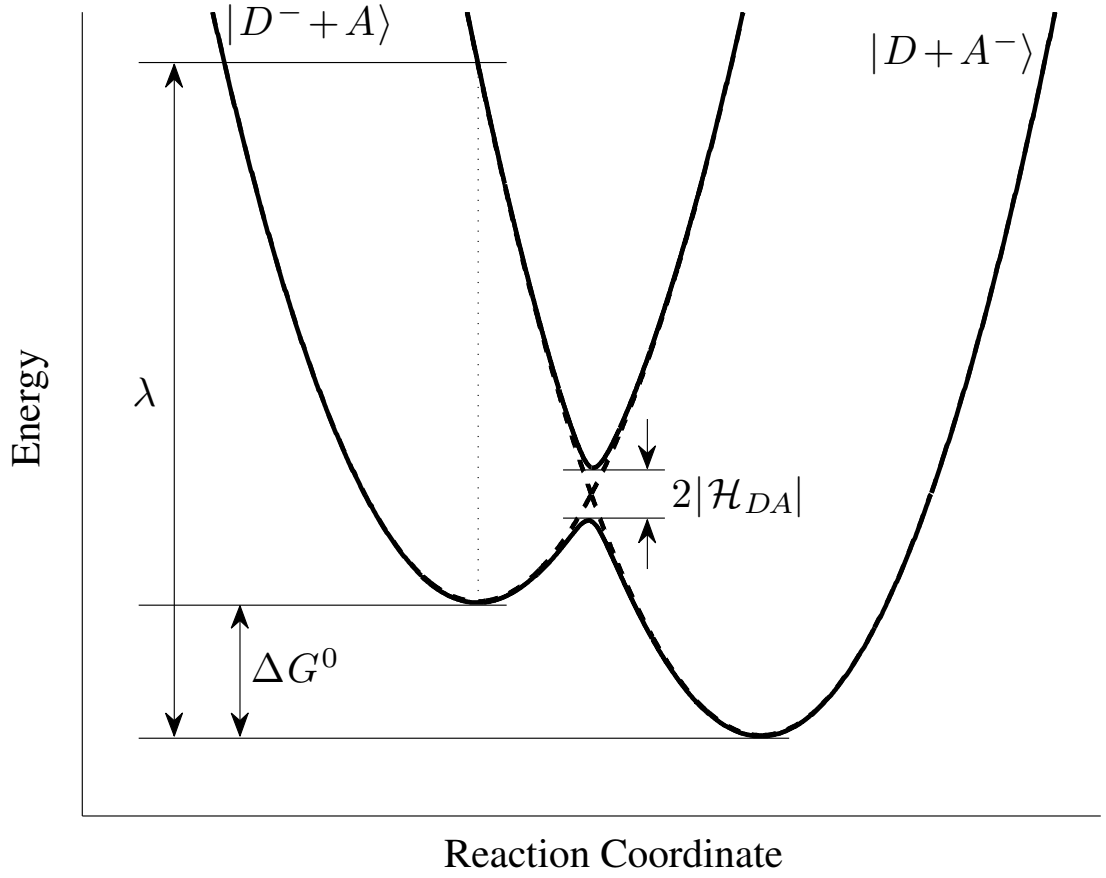

Figure 7.1: Diagram shows the Marcus reactant ("$|D^- + A\rangle$") and product ("$|D + A^-\rangle$") diabatic energy surfaces, approximated as a pair of identical one-dimensional harmonic wells (dashed curves). The wells are superimposed on the hybrid adiabatic surfaces (solid curves) to show the energy gap at the crossing point. I calculated the curves using MATLAB$^{\mathrm{TM}}$ with the generic parameters $-\Delta G^\circ = 5|\mathcal{H}_{\mathrm{DA}}|$ and $\lambda = 25|\mathcal{H}_{\mathrm{DA}}|$, where $|\mathcal{H}_{\mathrm{DA}}|$ provides the lowest order contribution to $|\mathcal{T}_{\mathrm{DA}}|$ in eq. (7.11).

According to eq. (7.11), the Gibbs free energy ΔG° and the reorganization free energy λ jointly control the probability that the reactant and product redox states reach a resonant configuration. By definition, reactant-product resonance occurs as thermal fluctuations render the energies of the reactant and product states degenerate. When applied to biological reactions, the few parameters contained in eq. (7.11) can conceal a wealth of underlying kinetic complexity. Empirical studies reveal that minor structural

variations in the reactants can produce major variations in the reaction parameters [219]. In some cases, these variations so severely alter the kinetic mechanism of an ET reaction that eq. (7.11) ceases to accurately describe it [14].

It is established that "protein structures tune thermodynamic properties and electronic coupling interactions to facilitate" electron transfer reactions [192]. However, it is not yet clear how this is accomplished in metabolic ET systems. Studies of pseudo-biological ET reactions (in Ru-modified proteins, for example) do not capture the nuances of metabolic ET reactions. It follows that the fundamental challenge facing nonadiabatic redox enzymology today is to determine how structural and environmental features control the parameters comprising eq. (7.11), and hence to identify how biological systems modulate these features to regulate the energetic resonances that determine redox reaction rates.

7.3 Complexity of Electron Transfer Kinetics

Living organisms respond to their environments and regulate their bodies [19]. The high sensitivity of reaction rates to modest structural or environmental variations enables a subtlety of control that makes homeostatic regulation viable.

For example, if the dominant mechanism effecting a reaction depends on the ionic content of the surrounding aqueous environment, the change in the reaction mechanism that accompanies a change in the local ionicity can provide an essential form of homeostatic feedback, allowing an organism to respond to and rapidly-counteract potentially-deadly fluctuations in its internal biochemistry [220]. When the ET reaction rate is modulated by an independent non-ET reaction or conformational change, additional parameters become necessary to predict the reaction rate. A number of other kinetic models have been developed to treat kinetically-complex ET reactions [219, 220, 221, 222, 223, 224, 225].

7.3.1 True Electron Transfer Reactions

The rates of "true" ET reactions, as already mentioned, are limited by the kinetics of the ET "event" itself. According to the Marcus Theory of ET [86, 217], a nonadiabatic ET event comprises two concomitant processes:

1. The translation of the nuclei from the electrostatic equilibrium conformation that immediately precedes ET to an "activated" conformation satisfying the condition of reactant-product degeneracy (according to the Franck-Condon Principle [84]).

2. The nonadiabatic quantum transition of the electronic subsystem from its reactant configuration to its product configuration.

Following ET, the system relaxes to the equilibrium configuration of the products.

Experimenters characterize the rates of biological ET reactions using the semi-empirical form of the Marcus equation,

$$k_{\mathrm{ET}} \approx k_{\circ}\, e^{-\beta(r-r_{\circ})}\, e^{-(\Delta G^{\circ}+\lambda)^2/4\lambda RT}. \tag{7.12}$$

In eq. (7.12), k_{ET} is the same molecular rate as that given by eq. (7.11), $k_{\circ}$ is the characteristic frequency of the nuclei usually taken to be about $10^{13}\,\mathrm{s}^{-1}$ [86, 14], $r_{\circ}$ is defined to be the distance between the redox cofactors at which the activationless ET rate equals $k_{\circ}$ [86], r is the actual distance between the redox cofactors, and β is an empirically determined tunnelling decay factor [192, 86] as described in Section 7.1.2, and R is the ideal gas constant. Given values for the other parameters in eq. (7.12), estimates of the reaction coupling matrix element $|\mathcal{T}_{\mathrm{DA}}|$ can be obtained by comparing eq. (7.12) directly with eq. (7.11).

Biological reactions are often highly complex, and multiple non-ET steps may be necessary to optimize a biochemical redox complex after binding but prior to the ET event [14]. These non-ET steps may include protein-protein interactions, conformational

rearrangements, and other chemical reactions such as proton transfers [221]. However, if the forward rate constant k_x associated with a requisite non-ET step x is much faster than the ET rate constant k_{ET}, and also faster than the corresponding reverse rate constant k_{-x}, then these non-ET steps will not contribute to λ and the observed reaction rate will be $k_{\mathrm{obs}} \approx k_{\mathrm{ET}}$ [226]; kinetically complex reactions of this type are also categorized as "true" ET reactions [63, 220, 221, 219].

7.3.2 Kinetically Gated Electron Transfer Reactions

An ET reaction is classified as "gated" when the ET event itself is preceded by a much slower adiabatic reaction step x that is necessary to activate the redox complex for ET [63, 219, 220, 221]. The step x may represent a chemical reaction or a reorganization of the nuclear configuration. Because the rate constant k_x describing the reaction step x is much slower than the ET rate itself ($k_x \ll k_{\mathrm{ET}}$), x becomes the rate-determining step such that $k_{\mathrm{obs}} \approx k_x$. The experimentally-observed *adiabatic* reaction rate may be plotted using parameters derived from transition state theory, where the rate constant is determined by the adiabatic Gibbs free energy of activation $\Delta G_x^{\ddagger}$ and given by the Eyring equation [227],

$$k_x = \frac{k_{\mathrm{B}}T}{2\pi\hbar} e^{-\Delta G_x^{\ddagger}/k_{\mathrm{B}}T}. \tag{7.13}$$

Gating effects can accelerate the rates of otherwise-slow ET reactions [220], by controlling the ambient chemical conditions prior to the ET event. Davidson has observed that chemical gating effects can introduce regulatory mechanisms into metabolic ET systems [220]:

> Chemical gating allows the rate of an ET process to be controlled by concentrations of specific metabolites, effector molecules, or pH. By having large differences in rates of the slow ungated true ET, and the very rapid gated ET, flow of electrons through the system may be effectively regulated.

A gated ET reaction may be empirically distinguished from a true ET reaction by analyzing the ET reaction's rate-dependence with respect to ΔG° and T. The rate constant for a gated reaction will not depend predictably on ΔG°, because the reaction step x is "not being driven by the redox potential difference between the reactants" and products [226]. When the temperature-dependence of the rate constant of a gated ET reaction is analyzed, the values obtained for $|\mathcal{T}_{\mathrm{DA}}|$ and λ will likewise be unrelated to the properties of the ET complex [226]. Fitted values of $|\mathcal{T}_{\mathrm{DA}}|$ will likely exceed the "adiabatic limit" of $80\,\mathrm{cm}^{-1}$ [226, 220], and λ will likely fail to corroborate the relevant structural and dielectric properties of the system.

7.3.3 Kinetically Coupled Electron Transfer Reactions

"Kinetically coupled" ET occurs when a nonadiabatic ET event is preceded by a necessary, independent reaction step x that is fast compared to the ET reaction itself ($k_x \gg k_{ET}$) but kinetically unfavourable ($k_x \ll k_{-x}$) [221, 220, 219, 63]. Because the forward reaction rate k_x is much slower than the back reaction rate k_{-x}, the equilibrium constant K_x defined by k_x and k_{-x} obeys $K_x \ll 1$. As a result, the net probability of the ET event depends on the relative probability K_x [221, 220, 219, 63], such that

$$k_{\mathrm{obs}} \approx K_x \cdot k_{\mathrm{ET}}. \tag{7.14}$$

Coupled ET reactions are markedly difficult to distinguish from true ET reactions, because the reaction rate constant of a coupled ET reaction still depends on eq. (7.11) via eq. (7.14). If k_{obs} is naively equated to eq. (7.11) in order to analyze a kinetically coupled ET reaction, distorted estimates of λ and $|\mathcal{T}_{\mathrm{DA}}|$ will be obtained because of the attenuating effect of K_x on the reaction rate. The enthalpy ΔH_x and entropy ΔS_x associated with K_x obey the equilibrium relationship [222],

$$\ln K_x = -\frac{\Delta H_x}{k_{\mathrm{B}} T} + \frac{\Delta S_x}{k_{\mathrm{B}}}. \tag{7.15}$$

If the reaction free energy ΔG° of a kinetically-coupled reaction is varied at constant temperature in order to determine λ and $|\mathcal{T}_{\rm DA}|$, a correct value of λ will be obtained but the apparent value of $|\mathcal{T}_{\rm DA}|$ will be less than the true value [222]. If T is varied instead, the apparent value of λ will exceed the actual value, increasing with the magnitude of ΔH_x; the apparent value of $|\mathcal{T}_{\rm DA}|$ will scale monotonically with the magnitude and sign of ΔS_x [222]. The most conclusive confirmation of the kinetic coupling in an ET reaction is obtained by combining these thermodynamic analyses with the relevant complementary empirical techniques [226].

7.3.4 Dynamic Docking

Inspired by the experimental confirmation that multiple bound protein conformations can affect the rates of interprotein ET reactions [223], Hoffman and coworkers developed a "dynamic docking" model of biological ET kinetics [224, 225]. The dynamic docking model expands upon the standard Marcus picture of ET (Fig. 7.1) by defining multiple pre-ET and ET-active conformations in phase space. The equilibrium constant for each pre-ET (electrostatic equilibrium) conformation i is defined to be $K_x^i = k_x^i/k_{-x}^i$ [224]. It also represents a generalization of Davidson and coworkers' "gated/coupled" framework that includes multiple ET and conformational rate constants, respectively defined by the sets $\{k_{\rm ET}^i\}$ and $\{k_x^i, k_{-x}^i\}$ [223, 224, 225]. By construction, the microscopic coordinates described by $\{k_x^i\}$ are all orthogonal to those described by $\{k_{\rm ET}^i\}$. Within this dynamic docking framework, the observed ET rate constant $k_{\rm obs}$ becomes [225],

$$k_{\rm obs} = \sum_i k_{\rm ET}^i \frac{k_x^i}{k_{-x}^i + k_{\rm ET}^i} \tag{7.16}$$

Notice that eq. (7.16) reduce to $k_{\rm obs} \approx \sum_i k_x^i$ in the limit where $k_{\rm ET} \gg k_x^i$ and $k_{\rm ET} \gg k_{-x}^i$, which is consistent with the concept of "gated" ET. In the opposite limit, where $k_{\rm ET} \ll k_x^i \ll k_{-x}^i$, we find $k_{\rm obs} \approx \sum_i K_x^i \times k_{\rm ET}^i$, making this model conceptually consistent

with "coupled" ET [14, 225]. Hoffman and coworkers's dynamic docking framework naturally accommodates a wide range of conformationally-distinct reaction mechanisms, making it particularly suitable to biological ET reactions that exhibit high degrees of kinetic complexity. Hoffman *et al.* [223] have mused that,

> It is intriguing to speculate that some physiological protein–protein electron-transfer processes might be tuned or even switched on/off by reversible protein surface modifications, which are well-known to play an important role in regulating protein–protein recognition events in living systems.

The dynamic docking model introduces an important distinction between the binding of the protein-protein complex itself (described by K_{d}), and the docking of the bound complex into its ET-active conformers.

7.3.5 Non-Condon Effects

As exhibited by eq. (7.11), Marcus theory assumes only a single value for the transition element $|\mathcal{T}_{\mathrm{DA}}|$ that couples the reactant and product electronic states. The assumption that "the dependence of the electric dipole matrix elements on the nuclear positions" may be neglected is called the "Condon approximation" [84]. This assumption is valid for ET activation that can be modelled by a low-order perturbation of the energy of a single nuclear equilibrium conformation, as it is by Marcus Theory.

When the Condon approximation breaks down, Marcus Theory can be recovered in a piecemeal fashion according to the dynamic docking model, if each distinct value of $|\mathcal{T}_{\mathrm{DA}}|$ corresponds to the activation of a distinct electrostatic equilibrium conformation of the nuclei. If this is not the case, and the value of $|\mathcal{T}_{\mathrm{DA}}|$ varies widely even in the vicinity of a local minimum on the Born-Oppenheimer electronic potential surface, then Marcus Theory cannot be recovered by either the kinetic coupling or the dynamic docking framework.

7.4 Enzymatic Electron Transfer

Studies of metabolism in single-celled organisms allow for a high degree of experimental precision, because these organisms can be cultured under tightly-controlled living conditions to allow for in-depth studies of specific chemical reaction pathways during metabolism. Site-directed mutagenesis studies allow the consequences of *in vitro* structural changes performed on bacterial enzymes to be explored *in vivo*. Discoveries made during studies of the electron transfer reactions of bacterial respiration are broadly applicable across biology, because all known forms of life use electron transfer to convert energy from their surroundings into metabolic energy.

7.4.1 Copper Enzymes

Copper-containing enzymes play multiple roles in living systems. They are crucial for respiration, photosynthesis and efficient metabolism throughout the "tree of life" [63]. The atomic copper centres contained in these proteins are involved in many chemical functions, including electron transport, molecular oxygen transport, and enzymatic oxidation-reduction reactions [63].

Copper-containing proteins are categorized numerically by the "types" of "copper centres" that they contain. A copper centre is defined by the geometrical arrangement of the molecules ("ligands") bonded to the central copper atom(s), coordinating the atomic position(s) inside the protein [228]. The ligands of "Type I" copper centres have tetrahedral or bipyramidal geometries (see, for example, Fig. 7.2), and these copper centres are found primarily in plants and bacteria [63]. "Type II" copper centres have square planar ligand geometries and predominate in fungi and animals [63]. "Type III" copper centres contain a pair of twinned copper atoms each coordinated by three (histidine) ligands, and these are also found in fungi and animals [63]. Proteins containing multiple types of copper centres are common [63].

"Type I" copper proteins, called "cupredoxins" [63], function primarily as ET mediators during bacterial and plant respiration [229]. They have been studied extensively "as model systems for protein electron transfer reactions" [63]. A cupredoxin makes an ideal research prototype, because its relatively small size (10–14 kDa [230]) and single metallo-atomic centre limit the potential for experimental confounds. Because many cupredoxins have a bacterial origin, they are straightforward to synthesize biologically using bacterial cultures, natively or in a genetically-engineered host. Several cupredoxins are well-characterized, structurally, kinetically, and thermodynamically [63]. Thorough characterization is particularly important for the determination of the structural origins of functional variations, among native cupredoxins as well as their mutagenic variants.

7.4.2 Cupredoxin Structure

The cupredoxin copper centre contains a single copper atom that is strongly coordinated by a trigonal-planar arrangement of ligands comprising a cysteine and two histidine residues [63, 229]. One or two axial ligands sometimes complement this arrangement to form a trigonal-pyramidal or -bipyramidal geometry. This coordination geometry is not optimal for either the Cu^{+1} or the Cu^{+2} redox state, and it does not change significantly upon the transition of one redox state to the other [63, 229]. This characteristic helps minimize the cupredoxin's "inner-sphere" (*i.e.*, ligand) reorganization energy [229]. Cupredoxins also share in common the presence of a hydrophobic patch around the active site [230] to help ensure binding affinity with redox partners [231, 230].

Cupredoxins are also commonly referred to as "blue copper proteins" because they exhibit an unusual ligand-to-metal charge transfer transition near 600 nm in their Cu^{+2} form [86, 229]. Secondary and tertiary protein structure is generally well-preserved across the blue copper proteins, which all share a similar folded structure of roughly eight bundled β-strands [63]. Despite their simple and well-conserved structures, copper-containing

proteins of the Type I family are generally not functionally interchangeable, and subtle structural alterations can lead to dramatic shifts in functionality [219]. Their functional sensitivity to structural variations, along with their accessible *in vitro* redox chemistry, make blue copper proteins exemplary prototypes to use in investigations of the factors that enforce efficient molecular recognition [232] in biological redox systems.

7.4.3 Methylamine Metabolism in *Paracocous denitrificans*

The cupredoxin amicyanin is essential to the bacterium *Paracocous denitrificans'* ability to metabolize methylamine as a food source. Gene-replacement experiments have shown that *P. denitrificans* loses its ability to survive on an exclusive diet of methylamine after losing the ability to synthesize amicyanin [54]. The amicyanin redox cycle affords an important empirical control in the study of cellular respiration, because it has been identified as critical metabolic bottleneck during methylamine digestion by *P. denitrificans*.

P. denitrificans does not use amicyanin to oxidize methylamine directly. Instead, methylamine is oxidized by the globular protein methylamine dehydrogenase (MADH), which in turn donates the absorbed electron to amicyanin. Amicyanin is then oxidized by a cytochrome molecule as the electron continues down its pathway through the electron transport chain, ultimately driving the production of adenosine triphosphate (ATP).

The active site of MADH is a tryptophan tryptophylquinone (TTQ) prosthetic group comprising a pair of posttranslationally-modified tryptophan residues from the protein's "light" β-subunit [233, 47], located at the amicyanin-binding site. Residues tryptophan 57 (Trp57) and tryptophan 108 (Trp108) of the β-subunit of MADH have covalently-linked indole groups; the benzene ring of Trp57 is linked to the benzene ring of Trp108 [55]. Additionally, in the TTQ's fully-oxidized ("O-quinone") state, the two adjacent carbon atoms of the Trp57 benzene ring are carbonylated to form a dione edge at the location where methylamine (or dithionite) oxidation actually occurs (Fig. 7.3) [55].

Amicyanin's copper centre is spatially coordinated by a distorted tetrahedral arrangement of ligands consisting of a methionine, a cysteine, and two histidines (Fig. 7.2) [63]. Like that of other cupredoxins, this coordination geometry is intermediate between the electronic orbital geometries preferred by the Cu^{+1} and Cu^{+2} redox states [63]. Seven amino acid residues surround the histidine 95 (His95) ligand of the active copper site on the surface of amicyanin. These seven residues form a hydrophobic patch comprising methionine 28 (Met28), methionine 51 (Met51), proline 52 (Pro52), methionine 71 (Met71), proline 94 (Pro94), proline 96 (Pro96), and phenylalanine 97 (Phe97) [55, 63, 234]. These residues comprise a major portion ($\sim$60%) of the binding interface at which MADH attaches itself in crystals of the binary [55] and ternary [47] complexes.

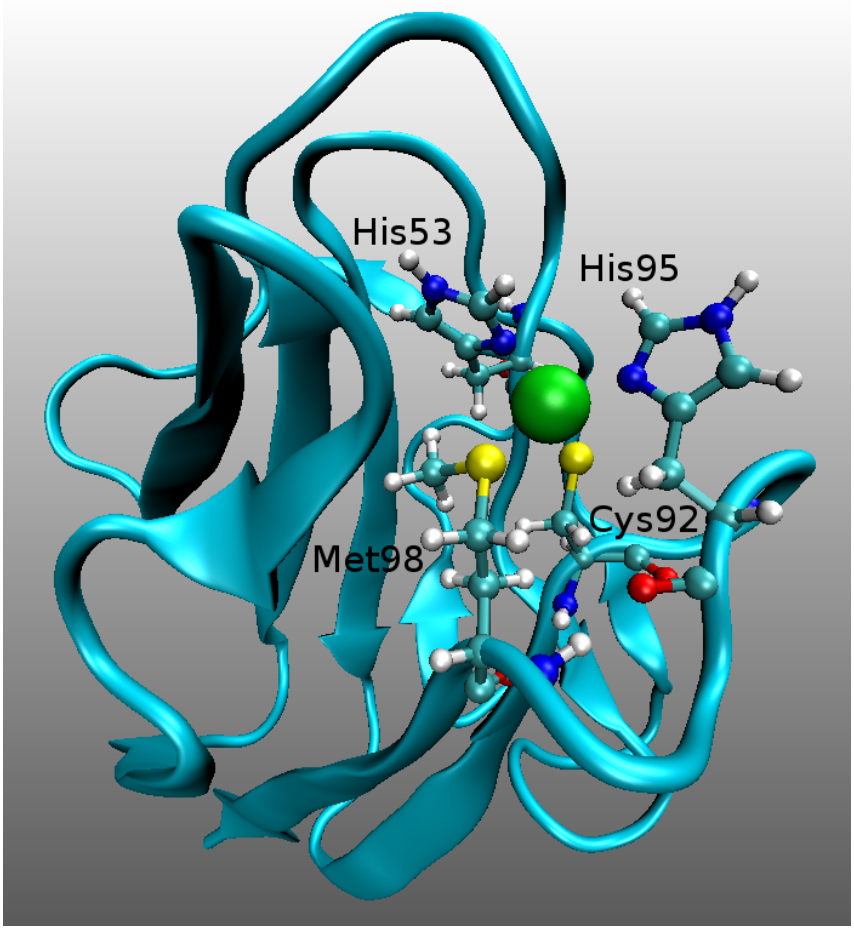

Figure 7.2: Amicyanin's copper centre is coordinated by His53, His95, Met98 and Cys92.

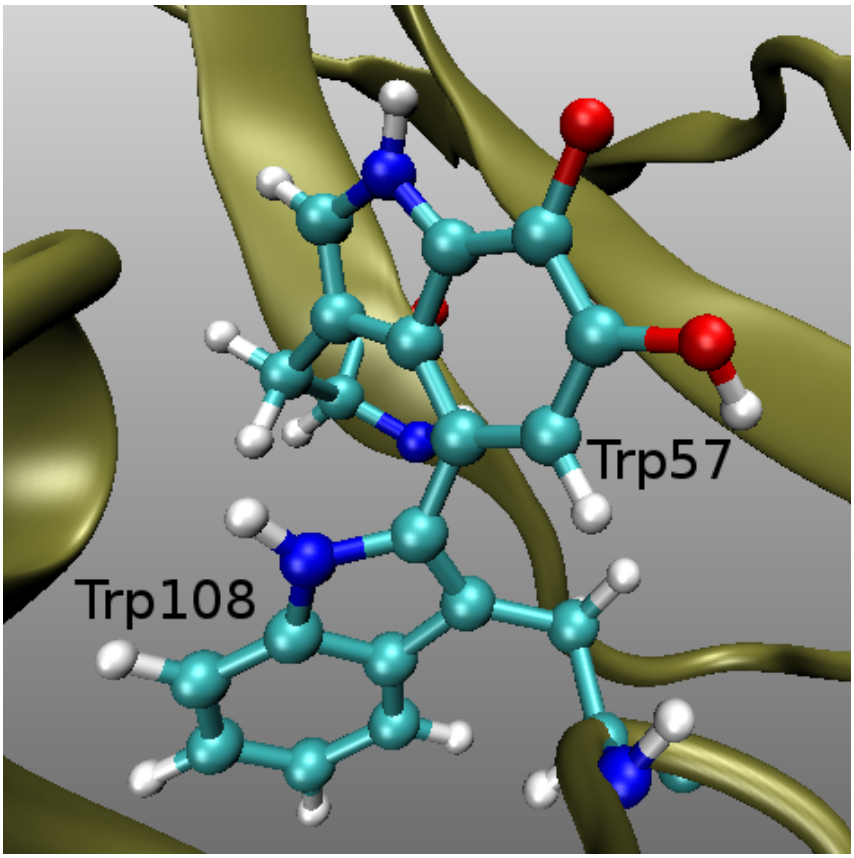

Figure 7.3: MADH's TTQ cofactor comprises Trp57 and Trp108.

The binary and ternary crystal structures corroboratively provide a good model for the structure of the redox complex in solution [235, 236]. In solution, the MADH–amicyanin redox complex (Fig. 7.4) is stabilized by hydrophobic and ionic interactions in a predictable way that is consistent with the known crystal structures [234, 237]. Amicyanin has also been demonstrated to be catalytically competent to transfer electrons from MADH to cytochrome c_{551i} in crystalline form [238, 239]. The question of whether amicyanin transfers electrons from MADH to cytochrome c_{551i} during the formation of a ternary complex [63] or by way of a shuttle ("ping-pong") mechanism [236] during metabolism remains an ongoing topic of debate.

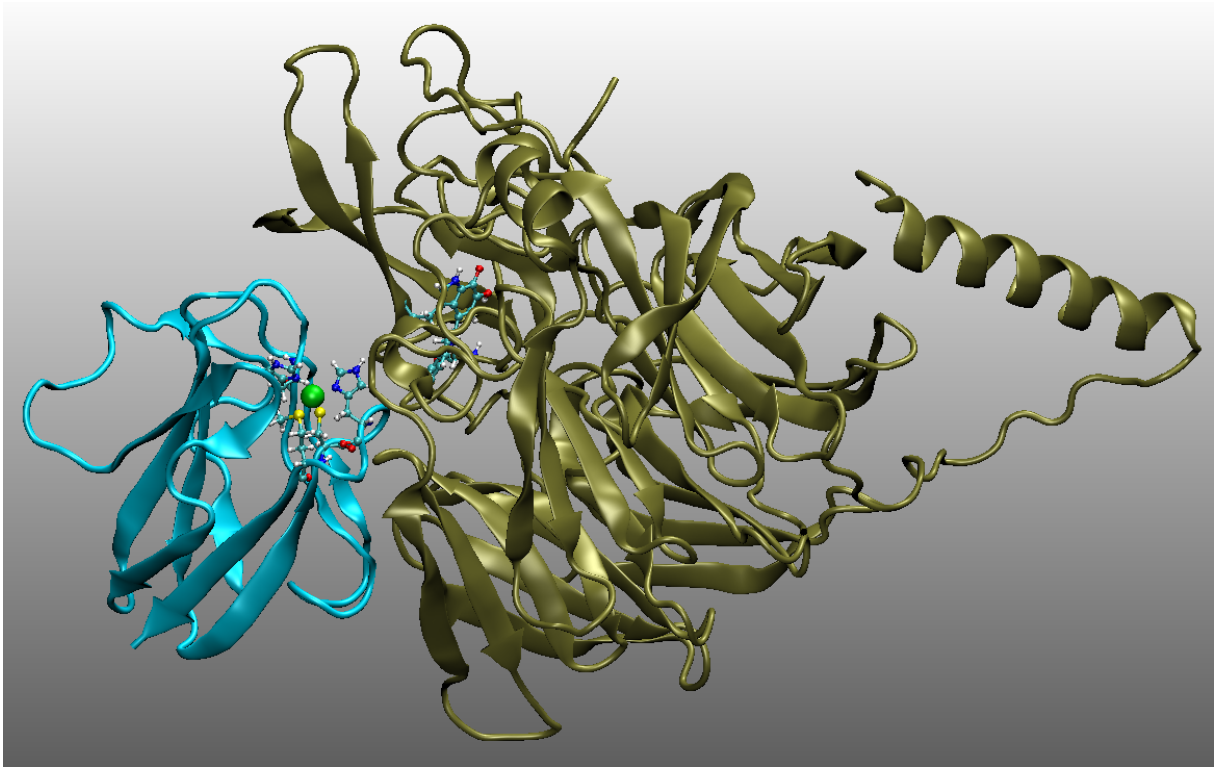

Figure 7.4: The complex of amicyanin (cyan) and MADH (tan) is shown graphically using a ribbon motif generated using VMD. The active site of each complex is also depicted using a colour-coded ball-and-stick representation, where hydrogen atoms are shown in white, carbon in light blue, nitrogen in dark blue, oxygen in red, sulphur in yellow, and copper in green.

7.4.4 True Electron Transfer from MADH to Native Amicyanin

Throughout the 1980s and 1990s, Davidson and coworkers performed extensive kinetic and thermodynamic studies to characterize electron transfer between various reduced forms of MADH, amicyanin, and cytochrome *c* [227, 235, 238, 240, 241, 242, 243, 244]. These studies revealed the oxidation of amine-reduced ("N-quinol") MADH by amicyanin to be a catalytically-gated ET reaction (rate-limited by an adiabatic proton transfer step), Davidson ultimately concluded that oxidation of dithionite-reduced ("O-quinol") MADH by amicyanin to be a "true" ET reaction with an "unusually large" reorganization energy [235]. On the other hand, Davidson and his colleagues determined that the oxidation of dithionite-reduced ("O-quinol") MADH by amicyanin was a "true" ET

reaction with a rate predicted by the Marcus equation, summarizing their perspective neatly in a follow-up article [245],

> In the case of the reaction between O-quinol MADH and amicyanin, it was proven that this is a true ET reaction by demonstrating that the same λ value was obtained from both temperature and ΔG° dependence studies of the reaction rate (10). This would not be expected for a coupled ET reaction (14). Furthermore, mutations at the MADH–amicyanin interface that affected binding had no effect on the λ for the ET reaction from TTQ to copper (15). Thus, the large λ for this reaction is not believed to be due to kinetic complexity.[1]

This result is surprising, because the "unusually large" value of $\lambda = 2.3\,\mathrm{eV}$ needed to model ET from O-quinol MADH to amicyanin using Marcus Theory was previously suggested to be due to an extra "conformational" reaction step rate-limiting the ET reaction [235], and the studies that confirmed the status of ET from O-quinol MADH to amicyanin as a "true" ET reaction gave no indication as to why the reaction's reorganization energy should be so much larger than other ET reactions of its kind.

7.4.5 Species-Specific Electron Transfer

Soluble charge-carrying proteins such as MADH and amicyanin must recognize [232] and distinguish their predefined redox partners from *everything else* floating in the periplasmic or cytoplasmic cellular space where they reside. The question of whether conformational motions of the protein complex contribute to the unusually large reorganization energy exhibited by the oxidation of MADH by amicyanin is related to the issue of "species-specific" electron transfer.

[1] Quoted references (10), (14), and (15) correspond respectively to references [246], [222], and [244].

A striking example of species-specific ET is evident in the comparison of the MADH–amicyanin ET pair with the functionally-analogous AADH–azurin pair. Under metabolic conditions, aromatic amine dehydrogenase (AADH) oxidizes alkylamines and donates electrons to the cupredoxin azurin. MADH and AADH have similar structural and kinetic properties, each possessing a TTQ redox cofactor at the redox interface [63]. Similar to amicyanin, azurin is a cupredoxin made of eight β-strands and an α-helix. Azurin's Type 1 copper centre is coordinated by a trigonal bipyramindal structure consisting of a cysteine, a methionine, and two histidine residues [63]. Despite structural similarities, the MADH–amicyanin and AADH–azurin redox pairings are mutually exclusive. MADH cannot transfer electrons to azurin and AADH cannot transfer electrons to amicyanin [63].

A number of factors can contribute to the partner-exclusivity exhibited by the MADH–amicyanin and AADH–azurin pairs. For example, amicyanin is known to dock with MADH at a different angle than azurin does with AADH. While both complexes are stabilized by hydrophobic interactions, amicyanin's docking configuration also involves at least one ionic interaction that azurin's does not [63, 234]. Amicyanin's copper center is coordinated by four ligands in a tetrahedral geometry, whereas azurin's copper center is coordinated by five ligands in a trigonal bipyramidal geometry. Both geometries contain pairs of nitrogen and sulphur atoms that together form a tetrahedron, but azurin's geometry includes an additional backbone carbonyl oxygen to provide a second axial ligand to create the trigonal bipyramidal arrangement [63].

7.4.6 Proline 52 Mutation of Amicyanin

In a 2006 study performed under the direction of Victor Davidson, Ma and coworkers sought to determine whether it would be possible to introduce the copper-binding geometry of azurin into amicyanin—and if it did prove possible, to determine what effect this geometrical change would have on amicyanin's capacity to oxidize MADH [13].

Amicyanin's copper centre is coordinated by the two N^{δ} atoms of histidine 95 (His95) and histidine 53 (His53) residues, as well as the sulphur atoms of cysteine 92 (Cys92) and methionine 98 (Met98). A nearby proline 52 (Pro52) residue is situated so that it could provide an additional carbonyl oxygen ligand to form a trigonal bipyramidal geometry like azurin's, except that the carbonyl oxygen of Pro52 is oriented away from the copper center rather than towards it [13]. In azurin, the axial carbonyl oxygen ligand is provided by a glycine residue that is oriented properly in order to bind to the copper center.

Ma and coworkers hence carried out a "P52G" mutation on amicyanin, replacing Pro52 with glycine, in the hope of reproducing an azurin-like ligand geometry in amicyanin [13]. The P52G mutation failed to produce its intended effect, as it generated "no structural rearrangement that would allow the carbonyl oxygen of Pro52 to form a fifth ligand to the copper atom" [13]. However, the P52G mutation did generate a number of other unanticipated effects of interest:

Changed ET Kinetics.—Most significantly, Ma *et al.* found that "the mutation of Pro52 alters the positions of residues that are involved in protein–protein interactions within the ET protein complex with MADH and consequently alters the kinetic mechanisms of the ET reactions from MADH to amicyanin" [13]. The oxidation-rate of O-quinol MADH by P52G amicyanin was fit to the Marcus equation with parameters of $\Delta G^{\circ} = -4.8\,\mathrm{kJ/mol}$, $\lambda = 2.8 \pm 0.1\,\mathrm{eV}$, and $|\mathcal{T}_{\mathrm{DA}}|/hc = 78 \pm 34\,\mathrm{cm}^{-1}$ [13]. These parameters "do not likely describe a true ET reaction" [13]. The remarkably-large apparent value of $|\mathcal{T}_{\mathrm{DA}}|$, in particular, corresponds to a donor–acceptor separation distance of $6.0 \pm 0.9\,\text{Å}$ [13], about two-thirds of the structurally-realistic distance obtained from a Marcus analysis of the ET rate from O-quinol MADH to native amicyanin. Steric restrictions prevent the donor and acceptor cofactors from coming this close together without severely deforming (*e.g.*, squishing) the equilibrium complex structure [13], a possibility unaccounted for by either Marcus Theory or classical MD force fields.

Neglecting the possibility of a "squished" ET-active conformation, Ma *et al.* concluded that the large apparent value of the matrix element obtained for the O-quinol/P52G reaction instead indicated that the reaction had become conformationally gated. They came to this conclusion after comparing the O-quinol and N-quinol reaction rates, based on the marked loss of salt-dependence of the N-quinol reaction and the additional fact that the "rates of the reactions of P52G amicyanin with the O-quinol and N-quinol are essentially identical in a 10 mM phosphate buffer" [13]. They reasoned that the identical rates of the O-quinol and N-quinol reactions must be indicative of a single rate-limiting step governing both reactions [13].

Changed Equilibrium Constants.—Ma *et al.* found that the equilibrium dissociation constant for the O-quinol reaction increased from $K_\mathrm{d} = 4.5 \pm 0.5\,\mu\mathrm{M}$ (native) to $K_\mathrm{d} = 38 \pm 12\,\mu\mathrm{M}$ (P52G), a finding that "supports the notion that the protein–protein interface has been perturbed" [13]. Ma and coworkers also found that the magnitude of the standard Gibbs free energy of the O-quinol reaction increased by more than fifty percent, from $\Delta G^\circ = -3.2\,\mathrm{kJ/mol}$ (native) to $\Delta G^\circ = -4.8\,\mathrm{kJ/mol}$ (P52G) [13]. This dramatic increase in the reaction's driving force was not attributed to any change in the electronic properties of the copper centre, and instead it was attributed to a shift in the acid dissociation constant K_a of P52G amicyanin towards a more acidic value [13].

Changed Crystal Structures.—Ma *et al.* obtained the crystal structure of oxidized P52G amicyanin at a resolution of 1.25 Å and the crystal structure of reduced P52G amicyanin at 0.92 Å. Although the structural differences between native and P52G amicyanin crystal structures are relatively minor, Ma *et al.* were unable to crystallize P52G amicyanin in complex with MADH [13]. In both the oxidized and reduced forms of crystallized amicyanin, the largest deviation from the structure of the native backbone was found in a "very flexible" loop segment comprising residues 18 through 20 [13]. These residues make up a flexible loop that is far removed from the copper site and does not

participate in binding to MADH. Excluding these three residues, the root-mean-square deviation of the positions of the oxidized P52G mutant's remaining 102 α-carbons (with respect to those of the native) is 0.42 Å, while the reduced P52G mutant's is 0.27 Å [13].

Ma *et al.* attributed the failure of P52G amicyanin to crystallize in complex with MADH to a weakening of the hydrophobic interactions between the two proteins [13]. In native amicyanin, Pro52 contributes three carbon atoms to the hydrophobic patch that stabilizes complex formation with MADH [13]. Simulations indicated that the surface area of amicyanin "buried" in the complex is reduced from 783 Å^2 to 764 Å^2 due to the P52G mutation, while MADH's buried surface area is reduced from 725 Å^2 to 710 Å^2 [13].

Ma *et al.* found notable differences between the positions of the methionine 51 residue in the crystal structures of native amicyanin in complex, native amicyanin in isolation, oxidized P52G amicyanin, and reduced P52G amicyanin. In particular, significant differences were found in the position of atom C^{ϵ} of amicyanin methionine 51, reflecting the possibility of altered interactions with MADH β Val56 [13]. This change in the position of the side chain of Met51 "eliminated the contacts with the side chain of β Val58 of MADH that are seen in the structure of the complex of native amicyanin with MADH" [14].

7.4.7 Methionine 51 Mutations of Amicyanin

In order to distinguish the effect of the reorientation of the Met51 residue from the effect of the loss of the three carbon atoms from Pro52, Ma *et al.* devised a new set of site-directed mutagenesis experiments. By replacing amicyanin's Met51 with each of alanine (Ala), lysine (Lys), and leucine (Leu), Ma *et al.* generated three new mutant forms of amicyanin, denoted M51A, M51K, and M51L respectively [14].

Ma *et al.* found that the values of K_{d} for mutant amicyanin in complex with MADH were consistent with those of native amicyanin, while the kinetics of ET from MADH to

the Met51 mutants were anomalous. They reached the following conclusion [14]:

> These data indicate that the loss of the interactions involving Pro52 were primarily responsible for the change in K_d for P52G amicyanin, while the interactions involving the Met51 side chain are entirely responsible for the change in ET parameters and conversion of the true ET reaction of native amicyanin into a conformationally gated ET reaction.

Ma and coworkers chose to mutate methionine 51 into alanine ("M51A") in order to mimic the loss of the interaction of amicyanin Met51 with MADH β valine 58 (Val58) that was observed during the P52G experiments [14]. Ma *et al.* also performed two additional experiments, mutating Met51 into lysine ("M51K") and also Met51 into leucine ("M51L"), in order "to provide further insight into the mechanism of this regulation" [14].

Crystal Structure of M51A amicyanin.—Ma *et al.* obtained the crystal structures of the oxidized and reduced forms of M51A amicyanin at resolutions of 0.89 Å and 0.90 Å, respectively [14]. Ma *et al.* catalogued several differences between the mutant and native crystal structures [14], but none of them were especially substantial or obviously consequential. The root-mean-square deviations of the α-carbons of the relatively-rigid 84-residue chain constituting the main body of amicyanin (residues 22-105) ranged from 0.1 Å to 0.3 Å for pairwise comparisons of the native, oxidized P52G, and oxidized M51A crystals—a small fraction of the resolution of the structures themselves.

Both oxidized and reduced forms of M51A amicyanin exhibited alternate conformations of the side chain of Met71 [14]. On both of these structures, Met28 had been modified by the addition of an oxygen atom to form a sulphoxide product [14]. The α-carbons of M51A amicyanin's patch residues Met28, Ala51, and Pro52 were all displaced by more than 0.2 Å from their locations in native amicyanin [14]. The M51A mutation alters the positions of amicyanin residues 26–28 to a greater degree than the P52G mutation, with potential consequences to the binding-functionality of the hydrophobic patch

as well as the free energy barrier of the ET event itself [14]. Any or all of these factors may have contributed to Ma *et al.'s* failure to crystallize M51A amicyanin in complex with MADH.

Equilibrium Constants.—The equilibrium dissociation constants of the M51A, M51K, and M51L mutant complexes were respectively 6.8 μM, 11 μM, and 6.8 μM, all of which compare favourably to the native value of $K_{\mathrm{d}} = 4.9\,\mu\mathrm{M}$ [14]. Variations in ΔG° were also modest, as M51A, M51K, and M51L respectively produced values of $-2.8\,\mathrm{kJ/mol}$, $-3.4\,\mathrm{kJ/mol}$, and $-3.7\,\mathrm{kJ/mol}$, compared to the native's $\Delta G^{\circ} = -3.2\,\mathrm{kJ/mol}$ [14]. These findings indicate that the thermodynamic properties of the protein–protein complex in solution were qualitatively unperturbed, absent considerations specifically-related to biological regulation. Having ruled out confounds resulting from different bulk chemical properties of the native and mutant enzymes, Ma and coworkers were able to directly investigate the subtle "logical structure" [15] of the molecular recognition process.

Reduction of N-quinol MADH by Met51 Mutant Amicyanins.—Electron transfer from N-quinol MADH to native amicyanin is chemically gated by the deprotonation of the N-quinol TTQ cofactor. The first-order rate constant of this reaction in solution depends upon the salt concentration because the rate-limiting proton transfer requires the presence of a monovalent cation at the active site [247]. The reaction demonstrates a linear dependence on the solution's potassium chloride concentration up to 200 mM [14].

The reaction rates of N-quinol MADH with oxidized M51A, M51K, and M51L amicyanin are also salt-dependent, but to a much lesser extent [14]. The rate and the salt-dependence of the M51A reaction is practically identically to that of the P52G reaction up to a salt concentration of [KCl] = 200 mM [14], indicating that both of these reactions share the same underlying kinetic mechanism. Both the M51A and M51K reaction rates increase up to a KCl concentration of 200 mM and then plateau, whereas the M51L reaction rate "exhibits a gradual hyperbolic increase that has not yet reached a

plateau at a 200 mM KCl" [14]. The kinetics of the M51L reaction qualitatively resemble those of the native reaction, whereas the M51A and P52G kinetics do not. The M51K reaction kinetics fall in between those of M51L and M51A (see Fig. 4 of ref. [14]). These finding demonstrate a remarkable advance for the controlled study of reaction kinetics—by interchanging just one amino acid in the primary structure of amicyanin, Ma and coworkers were able to incrementally reprogram the functional output of this enyzme.

Reduction of O-quinol MADH by Met51 Mutant Amicyanins.—Based on the values of $K_{\rm d}$ and ΔG° obtained from equilibrium analyses of the oxidation of O-quinol MADH by M51A amicyanin, it follows that "if ET from O-quinol MADH to M51A amicyanin were also a true ET reaction, then $k_{\rm ET}$ should be only slightly less than that observed for the reaction with native amicyanin" [14]. Instead, the observed value of the reaction rate constant $k_{\rm obs}$ of the M51A reaction was eight times smaller than that of the native reaction [14]. The M51K and M51L mutant rate constants were also smaller than that of the native reaction, but to a lesser extent [14]. When plotted against the solution temperature, the observed reaction-rate constants $k_{\rm obs}$ of the three mutants exhibited an incremental loss of temperature-dependence qualitatively the same as the corresponding loss of salt-dependence of the N-quinol reaction (compare Figs. 3 and 4 of Ref. [14]). Likewise, when plotted against the solution amicyanin-concentration, the net reaction-rate constants $k_{\rm net}$ exhibited the same incremental pattern again in their loss of amicyanin-dependence (compare Fig. 2 to Figs. 3 and 4 in Ref. [14]).

The temperature-dependent reaction-rate constants exhibited some severe anomalies when they were fit to the Marcus equation [14]. The nonequilibrium parameters derived by Ma *et al.* from the fittings of native and mutant experimental data to eqs. (7.11) and (7.12) are shown in Table 7.1. The values of $|\mathcal{T}_{\rm DA}|$ obtained from the fittings of the M51A and M51K mutant rates were unreasonably large, widely exceeding the so-called "nonadiabatic limit" [14]. Within the nonadiabatic limit $|\mathcal{T}_{\rm DA}|/hc \ll 80\,{\rm cm}^{-1}$, the reaction

Marcus Parameters for the Oxidation of O-quinol MADH			
Species	λ (eV)	$\lvert\mathcal{T}_{\mathrm{DA}}\rvert$ (hc/cm)	r (Å)
Native	2.30 ± 0.10	12 ± 7	9.5 ± 0.8
P52G	2.80 ± 0.10	78 ± 30	6.0 ± 0.9
M51A	3.07 ± 0.03	142 ± 20	4.7 ± 0.3
M51K	3.00 ± 0.04	194 ± 40	4.1 ± 1.0
M51L	2.55 ± 0.10	23 ± 10	8.3 ± 0.4

Table 7.1: Marcus parameters taken from Refs. [13] and [14].

rate is limited by the weak electronic coupling and the rate constant is proportional to $2\pi|\mathcal{T}_{\mathrm{DA}}|^2/\hbar$ [62, 208]. In the opposite limit $|\mathcal{T}_{\mathrm{DA}}|/hc \gg 80\,\mathrm{cm}^{-1}$, the reaction becomes "solvent-controlled" such that it is rate-limited by the adiabatic solvent reorganization rate [62, 248]. Fitted values of $|\mathcal{T}_{\mathrm{DA}}|/hc$ on the order of $200\,\mathrm{cm}^{-1}$ unambiguously demonstrate that eq. (7.11) is not appropriate to describe the M51A and M51K ET reactions.

Altered Kinetic Mechanisms.—Based on these collective findings, Ma *et al.* concluded that the Met51 mutations altered the kinetic mechanisms of both the N-quinol and O-quinol ET reactions, and that in each case both the P52G and M51A reactions had become gated by the same rate-limiting step [13, 14]. The intermediate character of the M51K and M51L reaction kinetics suggests that these reactions are also rate-limited by the same kinetic step as the P52G and M51A reactions, although to a lesser degree such that the M51K and M51L reactions are kinetically-coupled rather than gated [14]. In regard to the character of the kinetic step in question, Ma *et al.* made the inference [14],

> It is not obvious how the M51A mutation could introduce a new reaction step as was suggested for the P52G mutation since the binding process seems not to be perturbed. Therefore, it is likely that this mutation has slowed the rate of an existing but previously unrecognized conformational rearrangement that normally occurs in the native amicyanin-MADH complex subsequent to binding and prior to ET.

This finding appears as a contrast to Davidson and coworkers' previous conclusion that "the large λ for this reaction is not ... due to kinetic complexity" [245]. Yet the conclusion [245] that "the reaction between O-quinol MADH and amicyanin ... is a true ET reaction" stands unaffected, because it was derived empirically from the results of a cumulative series of rigorous temperature- and ΔG°-dependence studies [235, 243, 246], without regard for the kinetic underpinnings of these quantities. Evidently, the "true" character of the ET reaction of MADH with amicyanin belies an underlying kinetic complexity, not explicitly accounted for by the Marcus equation (7.11).

7.5 Further Considerations

The MADH–amicyanin ET reaction exhibits other anomalous characteristics that cast doubt on the adequacy of Marcus Theory to describe it. The thermodynamic reaction coordinate used to derive Marcus Theory does not allow for the protein and solvent molecules to undergo "their actual complicated coupled anharmonic motions" [86], and instead is limited to a "dielectrically unsaturated" picture of the ET medium [217]. This limitation creates a problem for the description of the reaction in terms of reactant and product equilibrium states (*i.e.*, the minima of Fig. 7.1), because the electrostatic properties of amicyanin in complex with MADH differ from its equilibrium electrostatic properties when free in solution.

The acidity of amicyanin (as quantified by its acid dissociation constant $\mathrm{p}K_{\mathrm{a}}$) changes dramatically upon binding to MADH [63]. This finding indicates that the docking of MADH with amicyanin introduces a non-equilibrium constraint on amicyanin's redox potential, so that "over the physiologic range of pH, the E_{m} value of free amicyanin varies with pH, but the E_{m} value of amicyanin in complex with MADH does not" [249]. The oxidation-reduction midpoint potential E_{m} measures the average electrostatic po-

tential of an oxidant in solution (against a standard hydrogen electrode) when half of its concentration has been reduced.

Plots of oxidation-reduction midpoint value E_{m} for free amicyanin and amicyanin in-complex with MADH against pH do not cross [249], so the values of E_{m} for complexed amicyanin do not correspond to any of the values of free amicyanin within the physiological range. The equilibrium nuclear conformation of oxidized free amicyanin resembles the nuclear conformation of oxidized amicyanin in-complex with MADH [249], suggesting that oxidized amicyanin in-solution provides a good electrostatic model for oxidized amicyanin in-complex with MADH. The same is not true for its reduced form [249].

Davidson and coworkers had previously found that "the E_{m} value of amicyanin (+294 mV) is more positive than that of cytochrome c-551i (+190 mV)" [63, 250]. This informs us that "when amicyanin is free in solution and interacts with the cytochrome, the direction of electron transfer would be ... the reverse of the physiological direction" [63]. On the other hand, the oxidation-reduction midpoint potential of amicyanin in-complex with MADH is +221 mV [251], providing a situation much more favourable for electron transfer to cytochrome [63]. This presents a curious situation [249]:

> The pH dependencies of the E_{m} values of amicyanin free and in complex with MADH were dramatically different. The redox potential of free amicyanin exhibited a clear dependence on pH, whereas the E_{m} value of amicyanin in complex was essentially independent of pH ...

Reduced amicyanin's docked state does not describe its undocked (bulk) equilibrium state, because amicyanin is sterically-constrained away from equilibrium when it is docked in-complex with MADH [249]. Production of this nonequilibrium electrostatic state presents an additional thermodynamic cost of complex formation that must be taken into acount somewhere in the reaction description.

Furthermore, the reduction of amicyanin in solution is accompanied by a bond-breaking event at the His95 ligand of the copper active site. According to Marcus theory, "no bonds are broken or formed" during an ET reaction [81]. The dissolution of the His95 ligand and the resulting conformational transport of His95 from the inner sphere to the outer sphere of the system defines a striking departure from the basic assumptions of Marcus theory. However, when reduced amicyanin is in complex with MADH [249],

> His 95 is prevented from dissociating from the copper coordination sphere upon reduction, and the redox potential of amicyanin in complex remains similar to that of free amicyanin at the highest values of pH, where it is singly protonated and unflipped.

A high degree of underlying kinetic complexity of the MADH-amicyanin ET reaction is indicated in the dramatically-altered kinetics of the Met51 mutation experiments, the native reaction's unusually large reorganization free energy, the non-equilibrium electrostatic state of the complex, and finally the explicit inner-sphere bond-breaking event.

Taken all together, the anomalous characteristics reveal a picture of an ET reaction that is not likely to conform to the standard assumptions of Marcus Theory [86], because the Marcus ET reaction coordinate does not account for the nontrivial thermodynamic cost necessary to accomodate these complex effects [86]. The kinetic changes due to the Met51 mutations do not appear relevant to the thermodynamic coordinate used to describe complex association and dissociation (because K_{d} was not significantly perturbed by mutations), so the reversible thermodynamic cost associated with all this kinetic complexity must be accounted for along the empirically-motivated nonadiabatic ET coordinate—even if the conditions used to ensure the reversibility of ET-activation according to Marcus Theory are not met.

Chapter 8

Water Bridges to Enhance Electron Transfer

> *It has become increasingly clear over the past two decades or so that water is not simply "life's solvent" but is indeed a matrix more akin to the one Paracelsus envisaged: a substance that actively engages and interacts with biomolecules in complex, subtle, and essential ways.*
>
> —Philip Ball, 2008 [46]

My six main contributions to the work described in Chapter 8 are summarized as follows:

1. *I construct computational representations of hypothetical crystallographic structures of mutant forms (M51L, M51K, M51A, M51C) of the bacterial blue copper enzyme amicyanin, based on existing crystallographies (Section 8.2).*

2. *I initialize and run numerical implementions of Langevin dynamics of each of these amicyanin mutants in complex with native amicyanin's physiological reductant methylamine dehydrogenase in aqueous solution (Section 8.3).*

3. *I carry out semi-empirical "tunneling pathway" and "packing density" calculations to estimate the relative donor-acceptor electronic transition amplitudes exhibited by the mutant redox complexes, identifying a pattern of reduced electronic coupling in the experimentally-relevant mutant complexes (Section 8.4).*

4. *I perform extensive qualitative and quantitative analyses on the atomic coordinate trajectories generated by these simulations, with regard to distinctions between the interprotein solvent dynamics of the mutant complexes (Section 8.5).*

5. *I demonstrate that the reduced electronic coupling exhibited by the simulated mutant complexes is due to the disruption of the stability of an inteprotein "water bridge," numerically confirming a long-standing hypothesis (Section 8.6).*

6. *I hypothesize that the hydrophobic ring of amino acid residues surrounding amicyanin's active ET site functions as a "molecular breakwater" that protects the ET-mediating water bridge in the native protein complex (Section 8.7).*

8.1 Introduction: Water-Bridged Electron Transfer

Contemporary studies have suggested that the geometric ordering of the intervening water molecules between ET donor and acceptor cofactors may play a crucial role enabling or disabling ET processes [51, 46]. Researchers became interested in the possibility that the protein fold might organize solvent molecules in order to facilitate electron transfer as early as 1994, when Chen and coworkers suggested that the presence of a particular water molecule at the MADH–amicyanin ET interface might increase the interprotein electronic tunneling rate by as much a factor of three [47].

In 2001, Tezcan *et al.* examined redox reactions in protein crystals, experimentally demonstrating that "water-mediated hydrogen bonds are effective coupling elements for tunneling across a protein–protein interface" [49]. Interest in solvent-mediated ET surged after investigators in Judith Klinman's laboratory concluded, based on kinetic isotope experiments (and an aggregate of previous work) that the protein known as peptidylglycine α-hydroxylating monooxygenase (PHM) most likely uses available solvent molecules to generate a charge transfer conduit during the ET step of its enzymatic action [50].

Inspired by the conclusions of Klinman *et al.* [50] and motivated by other studies of enzymatic interprotein ET [49, 197, 58, 51], Aurélien de la Lande and coworkers performed molecular dynamics (MD) simulations of the PHM enzyme and experimentally-relevant

mutant forms of it [52]. As part of their study, they performed a tunneling pathway analysis on the nuclear trajectories generated by these MD simulations in order to estimate the donor-acceptor electronic couplings. They established a model of the electronic coupling mechanism that depended on the presence of an inter-cofactor water bridge, and showed that their model produced "good agreement between the experimentally determined relative maximum rate of the mutants and the predicted square of the electronic couplings" [52]. Estimates of the magnitude of the electronic coupling were lower in mutants with less stable water bridges. De la Lande and coworkers also identified key amino acid residues involved in stabilizing the putative water bridges, lending credence to a previous hypothesis by Lin *et al.* [51] that "enzymes could organize this kind of water-mediated electron transfer" [52].

8.1.1 Simulation of Native MADH–Amicyanin Complex

Buoyed by the affirmative results of his numerical study of the PHM enzyme, de la Lande selected the MADH–amicyanin metabolic redox pair as his next topic of investigation. Whereas PHM represents an example of solvent-mediated intraprotein ET, the MADH–amicyanin pair represents a true interprotein ET reaction incorporating the added subtlety and complexity of globular protein-protein recognition processes.

As the starting structure for this new set of MD simulations, de la Lande chose the ternary crystal structure of MADH, amicyanin, and cytochrome $c_{551\mathrm{i}}$ in-complex (Brookhaven Protein Data Bank entry 2GC4), resolved at 1.9Å by X-ray crystallography [252]. The crystal structure of the MADH-amicyanin-cytochrome-$c_{551\mathrm{i}}$ had been shown to be catalytically viable for amicyanin-mediated ET from MADH to cytochrome *c* [238]. Furthermore, the orientation of MADH with respect to amicyanin in the ternary complex is believed to be similar to that of the binary complex, uniformly across crystalline and solution phases [55, 236].

After deleting the cytochrome-$c_{551\mathrm{i}}$ from the simulated structure, de la Lande used the Chemistry at HARvard Molecular Mechanics (CHARMM) software package to add hydrogen atoms (which were not resolved in the crystallography) to the simulated structure, based on known equilibrium molecular geometries (via the "hbuild" command [253]). The proteins' histidine residues were monoprotonated consistent with the experimental pH of 7.5 [14]. The hydrogen atoms were inserted at fixed bond lengths, and these lengths remained fixed for the duration of the MD simulation. Protein-bonded hydrogen geometries were solved at each time-step of the MD simulation using the "SHAKE" constraint algorithm [254].

After introducing hydrogen atoms to the structure of the simulated protein complex, de la Lande used an algorithm written by Lennart Nilsson of the Karolinska Institutet to introduce water molecules in the form of a "water box" of dimensions $115 \times 80 \times 80\,\text{Å}^3$ surrounding the protein complex structure. The TIP3P potential function [255] was used to parameterize the Coulomb and Lenard-Jones potential terms for the water molecules.

To model the protein and solvent interactions, de la Lande selected the "CHARMM27" force field which is composed from the all-atom "CHARMM22" force field with corrections to improve the accuracy of dihedral (angle) energy terms [256, 257]. The CHARMM27 force field has been shown to produce good overall agreement with experimental (RMSD) data when simulating the native structure of folded proteins with the TIP3P water model [257]. The CHARMM27 force field tends to over-estimate the stability of the α-helices, making it suitable for simulating protein folding for α-helix structures but not β-sheets [257]. The stability advantages of the CHARMM27 force field made it the best available force field in 2007 when the simulations were performed [257]. The disadvantages of the force field, with respect to α-helix overstabilization and β-sheet folding, would not be expected to produce deleterious effects because protein folding and unfolding were not being simulated.

The CHARMM27 force field parameter sets did not contain all the necessary information regarding the TTQ cofactor of MADH or the copper center of amicyanin, making it necessary to manually enter the force field parameters for these cofactors. Force field parameters for the blue copper centre were adapted from a study employing density functional theory calculations to develop general force field parameters for blue copper proteins [258]. The Lennard-Jones parameters for the copper ion were $\epsilon = 0.05\,\mathrm{kJmol}$ and $\sigma = 2.13\,\text{Å}$ [258]. The calculation of long-range (nonbonded) molecular interactions was limited to a 12 Å radius, tapering off between 10 Å and 12 Å. This is the recommended default setting for continuously cutting off computationally-costly long-range interactions when using the CHARMM27 force field.

De la Lande next geometrically-optimized the system structure using 500 steps of a steepest descent method followed by 1500 steps using an adopted basis Newton-Raphson method. These optimization steps were implemented as a basic precaution in order to eliminate the most energetically costly (and therefore unfavourable) interactions from the starting structure for the simulation. He next added sodium ions in order to neutralize the total charge of the solvated MADH-amicyanin complex. He then optimized the system again by a further 1500 adopted basis Newton-Raphson steps. This optimization procedure is typical for simulations of this type.

The MD simulations themselves were performed using Langevin dynamics as implemented in CHARMM. During Langevin dynamics, the usual Newtonian equation of motion for a particle of mass m at position $\vec{x}$, given by $m\ddot{\vec{x}} = -\vec{\nabla}V(\vec{x})$, is augmented by a damping term $-\gamma m\dot{\vec{x}}$, and a pseudo-random noise term $\sqrt{2\gamma mkT}\vec{\mathcal{R}}(t)$. The term $\vec{\mathcal{R}}(t)$ simulates a stationary three-dimensional Gaussian process obeying $\langle\vec{\mathcal{R}}(t)\rangle = \vec{0}$ and $\langle\vec{\mathcal{R}}(t)\cdot\vec{\mathcal{R}}(t')\rangle = \delta(t-t')$, where $\delta(t-t')$ is the Dirac delta distribution. Thus, the equation of motion for each particle labeled i is given by

$$m_i\ddot{\vec{x}}_i = -\vec{\nabla}V(\vec{x}_i) - \gamma m_i\dot{\vec{x}}_i + \sqrt{2\gamma m_i k_\mathrm{B}T}\,\vec{\mathcal{R}}_i(t). \tag{8.1}$$

Langevin dynamics were chosen by de la Lande to ensure a constant temperature and a thorough sampling of the nuclear phase space over the simulation duration. Langevin dynamics have been described as "a method closely related to MD, as a potential tool for conformational search" [259]. The time-dependent functional form of the stochastic trajectory of nuclear coordinates generated by Langevin dynamics should *not* be confused with the true time-dependent classical dynamics of a system of particles propagated using Newton's laws of motion. Rather, Langevin dynamics represent a method of conformational sampling intended to approximately reproduce the statistics of a canonical ensemble in contact with a thermal reservoir at constant temperature. A friction coefficient of $\gamma = 10\,\mathrm{ps}^{-1}$ and a temperature of $T = 298\,\mathrm{K}$ were used to calibrate the Langevin thermostat, ensuring canonical conditions with good temperature coupling [260].

De la Lande initialized and ran molecular dynamics simulations of the native MADH–amicyanin complex for 41 ns of simulated time with these settings, with snapshots of atomic coordinates saved once every 100 fs for the last 40 ns of simulation time. Nanoseconds timescale simulations of this kind have been recommended as optimal for Langevin dynamics simulations of small peptides [259] with robust generalization to macromolecular systems in solution at constant temperature [260]. No explicit boundary conditions were imposed on the system during the simulation, so the protein/solvent system evolved as a droplet floating in free space, without artifacts due to periodic boundary condtions.

8.2 Production of Mutant Amicyanin Structures

In this Section, I describe my construction of computational representations of four mutant forms of the globular redox enzyme amicyanin.

Following experiment [14], I chose to replace amicyanin's methionine 51 residue with each of alanine, leucine, and lysine. As an additional selection, I carried out a fourth

mutation to investigate the effect of replacing methionine 51 with a smaller cysteine residue without eliminating the seemingly-relevant sulphur atom from the vicinity of the 51 position of the amicyanin protein chain. I generated these mutant amicyanin structures by loading the 2GC4 amicyanin PDB structure into the molecular pre- and post-processing software package "Molden" [261], graphically selecting and deleting the Met51 residue, replacing it with each mutant residue in turn, and saving the resulting structure as a new PDB file.

8.3 Simulations of the Mutant Complexes

In this Section, I describe my initialization and production of numerical implementaions of Langevin dynamics of the mutant complexes in solution.

I followed de la Lande's system initialization and simulation procedure as described in Section 8.1.1, replacing the native amicyanin structure with each mutant in turn. I carried out these simulations using the CHARMM [56] molecular dynamics software (version 33a), on parallel computing hardware provided by WestGrid (www.westgrid.ca) and Compute Canada Calcul Canada (www.computecanada.ca).

8.4 Comparison of Pathway and Packing Density Models

In this Section, I describe the results of "pathway" and "packing density" calculations that I carried out to estimate the relative electronic coupling strengths between native and mutant electron transfer complexes.

The semiempirical pathway and packing density models of ET are presented in Sections 7.1.3 and 7.1.4 respectively. Both of these models rely on the calculation of the inter-cofactor electronic transmission decay factor $\varepsilon_{\mathrm{DA}}$, where the total transition am-

		M51L	M51K	M51A	M51C
r_k^{mut}	(experiment)	0.68	0.49	0.13	—
$r_\epsilon^{\mathrm{mut}}$	(pathway)	0.47	0.36	0.57	0.76
$r_\epsilon^{\mathrm{mut}}$	(packing density)	0.36	0.42	0.62	2.29

Table 8.1: Native-to-mutant ratios describing the relationship between the experimental ET rates ($r_k^{\mathrm{mut}} = k_{\mathrm{ET}}^{\mathrm{mut}}/k_{\mathrm{ET}}^{\mathrm{nat}}$) [14] and the simulated decay factors ($r_\epsilon^{\mathrm{mut}} = \bar{\epsilon}^{\mathrm{mut}}/\bar{\epsilon}^{\mathrm{nat}}$).

plitude $\mathcal{T}_{\mathrm{DA}}$ is a product of the "close-contact" transition amplitude $\mathcal{T}_{\mathrm{DA}}^0$ and the decay factor $\varepsilon_{\mathrm{DA}}$, *i.e.*, $\mathcal{T}_{\mathrm{DA}} = \mathcal{T}_{\mathrm{DA}}^0 \cdot \varepsilon_{\mathrm{DA}}$. In our case, where all of the native and mutant complexes share the same donor and acceptor cofactors (in essentially the same orientations), it is adequate to compare only the decay factors in order to assess the change in the electronic coupling strength induced by the mutations.

The algorithms that I used to carry out these calculations were implemented by Jan Řezáč using a variant on the "Ruby" programming language (*i.e.*, "Cuby3") and compiled for Unix-based operating systems. I carried out these calculations on the nuclear coordinate trajectories using compiled versions of Řezáč's code. Based on the results of DFT calculations performed by Aurélien de la Lande, I selected the catechol ring of MADH β Trp57 as the donor and the copper center of amicyanin as the acceptor.

I used the results of these calculations to estimate the mutant-to-native ratio $r_\epsilon^{\mathrm{mut}}$ of the donor-acceptor decay factor where $r_\epsilon^{\mathrm{mut}} = \bar{\epsilon}^{\mathrm{mut}}/\bar{\epsilon}^{\mathrm{nat}}$, and where $\bar{\epsilon}^{\mathrm{mut}}$ and $\bar{\epsilon}^{\mathrm{nat}}$ are respectively the average decay factors computed from the mutant and native trajectories. I found that all the experimentally-investigated mutant complexes exhibited decreased electronic coupling compared to the native complex, according to both the pathway and the packing density models (Table 8.1). Both the pathway and packing density model calculations qualitatively reproduced the overall trend in reduced ET efficacy demonstrated by the experimentally-relevant ET complexes. This finding is ambiguous on its own, because it compares experimentally-determined *rates* to hypothetical *decay factors* that do not account for reduced ET as a consequence of decreased ET activation

via the Franck-Condon factor ϱ_{FC}. In order to interpret the meaning of the decreased ET coupling predicted by simulations, with regard to the altered conformational dynamics hypothesized by experimenters [14], it is necessary to consider the underlying mechanism.

The data presented in Table 8.1 are subject to statistical sampling errors due to the finite size of the sampled data set (400 000 nuclear conformations). Classical sampling theory allows for general conclusions about the characteristics of a population to be made using a finite amount of sample data drawn from that population, according to the Central Limit Theorem [262]. The "confidence interval" around the mean value of a finite set of sampled data reflects the degree to which the statistician may be confident that mean value of the sample reproduces the mean values of the actual population. The confidence interval of a sampled data set is given by $\pm\sigma/\sqrt{n\rho}$, where σ is the standard deviation of the sampled set, n is the number of elements in the set, and ρ is the statistical "efficiency" of the sampling (*i.e.*, a perfectly efficient sample set is identically and independently distributed) [262, 263]. Confidence approaches certainty in the limit of an infinitely large, independently and identically distributed sample set. The statistical error analysis carried out by de la Lande for the data presented in Table 8.1 is given in Ref. [5], with confidence intervals ranging from $\pm 3\%$ to $\pm 17\%$. Comparable statistical confidence may be expected for the results presented in the following sections.

8.5 Analysis of Solvent Organization

In this Section, I describe qualitative and quantitative geometrical analyses that I performed on the coordinate trajectories generated by the molecular dynamics simulations of the native and mutant MADH–amicyanin complexes.

In order to decipher the role of solvent conformations in modulating the ET rate, I carried out extensive visual inspections of the trajectory data. For this task, I employed

the Visual Molecular Dynamics (VMD) software developed at the University of Illinois at Urbana-Champaign [57]. Focusing my attention on the inter-complex region situated between the donor and acceptor cofactors, I found that a water molecule was consistently and simultaneously hydrogen-bonded to particular surface atoms of both MADH and amicyanin, namely MADH β Ser56O and amicyanin His95HE2, in accordance with the original interprotein "water-bridge" hypothesis posed by Chen and coworkers [47]. The water molecule in this position was visibly less stable in the simulated mutant complexes, being frequently jostled out of position by the greater numbers of adjacent water molecules observed in the inter-protein space of the mutant complexes.

In order to quantitatively verify these qualitative observations, I conceived of three numerical measures of solvent occupation and dynamics in the interprotein region, and I implemented them in CHARMM:

1. I calculated P_{HB}, the average probability that a single water molecule should be simulatenously hydrogen-bonded to both MADH β Ser56O and amicyanin His95HE2, finding the probability significantly higher in the native complex than in any of the mutant complexes (Table 8.2).

2. I calculated τ, the total number of distinct water molecules (per unit time), to take up the bridging position during each simulation, finding that significantly fewer different water molecules occupied that position in the native complex (Table 8.2).

3. I calculated the average number $N_{\mathrm{H_2O}}(r)$ of water molecules found inside a spherical volume (the "ET region") of varying radius r, centered equidistantly between the atoms MADH β Ser56O and amicyanin His95HE2, finding significantly more water molecules present inside the mutant complexes (Fig. 8.1f).

These findings demonstrated that the water "bridge" linking MADH to amicyanin directly across the interprotein gap was mostly stable in the native complex, being oc-

	Native	M51L	M51K	M51A	M51C
P_{HB}	0.53	0.15	0.19	0.18	0.16
τ	0.23	0.45	1.20	0.50	2.25
$N_{\mathrm{H_2O}}$	1.8	2.8	2.4	2.5	2.1

Table 8.2: The unit-normalized probability P_{HB} of formation of the Ser56O–His95HE2 hydrogen-bonded water-bridge, the "turnover" τ denoting the time-averaged number of different water molecules to occupy the bridging position (in units of ns^{-1}) for the native and mutant systems, and the average number $N_{\mathrm{H_2O}}$ of water molecules within a sphere of radius $r = 3.0\,\text{Å}$ centred around the water bridge.

cupied the majority of the time, and replaced relatively infrequently. In contrast, this single-molecule bridge was usually not intact in the mutant complexes, and when it was present, it was more frequently displaced and exchanged with another molecule from the surrounding solvent. The greater numbers of water molecules observed in the spherical "ET region" suggested that the destabilization of the water bridge in the mutant complexes was due to increased interactions with the surrounding bulk solvent, compared to bulk-solvent interactions in the native complex.

These findings support the original hypothesis by Chen, Durley, Matthews and Davidson [47] that ET may be facilitated by the use of a water molecule to electronically couple the donor and acceptor orbitals. The bridging water molecule that I observed in the native and mutant simulations is located in the same position as the one they observed in Chen and coworkers' crystallography (PDB entry 2MTA). The results of the mutant MD simulations also corroborate Chen *et al.*'s concerns that the solvent bridge position "might not always be occupied" [47]. Rigorously establishing the role of the water bridge as an electron transfer facilitator thus required confirmation that the bridge itself provided the enhanced coupling.

8.6 Analysis of Electronic Transition Amplitudes

In this Section, I describe my analysis and categorization of the ET "pathway" and "packing density" analyses that I performed on the nuclear coordinate trajectories generated by molecular dynamics simulations of the native and mutant complexes.

The ET pathway model calculation generated a set of real-valued electronic transition decay factors accompanied by ASCII regular expressions representing the corresponding atomistic pathways from the donor to the acceptor. I employed MATLAB^{TM} to perform detailed analyses on these results, for the purpose of establishing a comprehensive system for categorizing variations between the different pathways. According to my analysis, the vast majority of the pathways could be categorized by the amino acid residue through which the dominant ET pathway exited the MADH β-subunit, namely one of Ser56, Trp57, Val58, or Trp108. More than 99% of the dominant ET pathways involved some solvent molecule(s) and entered amicyanin through its His95 copper-ligand. I labeled each pathway alphabetically, according to the residue by which it exited MADH:

- pathways exiting via Ser56 were labeled "A",
- those exiting by Trp57 were labeled "B",
- those exiting by Val58 were labeled "C",
- those exiting by Trp108 were labeled "D",
- and all remaining pathways were labeled "E".

All the pathways labeled A through D involved some water molecule(s) and entered amicyanin through His95. I divided the E-labeled pathways into pathways involving any water molecule(s) ("E_{wet}"), and pathways involving a "through space jump" from MADH to amicyanin ("E_{dry}"). The average value $\bar{\epsilon}$ of the relative coupling element ϵ for each pathway motif (or "tube"), and its overall probability, are given in Table 8.3.

	Native		M51L		M51K		M51A		M51C	
	$\bar{\epsilon}$	%	$\bar{\epsilon}$	%	$\bar{\epsilon}$	%	$\bar{\epsilon}$	%	$\bar{\epsilon}$	%
A	1.02	59.4	0.63	49.6	0.75	45.2	0.78	32.4	0.80	33.3
B	0.74	39.8	0.48	29.1	0.60	35.3	0.68	66.1	0.69	39.0
C	0.56	0.4	0.48	20.4	0.55	17.4	0.6	0.8	0.61	12.9
D	1.25	0.2	0.23	0.4	0.76	1.4	1.06	0.2	0.96	13.9
E_{wet}	0.32	<0.1	0.09	0.2	0.25	0.1	0.14	<0.1	0.33	0.3
E_{dry}	0.14	0.1	0.06	0.3	0.18	0.5	0.19	0.4	0.3	0.7

Table 8.3: Averaged coupling decay factors $\bar{\epsilon}$ (in units of 10^{-3}), and occurance probabilities (as percent) of the four main pathway motifs (A, B, C, D) and all other remaining solvent-mediated (E_{wet}) and through-space (E_{dry}) pathways from donor to acceptor.

The native simulations reveal the dominant character of the A-labeled pathways, exhibiting strong coupling ($\bar{\epsilon} = 1.02$) the majority (59.4%) of the time. The D-labeled pathways (exiting MADH through the Trp108 redox cofactor) exhibited somewhat stronger coupling ($\bar{\epsilon} = 1.25$) in the native system, but these pathways were viable only 0.2% of the time, making their contribution to the overall ET coupling practically negligible. The mutant complexes exhibited siginificantly weaker coupling overall and reduced prevalence of A-labeled pathways in particular.

In order to quantify the significance of the Ser56-His95 water bridge in facilitating electronic coupling, it is necessary to examine the prevalence of precisely this ET pathway in contributing to the overall ET coupling. For this reason, I subdivided the A-labeled category into three subcategories labeled A_1, A_2, and A_3, as follows:

- pathways passing across a completely-hydrogen-bonded, single-molecule, water bridge from MADH Ser56O to amicyanin His95HE2 were labeled "A_1",
- pathways passing across a completely-hydrogen-bonded, multi-molecule, water bridge from MADH Ser56O to amicyanin His95HE2 were labeled "A_2", and
- pathways involving through-space jumps but still passing across water molecules from MADH Ser56O to amicyanin His95HE2 were labeled "A_3".

	Native		M51L		M51K		M51A		M51C	
	$\bar{\epsilon}$	%	$\bar{\epsilon}$	%	$\bar{\epsilon}$	%	$\bar{\epsilon}$	%	$\bar{\epsilon}$	%
A_1	1.10	52.8	0.91	26.2	0.99	29.0	0.94	24.9	1.00	23.0
A_2	0.44	3.0	0.38	13.0	0.43	5.1	0.43	1.9	0.44	4.5
A_3	0.25	3.6	0.23	10.4	0.28	11.1	0.24	6.2	0.26	5.8

Table 8.4: Averaged coupling decay factors $\bar{\epsilon}$ (in units of 10^{-3}), and occurance probabilities (as percent) of three submotifs A_1, A_2, and A_3 of the A type of pathway.

Table 8.4 shows how the overwhelming majority of A-labeled pathways in the native complex actually represent the A_1 pathway originally hypothesized by Chen *et al.* [47]. The ET coupling generated by the A_1 pathway in the mutant complexes is closely comparable to that of the native complex, but signficantly less likely to contribute to the overall ET coupling. This finding demonstrates that the disruption of the Ser56O–His95HE2 water bridge observed in the mutant complexes leads directly to the reduced likelihood of ET coupling via the A_1 pathway, and reduced overall electronic coupling as a result.

This preeminence of the A_1 pathway can be visually established by comparing weighted histograms showing the relative coupling strength and probability of each of the (A_1, A_2, A_3, B, C, D, E) pathway categories, as plotted graphically in Figs. 8.1a-e. The blue data points plotted in Fig. 8.1a shows how the dominant A_1 pathway manifests the highest overall probability and the largest average coupling strength in the native system.

8.7 Molecular Breakwater Hypothesis

In this Section, I describe the "molecular breakwater" hypothesis I developed in order to explain the role of protein surface residues in organizing the structure of inter-complex water molecules to promote enhanced electronic coupling between MADH and amicyanin.

Having established that simulations of native and mutant MADH–amicyanin complexes exhibit the presence of an ET-enhancing water bridge at the position and orienta-

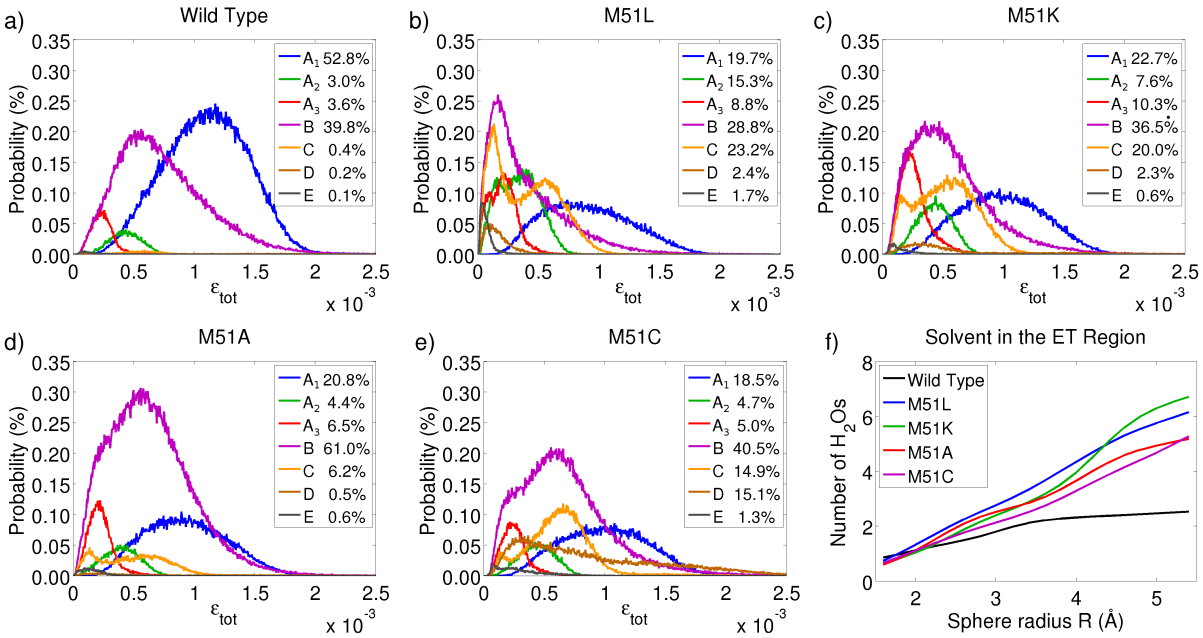

Figure 8.1: Plots a-e depict histograms showing the relative coupling strength and probability of occurance of the pathways categorized A_1, A_2, A_3, B, C, D, E for the native ("wild type") and mutant complexes. Plot f depicts the number of water molcules found in a spherical inter-protein "ET region" of varying size for each of these complexes. Plots are reproduced from Ref. [5] with permission from the publisher.

tion to form a hydrogen-bonded single-molecule link from MADH β Ser56O to amicyanin His95HE2 according to the water-bridge hypothesis originally proposed by Chen *et al.* in 1994 [47], it remained to establish a causal mechanism linking the mutations performed on the methionine 51 residue of amicyanin to the disruption of the water bridge itself. The increased occupation of solvent molecules in the interprotein "ET region" of the mutant structures, along with the increased interchange between water molecules in this region with those from the surrounding bulk solvent, suggested that the mutations performed on the Met51 residue led to increased exposure of the sterically-constrained interprotein region to the dynamics of the surrounding solvent milieu.

In the original motivating experiment, Ma and coworkers mutated amicyanin's proleine 52 residue into glycine in order to investigate whether the ligand geometry of azurin's copper center could be introduced into amicyanin [13]. They found instead that "the

mutation of Pro52 alters the positions of residues that are involved in protein-protein interactions within the ET protein complex with MADH and consequently alters the kinetic mechanisms of the ET reactions from MADH to amicyanin" [13]. In particular, the mutation of Pro51 into Gly51 resulted in the reorientation of the adjacent Met51 residue, leading Ma *et al.* to hypothesize that the P52G mutation produced a change in the interaction between amicyanin Met51 and MADH β Val58 during ET complex-formation. Follow-up experiments involving mutations performed on Met51 supported the hypothesis that "the P52G mutation resulted in a change in position of the side chain of Met51, which eliminated the contacts with the side chain of βVal58 of MADH that are seen in the structure of the complex of native amicyanin with MADH" [14].

From these experimental conclusions it was natural to infer that the loss of these complex-stabilizing interactions between amicyanin and MADH β Val58 led to increased contact and interchange between the water molecules contained inside the redox complex and those of the surrounding bulk. However, the logical consistency of this inference required the additional assumption that the inter-protein contact points surrounding the redox cofactors of MADH and amicyanin should form a water-tight seal upon complex formation—sealing in a small number of ET-mediating water molecules, while sealing out the surrounding bulk solvent. The generation of this assumption represented a novel conceptual addition to established models describing the function of the ring of hydrophobic surface residues surrounding amicyanin's redox cofactor.

Amicyanin has a hydrophobic patch of seven amino acid residues on its surface (surrounding the His95–copper ligand) that is believed to stabilize its formation of a redox complex with MADH [234, 237]. This hydrophobic patch is common to blue copper proteins [230], and is believed to play a role ensuring redox complex stability [230] and specificity [231]. It had not, however, been previously supposed that this surface structure might "dynamically organize water bridges to enhance electron transfer between

proteins" [5]. Therefore, based on my numerical findings, I proposed the novel hypothesis that the hydrophobic ring surrounding the active site of amicyanin (along with its negative counterpart on MADH) *also* functions as a "molecular breakwater" that protects and supports the stability of the ET-mediating solvent bridge by limiting solvent interchange between the sterically constrained ET region and the surrounding bulk [5].

8.8 Concluding Remarks

In conclusion, I have presented my production and analysis of data drawn from computer simulations of MADH in complex with mutant forms of amicyanin, in comparison with data from the native complex. I conceived, designed, and implemented quantitative measures of the atomic coordinate trajectory data generated by the native and mutant simulations, in order to demonstrate qualitative changes in the interprotein solvent dynamics that occur in the mutant complexes as a result of the mutations. I implemented tunneling "pathway" and "packing density" calculations using data from the coordinate trajectories. I conceived and implemented analytical techniques to interpret data produced by the pathway calculations, demonstrating that these mutations resulted in the destabilization of an interprotein water bridge that facilitates electronic coupling between the redox cofactors of the ET complex.

Although the reduced electronic coupling observed in each mutant simulation might by itself be construed as a numerical artifact or a statistical fluke, the collective findings that I have presented in this Chapter corroborate to form a robust physical picture of solvent-mediated ET that cannot be summarily dismissed. It is exponentially unlikely that all of the simulated mutant complexes could have randomly exhibited reduced ET coupling (according to the pathway analysis) with respect to the native complex. Furthermore, the presence of the consistently occupied ET-enhancing bridge in the native

complex, taken along with its absence in the mutant complexes, forms an explanatory picture of the actual ET-enhancing mechanism that is inconsistent with the concept of a fluke. The loss of bridge stability is causally related to the mutations themselves by the increased numbers of more rapidly fluctuating solvent molecules in the "ET region" of the mutant complexes, because of the mutation-induced loss of solvent-repelling hydrophobic interactions between the proteins. These findings therefore provide sound numerical evidence in support of the original hypothesis by Chen and coworkers that charge transport in this system is enhanced by solvent-mediated ET which "depends critically on the presence of a water molecule that might not always be occupied" [47].

My finding are supported by follow-up calculations of interprotein solvent occupation, performed by Chen "Tina" Liu [6] using these coordinate trajectories. Liu's calculations showed marked increases in solvent occupation in the vicinity of amicyanin residue 51 and MADH β-subunit residues Val58 and Glu101 in the simulated mutant complexes with respect to the native complex. My findings are also supported by the results of independent simulations of the native and mutant MADH–amicyanin complexes in solution, performed by Ehsan Zahedinejad. Zahedinejad performed these simulations using the Not just Another Molecular Dynamics (NAMD) program [264], using periodic boundary conditions and temperature regulation by means of a Lowe-Anderson thermostat [265]. Zahedinejad performed the same calculations on his data set as those represented by Tables 8.2, 8.3, and 8.4, reproducing the same pattern of interprotein solvent-stabilization and enhanced A_1-bridge-mediated electronic coupling in the native complex [266].

These findings collectively provide strong support for the hypothesis that the puckered hydrophobic ring around the active site on the surface of amicyanin, in cooperation with the residues they interact with on the surface of MADH, collaboratively operate to "dynamically stabilize" the interprotein solvent molecules to enable enhanced ET. They were published in the article, "Surface residues dynamically organize water bridges to

enhance electron transfer between proteins," in the *Proceedings of the National Academy of Science*. That article has been cited in twenty-three (23) different peer-reviewed scientific articles [64, 63, 66, 267, 268, 269, 68, 6, 270, 271, 272, 273, 274, 69, 275, 65, 276, 277, 278, 279, 280, 281, 67] since the time of its publication. The article has garnered recognition from Davidson himself [63]:

> It was subsequently shown using molecular dynamics simulations that the interactions between Met51 and MADH comprised a "molecular breakwater" that optimized the position of water molecules at the protein interface, and that the M51A mutation disrupted this breakwater resulting in a decreased availability of the optimum configuration for electron transfer These results highlight the fact that specific individual residues at the surface of redox proteins not only dictate specificity for initial binding to their redox protein partners, but also are critical to optimize the configuration of the redox centers and intervening media within the protein complex for the electron transfer event.

The article is reproduced in the Appendix with written permission from the publisher.

Chapter 9

Concluding Discussion

The medium is the message.

—Marshall McLuhan, 1964 [282]

During the 1960s, Marshall McLuhan famously promoted the principle that the dissemination of a technological medium in a human environment itself defines a message in that environment [282]. He defined his principle succinctly [282]:

> This is merely to say that the personal and social consequences of any medium—that is, of any extension of ourselves—result from the new scale that is introduced into our affairs by each extension of ourselves, or by any new technology.

The application of this principle need not be limited to the scope of human affairs. Living cells exhibit *agency*; they are able to respond to external stimuli and they are capable of internal self-regulation [19]. These faculties represent complex information processing tasks defined according to the precepts of communication theory [18].

Chemistry is used to define the "basis of life" [19]. In the case of partner-specific biological electron transfer, the enzymatic reactants encode the information necessary to definitively identify each other during metabolism—the medium *is* the message. The natural intelligence exhibited by redox enzymes as they efficiently carry out complex metabolic tasks differentiates them from the simple oxidants and reductants that are traditional to chemistry. As Davies has proposed [15], the hierarchy of complexity that is found in a living system presents the need for a reevaluation of the traditional models and assumptions of chemistry with regard to metabolic biochemistry.

9.1 Summary and Conclusions

Summary of Part I

In Part I of this Thesis, I presented my prototype design for a two-qubit $\sqrt{\text{SWAP}}$ gate that operates according to the adiabatic approach and reseparation of a pair of atomic qubits trapped individually using optical tweezers [2]. Previous proposals [28] and demonstrations [29] of this exchange gate relied on qubits stored using the nuclear spin states of the atoms. In contrast, I chose to consider gate operation using decoherence-resistant non-magnetic electronic states, such as the $^1S_0$ and $^3P_0$ states of alkaline-earth atoms. I derived a simple criterion to ensure adiabatic gate operation and I performed numerical analyses to evaluate gate fidelity over a range of speeds [2]. I helped develop a "loophole-free" Bell inequality test based on the use of this gate, and I carried out an order-of-magnitude feasibility analysis to assess whether the test is viable given realistic technological limitations [3]. Using a mathematical technique devised by Wiebe, I invented an asymptotic error-correction scheme to polynomially improve the gate's fidelity without decreasing its speed [4].

The decoherence-resistance gate that I propose represents a means of realizing a crucial entanglement-generating component to neutral atom-based QIP architectures, and it can be adapted readily to ionic QIP systems [30]. My contribution to the development of an atom-based Bell test provides a critical alternative route to performing a conclusive test of local realism, should current photon-based approaches encounter insurmountable difficulties [157]. My scheme to improve gate operation by harnessing nonadiabatic interference effects provides an essential contribution to the development of error-correcting techniques for atomistic QIP architectures that rely on adiabatic transport.

This vibrationally-adiabatic exchange gate generates a nonadiabatic transition between the initially-degenerate logical qubit basis states $|0_L 1_R\rangle$ and $|1_L 0_R\rangle$. At large

trap separation distances, the cluster separability [83] of the individual atoms allows the neglect of the identical character of the two systems, so that the atoms become effectively distinguishable. As the traps converge, the controlled breakdown of the Born-Oppenheimer approximation is exploited to implement the two-qubit entangling gate, as the two atomic centre-of-mass wavefunctions are brought into overlap for exchange.

For qubits encoded into the joint electronic levels of the two atoms, the logical "diabatic" basis states $|0_{\rm L}1_{\rm R}\rangle$ and $|1_{\rm L}0_{\rm R}\rangle$ are initially degerate. This degeneracy is split into two (symmetric and antisymmetric) non-degenerate adiabatic states $|\chi^{+}\rangle \otimes |\Psi^{+}\rangle$ and $|\chi^{-}\rangle \otimes |\Psi^{-}\rangle$ as the atomic centre-of-mass wavefunctions come into overlap. Thus, the $\sqrt{\rm SWAP}$ gate physically realizes half of one "nonadiabatic" electronic transition between the diabatic basis states $|0_{\rm L}1_{\rm R}\rangle$ and $|1_{\rm L}0_{\rm R}\rangle$ as the traps converge.

Whereas I have considered a pair of logical states $|0_{\rm L}1_{\rm R}\rangle$ and $|1_{\rm L}0_{\rm R}\rangle$ with regard to the orbital angular momentum states of a pair of divalent atoms, these generic logical states could be physically reconcieved as charge occupation states to describe the physics of inter-particle nonadiabatic ET (*e.g.*, $|0\rangle$ = "unoccupied" and $|1\rangle$ = "occupied"). In this case, my logic gate provides an immediate physical analogue to an intermolecular ET system, as the size and complexity of the redox-partners scale from individual atoms to whole macromolecules. The controlled collision of a pair of one-dimensional particles to generate an electronically-nonadiabatic quantum logic gate from a vibrationally-adiabatic evolution represents a profound simplification of the kind of nonadiabatic electronic transition that occurs during amicyanin's collision with MADH. Nevertheless, the physical realization of this gate defines a small but fundamentally-important step towards the kind of full-scale analogue simulation that Feynman and others have envisioned.

Summary of Part II

In Part II of this Thesis, I investigated ET reaction experiments performed on native and mutant forms of the MADH–amicyanin redox complex derived from *P. denitrificans*. I implemented molecular dynamics simulations of native and mutant forms of the solvated MADH–amicyanin complex, and I analyzed the resulting nuclear coordinate trajectories geometrically and according to a tunneling pathway analysis. I found that the interprotein solvent dynamics of the mutant systems differed dramatically from those of the native system, and that the stability of an ET-mediating "water bridge" was compromised in the mutant complexes. I concluded that the mutations disrupted the structure of a protective "molecular breakwater" on the surface of amicyanin that stabilizes the interprotein water bridge in the native complex.

My findings highlight the need for novel experiments involving mutations of protein surface residues, in order to determine how these residues are able to "optimize the configuration of the redox centers and intervening media within the protein complex for the electron transfer event" [63]. In this respect, my molecular breakwater hypothesis has already been used to interpret the result of one such follow-up experiment subsequently performed in Victor Davidson's laboratory [64]. My findings have had a considerable impact on the opinion of the biochemical community, as ET-mediating structured water has become a subject of serious and widespread interest [67, 68, 69].

The anomalous characteristics of the MADH–amicyanin ET reaction make it a suitable object for investigations regarding molecular recognition processes [232]. As we have discussed in Section 7.5, the reaction exhibits an anomalously large reorganization energy, which could be due to the non-equilibrium electrostatic properties of amicyanin in-complex or the inner-sphere (Cu–His95) bond-breaking event that accompanies amicyanin reduction. These anomalies raise questions about the reaction's theoretical status as a "true" ET reaction (defined in Section 7.3.1). The non-Condon effects (see Sec-

tion 7.3.5) that are introduced into the ET reaction in the mutant complexes (due to variations in the ET couplings afforded by the different nuclear-conformation-dependent tunneling pathways) suggest that part of the breakwater's function is to help ensure that the Condon approximation is satisified during ET by limiting the number of accessible solvent conformations in the native complex upon docking. The thermodynamic cost of generating this solvent-organizing effect is not taken into account by the empirically-defined reaction coordinates used to describe the experiment [242, 283]. All these issues raise questions about the whether the physical characteristics of the reaction conform to the theoretical assumptions of Marcus Theory (see Sections 7.2, 7.3, and 7.5).

These findings suggest that the degrees of freedom used to define the thermodynamic cost to activate a metabolic ET reaction can be different from those of a non-metabolic one. For example, the non-negligible cost to ensure reaction specificity needs to be taken into account in the definition of the reaction coordinate of a metabolic reaction. Both classical and quantum resources may need to be quantified in order to characterize nonadiabatic reactions that involve explicit dynamical quantum effects. An entanglement resource [21] needs to be prepared to enable a nonadiabatic electron transfer reaction, akin to any other quantum information processing tasks.

At a minimum, nonadiabatic ET requires the non-deterministic use of one exchange-mediated SWAP operation (equivalent to two $\sqrt{\text{SWAP}}$ operations) in order to reversibly transfer the electron from donor to acceptor. The preparation of this entanglement resource at physiological temperature defines a non-trivial QIP task, even if preparation succeeds with minimal probability. It is metabolically important for the ET event to occur reversibly via quantum mechanical exchange, rather than classically via thermal hopping, in order to minimize the risk of oxidative damage due to electron loss. This subtlety reveals how a living organism can exploit a modest QIP resource in order to gain a significant survival advantage.

9.2 Perspective

The findings presented in Part I and Part II both highlight the need for a deeper understanding of the conditions that govern nonadiabatic transitions during approximately-adiabatic evolutions. Ordered expansions of nonadiabatic effects, such as those considered by Wiebe and myself [4], can be used to characterize the degree of nonadiabaticicity exhibited by quantum chemical system when nuclear momenta cannot be satisfactorily neglected or treated separably.

The two-qubit exchange gate considered in Part I provides a key component to digital QIP architectures, but its value is not strictly limited to quantum computing applications. It introduces an experimental technique for the practical realization of traditional *Gedankenexperiments* in physics, such as the EPR "paradox" via a Bell inequality test [3], and *also* for traditional *Gedankenexperiments* in chemistry, such as formation of Heitler and London's hydrogen molecule via an adiabatically-controlled atomic collision [2]. QIP experiments involving the controlled breakdown of the adiabatic description of a chemical system may promote insights with regard to the traditional models and assumptions of chemical theory.

As we have discussed in Section 2.2, chemical systems are defined according to an adiabatic description. The assumption that vibronic transitions may be neglected (piecewise) along the chemical reaction coordinate dictates that the electronic subsystem remains in its instantaneous quantum adiabatic ground state during the activation step of a chemical reaction. The assumption that the electronic ground state of the system evolves quantum-adiabatically from the reaction's initial equilibrium state to the transition state is mathematically identical to the definition of an adiabatic quantum algorithm that "interpolates between an initial Hamiltonian, whose ground state is easy to construct, and a final Hamiltonian, whose ground state encodes the satisfying assignment" [108].

The controlled chemical reactions that occur during metabolism define complex information processing tasks: the biochemical medium is the message. Chemical reactions, considered as information processing tasks, are hard to solve. The time needed to (non-deterministically) generate a reaction's transition state from its equilibrium state increases exponentially with the size of the free energy gap separating them. Enzymatic catalysts can increase the rates of chemical reactions by many orders of magnitude [284]. The physical basis for this rate-enhancement is not well-understood [284].

The enormous rate-enhancements that enzyme-catalyzed reactions exhibit over uncatalyzed reactions are reminiscent of the speed-enhancements that quantum computing algorithms exhibit over classical computing algorithms. This suggests that the mathematical techniques developed to analyze and enhance the rates of adiabatic quantum algorithms may also promote insights into the mechanisms governing enzyme catalysis. For example, Kieferová and Wiebe found that the computational power of a nearly-adiabatic process can be increased with the application of weighted superpositions of otherwise-classical control parameters (*i.e.*, potentials) [77]. This finding indicates that non-Born-Oppenheimer superpositions of the nuclei can be used to increase the computational power of a chemical system. Quantum nuclear motions have been shown to modulate activation free energies during enzyme catalysis [285] and classical nuclear motions can produce geometrically-weighted coherence effects during ET [213]. It follows that enzymes may be able to exploit combinations of transient nonadiabatic evolutions in order to enhance and control the activation rates of the reactions that they catalyze.

Here I have provided just a few examples to suggest how new models and hypotheses may be generated by formulating chemical reaction theory in quantum information theoretic terms. This formulation is essential to quantify the resources employed during the enzymed-catalyzed activation of a reaction because enzymes operate reversibly.

Bibliography

[1] R. A. Heinlein, *Time Enough for Love*, G. P. Putnam's Sons, New York (1973).

[2] N. S. Babcock, R. Stock, M. G. Raizen, B. C. Sanders, "Entangling identical bosons in optical tweezers via exchange interaction," *Canadian Journal of Physics* **86**, 549 (2008).

[3] R. Stock, N. S. Babcock, M. G. Raizen, B. C. Sanders, "Entanglement of group-II-like atoms with fast measurement for quantum information processing," *Physical Review A* **78**, 022301 (2008).

[4] N. Wiebe, N. S. Babcock, "Improved error-scaling for adiabatic quantum evolutions," *New Journal of Physics* **14**, 013024 (2012).

[5] A. de la Lande, N. S. Babcock, J. Řezáč, B. C. Sanders, D. R. Salahub, "Surface residues dynamically organize water bridges to enhance electron transfer between proteins," *Proceedings of the National Academy of Science* **106**, 11799 (2010).

[6] A. de la Lande, N. S. Babcock, J. Řezáč, B. Lévy, B. C. Sanders, D. Salahub, "Quantum effects in biological electron transfer," *Physical Chemistry Chemical Physics* **14**, 5902 (2012).

[7] M. Kisilak, H. Anderson, N. S. Babcock, M. R. Setzer, S. H. J. Idziak, E. B. Sirota, "An x-ray extensional flow cell," *Review of Scientific Instruments* **72**, 4305 (2001).

[8] B. Nieman, X. Commeinhes, N. S. Babcock, I. Frola, R. Forgett, S. H. J. Idziak, "An x-ray confinement cell for studies of complex fluids under shear and confinement," *Review of Scientific Instruments* **75**, 936 (2004).

[9] N. S. Babcock, "Towards a Quantum Carnot Engine," Undergraduate Thesis, University of Waterloo (2005).

[10] N. S. Babcock, "The Impact of Quantum Information Science: 45 Years Later and Still Plenty of Room," First Prize Winner of the Grand Opening Essay Contest, Institute for Quantum Information Science University of Calgary (2005).

[11] N. S. Babcock, "Quantum Theory at Burning Man," *The Quantum Times* **3**, 1 (2008).

[12] N. S. Babcock, "Canonical Rate-Expression for Nonadiabatic Electron Transfer," manuscript in preparation.

[13] J. K. Ma, C. J. Carrell, F. S. Mathews, V. L. Davidson, "Site-Directed Mutagenesis of Proline 52 To Glycine in Amicyanin Converts a True Electron Transfer Reaction into One that Is Conformationally Gated," *Biochemistry* **45**, 8284 (2006).

[14] J. K. Ma, Y. Wang, C. J. Carrell, F. S. Mathews, V. L. Davidson, "A Single Methionine Residue Dictates the Kinetic Mechanism of Interprotein Electron Transfer from Methylamine Dehydrogenase to Amicyanin," *Biochemistry* **46**, 11137 (2007).

[15] P. Davies, "The secret of life won't be cooked up in a chemistry lab," *The Guardian* 13 January 2013. Retrieved from http://www.theguardian.com.

[16] J. D. Watson, F. H. C. Crick, "Molecular Structure of Nucleic Acids," *Nature* **171**, 737 (1953).

[17] F. H. C. Crick, L. Barnett, S. Brenner, R. J. Watts-Tobin, "General Nature of the Genetic Code for Proteins," *Nature* **192**, 1227 (1961).

[18] C. Shannon, "A Mathematical Theory of Communication," *The Bell System Technical Journal* **27**, 379.

[19] G. Karp, *Cell and Molecular Biology Concepts and Experiments*, John Wiley & Sons, Inc., New York (1996).

[20] M. Mohseni, W. Omar, G. S. Engel, M. B. Plenio, eds., *Quantum Effects in Biology*, Cambridge University Press, Cambridge (2014).

[21] M. A. Nielsen, I. Chuang, *Quantum Computation and Quantum Information*, Cambridge University Press, Cambridge (2000).

[22] R. P. Feynman, "Simulating physics with computers," *International Journal of Theoretical Physics* **21**, 467 (1982).

[23] P. Benioff, "The Computer as a Physical System: A Microscopic Quantum Mechanical Hamiltonian Model of Computers as Represented by Turing Machines," *Journal of Statistical Physics* **22**, 563 (1980).

[24] R. P. Feynman, *Feynman Lectures on Computation*, Perseus Books, Reading, Massachusetts (1996).

[25] S. Rich, B. Gellman, "NSA seeks to build quantum computer that could crack most types of encryption," *The Washington Post* 2 January 2014. Retrieved from http://www.washingtonpost.com.

[26] Z. Merali, "Quantum Mechanics Braces for the Ultimate Test," *Science* **331**, 1380 (2011).

[27] D. Loss, D. P. DiVincenzo, "Quantum computation with quantum dots," *Physical Review A* **57**, 120 (1998).

[28] D. Hayes, P. Julienne, I. Deutsch, "Quantum Logic via the Exchange Blockade in Ultracold Collisions," *Physical Review Letters* **98**, 070501 (2007).

[29] M. Anderlini, P. J. Lee, B. L. Brown, J. Sebby-Strabley, W. D. Phillips, J. V. Porto, "Controlled exchange interaction between pairs of neutral atoms in an optical lattice," *Nature* **448**, 452 (2007).

[30] A. V. Gorshkov, A. M. Rey, A. J. Daley, M. M. Boyd, J. Ye, P. Zoller, M. D. Lukin, "Alkaline-Earth-Metal Atoms as Few-Qubit Quantum Registers," *Physical Review Letters* **102**, 110503 (2009).

[31] W. Yi, A. J. Daley, G. Pupillo, P. Zoller, "State-dependent, addressable subwavelength lattices with cold atoms," *New Journal of Physics* **10**, 073015 (2008).

[32] D. Cheung, P. Høyer, N. Wiebe, "Improved error bounds for the adiabatic approximation," *Journal of Physics A* **44**, 415302 (2011).

[33] D. G. Kotsifaki, M. Makropoulou, A. A. Serafetinides, "Efficient and low cost multiple optical trap, based on interference," *Optik* **124**, 617 (2013).

[34] E. H. Lapasar, K. Kasamatsu, Y. Kondo, M. Nakahara, T. Ohmi, "Scalable Neutral Atom Quantum Computer with Interaction on Demand: Proposal for Selective Application of Two-Qubit Gate," *Journal of the Physical Society of Japan* **80**, 114003 (2011).

[35] S. Stellmer, M. K. Tey, R. Grimm, F. Schreck, "Bose-Einstein condensation of ^{86}Sr," *Physical Review A* **82**, 041602 (2010).

[36] K. R. A. Hazzard, V. Gurarie, M. Hermele, A. M. Rey, "High-temperature properties of fermionic alkaline-earth-metal atoms in optical lattices," *Physical Review A* **85**, 041604 (2012).

[37] S. Uetake, R. Murakami, J. M. Doyle, Y. Takahashi, "Spin-dependent collision of ultracold metastable atoms," *Physical Review A* **86**, 032712 (2012).

[38] A. Frisch, K. Aikawa, M. Mark, F. Ferlaino, E. Berseneva, S. Kotochigova, "Hyperfine structure of laser-cooling transitions in fermionic erbium-167," *Physical Review A* **88**, 032508 (2013).

[39] B. Mohring, M. Bienert, F. Haug, G. Morigi, W. P. Schleich, M. G. Raizen, "Extracting atoms on demand with lasers," *Physical Review A* **90**, 063425 (2005).

[40] A. M. Dudarev, M. G. Raizen, Q. Niu, "Quantum Many-Body Culling: Production of a Definite Number of Ground-State Atoms in a Bose-Einstein Condensate," *Physical Review Letters* **98**, 063001 (2007).

[41] F. Serwane, G. Zürn, T. Lompe, T. B. Ottenstein, A. N. Wenz, S. Jochim, "Deterministic Preparation of a Tunable Few-Fermion System," *Science* **332**, 336 (2011).

[42] A. M. Kaufman, B. J. Lester, C. A. Regal, "Cooling a Single Atom in an Optical Tweezer to Its Quantum Ground State," *Physical Review X* **2**, 041014 (2012).

[43] A. V. Carpentier, Y. H. Fung, P. Sompet, A. J. Hilliard, T. G. Walker, M. F. Andersen, "Preparation of a single atom in an optical microtrap," *Laser Physics Letters* **10**, 125501 (2013).

[44] M. Ebert, A. Gill, M. Gibbons, X. Zhang, M. Saffman, T. G. Walker, "Atomic Fock State Perparation Using Rydeberg Blockade," *Physical Review Letters* **112**, 043602 (2014).

[45] A. Szent-Györgyi, *Cell-Associated Water*, chap. "Welcoming Address", Academic Press (1979).

[46] P. Ball, "Water as an Active Constituent in Cell Biology," *Chemical Reviews* **108**, 74 (2008).

[47] L. Chen, R. C. E. Durley, F. S. Mathews, V. L. Davidson, "Structure of an Electron Transfer Complex: Methylamine Dehydrogenase, Amicyanin, and Cytochrome c_{551i}," *Science* **264**, 86 (1994).

[48] U. Ermler, R. A. Siddiqui, R. Cramm, B. Friedrich, "Crystal structure of the flavohemoglobin *Alcaligenes eutrophus* at 1.75 Å resolution," *The EMBO Journal* **14**, 6067 (1995).

[49] F. A. Tezcan, B. R. Crane, J. R. Winkler, H. B. Gray, "Electron tunneling in protein crystals," *Proceedings of the National Academy of Sciences* **98**, 5002 (2001).

[50] W. A. Francisco, G. Wille, A. J. Smith, D. J. Merkler, J. P. Klinman, "Investigation of the Pathway for Inter-Copper Electron Transfer in Peptidylglycine α-Amidating Monooxygenase," *Journal of the American Chemical Society* **126**, 13168 (2004).

[51] J. Lin, I. A. Balabin, D. N. Beratan, "The Nature of Aqueous Tunneling Pathways Between Electron-Transfer Proteins," *Science* **310**, 1311 (2005).

[52] A. de la Lande, S. Martí, O. Parisel, V. Moliner, "Long Distance Electron Transfer Mechanism in Peptidylglycine α-Hydroxylating Monooxygenase: A Perfect Fitting for a Water Bridge," *Journal of the American Chemical Society* **129**, 11700 (2007).

[53] S. T. Prigge, R. E. Mains, B. A. Eipper, L. M. Amzel, "New insights into copper monooxygenases and peptide amidation: structure, mechanism and function," *Cellular and Molecular Life Sciences* **57**, 1236 (2000).

[54] R. J. M. van Spanning, C. W. Wansell, W. N. M. Reijnders, L. F. Oltmann, A. H. Stouthamer, "Mutagenesis of the gene encoding amicyanin of *Paracoccus denitrificans* and the resultant effect on methylamine oxidation," *FEBS Letters* **275**, 217 (1990).

[55] L. Chen, R. Durley, B. J. Poliks, K. Hamada, Z. Chen, F. S. Mathews, V. L. Davidson, Y. Satow, E. Huizinga, F. M. D. Vellieux, W. G. J. Hol, "Crystal Structure of an Electron-Transfer Complex between Methylamine Dehydrogenase and Amicyanin," *Biochemistry* **31**, 4959 (1992).

[56] B. R. Brooks, R. E. Bruccoleri, B. D. Olafson, D. J. States, S. Swaminathan, M. Karplus, "CHARMM: A program for macromolecular energy, minimization, and dynamics calculations," *Journal of Computational Chemistry* **4**, 187 (1983).

[57] W. Humphrey, A. Dalke, K. Schulten, "VMD: Visual molecular dynamics," *J. Mol. Graphics* **14**, 33 (1996).

[58] O. Miyashita, M. Y. Okamura, J. N. Onuchic, "Interprotein electron transfer from cytochrome c_2 to photosynthetic reaction center: Tunneling across an aqueous interface," *Proceedings of the National Academy of Sciences* **102**, 3558 (2005).

[59] A. Migliore, S. Corni, R. D. Felice, E. Molinari, "Water Effects on Electron Transfer in Azurin Dimers," *Journal of Physical Chemistry B* **110**, 23796 (2006).

[60] I. A. Balabin, D. N. Beratan, S. S. Skourtis, "Persistence of Structure Over Fluctuations in Biological Electron-Transfer Reactions," *Physical Review Letters* **101**, 158102 (2008).

[61] A. Jasaitis, M. P. Johansson, M. Wikström, M. H. Vos, M. I. Verkhovsky, "Nanosecond electron tunneling between the hemes in cytochrome *bo3*," *Proceedings of the National Academy of Science* **104**, 20811 (2007).

[62] J. R. Winkler, H. B. Gray, "Electron Transfer in Ruthenium-Modified Protelns," *Chemical Reviews* **92**, 369 (1992).

[63] M. Choi, V. L. Davidson, "*Cupredoxins—A study of how proteins may evolve to use metals for bioenergetic processes*," *Metallomics* **3**, 140 (2011).

[64] M. Choi, N. Sukumar, F. S. Mathews, A. Liu, V. L. Davidson, "Proline 96 of the Copper Ligand Loop of Amicyanin Regulates Electron Transfer from Methylamine Dehydrogenase by Positioning Other Residues at the Protein–Protein Interface," *Biochemistry* **50**, 12651273 (2011).

[65] M. Watkins, B. Reischl, "A simple approximation for forces exerted on an AFM tip in liquid," *The Journal of Chemical Physics* **138**, 154703 (2013).

[66] F. Lederer, "Another look at the interaction between mitochondrial cytochrome *c* and flavocytochrome b_2," *European Biophysics Journal* **40**, 1283 (2011).

[67] B. M. Savoiea, K. L. Kohlstedta, N. E. Jacksona, L. X. Chena, M. O. de la Cruza, G. C. Schatza, T. J. Marksa, M. A. Ratner, "Mesoscale molecular network formation in amorphous organic materials," *Proceedings of the National Academy of Sciences* **111**, 10055 (2014).

[68] C. A. Bortolotti, A. Amadei, M. Aschi, M. Borsari, S. Corni, M. Sola, I. Daidone, "The Reversible Opening of Water Channels in Cytochrome c Modulates the Heme Iron Reduction Potential," *Journal of the American Chemical Society* **134**, 13670 (2012).

[69] S. V. Antonyuk, C. Han, R. R. Eady, S. S. Hasnain, "Structures of protein–protein complexes involved in electron transfer," *Nature* **496**, 123 (2013).

[70] H. J. Kupka, *Transitions in Molecular Systems*, Wiley-VCH Verlag GmbH & Co. KGaA, Weinheim (2010).

[71] K. Gavroglou, *Fritz London: a scientific biography*, Cambridge University Press, Cambridge (1995).

[72] K.-P. Marzlin, B. C. Sanders, "Inconsistency in the Application of the Adiabatic Theorem," *Physical Review Letters* **93**, 160408 (2004).

[73] E. Torrontegui, X. Chen, M. Modugno, S. Schmidt, A. Ruschhaupt, J. G. Muga, "Fast transport of Bose-Einstein condensates," *New Journal of Physics* **14**, 013031 (2012).

[74] E. B. Wilson, "Impact of the Heitler–London Hydrogen Molecule Paper on Chemistry," *International Journal of Quantum Chemistry* **12**, 17 (1977).

[75] A. Szabo, N. S. Ostlund, *Modern Quantum Chemistry*, McGraw-Hill Publishing Company, New York (1982).

[76] B. H. Bransden, C. J. Jochain, *Quantum Mechanics, 2nd ed.*, Pearson Education Ltd., Dorchester, Dorset (2000).

[77] M. Kieferová, N. Wiebe, "On the power of coherently controlled quantum adiabatic evolutions," *New Journal of Physics* **16**, 123034 (2014).

[78] I. Kassal, J. D. Whitfield, A. Perdomo-Ortiz, M.-H. Yung, A. Aspuru-Guzik, "Simulating Chemistry Using Quantum Computers," *Annual Review of Physical Chemistry* **62**, 185 (2011).

[79] J. C. Slater, *Quantum Theory of Molecules and Solids*, vol. 1, McGraw-Hill Book Company, New York (1963).

[80] M. Born, J. R. Oppenheimer, "Zur Quantentheorie der Molekeln," *Annalen der Physik* **84**, 457 (1927).

[81] A. Nitzan, *Chemical Dynamics in Condensed Phases*, Oxford University Press, Oxford (2006).

[82] R. P. Feynman, "Forces in Molecules," *Physical Review* **56**, 340 (1939).

[83] A. Peres, *Quantum Theory: Concepts and Methods*, Kluwer Academic Publishers, Dordrecht (1993).

[84] M. Lax, "The Franck-Condon Principle and Its Application to Crystals," *The Journal of Chemical Physics* **20**, 1752 (1952).

[85] T. Calarco, E. A. Hinds, D. Jaksch, J. Schmiedmayer, J. I. Cirac, P. Zoller, "Quantum gates with neutral atoms: Controlling collisional interactions in time-dependent traps," *Physical Review A* **61**, 022304 (2000).

[86] R. A. Marcus, N. Sutin, "Electron transfers in chemistry and biology," *Biochimica et Biophysica Acta* **811**, 265 (1985).

[87] R. P. Feynman, "There's Plenty of Room at the Bottom," in J. Robbins, ed., "The Pleasure of Finding Things Out," Perseus Books, Cambridge, MA (1999).

[88] E. Schrödinger, "Discussion of Probability Relations Between Separated Systems," *Mathematical Proceedings of the Cambridge Philosophical Society* **31**, 555 (1935).

[89] A. Einstein, B. Podolsky, N. Rosen, "Can Quantum-Mechanical Description of Physical Reality Be Considered Complete?" *Physical Review* **325**, 777 (1935).

[90] J. S. Bell, "On the Einstein Podolsky Rosen Paradox," *Physics* **1**, 195 (1964).

[91] D. Bohm, "A Suggested Interpretation of the Quantum Theory in Terms of "Hidden" Variables I," *Physical Review* 166–179 (1952).

[92] D. Bohm, "A Suggested Interpretation of the Quantum Theory in Terms of "Hidden" Variables II," *Physical Review* 180–193 (1952).

[93] P. A. M. Dirac, *The Principles of Quantum Mechanics*, Oxford University Press, Oxford (1957).

[94] J. von Neumann, *Mathematical Foundations of Quantum Mechanics*, Princeton University Press, Princeton (1955).

[95] A. Turing, "On computable numbers, with an application to the Entscheidungsproblem," *Proceedings of the London Mathematical Society* **42**, 230 (1936).

[96] S. Wiesner, "Conjugate Coding," *ACM SIGACT News* **15**, 78 (1983).

[97] D. Deutsch, "Quantum theory, the Church-Turing principle and the universal quantum computer," *Proc. R. Soc. Lond. A* **400**, 97 (1985).

[98] D. Deutsch, "Quantum computational networks," *Proc. R. Soc. Lond. A* **425**, 73 (1989).

[99] D. P. DiVincenzo, "Two-bit gates are universal for quantum computation," *Physical Review A* **51**, 1015 (1995).

[100] A. Ekert, R. Jozsa, "Quantum computation and Shor's factoring algorithm," *Physical Review Letters* **68**, 733 (1996).

[101] P. W. Shor, "Scheme for reducing decoherence in quantum computer memory," *Physical Review A* **52**, 2493 (1995).

[102] S. Lloyd, "Capacity of the noisy quantum channel," *Physical Review A* **55**, 1613 (1997).

[103] N. Jones, "Computing: The quantum company," *Nature* **498**, 286 (2013).

[104] D. J. Griffiths, *Introduction to Quantum Mechanics*, Prentice Hall, Upper Saddle River, New Jersey (1995).

[105] R. Raußendorf, H.-J. Briegel, "A One-Way Quantum Computer," *Physical Review Letters* **86**, 5188 (2001).

[106] H. J. Briegel, R. Raußendorf, "Persistent Entanglement in Arrays of Interacting Particles," *Physical Review Letters* **86**, 910 (2001).

[107] R. Raußendorf, D. E. Browne, H. J. Briegel, "Measurement-based quantum computation on cluster states," *Physical Review A* **68**, 022312 (2003).

[108] E. Farhi, J. Goldstone, S. Gutmann, M. Sipser, "Quantum computation by adiabatic evolution," arXiv preprint, arXiv:quant-ph/0001106 (2000).

[109] R. Oliveira, B. M. Terhal, "The Complexity of Quantum Spin Systems on a Two-Dimensional Square Lattice," *Quantum Information and Computation* **8**, 0900 (2008).

[110] E. Mimoun, L. D. Sarlo, D. Jacob, J. Dalibard, F. Gerbier, "Fast production of ultracold sodium gases using light-induced desorption and optical trapping," *Physical Review Letters* **81**, 023631 (2010).

[111] K.-A. Suominen, "Physical Implementation of Large-Scale Quantum Computation," in G. Rozenberg, T. Bäck, J. Kok, eds., "Handbook of Natural Computing," 1493–1520, Springer Berlin, Heidelberg (2012).

[112] K. Eckert, J. Mompart, X. X. Yi, J. Schliemann, D. Bruß, G. Birkl, M. Lewenstein, "Quantum computing in optical microtraps based on the motional states of neutral atoms," *Physical Review A* **66**, 042317 (2002).

[113] W. D. Phillips, H. Metcalf, "Laser Deceleration of an Atomic Beam," *Physical Review Letters* **48**, 596 (1982).

[114] T. Grünzweig, A. Hilliard, M. McGovern, M. F. Andersen, "Near-deterministic preparation of a single atom in an optical microtrap," *Nature Physics* **6**, 951 (2010).

[115] C. Monroe, J. Kim, "Scaling the Ion Trap Quantum Processor," *Science* **339**, 1164 (2013).

[116] J. I. Cirac, P. Zoller, "Quantum Computations with Cold Trapped Ions," *Physical Review Letters* **74**, 4091 (1995).

[117] Q. A. Turchette, D. Kielpinski, B. E. King, D. Leibfried, D. M. Meekhof, C. J. Myatt, M. A. Rowe, C. A. Sackett, C. S. Wood, W. M. Itano, C. Monroe, D. J. Wineland, "Heating of trapped ions from the quantum ground state," *Physical Review A* **61**, 063418 (2000).

[118] J. Ye, H. J. Kimble, H. Katori, "Quantum State Engineering and Precision Metrology Using State-Insensistive Light Traps," *Science* **320**, 1734 (2008).

[119] J. Beugnon, C. Tuchendler, H. Marion, A. Gaëtan, Y. Miroshnychenko, Y. R. P. Sortais, A. M. Lance, M. P. A. Jones, G. Messin, A. Browaeys, P. Grangier, "Two-dimensional transport and transfer of a single atomic qubit in optical tweezers," *Nature Physics* **3**, 696 (2007).

[120] I. Bloch, "Quantum coherence and entanglement with ultracold atoms in optical lattices," *Nature* **453**, 1016 (2008).

[121] C. Weitenberg, S. Kuhr, K. Mølmer, J. F. Sherson, "Quantum computation architecture using optical tweezers," *Physical Review A* **84**, 032322 (2011).

[122] J. D. Thompson, T. G. Tiecke, A. S. Zibrov, V. Vuletic, M. D. Lukin, "Coherence and Raman Sideband Cooling of a Single Atom in an Optical Tweezer," *Physical Review Letters* **110**, 133001 (2013).

[123] G. K. Brennen, C. M. Caves, P. S. Jessen, I. H. Deutsch, "Quantum Logic Gates in Optical Lattices," *Physical Review Letters* **82**, 1060 (1999).

[124] G. K. Brennen, I. H. Deutsch, P. S. Jessen, "Entangling dipole-dipole interactions for quantum logic with neutral atoms," *Physical Review A* **61**, 062309 (2000).

[125] I. E. Protsenko, G. Reymond, N. Scholosser, P. Grangier, "Operation of a quantum phase gate using neutral atoms in microscopic dipole traps," *Physical Review A* **65**, 052301 (2002).

[126] T. Wilk, A. Gaëtan, C. Evellin, J. Wolters, Y. Miroshnychenko, P. Grangier, A. Browaeys, "Entanglement of Two Individual Neutral Atoms Using Rydberg Blockade," *Physical Review Letters* **104**, 010502 (2010).

[127] D. Jaksch, H.-J. Briegel, J. I. Cirac, C. W. Gardiner, P. Zoller, "Entanglement of atoms via cold controlled collisions," *Physical Review Letters* **82**(9), 1975 (1999).

[128] T. Calarco, H.-J. Briegel, D. Jaksch, J. I. Cirac, P. Zoller, "Entangling neutral atoms for quantum information processing," *Journal of Modern Optics* **47**, 2137 (2000).

[129] S. Chu, "The manipulation of neutral particles," *Reviews of Modern Physics* **70**, 685 (1998).

[130] S. Chu, "Cold atoms and quantum control," *Nature* **416**, 206 (2002).

[131] J. D. Weinstein, K. Beloy, A. Derevianko, "Entangling the lattic clock: Towards Heisenberg-limited timekeeping," *Physical Review A* **81**, 030302 (2010).

[132] P. O. Bugnion, G. J. Conduit, "Exploring exchange mechanisms with cold-atom gas," *Physical Review A* **88**, 013601 (2013).

[133] E. Mimoun, L. D. Sarlo, D. Jacob, J. Dalibard, F. Gerbier, "Fast production of ultracold sodium gases using light-induced desorption and optical trapping," *Physical Review A* **81**, 023631 (2010).

[134] A. Smith, B. E. Anderson, H. Sosa-Martinez, C. A. Fiofrío, P. S. Jessen, "Quantum Control in the Cs $^6S_{1/2}$ Ground Manifold Using Radio-Frequency and Microwave Magnetic Fields," *Physical Review Letters* **111**, 170502 (2013).

[135] M. Takamoto, H. Katori, "Spectroscopy of the $^1S_0$ - $^3P_0$ Clock Transition of ^{87}Sr in an Optical Lattice," *Physical Review Letters* **91**, 223001 (2003).

[136] Z. W. Barber, C. W. Hoyt, C. W. Oates, L. Hollberg, A. V. Taichenachev, V. I. Yudin, "Direct Excitation of the Forbidden Clock Transition in Neutral ^{174}Yb Atoms Confined to an Optical Lattice," *Physical Review Letters* **96**, 083002 (2006).

[137] L. Isenhower, E. Urban, X. L. Zhang, A. T. Gill, T. Henage, T. A. Johnson, T. G. Walker, M. Saffman, "Demonstration of a Neutral Atom Controlled-NOT Quantum Gate," *Physical Review Letters* **104**, 010503 (2010).

[138] T. L. Gustavson, A. P. Chikkatur, A. Leanhardt, A. Grlitz, S. Gupta, D. E. Pritchard, W. Ketterle, "Transport of Bose-Einstein Condensates with Optical Tweezers," *Physical Review Letters* **88**, 020401 (2002).

[139] A. J. Daley, "Quantum computing and quantum simulation with group-II atoms," *Quantum Information Processing* **10**, 865 (2011).

[140] M.-O. Mewes, M. R. Andrews, N. J. van Druten, D. M. Kurn, D. S. Durfee, W. Ketterle, "Bose-Einstein Condensation in a Tightly Confining dc Magnetic

Trap," *Physical Review Letters* **77**, 416 (1996).

[141] K. C. Young, R. Blume-Kohout, D. A. Lidar, "Adiabatic quantum optimization with the wrong Hamiltonian," *Physical Review A* **88**, 062314 (2013).

[142] M. M. Boyd, T. Zelevinsky, A. D. Ludlow, S. Blatt, T. Zanon-Willette, S. M. Foreman, J. Ye, "Nuclear spin effects in optical lattice clocks," *Physical Review A* **76**, 022510 (2007).

[143] T. Pellizzari, S. A. Gardiner, J. I. Cirac, P. Zoller, "Decoherence, Continuous Observation, and Quantum Computing: A Cavity QED Model," *Reviews of Modern Physics* **70**, 721 (1998).

[144] D. Jaksch, J. I. Cirac, P. Zoller, S. L. Rolston, R. Côté, M. D. Lukin, "Fast quantum gates for neutral atoms," *Physical Review Letters* **85**(10), 2208 (2000).

[145] J. Mompart, K. Eckert, W. Ertmer, G. Birkl, M. Lewenstein, "Quantum Computing with Spatially Delocalized Qubits," *Physical Review Letters* **90**, 147901 (2003).

[146] O. Mandel, M. Greiner, A. Widera, T. Rom, T. W. Hänsch, I. Bloch, "Controlled collisions for multiparticle entangelment of optically trapped atoms," *Nature (London)* **425**, 937 (2003).

[147] T. Keating, R. L. Cook, A. M. Hankin, Y.-Y. Jau, G. W. Biedermann, I. H. Deutsch, "Robust quantum logic in neutral atoms via adiabatic Rydberg dressing," *Physical Review A* **91**, 012337 (2015).

[148] I. Bloch, J. Dalibard, S. Nascimbène, "Quantum simulations with ultracold quantum gases," *Nature Physics* **8**, 267 (2012).

[149] T. P. Meyrath, F. Schreck, J. L. Hanssen, C.-S. Chuu, M. G. Raizen, "Bose-Einstein condensate in a box," *Physical Review A* **71**, 041604 (2005).

[150] L. Tonks, "The Complete Equation of State of One, Two and Three-Dimensional Gases of Hard Elastic Spheres," *Physical Review* **50**, 955 (1936).

[151] H. F. Trotter, "On the Product of Semi-Groups of Operators," *Proceedings of the American Mathematical Society* **10**, 545 (1959).

[152] J. F. Clauser, M. A. Horne, A. Shimony, R. A. Holt, "Proposed experiment to test local hidden-variable theories," *Physical Review Letters* **23**, 880 (1969).

[153] J. F. Clauser, M. A. Horne, "Experimental consequences of objective local theories," *Phys. Rev. D* **10**, 526 (1974).

[154] B. S. Cirel'son, "Quantum Generalizations of Bell's Inequality," *Letters in Mathematical Physics* **4**, 93 (1980).

[155] A. Aspect, P. Grangier, G. Roger, "Experimental Realization of Einstein-Podolsky-Rosen-Bohm Gedankenexperiment: A New Violation of Bell's Inequalities," *Physical Review Letters* **49**, 91 (1982).

[156] M. A. Rowe, D. Kielpinski, V. Meyer, C. A. Sackett, W. M. Itano, C. Monroe, J. Wineland, "Experimental violation of a Bell inequality with efficient detection," *Nature* **409**, 791 (2001).

[157] E. Santos, "Bell's theorem and the experiments: Increasing empirical support for local realism?" *Studies in History and Philosophy of Modern Physics* **36**, 544 (2005).

[158] H. P. Robertson, "The Uncertainty Principle," *Physical Review A* **34**, 163 (1929).

[159] R. B. Diener, B. Wu, M. G. Raizen, Q. Niu, "Quantum Tweezer for Atoms," *Physical Review Letters* **89**, 070401 (2002).

[160] Mark Raizen, private communication.

[161] T. Hong, C. Cramer, W. Nagourney, E. N. Fortson, "Optical Clocks Based on Ultranarrow Three-Photon Resonances in Alkaline Earth Atoms," *Physical Review Letters* **94**, 050801 (2005).

[162] D. Guéry-Odelin, J. G. Muga, "Transport in a harmonic trap: Shortcuts to adiabaticity and robust protocols," *Physical Review A* **90**, 063425 (2014).

[163] K. O. Roberts, T. McKellar, J. Fekete, A. Rakonjac, A. B. Deb, N. Kjærgaard, "Experimental violation of a Bell inequality with efficient detection," *Nature* **39**, 2012 (2014).

[164] G. Weihs *et al.*, "Violation of Bell's Inequality under Strict Einstein Locality Conditions," *Physical Review Letters* **81**, 5039 (1998).

[165] B. B. Jensen, H. Ming, P. G. Westergaard, K. Gunnarsson, M. H. Madsen, A. Brusch, J. Hald, J. W. Thomsen, "Experimental Determination of the ^{24}Mg I($3s3p$) $^3P_2$ Lifetime," *Physical Review Letters* **107**, 113001 (2011).

[166] K. Aron, P. M. Johnson, "The multiphoton ionization spectrum of xenon: Interatomic effects in multiphoton transitions," *The Journal of Chemical Physics* **67**, 5099 (1977).

[167] G. S. Hurst, M. G. Payne, S. D. Kramer, J. P. Young, "Resonance ionization spectroscopy and one-atom detection," *Reviews of Modern Physics* **51**, 767 (1979).

[168] F. Gerbier, J. Dalibard, "Gauge fields for ultracold atoms in optical superlattices," *New Journal of Physics* **12**, 033007 (2010).

[169] S. Stellmer, R. Grimm, F. Schreck, "Production of quantum-degenerate strontium gases," *Physical Review A* **87**, 013611 (2013).

[170] S. Stellmer, F. Schreck, "Reservoir spectroscopy of $5s5p^3P_2$–$5snd^3D_{1,2,3}$ transitions in strontium," *Physical Review A* **90**, 022512 (2014).

[171] E. Torrontegui, S. Ibánez, S. Martínez-Garaot, M. Modugno, A. del Campo, D. Guéry-Odelin, A. Ruschhaupt, X. Chen, J. G. Muga, "Shortcuts to adiabaticity," *Advances In Atomic, Molecular, and Optical Physics* **62**, 117 (2013).

[172] J. Roland, N. J. Cerf, "Quantum search by local adiabatic evolution," *Physical Review A* **65**, 042308 (2002).

[173] E. Knill, "Quantum computing with realistically noisy devices," *Nature* **434**, 39 (2005).

[174] E. Charron, E. Tiesinga, F. Mies, C. Williams, "Optimizing a Phase Gate Using Quantum Interference," *Physical Review Letters* **88**, 077901 (2002).

[175] E. Torrontegui, S. Ibáñez, X. Chen, A. Ruschhaupt, D. Gury-Odelin, J. G. Muga, "Fast atomic transport without vibrational heating," *Physical Review A* **83**, 013415 (2011).

[176] D. A. Lidar, A. T. Rezakhani, A. Hamma, "Adiabatic approximation with exponential accuracy for many-body systems and quantum computation," *Journal of Mathematical Physics* **50**, 102106 (2009).

[177] A. T. Rezakhani, A. K. Pimachev, D. A. Lidar, "Accuracy versus run time in an adiabatic quantum search," *Physical Review A* **8**, 052305 (2010).

[178] T. Albash, S. Boixo, D. A. Lidar, P. Zanardi, "Quantum adiabatic Markovian master equations," *New Journal of Physics* **14**, 123016 (2012).

[179] R. D. Somma, D. Nagaj, M. Kieferová, "Discussion of Probability Relations Between Separated Systems," *Physical Review Letters* **109**, 050501 (2012).

[180] G. Quiroz, D. A. Lidar, "High-fidelity adiabatic quantum computation via dynamical decoupling," *Physical Review A* **86**, 042333 (2012).

[181] Z. Cao, A. Elgart, "On the efficiency of Hamiltonian-based quantum computation for low-rank matrices," *J. Math. Phys.* **53**, 032201 (2012).

[182] M. Cullimore, M. J. Everitt, M. A. Ormerod, J. H. Samson, R. D. Wilson, A. M. Zagoskin, "Relationship between minimum gap and success probability in adiabatic quantum computing," *Journal of Physics A* **45**, 505305 (2012).

[183] K. C. Young, R. Blume-Kohout, D. A. Lidar, "Adiabatic quantum optimization with the wrong Hamiltonian," *Physical Review A* **88**, 062314 (2013).

[184] Z.-B. Feng, M. Li, "High-fidelity quantum state transfer using Cooper-pair box qubits," *Physica C* **507**, 65 (2014).

[185] I. Hen, A. P. Young, "Performance of the quantum adiabatic algorithm on constraint satisfaction and spin glass problems," *European Physical Journal Special Topics* **224**, 63 (2015).

[186] R. P. Feynman, "What Is and What Should Be the Role of Scientific Culture in Modern Society," in J. Robbins, ed., "The Pleasure of Finding Things Out," Perseus Books, Cambridge, MA (1999).

[187] J. Halpern, L. E. Orgel, "Oxidation-Reduction Reactions in Ionizing Solvents," *Discussions of the Faraday Society* **29**, 7 (1960).

[188] A. Szent-Györgyi, "Towards a New Biochemistry," *Science* **93**, 609 (1941).

[189] M. G. Evans, G. Gergely, "A Discussion of the Possibility of Bands of Energy Levels in Proteins," *Biochimica et Biophysica Acta* **3**, 188 (1949).

[190] B. Chance, G. R. Williams, "The respiratory chain and oxidative phosphorylation," *Advances in Enzymology* **17**, 65 (1956).

[191] D. D. Vault, B. Chance, "Studies of Photosynthesis Using a Pulsed Laser," *Biophysical Journal* **6**, 825 (1966).

[192] H. B. Gray, J. R. Winkler, "Electron tunneling through proteins," *Quarterly Reviews of Biophysics* **36**, 341372 (2003).

[193] J. R. Winkler, D. G. Nocera, K. M. Yocom, E. Bordignon, H. B. Gray, "Electron-Transfer Kinetics of Pentaammineruthenium(III)(histidine-33)–Ferricytochrome c. Measurement of the Rate of Intramolecular Electron Transfer between Redox Centers Separated by 15Å in a Protein," *Journal of the American Chemical Society* **104**, 5798 (1982).

[194] H. B. Gray, J. R. Winkler, "Long-range electron transfer," *Proceedings of the National Academy of Science* **102**, 3534 (2005).

[195] J. J. Hopfield, "Electron transfer between biological molecules by thermally activated tunneling," *Proceedings of the National Academy of Science* **71**, 3640 (1974).

[196] H. M. McConnell, "Intramolecular Charge Transfer in Aromatic Free Radicals," *Journal of Chemical Physics* **35**, 508 (1961).

[197] I. M. C. van Amsterdam, M. Ubbink, O. Einsle, A. Messerschmidt, A. Merli, D. Cavazzini, G. L. Rossi, G. W. Canters, "Dramatic modulation of electron transfer in protein complexes by crosslinking," *Nature Structural Biology* **9**, 48 (2002).

[198] D. N. Beratan, J. J. Hopfield, "Calculation of Electron Tunneling Matrix Elements in Rigid Systems: Mixed-Valence Dithiaspirocyclobutane Molecules," *Journal of the American Chemical Society* **106**, 1584 (1984).

[199] D. N. Beratan, J. N. Onuchic, J. J. Hopfield, "Limiting forms of the tunneling matrix element in the long distance bridge mediated electron transfer problem," *The Journal of Chemical Physics* **83**, 5325 (1985).

[200] D. N. Beratan, J. Onuchic, J. J. Hopfield, "Electron tunneling through covalent and noncovalent pathways in proteins," *Journal of Chemical Physics* **86**, 4488 (1987).

[201] D. N. Beratan, J. Onuchic, "Electron tunneling pathways in proteins: influences on the transfer rate," *Photosynthesis Research* **22**, 173 (1989).

[202] C. C. Moser, J. M. Keske, K. Warncke, R. S. Farid, P. L. Dutton, "Nature of biological electron transfer," *Nature* **355**, 796 (1992).

[203] C. C. Page, C. C. Moser, X. Chen, P. L. Dutton, "Natural engineering principles of electron tunnelling in biological oxidation-reduction," *Nature* **402**, 47 (1999).

[204] J. N. Onuchic, D. N. Beratan, "Molecular Bridge Effects on Distant Charge Tunneling," *Journal of the Americal Chemical Society.* **109**, 6771 (1987).

[205] J. N. Onuchic, D. N. Beratan, "A predictive theoretical model for electron tunneling pathways in proteins," *Journal of Chemical Physics* **92**, 722 (1990).

[206] D. N. Beratan, J. N. Betts, J. N. Onuchic, "Protein Electron Transfer Rates Set by the Bridging Secondary and Tertiary Structure," *Science* **252**, 1285 (1991).

[207] D. N. Beratan, J. N. Onuchic, J. R. Winkler, H. B. Gray, "Electron-tunneling pathways in proteins," *Science* **258**, 1740 (1992).

[208] J. N. Onuchic, D. N. Beratan, J. R. Winkler, H. B. Gray, "Pathway Analysis of Protein Electron-Transfer Reactions," *Annual Review of Biophysics and Biomolecular Structure* **21**, 349 (1992).

[209] D. N. Beratan, I. A. Balabin, "Heme-copper oxidases use tunneling pathways," *Proceedings of the National Academy of Science* **105**, 403 (2008).

[210] J. N. Gehlen, I. Daizadeh, A. A. Stuchebrukhov, R. A. Marcus, "Tunneling matrix element in Ru-modified blue copper proteins: pruning the protein in search of electron transfer pathways," *Inorganica Chimica Acta* **243**, 271 (1996).

[211] S. S. Skourtis, I. A. Balabin, T. Kawatsu, D. N. Beratan, "Protein dynamics and electron transfer: Electronic decoherence and non-Condon effects," *Proceedings of the National Academy of Science* **102**, 35523557 (2005).

[212] W. Koch, M. C. Holthausen, *A Chemist's Guide to Density Functional Theory*, Wiley-VCH, Weinheim (2002).

[213] I. A. Balabin, J. N. Onuchic, "Dynamically Controlled Protein Tunneling Paths in Photosynthetic Reaction Centers," *Science* **290**, 114 (2000).

[214] L. Turin, "A Spectroscopic Mechanism for Primary Olfactory Reception," *Chemical Senses* **21**, 773 (1981).

[215] J. C. Brooks, F. Hartoutsiou, A. P. Horsfield, A. M. Stoneham, "Could Humans Recognize Odor by Phonon Assisted Tunneling," *Physical Review Letters* **98**, 038101 (2007).

[216] V. May, O. Kün, *Charge and Energy Transfer Dynamics in Molecular Systems*, Wiley-VCH Verlag GmbH & Co. KGaA, Weinheim (2011).

[217] R. A. Marcus, "Nonadiabatic processes involving quantum-like and classical-like coordinates with applications to nonadiabatic electron transfers," *The Journal of Chemical Physics* **81**, 4494 (1984).

[218] R. B. Gennis, "Foundations and Applications of Physical Biochemistry," textbook pre-print, University of Illinois at Urbana-Champaign (2015).

[219] V. L. Davidson, "Protein Control of True, Gated, and Coupled Electron Transfer Reactions," *Accounts of Chemical Research* **41**, 730 (2008).

[220] V. L. Davidson, "Chemically Gated Electron Transfer. A Means of Accelerating and Regulating Rates of Biological Electron Transfer," *Biochemistry* **41**, 14633 (2002).

[221] V. L. Davidson, "Unraveling the Kinetic Complexity of Interprotein Electron Transfer Reactions," *Biochemistry* **35**, 14035 (1996).

[222] V. L. Davidson, "Effects of Kinetic Coupling on Experimentally Determined Electron Transfer Parameters," *Biochemistry* **39**, 4924 (2000).

[223] Z.-X. Liang, J. M. Nocek, I. V. Kurnikov, D. N. Beratan, B. M. Hoffman, "Electrostatic Control of Electron Transfer between Myoglobin and Cytochrome b_5: Effect of Methylating the Heme Propionates of Zn-Myoglobin," *Journal of the American Chemical Society* **122**, 3552 (2000).

[224] Z.-X. Liang, J. M. Nocek, K. Huang, R. T. Hayes, I. V. Kurnikov, D. N. Beratan, B. M. Hoffman, "Dynamic Docking and Electron Transfer between Zn-myoglobin and Cytochrome b_5," *Journal of the American Chemical Society* **124**, 6849 (2002).

[225] Z.-X. Liang, I. V. Kurnikov, J. M. Nocek, A. G. Mauk, D. N. Beratan, B. M. Hoffman, "Dynamic Docking and Electron-Transfer between Cytochrome b_5 and a Suite of Myoglobin Surface-Charge Mutants. Introduction of a Functional-Docking Algorithm for Protein Protein Complexes," *Journal of the American Chemical Society* **126**, 27852798 (2004).

[226] V. L. Davidson, "What Controls the Rates of Interprotein Electron-Transfer Reactions," *Accounts of Chemical Research* **33**, 87 (2000).

[227] G. R. Bishop, V. L. Davidson, "Intermolecular Electron Transfer from Substrate-Reduced Methylamine Dehydrogenase to Amicyanin Is Linked to Proton Transfer," *Biochemistry* **34**, 12082 (1995).

[228] V. Gold, K. L. Loening, A. D. McNaught, P. Sehmi, *Compendium of Chemical Terminology: IUPAC Recommendations*, Blackwell Scientific Publications, London (1987).

[229] C. Dennison, "Investigating the structure and function of cupredoxins," *Coordination Chemistry Reviews* **249**, 3025 (2005).

[230] F. de Rienzo, R. R. Gabdoulline, M. C. Menziani, R. C. Wade, "Blue copper proteins: A comparative analysis of their molecular interaction properties," *Protein Science* **9**, 1439 (2000).

[231] P. A. Williams, V. Fülöp, Y.-C. Leung, C. Chan, J. W. B. Moir, G. Howlett, S. J. Ferguson, S. E. Radford, J. Hajdu, "Pseudospecific docking surfaces on electron transfer proteins as illustrated by pseudoazurin, cytochrome c550 and cytochrome cd1 nitrite reductase," *Nature Structural & Molecular Biology* **2**, 975 (1995).

[232] S. H. Gellman, "Introduction: Molecular Recognition," *Chemical Reviews* **97**, 1231 (1997).

[233] W. S. McIntire, D. E. Wemmer, A. Chistoserdov, M. E. Lidstrom, "A New Cofactor in a Prokaryotic Enzyme: Tryptophan Tryptophylquinone as the Redox Prosthetic Group in Methylamine Dehydrogenase," *Science* **252**, 817 (1991).

[234] V. L. Davidson, L. H. Jones, M. E. Graichen, F. S. Mathews, J. P. Hosler, "Factors Which Stabilize the Methylamine Dehydrogenase-Amicyanin Electron Transfer Protein Complex Revealed by Site-Directed Mutagenesis," *Biochemistry* **36**, 12733 (1997).

[235] H. B. Brooks, V. L. Davidson, "Kinetic and Thermodynamic Analysis of a Physiologic Intermolecular Electron-Transfer Reaction between Methylamine Dehydrogenase and Amicyanin," *Biochemistry* **33**, 5696 (1994).

[236] F. Meschi, F. Wiertz, L. Lauss, C. Cavalieri, A. Blok, B. Ludwig, H. A. Heering, A. Merli, G. L. Rossi, M. Ubbink, "Amicyanin Transfers Electrons from Methylamine Dehydrogenase to Cytochrome c-551i via a Ping-Pong Mechanism, not a Ternary Complex," *Journal of the American Chemical Society* **132**, 14537 (2010).

[237] Z. Zhu, L. H. Jones, M. E. Graichen, V. L. Davidson, "Molecular Basis for Complex Formation between Methylamine Dehydrogenase and Amicyanin Revealed by Inverse Mutagenesis of an Interprotein Salt Bridge," *Biochemistry* **39**, 8830 (2000).

[238] A. Merli, D. E. Brodersen, B. Morini, Z. Chen, R. C. E. Durley, F. S. Mathews, V. L. Davidson, G. L. Rossi, "Enzymatic and Electron Transfer Activities in Crystalline Protein Complexes," *The Journal of Biological Chemistry* **271**, 9177 (1996).

[239] D. Ferrari, M. D. Valentin, D. Carbonera, A. Merli, Z. wei Chen, F. S. Mathews, V. L. Davidson, G. L. Rossi, "Electron transfer in crystals of the binary and ternary complexes of methylamine dehydrogenase with amicyanin and cytochrome *c*551i as detected by EPR spectroscopy," *Journal of Biological Inorganic Chemistry* **9**, 231 (2004).

[240] M. Husain, V. L. Davidson, "An Inducible Periplasmic Blue Copper Protein from Paracoccus denitrificans," *The Journal of Biological Chemistry* **260**, 14626 (1985).

[241] M. Husain, V. L. Davidson, "Characterization of Two Inducible Periplasmic c-Type Cytochromes from Paracoccus denitrificans," *The Journal of Biological Chemistry* **261**, 8577 (1986).

[242] H. B. Brooks, V. L. Davidson, "A method for extracting rate constants from initial rates of stopped-flow kinetic data: application to a physiological electron-transfer reaction," *Biochemical Journal* **294**, 211 (1993).

[243] G. R. Bishop, V. L. Davidson, "Electron Transfer from the Aminosemiquinone Reaction Intermediate of Methylamine Dehydrogenase to Amicyanin," *Biochemistry* **37**, 11026 (1998).

[244] V. L. Davidson, L. H. Jones, Z. Zhu, "Site-Directed Mutagenesis of Phe 97 to Glu in Amicyanin Alters the Electronic Coupling for Interprotein Electron Transfer from Quinol Methylamine Dehydrogenase," *Biochemistry* **37**, 7371 (1998).

[245] D. Sun, Z. wei Chen, F. S. Mathews, V. L. Davidson, "Mutation of αPhe55 of Methylamine Dehydrogenase Alters the Reorganization Energy and Electronic Coupling for Its Electron Transfer Reaction with Amicyanin," *Biochemistry* **41**, 13926 (2002).

[246] H. B. Brooks, V. L. Davidson, "Free Energy Dependence of the Electron Transfer Reaction between Methylamine Dehydrogenase and Amicyanin," *Journal of the American Chemical Society* **116**, 11201 (1994).

[247] G. R. Bishop, V. L. Davidson, "Catalytic Role of Monovalent Cations in the Mechanism of Proton Transfer Which Gates an Interprotein Electron Transfer Reaction," *Biochemistry* **36**, 13586 (1997).

[248] I. Rips, J. Klafter, J. Jortner, "Microscopic Solvation Dynamics and Solvent-Controlled Electron Transfer," *Journal of Physical Chemistry* **94**, 8557 (1990).

[249] Z. Zhu, L. M. Cunane, Z. wei Chen, R. C. E. Durley, F. S. Mathews, V. L. Davidson, "Molecular Basis for Interprotein Complex-Dependent Effects on the Redox Properties of Amicyanin," *Biochemistry* **37**, 17128 (1998).

[250] K. A. Gray, D. B. Knaff, M. Husain, V. L. Davidson, "Measurement of the oxidation-reduction potentials of amicyanin and c-type cytochromes from *Paracoccus denitrificans*," *FEBS Letters* **207**, 239 (1986).

[251] K. A. Gray, V. L. Davidson, D. B. Knaff, "Complex Formation between Methylamine Dehydrogenase and Amicyanin from *Paracoccus denitrificans*," *The Journal of Biological Chemistry* **263**, 13987 (1988).

[252] Research Collaboratory for Structural Informatics, Protein Data Bank entry 2GC4, http://www.rcsb.org/pdb/explore/explore.do?structureId=2GC4.

[253] http://www.charmm.org/documentation/c32b2/hbuild.html.

[254] J.-P. Ryckaert, G. Ciccotti, H. J. C. Berendsen, "Numerical integration of the cartesian equations of motion of a system with constraints: molecular dynamics of n-alkanes," *Journal of Computational Physics* **23**, 327341 (1977).

[255] W. L. Jorgensen, J. Chandrasekhar, J. D. Madura, R. W. Impey, M. L. Klein, "Comparison of simple potential functions for simulating liquid water," *The Journal of Chemical Physics* **79**, 926 (1983).

[256] A. D. M. Junior, M. Feig, C. L. B. III, "Extending the Treatment of Backbone Energetics in Protein Force Fields: Limitations of Gas-Phase QuantumMechanics in Reproducing Protein ConformationalDistributions in Molecular Dynamics Simulations," *Journal of Computational Chemistry* **2004**, 1400 (2004).

[257] K. Lindorff-Larsen, P. Maragakis, S. Piana, M. P. Eastwood, R. O. Dror, D. E. Shaw, "Systematic Validation of Protein Force Fields against Experimental Data," *PLoS One* **7**, e32131 (2012).

[258] P. Coomba, R. Remenyi, "A New Molecular Mechanics Force Field for the Oxidized Form of Blue Copper Proteins," *Journal of Computational Chemistry* **23**, 697 (2002).

[259] R. J. Loncharich, B. R. Brooks, R. W. Pastor, "Langevin Dynamics of Peptides: The Frictional Dependence of Isomerization Rates of N-Acetylalanyl-N'-Methylamide," *Biopolymers* **32**, 523 (1992).

[260] M. G. Paterlini, D. M. Ferguson, "Constant temperature simulations using the Langevin equation with velocity Verlet integration," *Chemical Physics* **236**, 243 (1998).

[261] G. Schaftenaar, J. Noordik, "Molden: a pre- and post-processing program for molecular and electronic structures," *Journal of Computer-Aided Molecular Design* **14**, 123 (2000).

[262] P. Gregory, *Bayesian Logical Data Analysis for the Physical Sciences*, Cambridge University Press, Cambridge (2005).

[263] M. P. Allen, D. J. Tildesley, *Computer Simulation of Liquids*, Oxford University Press, Oxford (1987).

[264] J. C. Phillips, R. Braun, W. Wang, J. Gumbart, E. Tajkhorshid, E. Villa, C. Chipot, R. D. Skeel, L. Kale, K. Schulten, "Scalable molecular dynamics with NAMD," *Journal of Computational Chemistry* **26**, 1781 (2005).

[265] E. A. Koopman, C. P. Lowe, "Advantages of a Lowe-Andersen thermostat in molecular dynamics simulations," *The Journal of Chemical Physics* **124**, 204103 (2006).

[266] Ehsan Zahedinejad, private communication.

[267] J. v. Vojtěch Klusáka, Petr Dobešb, J. Vondrášek, "How to fragment a polypeptide? An ab initio computational study of pair interactions between amino acids and ligand-amino acids in proteins," *Collection of Czechoslovak Communications* **76**, 605 (2011).

[268] A. Kurakin, "The self-organizing fractal theory as a universal discovery method: the phenomenon of life," *Theoretical Biology and Medical Modelling* **8**, 4 (2011).

[269] A. Heck, P. B. Woiczikowski, T. Kubař, B. Giese, M. Elstner, T. B. Steinbrecher, "Charge Transfer in Model Peptides: Obtaining Marcus Parameters from Molecular Simulation," *Journal of Physical Chemistry B* **116**, 2284 (2012).

[270] I. A. Balabin, X. Hu, D. N. Beratan, "Exploring biological electron transfer pathway dynamics with the *Pathways* Plugin for VMD," *Journal of Computational Chemistry* **33**, 906 (2012).

[271] E. E. Hammi, C. Houée-Lévin, B. L. Jan Řezáč b, I. Demachy, L. Baciou, A. de la Lande, "New insights into the mechanism of electron transfer within flavohemoglobins: tunnelling pathways, packing density, thermodynamic and kinetic analyses," *Physical Chemistry Chemical Physics* **14**, 13872 (2012).

[272] D. Mayweather, K. Danyal, D. R. Dean, L. C. Seefeldt, B. M. Hoffman, "Temperature Invariance of the Nitrogenase Electron Transfer Mechanism," *Biochemistry* **51**, 8391 (2012).

[273] J. Řezáč, B. Lévy, I. Demachy, A. de la Lande, "Robust and Efficient Constrained DFT Molecular Dynamics Approach for Biochemical Modeling," *Journal of Chemical Theory and Computation* **8**, 418 (2012).

[274] T. Kawatsu, "Review pathway analysis for peptide-mediated electronic coupling in the super-exchange mechanism of ET and EET," *Peptide Science* **100**, 100 (2012).

[275] D. N. Ferreiroa, L. Boechia, D. A. Estrina, M. A. Martí, "The key role of water in the dioxygenase function of *Escherichia coli* flavohemoglobin," *Journal of Inorganic Biochemistry* **119**, 75 (2013).

[276] A. D. Wilkins, E. Venner, D. C. Marciano, S. Erdin, B. Atri, R. C. Lua, O. Lichtarge, "Accounting for Epistatic Interactions Improves the Functional Analysis of Protein Structures," *Bioinformatics* **29**, 2714 (2013).

[277] T. Miura, "Supramolecular Control of the Spin-Dependent Dynamics of Long-Lived Charge-Separated States at the Micellar Interface As Studied by Magnetic Field Effect," *Journal of Physical Chemistry B* **117**, 6443 (2013).

[278] C. Narth, N. Gillet, B. Lévy, I. Demachy, A. de la Lande, "Investigation of the molecular mechanisms of electronic decoherence within a quinone cofactor," *Canadian Journal of Chemistry* **91**, 628 (2013).

[279] F. Cailliez, P. Müller, M. Gallois, A. de la Lande, "ATP Binding and Aspartate Protonation Enhance Photoinduced Electron Transfer in Plant Cryptochrome," *Journal of the American Chemical Society* **136**, 12974 (2014).

[280] X. Chen, G. Ma, W. Sun, H. Dai, D. Xiao, Y. Zhang, X. Qin, Y. Liu, Y. Bu, "Water Promoting Electron Hole Transport between Tyrosine and Cysteine in Proteins via a Special Mechanism: Double Proton Coupled Electron Transfer," *Journal of the American Chemical Society* **136**, 4515 (2014).

[281] J. Pilmé, E. Luppi, J. Bergès, C. Houée-Lévin, A. de la Lande, "Topological analyses of time-dependent electronic structures: application to electron-transfers in methionine enkephalin," *Journal of Molecular Modeling* **20**, 2368 (2014).

[282] M. McLuhan, *Understanding Media: The Extensions of Man*, McGraw-Hill Book Company, New York (1966).

[283] S. Strickland, G. Palmer, V. Massey, "Determination of Dissociation Constants and Specific Rate Constants of Enzyme-Substrate (or Protein-Ligand) Interactions from Rapid Reaction Kinetic Data," *The Journal of Biological Chemistry* **250**, 4048 (1975).

[284] A. Warshel, P. K. Sharma, M. Kato, Y. Xiang, H. Lie, M. H. M. Olsson, "Electrostatic Basis for Enzyme Catalysis," *Chemical Reviews* **106**, 3210 (2006).

[285] J.-K. Hwang, A. Warshel, "How Important Are Quantum Mechanical Nuclear Motions in Enzyme Catalysis?" *Journal of the American Chemical Society* **118**, 11745 (1996).

Appendix

Published Manuscripts

Chapters 4, 5, 6, and 8 of this Thesis are based on my scientific contributions to publications in refereed journals, with elaborations for clarity. These respective four articles are collected here with written permission from the publishers. They are ordered as follows:

[2] Nathan S. Babcock, René Stock, Mark G. Raizen, and Barry C. Sanders, "Entangling identical bosons in optical tweezers via exchange interaction," *Canadian Journal of Physics* **86**, 549-555 (2008).

[3] René Stock, Nathan S. Babcock, Mark G. Raizen, and Barry C. Sanders, "Entanglement of group-II-like atoms with fast measurement for quantum information processing," *Physical Review A* **78**, 022301 (2008).

[4] Nathan Wiebe and Nathan S. Babcock, "Improved error-scaling for adiabatic quantum evolutions," *New Journal of Physics* **14**, 013024 (2012).

[5] Aurélien de la Lande, Nathan S. Babcock, Jan Řezáč, Barry C. Sanders, and Dennis R. Salahub, "Surface residues dynamically organize water bridges to enhance electron transfer between proteins," *Proceedings of the National Academy of Science* **107**, 11799-11804 (2010).

Copyright Permissions

Written statements of permission to reuse and reprint materials are given by the respective publishers on their world-wide websites as follows:

Ref. [2]: Canadian Journal of Physics / NRC Research Press

"Authors may reuse all or part of their manuscript in other works created by them for non-commercial purposes, provided the original publication in an NRC Research Press journal is acknowledged through a note or citation."

http://www.nrcresearchpress.com/page/authors/information/rights

Ref. [3]: Physical Review A / APS Physics

"Yes, the author has the right to use the article or a portion of the article in a thesis or dissertation without requesting permission from APS, provided the bibliographic citation and the APS copyright credit line are given on the appropriate pages."

https://journals.aps.org/copyrightFAQ.html#thesis

Ref. [4]: New Journal of Physics / IOP Publishing

"Authors, their institutions and third parties all have the same rights to reuse articles published in New Journal of Physics in accordance with the Creative Commons Attribution 3.0 Unported (CC-BY) license. This allows the articles to be shared, adapted and made commercial use of subject to appropriate attribution."

http://iopscience.iop.org/1367-2630/page/NJP%20copyright%20statement

Ref. [5]: Proceedings of the National Academy of Sciences of the USA

"As a PNAS author, you and your employing institution or company retain extensive rights for use of your materials and intellectual property. You retain these rights and permissions without having to obtain explicit permission from PNAS, provided that you cite the original source. . . "

http://www.pnas.org/site/aboutpnas/authorfaq.xhtml

Entangling identical bosons in optical tweezers via exchange interaction

Nathan S. Babcock, René Stock, Mark G. Raizen, and Barry C. Sanders

Abstract: We first devise a scheme to perform a universal entangling gate via controlled collisions between pairs of atomic qubits trapped with optical tweezers. Second, we present a modification to this scheme to allow the preparation of atomic Bell pairs via selective excitation, suitable for quantum information processing applications that do not require universality. Both these schemes are enabled by the inherent symmetries of identical composite particles, as originally proposed by Hayes *et al.* Our scheme provides a technique for producing weighted graph states, entangled resources for quantum communication, and a promising approach to performing a "loophole free" Bell test in a single laboratory.

Résumé :

[Traduit par la rédaction]

1. Introduction

Entanglement plays an indispensable role in many quantum information processing tasks, such as long-distance quantum communication [1], teleportation-based quantum computation [2, 3], and one-way quantum computation [4]. While great progress has been made entangling arrays of neutral atoms in optical lattices *en masse* [5], the current approach to generating such massive entangled states (via cold collisions) necessitates state-dependent traps [6]. This state-dependency results in increased noise sensitivity and decoherence of atomic qubits [5]. Other proposed approaches for entangling neutral atoms feature encodings in vibrational rather than internal electronic states of atoms [7, 8], but are subject to similar dephasing of qubits. Approaches based on atomic interactions other than ground state collisions have been suggested [9, 10], but none have been successfully implemented and atomic collisions still hold the most promise. Thus, there is a need for collisional quantum gates that allow more flexible encodings in robust electronic states—such as the clock states of Rb, Cs, or Group II atoms—that are held in state-insensitive traps to minimize decoherence.

In this work, we examine schemes to entangle pairs of bosonic atoms, analogous to the recently proposed fermionic spin-exchange gate [11]. Gates based on this exchange interaction offer a natural resistance to errors and more flexibility due to inherent symmetrization conditions. Furthermore, this

N. S. Babcock. Institute for Quantum Information Science, University of Calgary, Alberta, Canada.
e-mail: nbabcock@qis.ucalgary.ca
R. Stock. Department of Physics, University of Toronto, Toronto, Ontario, Canada.
e-mail: restock@physics.utoronto.ca
M. G. Raizen. Center for Nonlinear Dynamics and Department of Physics, University of Texas, Austin, Texas, U.S.A.
B. C. Sanders. Institute for Quantum Information Science, University of Calgary, Alberta, Canada.

 DOI: 10.1139/Z*xx-xxx*

exchange interaction allows the design of entangling operations for atoms with state-independent (e.g., Rb [5]) or partially unknown interaction strengths (e.g., Yb [12] or Sr [13]). The underlying exchange interaction for these gates has recently been experimentally demonstrated using bosonic Rb atoms in a double-well optical lattice [14]. However, a verifiable entangling gate between an individual pair of trapped neutral atoms has not yet been demonstrated. Here, we provide a detailed analysis of these operations as they may be carried out using a pair of individually controlled atomic qubits trapped via optical tweezers.

Our approach builds on disparate proposals and experiments for preparing individual atoms from a Bose-Einstein condensate [15–17], encoding qubits into long-lived electronic states, coherently manipulating and transporting atoms using optical tweezers [18,19], and performing two-qubit operations on pairs of atoms via collisional interactions [11, 14]. The combination of these elements allow for the design of a tunable two-qubit gate, which can create an arbitrary degree of entanglement between a pair of atoms. We also examine a scheme that exploits symmetrization rules to produce Bell pairs via selective excitation.

These entangling schemes may be realized using qubits stored in the electronic states of a pair of atoms trapped with moveable optical tweezers. Trapping at a "magic wavelength" makes the light shift potential state-independent. Encoding in atomic clock states—which are insensitive to fluctuations in the trapping field—avoids dephasing and ensures qubit coherence during the transport process. Unlike the case of a state-dependent optical lattice in which it is trivial to separate the atoms after interaction, we have state-independent potentials in which the system's dynamics determine the likelihood of the atoms being separated into opposite wells. Under adiabatic conditions, atom separation is guaranteed. We consider only the 1-D case for simplicity. Multidimensional effects such as trap-induced resonances cannot be captured by the 1-D delta-potential employed here [20] but could potentially be used to enhance the atomic interaction further.

2. Hamiltonian for identical particles in separated tweezers

The Hamiltonian for two atoms with internal structure in a pair of optical dipole traps (a.k.a., "tweezers") is given by,

$$H = \sum_{i,j=0,1} \left\{ \frac{p_{\rm a}^2}{2m} + V(x_{\rm a}, d) + \frac{p_{\rm b}^2}{2m} + V(x_{\rm b}, d) + 2a_{ij}\hbar\omega_\perp \delta(x_{\rm a} - x_{\rm b}) \right\} \otimes |ij\rangle\langle ij|, \tag{1}$$

where $x_{\rm a}$ and $x_{\rm b}$ are the positions of atoms a and b respectively, $p_{\rm a}$ and $p_{\rm b}$ are similarly the momenta, a_{ij} is the state-dependent scattering length that depends on internal atomic states $|i\rangle_{\rm a}$ and $|j\rangle_{\rm b}$ (using $|ij\rangle \equiv |i\rangle_{\rm a} \otimes |j\rangle_{\rm b}$), $\omega_\perp$ is the harmonic oscillation frequency due to transverse confinement [21], and d is the time-dependent centre-to-centre distance between wells. For Yb, Sr, and alkali atoms, one can usually choose a particular trap-laser wavelength (the "magic wavelength") so that the light shift potential becomes state-independent and each atom sees a double-well potential:

$$V(x, d) = -V_o e^{-(x-\frac{d}{2})^2/2\sigma^2} - V_o e^{-(x+\frac{d}{2})^2/2\sigma^2}. \tag{2}$$

Here, $V_o > 0$ is the depth of each Gaussian well and σ^2 is the variance.

The first three vibrational eigenstates of a single particle in this double-well potential are shown in Fig. 1 for varying d. In general, the single-particle eigenstates are $\{|\psi^A(d)\rangle, |\psi^B(d)\rangle, |\psi^C(d)\rangle, \ldots\}$ and d-dependence is assumed implicit (e.g., $|\psi^A\rangle \equiv |\psi^A(d)\rangle$) for notational simplicity. Note that as d increases, $|\psi^A\rangle$ and $|\psi^B\rangle$ become spatially delocalized and energetically degenerate. Thus, when $|d| \gg \sigma$ we can write $|\psi^L\rangle \equiv (|\psi^A\rangle - |\psi^B\rangle)/\sqrt{2}$ to represent a single particle localized in the ground state of the left well, and similarly $|\psi^R\rangle \equiv (|\psi^A\rangle + |\psi^B\rangle)/\sqrt{2}$ for the right well.

When a second particle is added to the double-well potential, the interaction term in the Hamiltonian may be treated as a perturbation. Accordingly, the new two-particle eigenstates may be written as

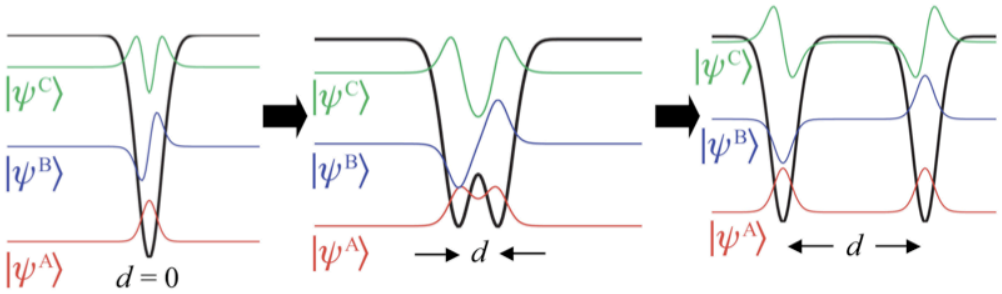

Fig. 1. The first three eigenstates of a single particle in a double-well potential for different well separations d.

a sum of perturbed tensor products of one-particle states. We will use a tilde to denote the perturbation to the terms composing the new symmetrized eigenstates. For a repulsive interaction between atoms ($a_{ij} > 0$), the first six two-particle eigenstates are (see Fig. 2a),

$$\begin{array}{ccc} d = 0 & & d \gg \sigma \\ |\widetilde{\psi^B\psi^B}\rangle & \longleftrightarrow & \frac{1}{2}(|\widetilde{\psi^A\psi^C}\rangle + |\widetilde{\psi^C\psi^A}\rangle - |\widetilde{\psi^B\psi^D}\rangle - |\widetilde{\psi^D\psi^B}\rangle) \quad (3a) \\ \frac{1}{\sqrt{2}}(|\psi^A\psi^C\rangle - |\psi^C\psi^A\rangle) & \longleftrightarrow & \frac{1}{\sqrt{2}}(|\psi^A\psi^C\rangle - |\psi^C\psi^A\rangle) \quad (3b) \\ \frac{1}{\sqrt{2}}(|\widetilde{\psi^A\psi^C}\rangle + |\widetilde{\psi^C\psi^A}\rangle) & \longleftrightarrow & \frac{1}{\sqrt{2}}(|\widetilde{\psi^L\psi^L}\rangle + |\widetilde{\psi^R\psi^R}\rangle) \quad (3c) \\ \frac{1}{\sqrt{2}}(|\widetilde{\psi^A\psi^B}\rangle + |\widetilde{\psi^B\psi^A}\rangle) & \longleftrightarrow & \frac{1}{\sqrt{2}}(|\widetilde{\psi^L\psi^L}\rangle - |\widetilde{\psi^R\psi^R}\rangle) \quad (3d) \\ \frac{1}{\sqrt{2}}(|\psi^A\psi^B\rangle - |\psi^B\psi^A\rangle) & \longleftrightarrow & \frac{1}{\sqrt{2}}(|\psi^L\psi^R\rangle - |\psi^R\psi^L\rangle) \quad (3e) \\ |\widetilde{\psi^A\psi^A}\rangle & \longleftrightarrow & \frac{1}{\sqrt{2}}(|\widetilde{\psi^L\psi^R}\rangle + |\widetilde{\psi^R\psi^L}\rangle). \quad (3f) \end{array}$$

States that are antisymmetric under exchange are not affected by the interaction at any separation and the tildes have been intentionally omitted from these states. States with atoms in opposite traps (e.g., 3a, 3f) are obviously not affected by the interaction in the limit $d \to \infty$. Note that there is the usual on-site interaction penalty for putting two atoms in same trap, resulting in an energy splitting at $d \gg \sigma$ between states having atoms in opposite traps (3e, 3f) and those having atoms in the same trap (3c, 3d), as shown in Fig. 2a.

In case of attractive interaction ($a_{ij} < 0$), the eigenstates are (see Fig. 2b),

$$\begin{array}{ccc} d = 0 & & d \gg \sigma \\ \frac{1}{\sqrt{2}}(|\psi^A\psi^C\rangle - |\psi^C\psi^A\rangle) & \longleftrightarrow & \frac{1}{\sqrt{2}}(|\psi^A\psi^C\rangle - |\psi^C\psi^A\rangle) \quad (4a) \\ |\widetilde{\psi^B\psi^B}\rangle & \longleftrightarrow & \frac{1}{2}(|\widetilde{\psi^A\psi^C}\rangle + |\widetilde{\psi^C\psi^A}\rangle + |\widetilde{\psi^B\psi^D}\rangle + |\widetilde{\psi^D\psi^B}\rangle) \quad (4b) \\ \frac{1}{\sqrt{2}}(|\widetilde{\psi^A\psi^C}\rangle + |\widetilde{\psi^C\psi^A}\rangle) & \longleftrightarrow & \frac{1}{\sqrt{2}}(|\widetilde{\psi^L\psi^R}\rangle + |\widetilde{\psi^R\psi^L}\rangle) \quad (4c) \\ \frac{1}{\sqrt{2}}(|\psi^A\psi^B\rangle - |\psi^B\psi^A\rangle) & \longleftrightarrow & \frac{1}{\sqrt{2}}(|\psi^L\psi^R\rangle - |\psi^R\psi^L\rangle) \quad (4d) \\ \frac{1}{\sqrt{2}}(|\widetilde{\psi^A\psi^B}\rangle + |\widetilde{\psi^B\psi^A}\rangle) & \longleftrightarrow & \frac{1}{\sqrt{2}}(|\widetilde{\psi^L\psi^L}\rangle - |\widetilde{\psi^R\psi^R}\rangle) \quad (4e) \\ |\widetilde{\psi^A\psi^A}\rangle & \longleftrightarrow & \frac{1}{\sqrt{2}}(|\widetilde{\psi^L\psi^L}\rangle + |\widetilde{\psi^R\psi^R}\rangle). \quad (4f) \end{array}$$

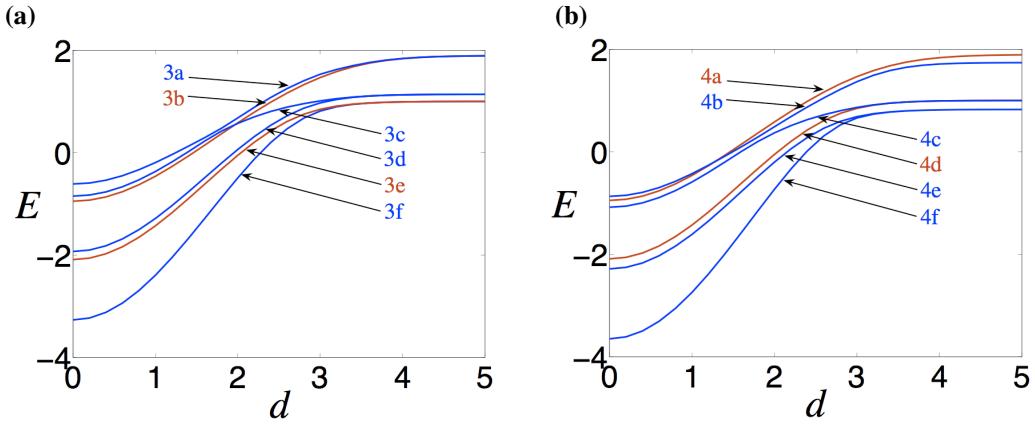

Fig. 2. Adiabatic energy levels as a function of well separation d for (a) $a_{ij} = 0.1\sigma$ and (b) $a_{ij} = -0.1\sigma$. Well separation is in units of σ. Energies are in units of $\hbar\omega_o$, where ω_o is the harmonic oscillation frequency of one atom in the ground state of a single well. Symmetric vibrational eigenstates are shown in blue, antisymmetric in red. Eigenstates for (a) and (b) are given by Eqs. (3) and (4), respectively. Notice that crossings between oppositely symmetrized states are unavoided because the Hamiltonian is symmetric.

The order of states in (4) is different from (3), since states with atoms in the same trap now posses a lower energy due to the attractive interaction.

Until this point we have neglected the internal structure of the particles (i.e., the qubits). The eigenstates of the full Hamiltonian (1) are tensor products of the vibrational wavefunctions and the symmetrized qubit states. For bosonic atoms, permissible eigenstates are tensor products of external (i.e., vibrational) and internal (i.e., qubit) states of the same symmetry. Thus, antisymmetrized spatial wavefunctions are permitted for a pair of composite bosons, so long as their internal structure is also antisymmetric.

We solve the Hamitonian (1) numerically for individual internal states. Examples of two-atom energy spectra as a function of well separation are plotted in Fig. 2 for positive and negative interaction strengths a_{ij}. We define $E^n_{|\varphi\rangle}(d)$ to be the energy of the n^{th} two-atom vibrational eigenstate with two-qubit internal state $|\varphi\rangle$ at well separation d. For example, the energy of $|\widetilde{\psi^A\psi^A}\rangle \otimes |11\rangle$ is $E^0_{|11\rangle}(d)$. As we have already discussed, not all combinations of n and $|\varphi\rangle$ are possible. For example, $E^0_{|\Psi^-\rangle}(d)$ is forbidden for identical bosons. This reduction of the size of the Hilbert space makes it possible to perform quantum gates adiabatically without losing coherence due to energetic degeneracies. Furthermore, the Hamiltonian's inherent particle and parity symmetries lead to selection rules which further enhance the fidelity of two-qubit operations.

3. Universal entangling gate

As shown by Hayes *et al.* [11], it is possible to exploit these symmetries in order to produce a two-qubit entangling operation. We begin with a pair of identical atoms localized to opposite wells of the double-well Hamiltonian (1) in the far separated case ($d \gg \sigma$). We prepare the qubit on the left in the state $|\varphi^\alpha\rangle \equiv (\alpha|0\rangle + \beta|1\rangle)$ and the qubit on the right in the state $|\varphi^\mu\rangle \equiv (\mu|0\rangle + \nu|1\rangle)$. The initial wavefunction $|\psi_{\text{i}}\rangle$, written as a tensor product of external and internal states, is then,

$$|\psi_{\text{i}}\rangle = \tfrac{1}{\sqrt{2}}(|\widetilde{\psi^L\psi^R}\rangle \otimes |\varphi^\alpha\varphi^\mu\rangle + |\widetilde{\psi^R\psi^L}\rangle \otimes |\varphi^\mu\varphi^\alpha\rangle). \tag{5}$$

Using $|\Psi^{\pm}\rangle = \frac{1}{\sqrt{2}}(|01\rangle \pm |10\rangle)$, we rewrite equation (5) to make the symmetrization explicit:

$$|\psi_{\rm i}\rangle = (|\psi^L\psi^R\rangle - |\psi^R\psi^L\rangle) \otimes (\tfrac{\alpha\nu-\beta\mu}{2}\,|\Psi^-\rangle) + (|\widetilde{\psi^L\psi^R}\rangle + |\widetilde{\psi^R\psi^L}\rangle) \otimes (\tfrac{\alpha\mu}{\sqrt{2}}|00\rangle + \tfrac{\alpha\nu+\beta\mu}{2}|\Psi^+\rangle + \tfrac{\beta\nu}{\sqrt{2}}|11\rangle). \tag{6}$$

As the wells are brought together and separated adiabatically, the external states evolve according to Fig. 2. That is, each vibrational eigenstate at $d \gg \sigma$ evolves continuously into its respective eigenstate at $d = 0$. As d decreases, the degeneracies between symmetric and antisymmetric eigenstates are lifted, resulting in a dynamic phase difference between $\frac{1}{\sqrt{2}}(|\widetilde{\psi^L\psi^R}\rangle + |\widetilde{\psi^R\psi^L}\rangle)$ and $\frac{1}{\sqrt{2}}(|\psi^L\psi^R\rangle - |\psi^R\psi^L\rangle)$, corresponding to the difference in respective energy curves (see energy curves 3e and 3f in Fig. 2a, or 4c and 4d in Fig. 2b). Furthermore, degeneracies between the even two-qubit states $\{|00\rangle, |11\rangle, |\Psi^+\rangle\}$ are removed if the interaction strengths a_{ij} differ, which is usually the case. This state-dependent interaction results in additional phase differences between qubit states of the same symmetry [22]. Thus, each joint internal and external state acquires a unique phase, and the final state $|\psi_{\rm f}\rangle$ upon re-separating the wells is,

$$|\psi_{\rm f}\rangle = (|\psi^L\psi^R\rangle - |\psi^R\psi^L\rangle) \otimes (\tfrac{\alpha\nu-\beta\mu}{2}e^{-i\phi_-}|\Psi^-\rangle) + (|\widetilde{\psi^L\psi^R}\rangle + |\widetilde{\psi^R\psi^L}\rangle) \otimes (\tfrac{\alpha\mu}{\sqrt{2}}e^{-i\phi_{00}}|00\rangle + \tfrac{\alpha\nu+\beta\mu}{2}e^{-i\phi_+}|\Psi^+\rangle + \tfrac{\beta\nu}{\sqrt{2}}e^{-i\phi_{11}}\,|11\rangle)\,. \tag{7}$$

For positive scattering lengths, the phases are given by,

$$\phi_{jj} \equiv \frac{1}{\hbar}\int_{t_{\rm i}}^{t_{\rm f}} E^0_{|jj\rangle}\,(d(t))\;{\rm d}t \quad \text{and} \quad \phi_{\pm} \equiv \frac{1}{\hbar}\int_{t_{\rm i}}^{t_{\rm f}} E^{\frac{1}{2}\mp\frac{1}{2}}_{|\Psi^{\pm}\rangle}\,(d(t))\;{\rm d}t. \tag{8}$$

Equation (7) is also valid for negative scattering lengths, although different phases will be acquired since $\frac{1}{\sqrt{2}}(|\widetilde{\psi^L\psi^R}\rangle + |\widetilde{\psi^R\psi^L}\rangle)$ is not the vibrational ground state when $a_{ij} < 0$.

Clearly, this evolution can be thought of as the identity acting on the vibrational subsystem tensored with a unitary U acting on the qubit subsystem. Thus, we can discard the vibrational terms and examine the unitary evolution of the qubit subsystem by itself. Using matrix notation,

$$|0\rangle = \begin{pmatrix}1\\0\end{pmatrix} \qquad \text{and} \qquad |1\rangle = \begin{pmatrix}0\\1\end{pmatrix}, \tag{9}$$

we can write U as,

$$\begin{aligned} U &= \frac{1}{2}\begin{pmatrix} 2e^{-i\phi_{00}} & 0 & 0 & 0 \\ 0 & e^{-i\phi_+}+e^{-i\phi_-} & e^{-i\phi_+}-e^{-i\phi_-} & 0 \\ 0 & e^{-i\phi_+}-e^{-i\phi_-} & e^{-i\phi_+}+e^{-i\phi_-} & 0 \\ 0 & 0 & 0 & 2e^{-i\phi_{11}} \end{pmatrix} \\ &= T\begin{pmatrix} e^{-i\phi_{00}} & 0 & 0 & 0 \\ 0 & e^{-i\phi_+} & 0 & 0 \\ 0 & 0 & e^{-i\phi_-} & 0 \\ 0 & 0 & 0 & e^{-i\phi_{11}} \end{pmatrix} T^\dagger, \qquad \text{where} \qquad T = \begin{pmatrix} 1 & 0 & 0 & 0 \\ 0 & \frac{1}{\sqrt{2}} & \frac{1}{\sqrt{2}} & 0 \\ 0 & \frac{1}{\sqrt{2}} & -\frac{1}{\sqrt{2}} & 0 \\ 0 & 0 & 0 & 1 \end{pmatrix}. \end{aligned} \tag{10}$$

This entangling operation is diagonal in the partial Bell basis $\{|00\rangle, |\Psi^{\pm}\rangle, |11\rangle\}$. As noted in [11], even if the interaction strengths are state-independent, the singlet state $|\Psi^-\rangle$ acquires a phase different from the triplet states (except in the limit as $a_{ij} \to \pm\infty$, when the gate is no longer feasible). State-dependent traps or atomic interactions generally result in state-dependent interactions with the

environment as well, making the qubits more sensitive to noise. Avoiding this state-dependence leads to the inherent robustness observed in initial experiments [14], as compared to earlier experiments wherein gate fidelities were severely limited because of dephasing due to state-dependent traps [5]. Furthermore, this gate works for a wide range of positive scattering lengths, as we show elsewhere [22]. This is especially important for experiments employing atomic species with unknown or approximately known scattering lengths (e.g., Yb or Sr).

A "controlled phase" gate (i.e., $e^{-i\pi|11\rangle\langle 11|}$) in the computational basis can be obtained by combining single qubit phase gates $S(\theta) = e^{-i\theta|1\rangle\langle 1|}$ with a pair of U gates:

$$G = U\left(S(\pi)\otimes S(0)\right)U = \begin{pmatrix} e^{-2i\phi_{00}} & 0 & 0 & 0 \\ 0 & e^{-i(\phi_+ + \phi_-)} & 0 & 0 \\ 0 & 0 & -e^{-i(\phi_+ + \phi_-)} & 0 \\ 0 & 0 & 0 & -e^{-2i\phi_{11}} \end{pmatrix}. \tag{11}$$

G is locally equivalent to the "tunable controlled-phase" gate $e^{-i\gamma|11\rangle\langle 11|}$, subject to the constraint:

$$\phi_{00} + \phi_{11} - \phi_+ - \phi_- = \left(2n \pm \tfrac{1}{2}\right)\gamma, \quad \forall\ n \in \mathbb{Z}. \tag{12}$$

While a simple controlled-phase gate is itself a universal entangling gate, many quantum algorithms (e.g., the quantum Fourier transform) can be performed more efficiently when tunable controlled-phase gates are available. Here, the value of γ can be easily tuned, simply by adjusting the speed at which the optical tweezers are combined and separated. The inherent robustness and easy tunability of this gate make it a highly desirable one for quantum information processing.

4. Alternative entanglement preparation

For some quantum information processing applications, universal entangling gates are not necessary and an ability to prepare entangled pairs will suffice. Atomic quantum repeaters based on entanglement swapping [23] provide an example of one such application. We next examine a scheme which uses symmetrization requirements and a selective excitation to produce Bell pairs.

We begin with two bosonic atoms in the ground state of a single well, both with internal state $|0\rangle$. The energy of this state is $E^0_{|00\rangle}(0)$. It is then possible to perform a coherent transition, selectively exciting to the eigenstate with energy $E^0_{|\Psi^+\rangle}(0)$. If the interaction for atomic qubits in the state $|\Psi^+\rangle$ is significantly different than that of $|11\rangle$, one can deterministically excite only to the $|\Psi^+\rangle$ qubit eigenstate, since the state $|11\rangle$ is off resonant and the overall state must remain symmetric. An excitation to the antisymmetric state $|\Psi^-\rangle$ is not possible as long as the two atoms are in the symmetric vibrational ground state. Thus, any initial population in antisymmetric vibrational states (e.g., due to heating) must be avoided to keep the fidelity of entanglement generation high. Furthermore, the vibrational spacing and sidebands due to the interaction energy must be spectroscopically resolvable. With typical vibrational energies on the order of kHz and on-site interaction shifts of close to 100Hz (dependent on atomic species but tunable by the tightness of traps), this selective excitation process is generally slow, but nevertheless viable. The final state after separating the atoms adiabatically is,

$$|\psi_{\text{final}}\rangle = \tfrac{1}{2}\left(|\widetilde{\psi^L\psi^R}\rangle + |\widetilde{\psi^R\psi^L}\rangle\right)\otimes\left(|01\rangle + |10\rangle\right). \tag{13}$$

This operation provides a novel way of creating Bell states deterministically, but does not constitute a universal two-qubit entangling gate. It does however allow for fundamental tests of quantum mechanics and Bell inequality violations, as well as basic quantum information processing and communication tasks.

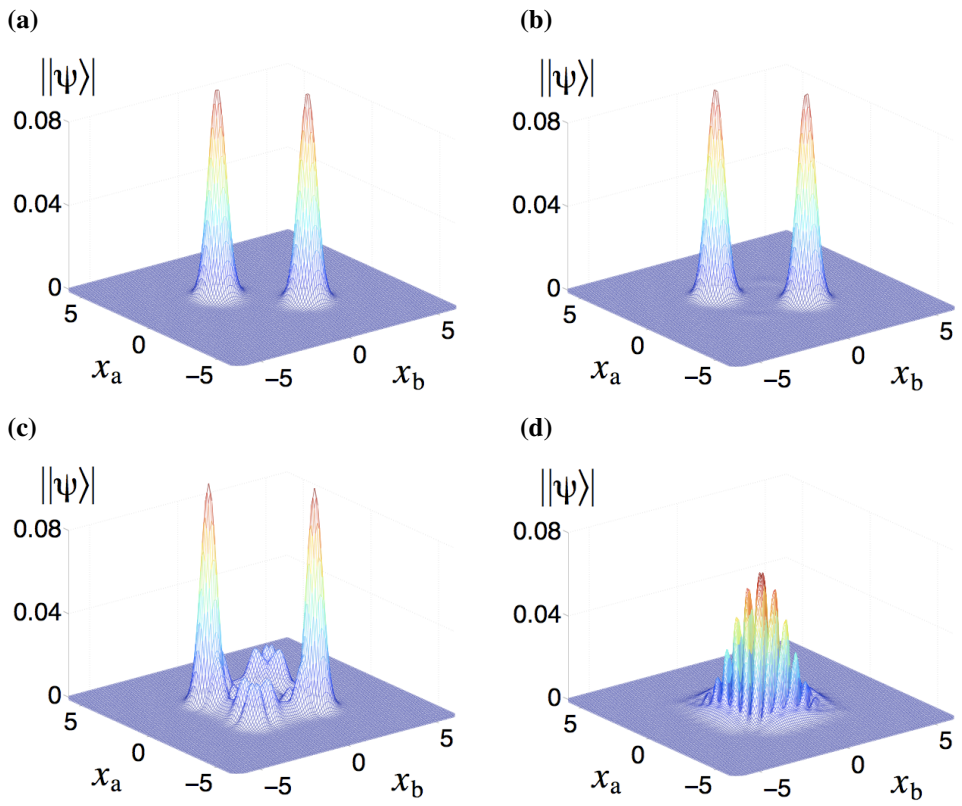

Fig. 3. Snapshots of the magnitude of the two-atom vibrational wavefunction ($||\psi\rangle| \equiv |\psi(x_a, x_b, t)\rangle|$) as a function of the position of each atom. Plot (a) shows the initial wavefunction, $|\psi_{\text{init}}\rangle = (|\psi^L\psi^R\rangle + |\psi^R\psi^L\rangle)/\sqrt{2}$. Plots (b-d) show the wavefunction after the wells have been brought together and separated. Initial conditions are the same for all figures, and only the well speed (in units of $v_o = \hbar\sigma\omega_{ab}^2/V_o$) is varied. The resulting vibrational state fidelities $f = |\langle\psi_{\text{init}}|\psi\rangle|^2$ are as follows: (b) $v \approx 0.01v_o$, $f = 0.9997$. (c) $v \approx 0.1v_o$, $f = 0.491$. (d) $v \approx v_o$, $f = 0.002$.

5. Speed constraints for adiabaticity

An approximation to the general adiabaticity criterion is given in [24]:

$$\left|\langle a|\,\frac{\partial\hat{H}}{\partial t}\,|b\rangle\right| \ll \hbar\omega_{ab}^2 \quad \forall\ |a\rangle \neq |b\rangle\,, \tag{14}$$

where $\omega_{ab} = \min(|E_b(t) - E_a(t)|\,/\hbar)$ and where $|a\rangle$ and $|b\rangle$ are time-dependent eigenstates of an arbitrary Hamiltonian. Since our specific Hamiltonian is invariant under exchanges of both symmetry and parity, transitions between vibrational states of different symmetry or parity are suppressed. Thus, in our case ω_{ab} is determined by the energy gap of the two closest states having both equal symmetry and parity. This restriction contributes significantly to the robustness of this gate. Since only the double-well potential is time-dependent, the left side of the equation reduces to $|\frac{\partial V(x,d(t))}{\partial t}|$. Assuming constant v and maximizing $|\frac{\partial V(x,d(t))}{\partial t}|$ with respect to x, we obtain the adiabaticity criterion:

$$v \ll \hbar\sigma\omega_{ab}^2/V_o. \tag{15}$$

Time-dependent numerical simulations confirm the validity of this simple criterion over a wide range of values of V_o and a_{ij} (including $a_{ij} < 0$). Plots of the two-particle wavefunction comparing adiabatic and non-adiabatic evolutions are shown in Fig. 3. Under adiabatic conditions, we recover both atoms in separate wells. Under non-adiabatic conditions both atoms may end up in the same well with non-negligible probability, resulting in an erroneous gate. However, time-dependent simulations have also shown significant revivals, with both atoms ending up in opposite wells with large probability even under non-adiabatic conditions. This suggests the very real possibility of producing a fast, coherent, non-adiabatic gate via optimal control.

6. Conclusion

In summary, we have proposed two schemes for preparing pairs of entangled atoms. We have shown it possible to construct a tunable universal entangling gate via the exchange interaction between identical bosons, promising high fidelity operation for positive (repulsive) and even negative (attractive) interaction strengths. This is of particular importance for quantum information processing applications that use novel species of atoms, such at Group II-like atoms (e.g., Yb and Sr) [22], for which the collisional interaction parameters are partially unknown. In addition, we have introduced a novel entanglement scheme allowing the creation of Bell pairs. This scheme could prove useful for quantum communication schemes and fundamental tests of quantum mechanics. The use of this entanglement operation for Group II-like atoms and its application to fundamental tests of quantum mechanics are studied in detail in other work [22].

7. Acknowledgments

We specially thank D. Hayes and I. Deutsch for insightful discussions on entangling atoms via exchange interactions. We further thank Michael Skotiniotis and Nathan Wiebe for helpful comments and discussion. This work was supported by NSERC, AIF, CIFAR, iCORE, MITACS, NSF, and The Welch Foundation.

References

1. H.-J. Briegel, W. Dür, J. I. Cirac, and P. Zoller, Phys. Rev. Lett. **81**, 5932 (1998).
2. D. Gottesman and I. L. Chuang, Nature **402**, 390 (1999).
3. E. Knill, R. Laflamme, and G. J. Milburn, Nature **409**, 46 (2001).
4. R. Raussendorf and H.-J. Briegel, Phys. Rev. Lett. **86**, 5188 (2001).
5. O. Mandel, M. Greiner, A. Widera, T. Rom, T. W. Hänsch, and I. Bloch, Nature (London) **425**, 937 (2003).
6. D. Jaksch, H.-J. Briegel, J. I. Cirac, C. W. Gardiner, and P. Zoller, Phys. Rev. Lett. **82**, 1975 (1999).
7. E. Charron, E. Tiesinga, F. Mies, and C. Williams, Phys. Rev. Lett. **88**, 077901 (2002).
8. K. Eckert, J. Mompart, X. X. Yi, J. Schliemann, D. Bruß, G. Birkl, and M. Lewenstein, Phys. Rev. A **66**, 042317 (2002).
9. G. K. Brennen, I. H. Deutsch, and C. J. Williams, Phys. Rev. A **65**, 022313 (2002).
10. D. Jaksch, J. I. Cirac, P. Zoller, S. L. Rolston, R. Côté, and M. D. Lukin, Phys. Rev. Lett. **85**, 2208 (2000).
11. D. Hayes, P. S. Julienne, and I. Deutsch, Phys. Rev. Lett. **98**, 070501 (2007).
12. M. Kitagawa, K. Enomoto, KentaroKasa, Y. Takahashi, R. Ciurylo, P. Naidon, and P. S. Julienne, arXiv:0708.0752 (2007).
13. M. Yasuda, T. Kishimoto, M. Takamoto, and H. Katori, Phys. Rev. A **73**, 011403(R) (2006).
14. M. Anderlini, P. J. Lee, B. L. Brown, J. Sebby-Strabley, W. D. Phillips, and J. V. Porto, Nature (London) **448**, 452 (2007).
15. A. M. Dudarev, M. G. Raizen, and Q. Niu, Phys. Rev. Lett. **98**, 063001 (2007).
16. C.-S. Chuu, F. Shreck, T. P. Meyrath, J. L. Hanssen, G. N. Price, and M. G. Raizen, Phys. Rev. Lett. **95**, 260403 (2005).

17. R. B. Diener, B. Wu, M. G. Raizen, and Q. Niu, Phys. Rev. Lett. **89**, 070401 (2002).
18. T. L. Gustavson, A. P. Chikkatur, A. Leanhardt, A. Grlitz, S. Gupta, D. E. Pritchard, and W. Ketterle, Phys. Rev. Lett. **88**, 020401 (2007).
19. J. Beugnon, C. Tuchendler, H. Marion, A. Gaetan, Y. Miroshnychenko, Y. R. P. Sortais, A. M. Lance, M. P. A. Jones, G. Messin, A. Browaeys, and P. Grangier, Nature Physics **3**, 696 (2007).
20. R. Stock, I. H. Deutsch, and E. L. Bolda, Phys. Rev. Lett. **91**, 183201 (2003).
21. T. Calarco, E. A. Hinds, D. Jaksch, J. Schmiedmayer, J. I. Cirac, and P. Zoller, Phys. Rev. A **61**, 022304 (2000).
22. R. Stock, N. S. Babcock, M. G. Raizen, and B. C. Sanders, arxiv:0711.0044 (2007).
23. L.-M. Duan, M. D. Lukin, J. I. Cirac, and P. Zoller, Nature **414**, 413 (2001).
24. B. H. Bransden and C. J. Jochain, *Quantum Mechanics, 2nd ed.* (Pearson Education Ltd., Dorchester, Dorset, 2000).

Entanglement of group-II-like atoms with fast measurement for quantum information processing

R. Stock,[1,2,*] N. S. Babcock,[1] M. G. Raizen,[3] and B. C. Sanders[4]

[1] *Institute for Quantum Information Science, University of Calgary, Alberta T2N 1N4, Canada*
[2] *Department of Physics, University of Toronto, Toronto, Ontario M5S 1A7, Canada*
[3] *Center for Nonlinear Dynamics and Department of Physics, University of Texas, Austin, Texas 78712, USA*
[4] *Institute for Quantum Information Science, University of Calgary, Alberta, Canada*

(Dated: January 5, 2014)

We construct a scheme for the preparation, pairwise entanglement via exchange interaction, manipulation, and measurement of individual group-II-like neutral atoms (Yb, Sr, etc.). Group-II-like atoms proffer important advantages over alkali metals, including long-lived optical-transition qubits that enable fast manipulation and measurement. Our scheme provides a promising approach for producing weighted graph states, entangled resources for quantum communication, and possible application to fundamental tests of Bell inequalities that close both detection and locality loopholes.

PACS numbers: 03.67.Mn, 34.50.-s, 32.80.Wr, 03.65.Ud

I. INTRODUCTION

Entanglement is a vital resource for most quantum information processing (QIP) tasks, including long-distance quantum communication [1], teleportation-based quantum computation [2, 3], and one-way quantum computation (1WQC) [4]. An under-appreciated but crucial aspect of QIP is the need for speed of single qubit operations, to enable applications including synchronization of quantum communication networks, measurement and feed-forward in 1WQC, and tests of local realism. For example, in 1WQC, the processor speed primarily depends on the time needed for measurement and feed-forward, whereas the entanglement operation may be slow and accomplished simultaneously before commencement of the computation. In atomic systems, single-qubit fluorescence measurements are limited to microseconds due to auxiliary state lifetimes, and in alkali metals single-qubit rotation times are hampered by the gigahertz spectroscopic separations of hyperfine states. In this work, we overcome these obstacles by encoding in long-lived optical clock transitions (e.g., $^1S_0 \leftrightarrow {}^3P_0$) of group-II-like neutral atoms, without sacrificing the advantages of other atomic schemes. Group II-like atoms such as Yb and Sr have long been considered for atomic clocks and much recent experimental and theoretical effort has been dedicated to this group of atoms [5, 6, 7, 8, 9, 10, 11, 12]. The recent cooling of Yb into a Bose-Einstein condensate (BEC) [9] and the ongoing study of interactions [12] make Yb an especially tantalizing candidate for atomic qubits. Our approach for entanglement and measurement of group-II atoms offers promising techniques for the high-speed synchronization needed for quantum communication and computing, and also for the near-term violation of a Bell inequality in a single laboratory, without any assumptions about signaling, sampling, or enhancement [13, 14, 15, 16].

Significant experimental progress has been achieved towards entangling atoms in optical lattices [17], which could lead to the creation of an initial state for 1WQC. Here we take a complementary approach, considering the entanglement of individual pairs of atoms on demand, comparable to other addressable neutral atom architectures [18]. Rather than creating a generic cluster state, we propose the creation of computation-tailored weighted graph states as a resource for 1WQC and other QIP tasks. Our technique combines efforts to prepare individual atomic qubits from a BEC [19], coherently manipulate and transport atoms [20, 21] using optical tweezers at a "magic wavelength," entangle atoms via an inherently robust exchange interaction [22, 23], rotate single qubits via a three-photon optical dipole transition [10], and perform fast (∼ns) measurements via resonantly enhanced multi-photon ionization (REMPI). A "loop-hole free" Bell inequality test imposes stringent requirements on detector separation [15] and efficiency (see, e.g. the experimental work in [16, 24]), and presents an enticing test-bed for fast measurements with applications to QIP. We study the limits of fast measurement for encoding in the optical clock states of Yb and Sr, which can be resolved spectroscopically and measured on a ∼10ns time scale, thereby admitting space-like separation over a few meters (as opposed to large spatial separations considered in [24]). We show that such Bell tests in a single laboratory should be feasible via a detailed theoretical analysis accompanied by comprehensive numerical simulations.

II. QUBIT PREPARATION AND TRANSPORT

Clock transitions in ions have been considered for effectively encoding qubits for ion trap-quantum computing due to extremely low decoherence rates [25, 26]. Simi-

*Electronic address: restock@physics.utoronto.ca

larly, in the case of neutral atoms, optical clock transitions in alkaline-earth and group-II-like atoms are appealing candidates for encoding qubits. Single atoms have been experimentally isolated [19] and transported in optical dipole traps [20, 21]. By trapping at a "magic wavelength" [7, 8], the light shift potential is made effectively state-independent, ensuring phase stability of the qubits for several seconds. For example, for the clock states of Sr, the light shift dependencies on the trap laser frequency ν differ by $d\Delta/d\nu = 2.3 \times 10^{-10}$ [7]. Therefore light shift fluctuations can be kept to less than 0.1 Hz by using a trap laser with linewidth of 100 MHz. Furthermore, the magic wavelength at 813.5 nm (easily accessible using commercial lasers) is far detuned from the excited states so that photon scattering rates are on the order of 10 s for trap light intensities of 10 kW/cm^2 [7]. This ensures a coherence time of 10 s or more for trapping and transporting atoms.

III. ENTANGLING OPERATION

We devise a universal entangling operation for bosons, analogous to the recently proposed fermionic spin-exchange gate [22]. This gate is based on the exchange interaction recently demonstrated for bosonic Rb atoms in a double-well optical lattice [23]. Because of inherent symmetrization requirements, gates based on this exchange interaction offer a natural resistance to errors and greater flexibility for encoding atoms, thereby enabling an entangling operation even for atoms with interaction strengths that are state-independent (e.g., Rb [23]) or partially unknown, as is the case for most group-II-like atoms (e.g., Yb [12]).

The entangling operation is achieved by temporarily bringing together a pair of atomic qubits via mobile optical tweezers. Unlike state-dependent optical traps wherein atoms are trivially separated into opposite wells after interaction, we have state-independent traps in which the dynamics of the system generally determine the likelihood of a successful separation. However, under adiabatic conditions the atoms definitely end up in opposite wells. We assume a strong confinement to one dimension (1D) by higher order Hermite Gaussian beams according to [19]. All the essential physics is captured in the 1D model we employ here, although performance could conceivably be enhanced by exploiting multi-dimensional effects such as trap-induced resonances [27].

The Hamiltonian for two trapped atoms a and b with internal structure ($|i\rangle_a, |j\rangle_b \in \{|0\rangle, |1\rangle\}$) is given by

$$H = \sum_{i,j=0,1} [H_a + H_b + 2a_{ij}\hbar\omega_\perp \delta(x_a - x_b)] \otimes |ij\rangle\langle ij| \quad (1)$$

for $H_{a,b} \equiv p_{a,b}^2/2m + V(x_{a,b} - d/2) + V(x_{a,b} + d/2)$, with $x_{a,b}$ and $p_{a,b}$ the position and momentum of atom a or b. The tweezer potential $V(x) = -V_0 \exp(-x^2/2\sigma^2)$ describes a Gaussian trap of depth V_0 and variance σ^2. The two wells are separated by a distance d, $\omega_\perp$ is the harmonic oscillation frequency of the transverse confinement [28], and a_{ij} is the state-dependent scattering length for the two-qubit states $|ij\rangle \equiv |i\rangle_a \otimes |j\rangle_b$. We numerically solve the Hamiltonian dynamics of individual qubit states using a split-operator method. Two-atom energy spectra are plotted as a function of well separation (Fig. 1) for different interaction strengths.

Due to symmetrization requirements, not all combinations of vibrational and qubit states are allowed. For example, a pair of composite bosons cannot share the ground state if the qubits are in the antisymmetric state $|\Psi^-\rangle$, defining $|\Psi^\pm\rangle \equiv (|01\rangle \pm |10\rangle)\sqrt{2}$. As in the fermionic case [22], it is possible to exploit these symmetrization requirements in order to produce a two-qubit entangling operation for bosonic atoms (see [29] for details). Consider a pair of identical bosons, one localized in the left trap ($|\psi^L\rangle$) and carrying a qubit in the state $|\varphi^\alpha\rangle = \alpha|0\rangle + \beta|1\rangle$, the other in the right trap ($|\psi^R\rangle$) and carrying a qubit in the state $|\varphi^\mu\rangle = \mu|0\rangle + \nu|1\rangle$. The initial symmetrized wavefunction (as a tensor product of vibrational and qubit states) is then $|\psi_i\rangle = (|\psi^L\psi^R\rangle \otimes |\varphi^\alpha\varphi^\mu\rangle + |\psi^R\psi^L\rangle \otimes |\varphi^\mu\varphi^\alpha\rangle)/\sqrt{2}$.

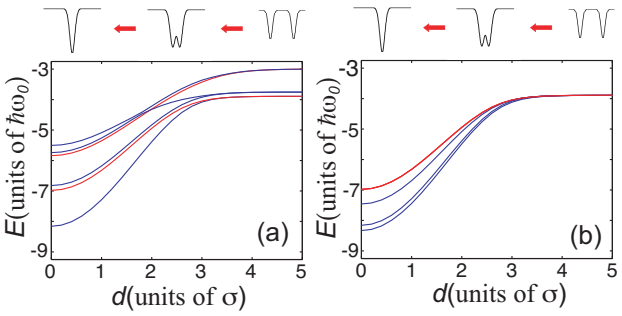

FIG. 1: (Colour online) Adiabatic energy levels as a function of well separation. Energies are measured in units of $\hbar\omega_0$, where ω_0 is the harmonic oscillation frequency of one atom in a single well. (a) Lowest six energy levels for $a_{ij} = 0.1\sigma$. Energy levels correspond to symmetric or antisymmetric external eigenstates. The antisymmetric curves (red) are the lower of the two curves at $E \approx -7\ \hbar\omega_0$ and the lowest of the three curves at $E \approx -5.8\ \hbar\omega_0$ for $d = 0$. (b) Lowest two levels of (a) for different scattering lengths. The lowest three energy curves (from bottom to top) correspond to $a_{ij} = 0$, $a_{ij} = 0.1\sigma$, and $a_{ij} = \sigma$, and asymptote to the antisymmetric (topmost) curve for infinite a_{ij}. The antisymmetric eigenstates are not affected by the interaction and hence the topmost (red) curve does not shift for different a_{ij}.

As the wells are brought together and separated adiabatically, the energies evolve as shown in Fig. 1, and each two-qubit state $|00\rangle$, $|11\rangle$, and $|\Psi^\pm\rangle$ acquires a phase ϕ_{00}, ϕ_{11}, and $\phi_\pm$, depending on its respective energy curve. Adiabaticity can be satisfied even for negative scattering lengths, since transitions between vibrational states of different symmetry or parity are suppressed. For constant tweezer speed v, the adiabaticity criterion is $v \ll \sigma\hbar\omega_{ab}^2/V_0$. Here, $\hbar\omega_{ab}$ is the energy difference

between any coupled states. Time-dependent numerical simulations confirm the validity of the adiabatic approximation over a wide range of values of V_0 and a_{ij} [29]. The final state after an adiabatic change of separation is

$$|\psi_{\rm f}\rangle = |\psi^-\rangle \otimes (\tfrac{\alpha\nu-\beta\mu}{\sqrt{2}} e^{-i\phi_-}|\Psi^-\rangle) \quad (2)$$
$$+ |\psi^+\rangle\otimes(\alpha\mu e^{-i\phi_{00}}|00\rangle + \beta\nu e^{-i\phi_{11}}|11\rangle + \tfrac{\alpha\nu+\beta\mu}{\sqrt{2}} e^{-i\phi_+}|\Psi^+\rangle),$$

using $|\psi^\pm\rangle \equiv (|\psi^L\psi^R\rangle \pm |\psi^R\psi^L\rangle)/\sqrt{2}$.

Evidently this process corresponds to a tensor product of the identity acting on the vibrational state and a unitary U acting on the qubit state. Thus, the internal qubit evolution simplifies to

$$U = e^{-i\phi_{00}}|00\rangle\langle 00| + \frac{e^{-i\phi_+}+e^{-i\phi_-}}{2}(|01\rangle\langle 01| + |10\rangle\langle 10|)$$
$$+ \frac{e^{-i\phi_+}-e^{-i\phi_-}}{2}(|01\rangle\langle 10| + |10\rangle\langle 01|) + e^{-i\phi_{11}}|11\rangle\langle 11|. \quad (3)$$

As in [30], a controlled-phase gate can be obtained even if $\phi_+ \neq \phi_-$ by sandwiching a single-qubit phase gate between a pair of U operations. That is, $G \equiv U\,[S(\pi)\otimes S(0)]\,U$ for $S(\theta) = \exp(i\theta|1\rangle\langle 1|)$. Thus defined, G is locally equivalent to $\exp(-i\gamma|11\rangle\langle 11|)$ if

$$\phi_{00} + \phi_{11} - \phi_+ - \phi_- = (2n \pm \tfrac{1}{2})\gamma, \quad \forall\ n \in \mathbb{Z}. \quad (4)$$

As shown in Eq. (2), the phases critical to this entangling operation are acquired in a non-separable basis. This leads to the inherent robustness observed in initial experiments [23]. In standard schemes, the important non-separable phase is usually acquired due to the internal state dependence of the interaction strengths a_{ij}. In the case of this exchange symmetry-based gate, however, there always is an energy gap between symmetric and antisymmetric curves. The singlet state $|\Psi^-\rangle$ therefore acquires a phase different from the triplet states even if the interaction strengths are state-independent (except as $a_{ij} \to \pm\infty$). This substantial phase difference enables the exchange gate to operate faster than standard collisional gates that rely on the difference in a_{ij}. Furthermore, this gate works over a large range of scattering lengths [see Fig 1(b)], which is especially important when designing experiments for atomic species with any currently unknown scattering lengths (e.g., Yb or Sr). Current studies of Yb interactions [12] already promise a wide applicability of this entanglement gate for different isotopes. (For ^{168}Yb, $a_{00} \approx 13$ nm and for ^{174}Yb, $a_{00} \approx 5.6$ nm. a_{01} and a_{11}, are not yet known.)

IV. SINGLE QUBIT ROTATION AND MEASUREMENT

Recent attempts to cool and trap neutral Yb and Sr have been very successful, and we therefore consider them primarily. Optical clock states in Yb and Sr have extremely low decoherence rates, due to the fact that electric dipole one- and two-photon transitions between $^1S_0$ and $^3P_0$ states are dipole and parity-forbidden, respectively [see Figs.2(a) and 3(a)for energy levels and transition wavelengths]. While affording long lifetimes, the selection rules also present a significant challenge to fast coherent manipulation and measurement of qubits. To overcome this challenge, we employ a coherent, three-photon transition to perform single qubit operations, utilizing the excited $^3S_1$ and $^3P_1$ states [10]. The three transitions $^1S_0 \to {}^3P_1$, $^3P_1 \to {}^3S_1$, and $^3S_1 \to {}^3P_0$ are electric-dipole allowed (see [5, 6] for transition matrix elements). Because three beams can always be arranged in a plane such that the transferred recoil cancels, this three-photon transition has the benefit of being recoil-free [10]. For Sr, the need for three lasers may be reduced to two, as explained below.

We model this three-photon transition by a master equation using the Liouvillian matrix given in [10]. Its fidelity is limited by the short-lived intermediate $^3S_1$ state, which decays primarily to the $^3P_1$ state. The fast coherent rotation of qubits is followed by the fast readout of the $^3P_0$ state via REMPI on a nanosecond or even picosecond time scale. Re-using the $^3S_1$ excited state, photoionization can then be accomplished in a two-step process. An on-resonant $^3P_0$ to $^3S_1$ transition is followed by a final ionization step at $\lambda < 563$ nm for Yb and $\lambda < 592$ nm for Sr. The main errors in this read-out scheme are due to population in the $^3P_1$ to $^3S_1$ states. During readout, any population in $^3P_0$ and $^3S_1$ will be counted as logical $|1\rangle$ (ionized). Population in $^1S_0$ and $^3P_1$ will be counted as logical $|0\rangle$ (not ionized).

The case of Sr is particularly interesting: the transitions $^1S_0 \to^3 P_1$ and $^3P_1 \to^3 S_1$ are close in energy difference (689 and 688 nm, respectively) so that a resonant two-photon transition $^1S_0 \to^3 S_1$ utilizing a single laser is possible. This reduces the laser requirement from three to two. Figure 2(b) shows fidelities for qubit rotation for wavelengths in the range 688 to 689.5 nm. The time for a π-rotation is minimized by tuning to 688.7 nm. Figure 2(c) shows the fidelity and time scales for a π-rotation as a function of laser powers. For fairly realistic mode-locked laser powers, 10^9 W/cm^2 (roughly 1 kW pulse peak power focused onto 100μm^2), rotations within a few nanoseconds are possible with better than 90% fidelity. Higher fidelities of 99.99% can be reached for the same detuning by using lower laser powers of 10^6 W/cm^2.

V. TESTS OF LOCAL REALISM

We show the efficacy of our fast measurement scheme by applying it to a test of local realism. This is expressed in the usual Clauser-Horne-Shimony-Holt (CHSH) form [13],

$$\langle B\rangle = \langle QS\rangle + \langle RS\rangle + \langle RT\rangle - \langle QT\rangle \leq 2, \quad (5)$$

for local realistic theories, whereas Tsirelson's quantum upper bound is $2\sqrt{2}$. For a $|\Psi^+\rangle$ entangled state, the quantum bound is saturated for $Q = Z$, $R = X$,

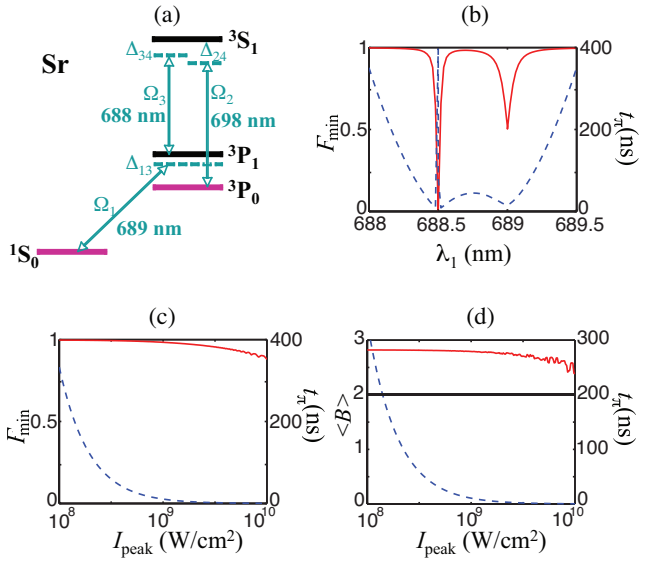

FIG. 2: (Colour online) (a) Energy levels of Sr and three-photon transition for manipulation of the qubit encoded in $^1S_0$ and $^3P_0$. (b) Minimum fidelity $F_{\rm min}$ of single qubit operation in Sr (solid red line) and time scale for π pulse (dashed blue line) as a function of λ_1 ($=\lambda_3$) using a peak laser pulse irradiance of 10^9 W/cm^2. λ_2 is determined by the on-resonance condition for the three-photon transition. (c) Minimum fidelity $F_{\rm min}$ of single qubit operation (solid red line) and time scale for π pulse (dashed blue line) as a function of laser irradiance $I_{\rm peak}$. Detuning is fixed to $\lambda_1 = 688.7$ nm. (d) Resulting expectation value of the Bell operator $\langle B\rangle$ and threshold for a local hidden variable model (solid black line).

$S = (X - Z)/\sqrt{2}$, and $T = (X + Z)/\sqrt{2}$, with X, Y, Z the Pauli operators. These measurements are obtained via basis rotations $\mathcal{R}(\theta) = \exp(+i\theta Y/2)$ applied to the state, followed by measurements in the z-basis. This corresponds to measurements of the form $Q = U_Q^\dagger Z U_Q$ with $U_Q = \mathbb{1}$, $U_R = \mathcal{R}(\pi/2)$, $U_S = \mathcal{R}(3\pi/4)$, and $U_T = \mathcal{R}(\pi/4)$.

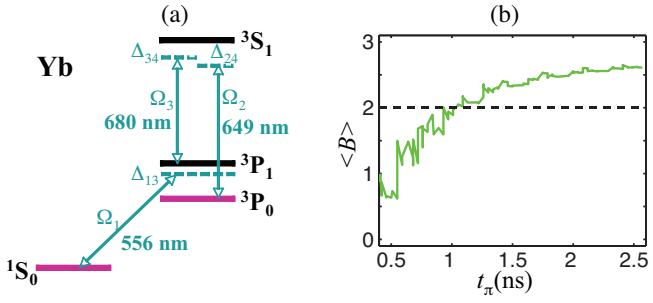

FIG. 3: (Colour online) (a) Energy levels of Yb and three-photon transition for manipulation of the qubit encoded in $^1S_0$ and $^3P_0$. (b) Expectation value of the Bell operator for imperfect single-qubit rotations in Yb as a function of time scale of the measurement for $I_{\rm peak} = 10^9$ W/cm^2.

Inequality (5) is tested by first preparing an entangled Bell state via a controlled phase gate as discussed above, then separating the atoms by a few meters. In a far-off-resonance, magic-wavelength trap, qubit coherence times are on the order of 10 s or longer. For accelerations of 200 mm/s^2 or faster [21], separations of a few meters should be feasible. At this distance, synchronous measurements on a nanosecond time scale are required to ensure space-like separation. Within this time window, the measurement basis is chosen randomly, qubits are rotated to reflect the choice of measurement basis, and qubit states are measured in the computational basis using REMPI. Fast random basis selection can be accomplished by using a light emitting diode (LED) as in [15]. The time necessary for this random basis selection can be minimized [e.g., by using shorter signal paths and custom-built electro-optic modulators (EOMs)] to ensure basis selection times of less than 10 ns. Rotation of the measurement basis is achieved via a coherent coupling of the qubit states via three-photon Raman transitions. The presence of the ion (i.e., the freed electron) will be detected via a single channel electron multiplier with above 99% efficiency [31] .

As in a typical single channel experiment [16], the measurement outcome can be only "ion"$\equiv |1\rangle$ or "no ion"$\equiv |0\rangle$. No data are discarded, and no assumptions are made about "fair sampling" [13] or "enhancement" [14]. Loss of an atom will result in a "no ion"$\equiv |0\rangle$ count, which reduces the degree of Bell inequality violation but does not open any loopholes. High transport and detector efficiencies are necessary to ensure that a violation occurs. A calculation of the CHSH-type Bell inequality violation [13], including errors in rotation and ionization readout, is shown in Fig. 2(d) for Sr and Fig. 3(b) for Yb. To achieve an average value of the Bell-operator larger than 2, as required for a violation, measurements on a time scale of a few nanoseconds (including signal processing times) should be possible with either atomic species.

VI. CONCLUSIONS

We propose schemes for fast recoil-free manipulation and measurement of qubits in Sr or Yb, and discuss an entangling operation for identical bosons in optical tweezers based on the exchange interaction first discussed for fermions in [22]. We furthermore show that it is possible to simultaneously close both space-like separation and detection loopholes for group-II-like atomic qubits separated on only a laboratory scale. This lays the groundwork for future exploration of measurement-based computation. Finally, our work identifies major challenges and provides concrete guidelines for experiments utilizing bosonic Yb or Sr for quantum information processing applications.

Acknowledgments

We thank P. Julienne and A. Derevianko for helpful discussions on Yb and Sr, W. Ketterle for discussions on long-distance transport of atoms, D. Hayes and I. Deutsch for discussions on entangling atoms via exchange interactions, and K. Resch and G. Weihs for discussions on Bell inequalities. This work was supported by NSERC, AIF, CIFAR, iCORE, MITACS, NSF, and The Welch Foundation.

[1] H.-J. Briegel, W. Dür, J. I. Cirac, and P. Zoller, Phys. Rev. Lett. **81**, 5932 (1998).
[2] D. Gottesman and I. L. Chuang, Nature **402**, 390 (1999).
[3] E. Knill, R. Laflamme, and G. J. Milburn, Nature **409**, 46 (2001).
[4] R. Raussendorf and H.-J. Briegel, Phys. Rev. Lett. **86**, 5188 (2001).
[5] H. G. C. Werij, C. H. Greene, C. E. Theodosiou, and A. Gallagher, Phys. Rev. A **46**, 1248 (1992).
[6] S. G. Porsev, Y. G. Rakhlina, and M. G. Kozlov, Phys. Rev. A **60**, 2781 (1999).
[7] M. Takamoto and H. Katori, Phys. Rev. Lett. **91**, 223001 (2003).
[8] S. G. Porsev, A. Derevianko, and E. N. Fortson, Phys. Rev. A **69**, 021403(R) (2004).
[9] Y. Takasu *et al.*, Phys. Rev. Lett. **91**, 040404 (2003).
[10] T. Hong, C. Cramer, W. Nagourney, and E. N. Fortson, Phys. Rev. Lett. **94**, 050801 (2005).
[11] Z. W. Barber *et al.*, Phys. Rev. Lett. **96**, 083002 (2006).
[12] M. Kitagawa *et al.*, Phys. Rev. A **77**, 012719 (2008).
[13] J. F. Clauser, M. A. Horne, A. Shimony, and R. A. Holt, Phys. Rev. Lett. **23**, 880 (1969).
[14] J. F. Clauser and M. A. Horne, Phys. Rev. D **10**, 526 (1974).
[15] G. Weihs *et al.*, Phys. Rev. Lett. **81**, 5039 (1998).
[16] M. A. Rowe, D. Kielpinski, V. Meyer, C. A. Sackett, W. M. Itano, C. Monroe, and J. Wineland, Nature **409**, 791 (2001).
[17] For a review, see special issue *Nature Insight: Ultracold Matter*, edited by K. Southwell, Nature (London) **416**, 205 (2002).
[18] R. Dumke *et al.*, Phys. Rev. Lett. **89**, 097903 (2002), K. Eckert *et al.*, Phys. Rev. A **66**, 042317 (2002), R. Folman *et al.*, Adv. At. Mol. Opt. Phys. **48**, 263-356 (2002).
[19] T. P. Meyrath *et al.*, Opt. Express **13**, 2843 (2005), A. M. Dudarev, M. G. Raizen and Q. Niu, Phys. Rev. Lett. **98**, 063001 (2007).
[20] J. Beugnon *et al.*, Nat. Phys. **3**, 696 (2007).
[21] T. L. Gustavson *et al.*, Phys. Rev. Lett. **88**, 020401 (2001).
[22] D. Hayes, P. S. Julienne, and I. H. Deutsch, Phys. Rev. Lett. **98**, 070501 (2007).
[23] M. Anderlini *et al.*, Nature (London) **448**, 452 (2007).
[24] J. Volz *et al.*, Phys. Rev. Lett. **96**, 030404 (2006).
[25] F. Schmidt-Kaler *et al.*, Appl. Phys. B **77**, 789 (2003).
[26] P. O. Schmidt *et al.*, Science **309**, 749 (2005).
[27] R. Stock, I. H. Deutsch, and E. L. Bolda, Phys. Rev. Lett. **91**, 183201 (2003).
[28] T. Calarco *et al.*, Phys. Rev. A **61**, 022304 (2000).
[29] N. S. Babcock, R. Stock, M. G. Raizen, and B. C. Sanders, Can. J. Phys. **86**, 549 (2008).
[30] D. Loss and D. P. DiVincenzo, Phys. Rev. A **57**, 120 (1998).
[31] G. S. Hurst, M. G. Payne, S. D. Kramer, and J. P. Young, Rev. Mod. Phys. **51**, 767 (1979).

New Journal of Physics
The open-access journal for physics

Improved error-scaling for adiabatic quantum evolutions

Nathan Wiebe[1,2,3] **and Nathan S Babcock**[1]

[1] Institute for Quantum Information Science, University of Calgary, Alberta, Canada
[2] Institute for Quantum Computing, University of Waterloo, Ontario, Canada
E-mail: nathanwiebe@gmail.com

New Journal of Physics **14** (2012) 013024 (15pp)
Received 15 September 2011
Published 16 January 2012
Online at http://www.njp.org/
doi:10.1088/1367-2630/14/1/013024

Abstract. We present a new technique that improves the scaling of the error in the adiabatic approximation with respect to the evolution duration, thereby permitting faster transfer at a fixed error tolerance. Our method is conceptually different from previously proposed techniques: it exploits a commonly overlooked phase interference effect that occurs predictably at specific evolution times, suppressing transitions away from the adiabatically transferred eigenstate. Our method can be used in concert with existing adiabatic optimization techniques, such as local adiabatic evolutions or boundary cancelation methods. We perform a full error analysis of our phase interference method along with existing boundary cancelation techniques and show a tradeoff between error-scaling and experimental precision. We illustrate these findings using two examples, showing improved error-scaling for an adiabatic search algorithm and a tunable two-qubit quantum logic gate.

[3] Author to whom any correspondence should be addressed.

Contents

The adiabatic approximation underpins many important present-day and future applications, such as stimulated rapid adiabatic passage (STIRAP) [1, 2], coherent control of chemical reactions [3] and quantum information processing (QIP) [4, 5]. This approximation asserts that a system will remain in an instantaneous eigenstate of a time-varying Hamiltonian if the time-variation happens slowly enough. Errors in this approximation correspond to transitions away from the instantaneous ('adiabatically transferred') eigenstate. For high-performance applications, it is not always practical to minimize errors by slowing things down. Ambitious future technologies, such as quantum computing devices, will demand simultaneous maximization of both accuracy and speed.

In this paper, we investigate a phase cancelation effect that appears during an adiabatic evolution and can be exploited to polynomially reduce the probability of a given transition at fixed maximum evolution time. This can lead to speed increases at fixed error probability. Unlike alternative methods that obtain improvements by modifying the adiabatic path [6, 7], our technique chooses the evolution time so that destructive interference suppresses the transition. Furthermore, this phase cancelation effect can be exploited to improve existing adiabatic error reduction strategies such as local adiabatic evolutions or boundary cancelation methods. We provide an error analysis of our method and conclude that the accuracy improvements come at the price of increasingly precise knowledge of the time-dependent Hamiltonian; this implies that accuracy is an important and quantifiable resource for quantum protocols utilizing adiabatic passage.

1. Adiabatic approximation

The adiabatic approximation states that if we consider the evolution of a quantum system under a time-dependent Hamiltonian that varies sufficiently slowly in time, then the time evolution operator approximately maps instantaneous eigenstates of the Hamiltonian at $t = 0$

to instantaneous eigenstates of the Hamiltonian at the final time $t = T$. That is to say, if we define $|\nu(t)\rangle$ to be an instantaneous eigenstate of the Hamiltonian $\mathcal{H}(t)$ and define $U(T, 0)$ to be the time evolution operator generated by $\mathcal{H}(t)$, then under the adiabatic approximation,

$$U(T, 0)|\nu(0)\rangle \approx \mathrm{e}^{-\mathrm{i}\int_0^T E(t)\mathrm{d}t}|\nu(T)\rangle. \tag{1}$$

This result is important because adiabatic evolution can be used to efficiently transfer the state $|\nu(0)\rangle$ to $|\nu(T)\rangle$. This is especially relevant in situations when the state $|\nu(0)\rangle$ can be easily prepared, but $|\nu(T)\rangle$ cannot. The aim in the design of adiabatic state transfer protocols is to maximize $|\langle\nu(T)|U(T, 0)|\nu(0)\rangle|$ while minimizing other resources such as the energy, time or experimental precision required for transfer. As a demonstrative example, consider the Hamiltonian,

$$\mathcal{H}(t) = (1 - f(t))\mathcal{H}_0 + g(t)\mathcal{H}_1, \tag{2}$$

where f and g map $[0, T] \mapsto [0, 1]$ with $f(0) = g(0) = 0$ and $f(T) = g(T) = 1$. Hamiltonians used in adiabatic state transfer may often be written in the form of equation (2). The simplest choice of the functions $f(t)$ and $g(t)$ is $f(t) = g(t) = t/T$, but infinitely many other choices are possible. If we define $|0\rangle$ to be the ground state of $\mathcal{H}_0$, then adiabatic evolution approximately maps $|0\rangle$ to the ground state of $\mathcal{H}_1$. The resources needed for adiabatic state transfer may then be optimized by choosing f, g and T appropriately.

2. Adiabatic error

Following previous authors [8, 9], we define the error $\mathcal{E}$ to be the component of the post-evolution state vector that is orthogonal to the state intended for adiabatic transfer. In many circumstances, the following criterion adequately estimates the magnitude of the total error $\mathcal{E}$ at time $t = T$ for a given Hamiltonian:

$$\|\mathcal{E}\| \lesssim \frac{1}{T}\max_s \frac{\|\frac{\mathrm{d}}{\mathrm{d}s}\mathcal{H}(s)\|}{\min_\nu |E_\nu(s) - E_0(s)|^2}, \tag{3}$$

where $E_\nu(s)$ ($\nu \neq 0$) is the instantaneous energy of the ν^{th} eigenstate of the Hamiltonian $\mathcal{H}(s)$ and $E_0(s)$ is the energy of the eigenstate being transferred (usually the ground state) [7, 10]. For convenience, we represent all mathematical terms as explicit functions of the 'reduced time' $s(t) = t/T$, where t is the time, T is the total evolution duration, and $0 \leqslant s \leqslant 1$. This parameterization leaves the form of the Hamiltonian $\mathcal{H}(s)$ unchanged as T varies. We also use the convention $\hbar = 1$.

Although equation (3) provides an expedient heuristic for estimating the accuracy of adiabatic passage, it is (in general) neither necessary nor sufficient to bound the fidelity of adiabatic state transfer [11, 12]. This equivocality opens the possibility of a modest allocation of resources being used to enable significantly improved error-scaling.

One method of improving the fidelity of adiabatic transfer is via the use of a 'local adiabatic' evolution [6, 7, 13]. The idea behind the local adiabatic approximation is to tailor variation of $\mathcal{H}$ with respect to s to minimize the instantaneous non-adiabatic transition rate $\|\frac{\partial}{\partial s}\mathcal{H}(s)\|/\min_\nu |E_\nu(s) - E_0(s)|^2$. Local adiabatic methods have lead to substantial improvements in the asymptotic error-scaling $\mathcal{E}$ with respect to the Hilbert space dimension N [6, 7, 13]. These methods do not however improve the scaling of the error with T.

Recently, methods were developed for improving the scaling of $\mathcal{E}$ with T from order $\mathcal{O}(1/T)$ to $\mathcal{O}(1/T^{m+1})$ by setting the first m derivatives of the Hamiltonian to zero at the beginning and end of the evolution [14, 15]. Error reduction techniques employing these results are collectively referred to as 'boundary cancelation methods.' Boundary cancelation methods have two main drawbacks: first, they assume that the first m derivatives of $\mathcal{H}(s)$ are exactly zero, leaving it unclear whether they are robust against small variations in the derivatives of the Hamiltonian; second, in the regime of short T these methods can have error-scaling that is inferior to the trivial case wherein no boundary cancelation technique is applied (i.e. $m = 0$). Our work addresses these problems: we first provide an analysis of the sensitivity of boundary cancelation methods to small variations in the values of the first m derivatives of $\mathcal{H}(s)$; we then show that phase interference can be used to further reduce errors without increasing m, improving the error-scaling for short T.

3. Main result

We present a new technique for quadratically suppressing the probability of a particular non-adiabatic transition during adiabatic passage. It works by exploiting a phase interference effect that appears in adiabatic systems with Hamiltonians obeying a simple symmetry. This effect can be exploited in a realistic class of time-dependent Hamiltonians that includes many adiabatic algorithms and transport protocols, as well as any Hamiltonian obeying $\mathcal{H}(0) = \mathcal{H}(1)$.

Consider a time-dependent Hamiltonian $\mathcal{H}(s)$ acting on an N-dimensional Hilbert space spanned by the instantaneous energy eigenvectors $|\nu(s)\rangle$ where $\nu = 0, 1, \ldots, N-1$. We define $|0(s)\rangle$ to be the state intended for adiabatic passage. We use the notation $\mathcal{H}^{(p)}(s) = (\frac{\partial}{\partial x})^p \mathcal{H}(x)|_s$. In section 4 we will show that errors in adiabatic passage can be reduced for Hamiltonians obeying the boundary symmetry condition,

$$\frac{\langle \nu(1)|\mathcal{H}^{(m+1)}(1)|0(1)\rangle}{(E_\nu(1) - E_0(1))^{m+2}} = \left(\frac{\langle \nu(0)|\mathcal{H}^{(m+1)}(0)|0(0)\rangle}{(E_\nu(0) - E_0(0))^{m+2}}\right) \mathrm{e}^{-\mathrm{i}\theta}, \tag{4}$$

where θ is an arbitrary phase factor, and m is the number of derivatives of $\mathcal{H}(s)$ that are zero at the boundaries $s = 0, 1$ (e.g., if $m = 2$ then the first and second derivatives of $\mathcal{H}(s)$ are zero at the boundaries, whereas if $m = 0$ then none are zero on the boundary). For a single fixed state $|\nu\rangle$, any time-dependent Hamiltonian may be adapted to satisfy equation (4) simply by adjusting its rate of change in s at the boundaries. For example, if $H(s)$ is of the form of equation (2) then we can independently vary the $(m+1)^{\text{th}}$ derivatives of $f(s)$ and $g(s)$ at $s = 0$, while keeping the derivatives at $s = 1$ fixed, to either increase or decrease the right-hand side of equation (4). The time rate-of-change of a Hamiltonian may also be optimized to approximately satisfy equation (4) for a finite number of eigenstates, as we show in section 7. If equation (4) is not exactly satisfied then the phase interference effect will still reduce errors, but it will not necessarily improve the asymptotic error-scaling with T.

Our method can also be used in conjunction with existing boundary cancelation methods to produce even greater improvements in the asymptotic error-scaling with T. Amplitudes of the transitions $|0(0)\rangle \to |\nu(1)\rangle$ are reduced from the order $\mathcal{O}(T^{-m-1})$ estimates given in [14, 15] to order $\mathcal{O}(T^{-m-2})$ at the discrete set of times $T = T_{n,\nu}$, where n is an even integer and

$$T_{n,\nu} = \frac{n\pi - \theta}{\int_0^1 [E_\nu(s) - E_0(s)]\,\mathrm{d}s}. \tag{5}$$

Using this expression, we can find times such that the probability of transition from $|0(0)\rangle$ to $|\nu(1)\rangle$ is diminished, but such times may not be exactly commensurate with the times when other transitions are suppressed. We show in section 7 how it is possible to choose n to approximately cancel several transitions. In most cases, however, the error is dominated by a few non-adiabatic transitions and in such cases our technique can lead to polynomial reductions in the scaling of the *overall* error with T.

We refer to boundary cancelation methods that are augmented by our scheme to produce order $\mathcal{O}(T^{-m-2})$ error-scaling as 'augmented boundary cancelation methods'. In section 5, we will analyze the error robustness of our augmented boundary cancelation method along with the original schemes laid out in [14, 15]. We show that performance improvements are derived from accurate knowledge of the system's eigenspectrum $\{E_\nu\}$, its total evolution time, and the derivatives of its Hamiltonian, and we provide quantitative error-bounds on these quantities. We provide numerical examples that verify the predictions of our theory in sections 6 and 7.

4. Theory

We will break our discussion of the theory of our method into two parts. First, we discuss the special case for which $m = 0$. This simple case is conceptually distinct from existing boundary cancelation techniques, which require $m > 0$ to produce improvements over equation (3). We then discuss the more general case in which $m > 0$.

To obtain our results, it is *not* necessary to assume that the instantaneous eigenvalues satisfy the ordering condition $E_0(s) < E_1(s) < \cdots < E_{N-1}(s)$. We do however require that $E_0(s) \neq E_\nu(s) \forall \nu > 0$, unless transitions between $|0(s)\rangle$ and $|\nu(s)\rangle$ are strictly forbidden by $\mathcal{H}(s)$. For convenience, we also assume that the phases of the instantaneous eigenvectors are chosen such that $\langle \dot{\nu}(s)|\nu(s)\rangle = 0$. This choice does not affect the quantum dynamics, but it simplifies the analysis of the error. We also assume that the Hamiltonian is differentiable $m+2$ times and that each derivative is bounded for all T. These last restrictions are put in place order to prevent issues that arise for Hamiltonians resembling that of the Marzlin–Sanders counterexample [11, 16].

Given the above assumptions, the error in the adiabatic approximation $\mathcal{E}$ for a Hamiltonian evolution acting on an N-dimensional Hilbert space is given by

$$\mathcal{E} = \sum_{\nu=1}^{N-1} \mathcal{E}_\nu \, \mathrm{e}^{-\mathrm{i}T \int_0^1 E_\nu(s)\,\mathrm{d}s} |\nu(1)\rangle + \mathcal{O}(T^{-m-2}). \tag{6}$$

We know from previous work that $\mathcal{E}_\nu \in \mathcal{O}(T^{-m-1})$ [14, 15], and asymptotically tight expressions are known for $\mathcal{E}_\nu$ in the $m = 0$ case [8, 16]. We therefore begin with this case to illustrate how our phase interference effect can be utilized. Given that $m = 0$, the form of $\mathcal{E}_\nu$ reduces to

$$\mathcal{E}_\nu = \left. \frac{\langle \nu(s)|\dot{\mathcal{H}}(s)|0(s)\rangle \, \mathrm{e}^{-\mathrm{i}T \int_0^s \gamma_\nu(\xi)\,\mathrm{d}\xi}}{-\mathrm{i}T\gamma_\nu^2(s)} \right|_{s=0}^{1}, \tag{7}$$

and where $\gamma_\nu(s) = E_0(s) - E_\nu(s)$. If we choose $\mathcal{H}(s)$ to obey (4), then the absolute value of equation (7) reduces to

$$|\mathcal{E}_\nu| = \left| \frac{\langle \nu(0)|\dot{\mathcal{H}}(0)|0(0)\rangle}{T\gamma_\nu^2(0)} (\mathrm{e}^{-\mathrm{i}(\theta + T\int_0^1 \gamma_\nu(s)\,\mathrm{d}s)} - 1) \right|. \tag{8}$$

Equation (8) has extrema at $T = T_{n,\nu}$. It is maximized when n is odd and vanishes when n is even. Thus, when $T = T_{n,\nu}$ (even n), phase interference causes the scaling of the magnitude of the ν^{th} component of $\mathcal{E}$ with T to be quadratically reduced from $\mathcal{O}(T^{-1})$ to $\mathcal{O}(T^{-2})$. This can lead to substantial error reductions in the adiabatic approximation if we choose T to suppress the non-adiabatic transition that dominates (6), as seen in sections 6 and 7.

If $m > 0$ then the phase interference effect also suppresses probability of excitation to $|\nu(1)\rangle$ at $T = T_{n,\nu}$ for any even integer $n > 0$, but this effect does not directly follow from existing results. We show in appendix A using a perturbative expansion (similar in reasoning to that of [14, 15]) that if the first m derivatives of $\mathcal{H}(s)$ are zero at the boundaries $s = 0, 1$ then

$$|\mathcal{E}_\nu| = \left| \frac{\langle \nu(s)|\mathcal{H}^{(m+1)}(s)|0(s)\rangle e^{-i\int_0^s \gamma_\nu(\xi)\,d\xi T}}{T^{m+1}\gamma_\nu^{m+2}(s)} \right|_{s=0}^{1}. \tag{9}$$

Similar to equation (7), equation (9) reveals an adiabatic phase interference effect also that suppresses the error at certain times. This suppression occurs when

$$\frac{\langle \nu(1)|\mathcal{H}^{(m+1)}(1)|0(1)\rangle\, e^{-iT\int_0^1 \gamma_\nu(s)\,ds}}{\gamma_\nu(1)^{m+2}} = \frac{\langle \nu(0)|\mathcal{H}^{(m+1)}(0)|0(0)\rangle}{\gamma_\nu(0)^{m+2}}, \tag{10}$$

implying that adiabatic phase interference effects reduce the order of transition amplitude $\mathcal{E}_\nu$ from $\mathcal{O}(T^{-m-1})$ to $\mathcal{O}(T^{-m-2})$ when $T = T_{n,\nu}$ for even n.

As an additional note, it may appear from applying the triangle inequality to equation (6) that the bounds we present here could exceed the value cited in equation (3) in the limit of large N. It can be seen by a more careful use of the triangle inequality that this result does not scale with N because $\| \sum_{\nu=1}^{N-1} |\nu(1)\rangle\langle\nu(s)| \| \leqslant 1$ for all s. It is shown in equations (30)–(32) of [16] that this observation leads us to the conclusion that equation (3) is, up to a constant multiple, an asymptotic upper bound for equation (6).

5. Tolerances

Limits on the precision of physical apparatus prevent perfect phase cancelation in realistic applications. Errors can result from imperfect modeling of the Hamiltonian, inexact calculations of the gap integrals, or inaccuracies in the timing or control apparatus. It is therefore necessary to address the impact of empirical imperfections on the feasibility of augmented boundary cancelation methods and determine when they methods can be experimentally realized.

'Symmetry errors' occur when the timing symmetry condition (4) is not precisely satisfied:

$$\Delta S_\nu = \left| \frac{\langle \nu(1)|\mathcal{H}^{(m+1)}(1)|0(1)\rangle}{\gamma_\nu(1)^{m+2}} - \frac{\langle \nu(0)|\mathcal{H}^{(m+1)}(0)|0(0)\rangle}{\gamma_\nu(0)^{m+2}} e^{-i\theta} \right| 0 \Big\rangle. \tag{11}$$

Comparing equation (11) with equation (9), we find that the contributions to $\mathcal{E}_\nu$ due to symmetry errors are of order $\mathcal{O}(T^{-m-2})$ so long as $\Delta S_\nu \in \mathcal{O}(T^{-1})$.

'Gap errors' occur when inaccuracies in the estimate of the gap integral leave condition (5) unsatisfied:

$$\Delta G_\nu = \left| \int_0^1 \gamma_\nu(\xi)\,d\xi - \frac{n\pi - \theta}{T_{n,\nu}} \right| 0 \Big\rangle. \tag{12}$$

Expanding equation (8) in powers of ΔG_v, we find that the contributions to $\mathcal{E}_v$ due to gap errors are of order $\mathcal{O}(T^{-m-2})$ if $\Delta G_v \in \mathcal{O}(T^{-2})$.

'Timing errors' occur when the actual evolution time T differs from the ideal evolution time $T_{n,v}$:

$$\Delta T_{n,v} = \left| T_{n,v} - T \right| 0 \rangle . \tag{13}$$

Expanding equation (8) in powers of $\Delta T_{n,v}$, we find that the contributions to $\mathcal{E}_v$ due to timing errors are of order $\mathcal{O}(T^{-m-2})$ if $\Delta T_{n,v} \in \mathcal{O}(T^{-1})$.

'Derivative errors' can also occur wherein one or more of the derivatives of the Hamiltonian that is assumed to be zero is not:

$$\Delta \mathcal{H}^{(p)} = \max_{s=0,1} \| \mathcal{H}^{(p)}(s) \| 0 \rangle, \tag{14}$$

for $p = 1, \ldots, m$. Such errors do not affect the error-scaling if for all such p,

$$\Delta \mathcal{H}^{(p)} \in \mathcal{O}(1/T^{m+2-p}). \tag{15}$$

In other words, given that the first m derivatives of $\mathcal{H}$ are *approximately* zero at the boundaries, the uncertainty in each derivative must shrink polynomially as T increases in order to achieve the full promise of an augmented boundary cancelation method. The proof that this criterion is sufficient is not simple: it requires a high-order perturbative analysis of the error in the adiabatic approximation. Details are provided in appendix B.

If m is a constant, then it follows that augmented boundary cancelation methods are error robust in the sense that their error tolerances scale polynomially with T^{-1}. This is not problematic for numerical studies because additional precision can be provided at poly-logarithmic cost. However, experimental errors cannot always be so conveniently reduced, and boundary cancelation techniques that use a large value of m may be impractical. The situation is even worse if exponential error-scaling is required, which can be obtained if $m \in \Theta(T/\log T)$. In such circumstances the tolerances $\mathcal{H}^{(p)}(s)$ decrease exponentially with T and therefore boundary cancelation methods are not error robust. This implies that boundary cancelation techniques (augmented or not) cannot in practice achieve exponential scaling without exceedingly precise knowledge of the derivatives of the Hamiltonian at the boundaries. The $m = 0$ method may therefore be more experimentally relevant than its higher-order brethren, because of its minimal precision requirements and its superior scaling for modestly short T.

As the performance improvements provided by boundary cancelation methods come at the price of increasingly accurate information about the Hamiltonian and the evolution time, such information may be viewed as a computational resource for protocols utilizing quantum adiabatic passage. This suggests that current analyses [17] of the resources required for generic adiabatic quantum computing may be incomplete. We illustrate this subtlety in section 6 by showing how to quadratically improve the total error-scaling $\|\mathcal{E}\|$ of an already 'optimal' quantum algorithm.

6. Search Hamiltonians

Adiabatic quantum computing (AQC) algorithms are natural candidates for error suppression by our technique. To demonstrate, we examine an algorithm that adiabatically transforms an

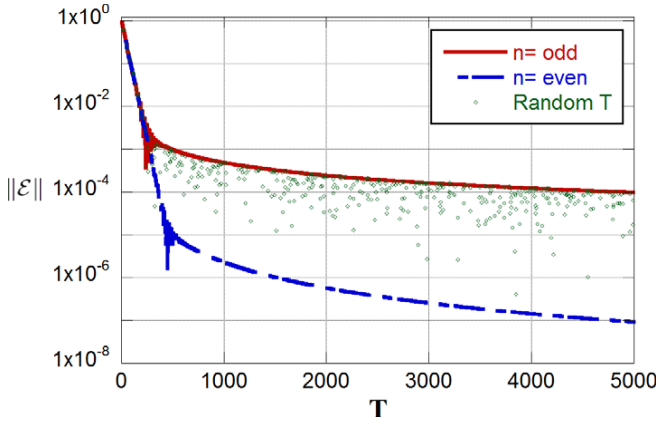

Figure 1. Final error amplitude $|\mathcal{E}|$ as a function of T for the search Hamiltonian (16) using $N = 16$ and $\phi(s) = s$.

initial guessed state into the sought state of a search problem [10]. The Hamiltonian for this algorithm is

$$\mathcal{H}(s) = I - (1 - \phi(s))|+^{\otimes n}\rangle\langle+^{\otimes n}| - \phi(s)|0^{\otimes n}\rangle\langle 0^{\otimes n}|, \tag{16}$$

where $|+\rangle = (|0\rangle + |1\rangle)/\sqrt{2}$, $|0^{\otimes n}\rangle$ is the state that the algorithm seeks, and $\phi : [0, 1] \mapsto [0, 1]$ obeys $\phi(0) = 0$ and $\phi(1) = 1$.

Two common choices for $\phi(s)$ [7, 13, 18] are $\phi(s) = s$ and

$$\phi(s) = \frac{\sqrt{N-1} - \tan[\arctan(\sqrt{N-1})(1-2s)]}{2\sqrt{N-1}}. \tag{17}$$

The latter choice (17) is said to generate a 'local' adiabatic evolution [7, 13]. In each case, the (dimensionless) energy gap is

$$\gamma_1(s) = \sqrt{1 - 4\left(1 - \frac{1}{N}\right)\phi(s)(1-\phi(s))}, \tag{18}$$

where $|0(s)\rangle$ is the ground state of equation (16) and $|1(s)\rangle$ is the only other eigenstate that is coupled to $|0(s)\rangle$ [19]. From the eigenvectors of $\mathcal{H}(s)$, it is straightforward to verify that both forms of $\phi(s)$ given above satisfy equation (4) with $m = 0$.

Figures 1 and 2 show that the choice $T = T_{n,v}$ (even n) produces quadratic improvements in the scaling of $\|\mathcal{E}\|$ for both $\phi(s) = s$ and equation (17) at large T. For odd values of n, the error is maximized, as expected. It is apparent that randomly selected times are extremely unlikely to exhibit maximum phase cancelation. Figures 1 and 2 also suggest a second benefit of our technique: existing boundary cancelation methods [14, 15] can improve the performance of adiabatic algorithms in the limit of large T, but these improvements come at the price of inferior error-scaling for small T, as seen in figure 3 of [14]. The results shown here in figures 1 and 2 exhibit no such tradeoff.

Figures 1 and 2 also shed light on the nature of the complexity of adiabatic algorithms. Several previous studies have taken the complexity of an adiabatic algorithm to be given by

IOP Institute of Physics DEUTSCHE PHYSIKALISCHE GESELLSCHAFT

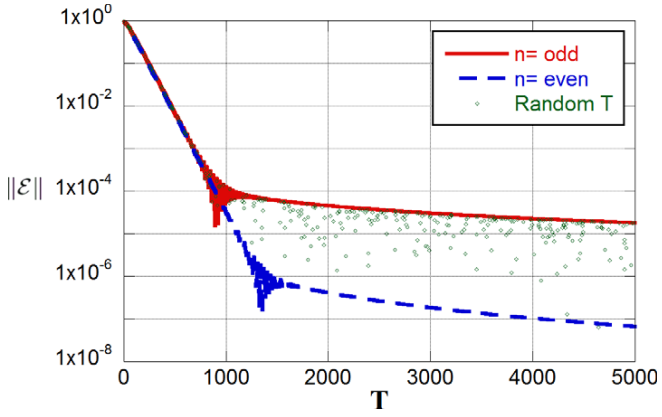

Figure 2. Final error amplitude $|\mathcal{E}|$ as a function of T for the search Hamiltonian (16) using $N = 16$ and equation (17).

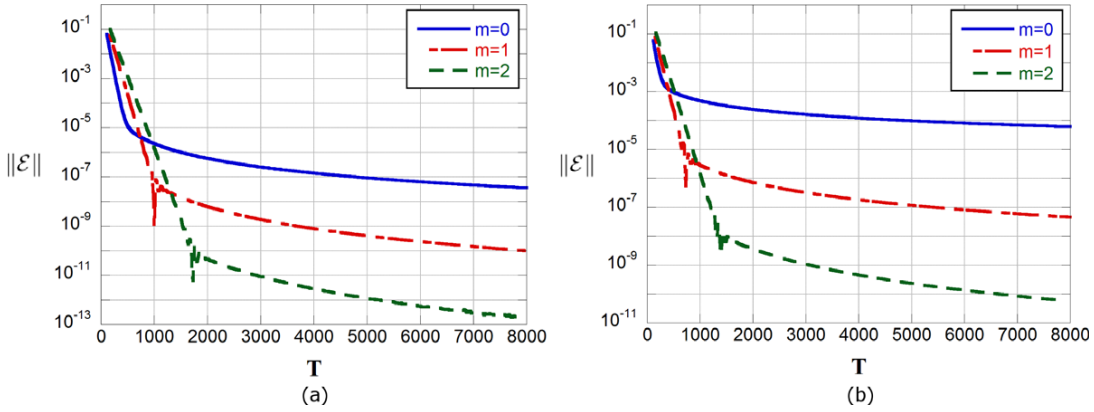

Figure 3. This figure shows that existing boundary cancelation methods can be augmented with our boundary cancelation method to achieve even higher-order error-scaling for a search Hamiltonian with $N = 16$ and $\phi(s)$ chosen as in equation (19). Figure 3(a) is a plot of the error at the times when our theory predicts improved error-scaling (i.e. even n), whereas figure 3(b) displays the times when the errors are predicted to be maximized (i.e. odd n).

the evolution time required for the error predicted by equation (3) to fall within a specified tolerance [7, 10, 13]. In the case of the local adiabatic evolution, this time scales as $\mathcal{O}(\sqrt{N})$, which is known to be optimal [7, 13]. Figure 2 show that this error can still be quadratically reduced by eliminating the $\mathcal{O}(T^{-1})$ contributions to it. These results do not violate quantum lower bounds because the time required for the $\mathcal{O}(1/T)$ to become dominant still scales as $\mathcal{O}(\sqrt{N})$ [14]. Therefore even an exponential improvement in the subsequent adiabatic regime would not violate quantum lower bounds. Paradoxically, these results suggest that the complexity of adiabatic algorithms may be dictated by the physics of the sudden approximation rather than the adiabatic approximation.

We demonstrate our generalized $m > 0$ technique in figure 3, where we plot $|\mathcal{E}_\nu|$ as a function of the total evolution time for a search Hamiltonian with $\phi(s)$ taken to be

$$\phi(s) = \frac{\int_0^s x^m(1-x)^m \,\mathrm{d}x}{\int_0^1 x^m(1-x)^m \,\mathrm{d}x}. \tag{19}$$

This interpolation was originally suggested in [14] and is chosen because it conveniently guarantees that the first m derivatives of $\mathcal{H}(s)$ are zero at $s = 0$ and $s = 1$. Additionally, in the $m = 0$ case it gives the linear interpolation $\phi(s) = s$ used in figure 1.

Figure 3 demonstrates the improvements that arise from combining our results with those taken from [14, 15]. It is notable to see that the $m = 0$ data in figure 3(a) nearly coincides with that for $m = 1$ in figure 3(b) for sufficiently large T. Similarly, the $m = 1$ data in figure 3(a) corresponds to the $m = 2$ data in 3(b) in the same limit. This shows that our technique can be used to improve the overall accuracy of boundary cancelation techniques *without* compromising the error-scaling for short T.

7. Two-qubit gate

Our technique naturally lends itself to Hamiltonians that couple the ground state to only one excited state, such as the search Hamiltonian given in equation (16). If the total error $\|\mathcal{E}\|$ is dominated by several transitions, this technique can still be adapted to approximately cancel multiple transitions simultaneously. To demonstrate, we show how to optimize the fidelity of an adiabatic two-qubit logic gate without decreasing its speed. Similar improvements were reported previously [20], without a broadly-applicable underlying theory or error bounds.

We apply of our method to an exchange-based two-qubit operation designed for neutral atom QIP [5, 21–23]. This operation exploits identical particle exchange to generate a partial 'swap' operation between qubits stored in nuclear spin [22] or valence electronic states [23] of optically trapped atoms. The gate generates a relative phase of $\mathrm{e}^{-\mathrm{i}\alpha}$ between the symmetric and antisymmetric components of the particles' vibrational degrees of freedom. The phase difference is then transferred to the respective components of the two-qubit subspace $\{|ij\rangle : i, j \in \{0, 1\}\}$. This produces an operation that (with single-qubit rotations) is locally equivalent to a tunable entangling controlled-phase gate $\mathrm{e}^{-2\mathrm{i}\alpha|11\rangle\langle 11|}$ [23].

Following previous work [5, 23], we examine a simple Hamiltonian governing two identical particles confined to one dimension and trapped by pair of moving potential wells. The Hamiltonian for particles 1 and 2 is given by

$$\mathcal{H}(x_1, x_2, p_1, p_2, s) = \mathcal{H}(x_1, p_1, s) + \mathcal{H}(x_2, p_2, s) + 2a\omega_\perp \delta(x_1 - x_2), \tag{20}$$

for $\mathcal{H}(x, p, s) = p^2/2m + V(x + (s - \frac{1}{2})d) + V(x - (s - \frac{1}{2})d)$, where x and p are the position and momentum of a particle of mass m. The potential $V(x) = -V_0 \exp(-x^2/2\sigma^2)$ describes a 1D Gaussian trap of depth V_0 and variance σ^2. Traps are initially separated by a distance $d = 3\sigma$. We consider a 1D s-wave scattering interaction, with scattering length $a\omega_\perp = 3\sigma$ and transverse confinement frequency $\omega_\perp$ [24]. As equation (20) is symmetric, transitions between symmetric and antisymmetric states are forbidden, and each symmetry subspace evolves independently.

We diagonalized equation (20) over the range $0 \leqslant s \leqslant 0.5$ at $\Delta s = 1/1200$ intervals. We then used a spline fitting to integrate equation (5), obtaining numerical estimates T of the ideal $T_{n,\nu}$. The quality of initial approximations were then improved using the relationship $|T_{n,\nu} - T| \approx T/\Delta n$, where Δn measures the beat frequency between T^{-1} and $T_{n,\nu}^{-1}$

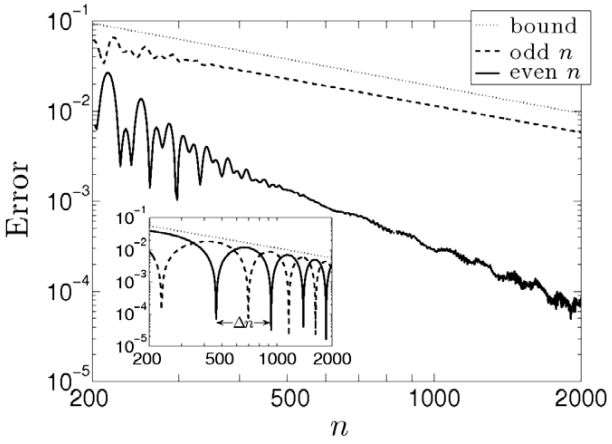

Figure 4. Transition amplitudes and bounds for $T = T_{n,5}$, over $200 \leqslant n \leqslant 2000$. Main figure shows $|\langle\psi_n^+|5\rangle| \approx |\mathcal{E}_5|$ for even n (solid) and odd n (dashed), which are bounded by $\max_s[2\|\frac{\mathrm{d}}{\mathrm{d}s}H(x,p,s)\|/(E_5(s)-E_0(s))^2]$ (dotted). Inset shows $|\langle\psi_n^-|6\rangle|$ bounded by $\max_s[2\|\frac{\mathrm{d}}{\mathrm{d}s}H(x,p,s)\|/(E_7(s)-E_1(s))^2]$.

(e.g., the distance between cusps on inset, figure 4). More sophisticated model Hamiltonians may be solved using more advanced numerical techniques and empirically refined in the same manner.

We numerically integrated the Shrödinger equation to obtain system dynamics of durations $\{T_{n,5}\}$, explicitly generating sets of wave functions $\{|\psi_n^+(s)\rangle\}$ and $\{|\psi_n^-(s)\rangle\}$ for two distinct initial states: the symmetric ground state $|\psi_n^+(0)\rangle = |0(0)\rangle$ and the antisymmetric (effective) ground state $|\psi_n^-(0)\rangle = |1(0)\rangle$. We chose $T_{n,5}$ because $|5(s)\rangle$ is the first eigenstate that significantly couples to $|0(s)\rangle$. This transition is dominant because the $0 \leftrightarrow 1$, $0 \leftrightarrow 2$ and $0 \leftrightarrow 3$ transitions are forbidden, and the $0 \leftrightarrow 4$ coupling is weak. We define $|\langle\psi_n^\pm|\nu\rangle| = |\langle\psi_n^\pm(1)|\nu(1)\rangle|$.

The error probabilities are improved by nearly three orders of magnitude over the bound set by equation (3) by applying our technique to this system (table 1). This corresponds to a tenfold increase in gate speed (given a maximum error rate of 10^{-4}), for the linear motion described by equation (20). Greater improvements could be achieved by choosing $\mathcal{H}(x,p,s)$ or $s(t)$ to satisfy equation (5) for more transitions simultaneously and with better synchronization.

Partial swap operations have been experimentally demonstrated using neutral atoms in a double-well optical lattice, but the adiabatic requirement limits gate times ($\sim$4 ms for high fidelity operation [21]). Our technique thus affords a significant advancement to inherently slow gates of this kind. Furthermore, because the phase α scales with T (see table 1), the precision necessary for accurate gate operation is itself comparable to that needed to implement our phase cancelation technique on an atomic quantum logic gate.

We have numerically demonstrated that error in the adiabatic approximation can be reduced for an experimentally relevant model of a quantum gate. An important remaining issue is whether the experimental uncertainties required to observe error reductions are reasonable for this model system. By first-order Taylor expansion of equation (7), we find that if

$$\Delta S_5 \Big/ \left(\frac{\beta_5(0)}{\gamma_5(0)}\right) < 33\% \quad \text{and} \quad \frac{\Delta G_5}{\int_0^1 \gamma_5(s)\mathrm{d}s} = \frac{\Delta T_5}{T_{460,5}} < 0.02\%, \tag{21}$$

Table 1. Error probabilities and the phase gap α (radians) obtained from simulation runs $\{T_{n,5}\}$ for $456 \leqslant n \leqslant 474$. For these times, local minima of $|\langle\psi_n^+|5\rangle|$ roughly match those of $|\langle\psi_n^-|6\rangle|$ (inset, figure 4) and $|\langle\psi_n^-|7\rangle|$. We denote total errors as $\|\mathcal{E}^+\|^2 = 1 - |\langle\psi_n^+|0\rangle|^2$ and $\|\mathcal{E}^-\|^2 = 1 - |\langle\psi_n^-|1\rangle|^2$. Equation (3) predicts $\|\mathcal{E}^+\|^2 \leqslant 0.046$ and $\|\mathcal{E}^-\|^2 \leqslant 0.62 \times 10^{-3}$ at $n = 460$.

Run	Error probabilities ($\times 10^{-4}$)					Phase
n	$\lvert\langle\psi_n^+\lvert 5\rangle\rvert^2$	$\lvert\langle\psi_n^-\lvert 6\rangle\rvert^2$	$\lvert\langle\psi_n^-\lvert 7\rangle\rvert^2$	$\lVert\mathcal{E}^+\rVert^2$	$\lVert\mathcal{E}^-\rVert^2$	α
456	0.024	0.012	0.245	0.988	0.535	1.645
458	0.022	0.007	0.180	0.771	0.433	−0.186
460	0.021	0.003	0.124	0.648	0.316	4.266
462	0.021	0.001	0.078	0.764	0.275	−3.849
464	0.023	<0.0001	0.043	0.980	0.249	0.603
466	0.023	<0.0003	0.018	1.010	1.201	−1.228
468	0.023	0.002	0.003	0.925	0.292	−3.059
470	0.023	0.004	<0.0001	0.763	0.452	1.392
472	0.022	0.007	0.006	0.721	0.502	−0.438
474	0.021	0.012	0.021	0.803	0.654	4.014

then the *observed* transition amplitude at $T \approx T_{460,5}$ will be less than half of that at $T = T_{459,5}$. These modest requirements imply that our $m = 0$ method may be rapidly incorporated into present-day or near-future atom-based QIP experiments. Such an experiment would also provide a highly sensitive test of the validity of the adiabatic approximation in open quantum systems.

8. Conclusion

We have presented a new technique for improving the fidelity of adiabatic transport. Our technique exploits an adiabatic phase cancelation effect that occurs at certain evolution times to produce improved error-scaling. In addition, our method applies directly to a host of experimentally relevant physical systems, often without modification to the adiabatic path $s(t)$. Our technique can also be used to improve the accuracy of existing boundary cancelation techniques, providing improved scaling over those methods when an easily satisfiable symmetry condition (4) is met. We show that these 'augmented' boundary cancelation techniques can provide unsurpassed accuracy, requiring comparably precise control over the Hamiltonian to achieve high-order error-scaling. Consequently, our work reveals that precision (in addition to energy and time) is a subtle and important resource to consider when devising algorithms and experiments that utilize adiabatic state transfer.

We have illustrated these claims using numerical examples of QIP applications. We numerically demonstrated the use of augmented boundary cancelation methods for $m = 0, 1, 2$ for an adiabatic search algorithm. We also optimized a simple adiabatic quantum logic gate using our $m = 0$ method. In that case we also performed an error analysis and found that the error tolerances needed to apply the method are experimentally reasonable.

Our results open several interesting avenues of further inquiry. We have shown that our technique can be used to improve the accuracy of some local adiabatic evolutions, but it would

be interesting to see if further improvements can be obtained by using our method in concert with more sophisticated adiabatic optimization methods such as the one given in [6]. In addition, determining the error tolerances for small deviations along the adiabatic path would be an important step towards fully characterizing precision as a resource for adiabatic processes. Our preliminary estimates suggest that it may be possible to observe error reductions for atom-based quantum logic using optical dipole traps, but other experimental setups may also be well-suited to study this effect, such as nuclear magnetic resonance (NMR) systems. Such experiments would not only be interesting as a test of the viability of augmented boundary cancelation methods as an error-reduction strategy, but would also provide a highly sensitive test of the limits of the adiabatic approximation itself.

Appendix A. Proof of equation (9)

In section 4 we claimed that phase cancelation can be used to accelerate the convergence of boundary cancelation techniques. Specifically, we claimed that our augmented boundary cancelation methods reduce $|\mathcal{E}_\nu|$ from order $\mathcal{O}(T^{-m-1})$ to $\mathcal{O}(T^{-m-2})$. We will now justify why this is the case.

Using the path-integral representation of the time-evolution operator presented in [8, 16, 18] we have that

$$\|\mathcal{E}_\nu(1)| = \left\| \int_0^1 \beta_{\nu,0}(s)\, \mathrm{e}^{-\mathrm{i}\int_0^s \gamma_\nu(\xi)\,\mathrm{d}\xi\, T}\,\mathrm{d}s + \sum_\mu \int_0^1 \beta_{\nu,\mu}(s)\, \mathrm{e}^{-\mathrm{i}\int_0^s \gamma_{\nu,\mu}(\xi)\,\mathrm{d}\xi\, T} \int_0^s \beta_{\mu,0}\, \mathrm{e}^{-\mathrm{i}\int_0^{s_2} \gamma_\mu(\xi)\,\mathrm{d}\xi\, T}\,\mathrm{d}s_2\,\mathrm{d}s + \cdots \right\|, \tag{A.1}$$

where $\beta_{\nu,\mu}$ is defined for any ν and μ in the set $\{0, \ldots, N-1\}$ by

$$\beta_{\nu,\mu}(s) = \begin{cases} 0, & \text{if } E_\nu(s) = E_\mu(s), \\ \dfrac{\langle \nu(s)|\dot{\mathcal{H}}(s)|\mu(s)\rangle}{E_\nu(s) - E_\mu(s)}, & \text{otherwise.} \end{cases} \tag{A.2}$$

We analyze the series under the assumption that the first m derivatives of the Hamiltonian are zero at the boundaries $s = 0, 1$. Using integration by parts, we find that

$$\int_0^1 \beta_{\nu,0}(s)\mathrm{e}^{-\mathrm{i}\int_0^s \gamma_\nu(\xi)\,\mathrm{d}\xi\, T}\mathrm{d}s = \frac{\langle \nu(s)|\mathcal{H}^{(1)}(s)|0(s)\rangle}{-i\gamma_\nu^2(s)T}\mathrm{e}^{-\mathrm{i}\int_0^s \gamma_\nu(s)\,\mathrm{d}s\, T}\Big|_0^1 - \int_0^1 \left(\frac{\partial}{\partial_s}\frac{\beta_{\nu,0}(s)}{-i\gamma_\nu(s)T}\right)\mathrm{e}^{-\mathrm{i}\int_0^s \gamma_\nu(\xi)\,\mathrm{d}\xi\, T}\,\mathrm{d}s. \tag{A.3}$$

Then, using the fact that $\mathcal{H}^{(1)}(0) = \mathcal{H}^{(1)}(1) = 0$, the first term on the right side of equation (A.3) is zero. Evaluating the second term using integration by parts, we obtain

$$-\left(\frac{\partial}{\partial_s}\frac{\langle \nu(s)|\mathcal{H}^{(1)}(s)|0(s)\rangle}{-\mathrm{i}\gamma_\nu(s)^2 T}\right)\mathrm{e}^{-\mathrm{i}\int_0^s \gamma_\nu(\xi)\,\mathrm{d}\xi\, T}\Big|_0^1 + \int_0^1 \left(\frac{\partial}{\partial_s}\frac{1}{\gamma_\nu(s)T}\left(\frac{\partial}{\partial_s}\frac{\beta_{\nu,0}(s)}{-\mathrm{i}\gamma_\nu(s)T}\right)\right)\mathrm{e}^{-\mathrm{i}\int_0^s \gamma_\nu(\xi)\,\mathrm{d}\xi\, T}\,\mathrm{d}s. \tag{A.4}$$

As before, the first term in this expression is zero because the first two derivatives of the Hamiltonian are zero. We then continue this reasoning, applying integration by parts $m+1$ times. Then after dropping the first m derivatives of the states, Hamiltonian, and energy gaps at $s = 0, 1$, we find

$$\left|\int_0^1 \beta_{\nu,0}(s)\, \mathrm{e}^{-\mathrm{i}\int_0^s \gamma_\nu(\xi)\mathrm{d}\xi T}\, \mathrm{d}s\right| = \left|\frac{1}{T^{m+1}}\left(\frac{\langle \nu(1)|\mathcal{H}^{(m+1)}(1)|0(1)\rangle\, \mathrm{e}^{-\mathrm{i}\int_0^1 \gamma_\nu(s)\,\mathrm{d}s\, T}}{\gamma_\nu(1)^{m+2}} - \frac{\langle \nu(0)|\mathcal{H}^{(m+1)}(0)|0(0)\rangle}{\gamma_\nu(0)^{m+2}}\right)\right| + \mathcal{O}(1/T^{m+2}). \tag{A.5}$$

We then see that the symmetry condition in equation (4) implies that if $T = T_{n,\nu}$ then the first term in the expansion in equation (A.3) is $\mathcal{O}(1/T^{m+1})$. The result of equation (9) then holds if the remaining terms in equation (A.1) are asymptotically negligible.

Turning our attention the remaining path-integrals in equation (A.1), we find that all of the remaining terms are $\mathcal{O}(1/T^{m+2})$. This is because these terms involve contain multiple products of $\beta_{\mu,\nu}$. Therefore, if we perform integration by parts $m+1$ times on the outermost integral, then the term involving $\mathcal{H}^{(m+1)}$ becomes multiplied by at least one $\beta_{\mu,\nu}$ term, which is zero on the boundary by definition. Therefore, no nonzero terms appear in the expansion of these integrals to $\mathcal{O}(1/T^{m+2})$. Hence, the first term in equation (A.1) is asymptotically dominant as anticipated [8, 16]. Since the first term is asymptotically dominant and also of order $\mathcal{O}(1/T^{m+2})$ given $T = T_{n,\nu}$, the augmented boundary cancelation technique proposed in section 5 combines with existing methods.

Appendix B. Error-robustness of augmented boundary cancelation methods

In section 5 we claimed without proof that if the uncertainty in the p^{th} derivative of $\mathcal{H}(s)$ is $\mathcal{O}(T^{-m-2+p})$ for all $p = 1, \ldots, m$, then that derivative can safely be assumed to be negligible. We prove this now by demonstrating that the leading order terms involving $\mathcal{H}^{(p)}(0)$ or $\mathcal{H}^{(p)}(1)$ for $p = 1, \ldots, m$ are of order $\mathcal{O}(T^{-m-2})$ under this assumption.

We begin by assuming that, for some q, $\mathcal{H}^{(q)}(s)$ is nonzero at the boundaries $s = 0, 1$ and that all lower derivatives are negligible there. Following the argument put forward in appendix A, the lowest order term that appears after applying integration by parts q times to equation (A.1) is

$$\left|\frac{1}{T^q}\left(\frac{\langle \nu(1)|\mathcal{H}^{(q)}(1)|0(1)\rangle\, \mathrm{e}^{-\mathrm{i}\int_0^1 \gamma_\nu(s)\,\mathrm{d}s\, T}}{\gamma_\nu(1)^{q+1}} - \frac{\langle \nu(0)|\mathcal{H}^{(q)}(0)|0(0)\rangle}{\gamma_\nu(0)^{q+1}}\right)\right|. \tag{B.1}$$

If $\mathcal{H}^{(q)}(1)$ and $\mathcal{H}^{(q)}(0)$ are both of order $\mathcal{O}(T^{-m-2+q})$, then the term (B.1) is reduced to order $\mathcal{O}(T^{-m-2})$. As argued in appendix A, other terms that appear in the perturbative series after repeated integrations by parts are asymptotically smaller than this term and therefore do not affect the error-scaling. Thus, it is sufficient to render errors in the q^{th} derivative of $\mathcal{H}(s)$ negligible by taking them to be $\mathcal{O}(T^{-m-2+q})$.

By the same reasoning, if the uncertainty in the p^{th} derivative of $\mathcal{H}(s)$ is $\mathcal{O}(T^{-m-2+p})$ for all $p = 1, \ldots, m$, then the total contribution of derivative errors is $\mathcal{O}(T^{-m-2})$ given that $m \in \mathcal{O}(1)$. This implies that augmented boundary cancelation methods are robust to derivative errors given

that m is a fixed integer. This result also trivially implies that existing boundary cancelation methods are robust to derivative errors under the same circumstances.

If m is not bounded from above by a constant then this analysis fails because the previous analysis ignored multiplicative factors of m that appear in the analysis. Such terms could make the neglected higher-order derivative terms much larger if m is an increasing function of T. This means that if we wish to achieve exponential error-scaling by taking $m \in \Theta(T/\log(T))$, then the tolerance for derivative errors must shrink even further from the already exponentially small error tolerances obtained by substituting $m \in \Theta(T/\log(T))$ into $\mathcal{O}(T^{-m-2+p})$ for fixed p. We conclude that boundary cancelation methods that exhibit exponential error-scaling are not robust to derivative errors.

Acknowledgments

We wish to thank Emily Pritchett, Mark Raizen and Barry Sanders for helpful discussions. This work was supported by NSERC, AIF, iCORE, MITACS research network, General Dynamics Canada and USARO.

References

[1] Oreg J, Hioe F T and Eberly J H 1984 *Phys. Rev.* A **29** 690
[2] Kuklinski J R, Gaubatz U, Hioe F T and Bergmann K 1989 *Phys. Rev.* A **40** 6741–4
[3] Shapiro M and Brumer P 2006 *Phys. Rep.* **425** 1950264
[4] Averin D 1998 *Solid State Commun.* **105** 659–64
[5] Babcock N S, Stock R, Raizen M G and Sanders B C 2008 *Can. J. Phys.* **86** 549–55
[6] Rezakhani A T, Lidar D A, Hamma A and Zanardi P 2009 *Phys. Rev. Lett.* **103** 080502
[7] Roland J and Cerf N J 2002 *Phys. Rev.* A **65** 042308
[8] MacKenzie R, Marcotte E and Paquette H 2006 *Phys. Rev.* A **73** 042104
[9] Jansen S, Ruskai M B and Seiler R 2007 *J. Math. Phys.* **48** 102111
[10] Farhi E, Goldstone J, Gutmann S and Sipser M 2000 arXiv:quant-ph/0001106
[11] Marzlin K-P and Sanders B C 2004 *Phys. Rev. Lett* **93** 160408
[12] Teufel D 2003 Adiabatic perturbation theory in quantum dynamics *(Lecture Notes in Mathematics* vol 1821) (Berlin: Springer) pp 6–10
[13] van Dam W, Mosca M and Vazirani U 2001 *Proc. 42nd Annu. IEEE Symp. on the Foundations of Computer Science (FOCS'01)* pp 279–87
[14] Rezakhani A T, Pimachev A K and Lidar D A 2010 *Phys. Rev.* A **82** 052305
[15] Lidar D A, Rezakhani A T and Hamma A 2009 *J. Math. Phys.* **50** 102106
[16] Cheung D, Høyer P and Wiebe N 2011 *J. Phys. A: Math. Theor.* **44** 415302
[17] Aharonov D, van Dam W, Kempe J, Landau Z, Lloyd S and Regev O 2004 *Proc. 45th Annu. IEEE Symp. on Foundations of Computer Science (FOCS'04)* pp 42–51
[18] Farhi E, Goldstone J and Gutmann S 2002 arXiv:quant-ph/0208135
[19] Roland J and Cerf N J 2003 *Phys. Rev.* A **68** 062311
[20] Charron E, Tiesinga E, Mies F and Williams C 2002 *Phys. Rev. Lett.* **88** 077901
[21] Anderlini M, Lee P J, Brown B L, Sebby-Strabley J, Phillips W D and Porto J V 2007 *Nature* **448** 452
[22] Hayes D, Julienne P S and Deutsch I H 2007 *Phys. Rev. Lett.* **98** 070501
[23] Stock R, Babcock N S, Raizen M G and Sanders B C 2008 *Phys. Rev.* A **78** 022301
[24] Calarco T, Hinds E A, Jaksch D, Schmiedmayer J, Cirac J I and Zoller P 2000 *Phys. Rev.* A **61** 022304

Surface residues dynamically organize water bridges to enhance electron transfer between proteins

Aurélien de la Lande[a,b,2], Nathan S. Babcock[c,d], Jan Řezáč[a,b,3], Barry C. Sanders[c,d], and Dennis R. Salahub[a,b,e,1]

[a]Department of Chemistry, [b]Institute for Biocomplexity and Informatics, [c]Department of Physics and Astronomy, [d]Institute for Quantum Information Science, and [e]Institute for Sustainable Energy, Environment and Economy, University of Calgary, 2500 University Drive NW, Calgary, Alberta, Canada, T2N 1N4

Edited by David N. Beratan, Duke University, Durham, NC, and accepted by the Editorial Board May 17, 2010 (received for review December 15, 2009)

Cellular energy production depends on electron transfer (ET) between proteins. In this theoretical study, we investigate the impact of structural and conformational variations on the electronic coupling between the redox proteins methylamine dehydrogenase and amicyanin from *Paracoccus denitrificans*. We used molecular dynamics simulations to generate configurations over a duration of 40 ns (sampled at 100-fs intervals) in conjunction with an ET pathway analysis to estimate the ET coupling strength of each configuration. In the wild-type complex, we find that the most frequently occurring molecular configurations afford superior electronic coupling due to the consistent presence of a water molecule hydrogen-bonded between the donor and acceptor sites. We attribute the persistence of this water bridge to a "molecular breakwater" composed of several hydrophobic residues surrounding the acceptor site. The breakwater supports the function of nearby solvent-organizing residues by limiting the exchange of water molecules between the sterically constrained ET region and the more turbulent surrounding bulk. When the breakwater is affected by a mutation, bulk solvent molecules disrupt the water bridge, resulting in reduced electronic coupling that is consistent with recent experimental findings. Our analysis suggests that, in addition to enabling the association and docking of the proteins, surface residues stabilize and control interprotein solvent dynamics in a concerted way.

respiratory chain | Marcus theory | pathway model | dynamic docking | blue copper proteins

The electron transport chain is the cornerstone of biological energy transduction. All known life-forms use membrane-bound chains of redox proteins to convert energy from food or sunlight into chemical energy stored in adenosine triphosphate (1). Biological electron transfer (ET) often occurs over long distances (>1 nm) between protein-encapsulated redox cofactors separated by intervening protein or solvent molecules. Over the last two decades, there has been increasing interest in water as an "active constituent in cellular biology" (2). Today there is a growing body of evidence suggesting that water plays an important role mediating long-range ET and that conformational fluctuations are critical to protein-solvent interactions at ET interfaces (3–10). Notably, previous authors have suggested that "ordered water molecules in the protein-protein interface may considerably influence electronic coupling between redox centers" (4) and that "water may be a particularly strong tunneling mediator when it occupies a sterically constrained space between redox cofactors with strong organizing forces that favor constructively interfering coupling pathways" (7).

In general, however, the degree of sophistication of solvent-organizing effects at aqueous ET interfaces remains unknown. In this study, we show that a pair of solvent-organizing residues in direct contact with a bridging water molecule may be aided by surrounding residues that help stabilize local solvent dynamics by mediating contact with the bulk. We predict that surface residues at protein-protein interfaces can act collectively to organize and stabilize solvent structures and dynamics during long-range ET.

The timely passage of electrons from protein to protein is crucial for proper metabolic regulation (11) and relies on all the physical and chemical phenomena (i.e., diffusion, protein docking, and ET reaction steps) that participate in overall electron transmission. Here we investigate the redox reaction between methylamine dehydrogenase (MADH) and amicyanin taken from *Paracoccus denitrificans*. This redox pair is representative of a broad class of interprotein ET reactions involving blue copper proteins (12). Under methylotrophic growth conditions, MADH supplies electrons to amicyanin, a blue copper protein that in turn shuttles electrons to various c-type cytochromes (13). In vitro, the transfer occurs between the reduced tryptophan tryptophylquinone (TTQ) group on the MADH β-subunit and a cupric complex buried just under the amicyanin surface (Fig. 1). The oxidation of MADH by amicyanin is a "true" ET reaction, limited by the ET reaction rate k_{ET} (14). Ma et al. recently reported a series of site-directed mutations performed on the amicyanin methionine 51 residue by alanine, lysine, and leucine (Fig. 1) (15). Kinetic measurements revealed nearly a tenfold decrease in k_{ET} without significant changes to the proteins' overall structural, binding, or redox potentials. Ma et al. concluded that "surface residues of redox proteins may not only dictate specificity for their redox protein partners but also be critical to optimize the orientations of the redox centers and intervening media within the protein complex for the ET event" (15).

To analyze an interprotein ET reaction such as the reduction of amicyanin by MADH, it is necessary to consider large ensembles of protein-protein complex configurations that contribute to the average ET rate (16). For a true ET reaction, the ET rate k_{ET} can be estimated by nonadiabatic Marcus–Hush–Levich theory (17, 18),

$$k_{ET} = \frac{2\pi}{\hbar}\frac{1}{\sqrt{4\pi\lambda k_B T}}|T_{DA}|^2 \exp\left(\frac{-\Delta G^{\ddagger}}{k_B T}\right) = \frac{2\pi}{\hbar}\frac{1}{\sqrt{4\pi\lambda k_B T}}|T_{DA}|^2 \exp\left(\frac{-(\Delta G^{\circ}+\lambda)^2}{4\lambda k_B T}\right), \quad [1]$$

where $\hbar$ is the reduced Planck's constant, k_B is Boltzmann's constant, T is the temperature, $\Delta G^{\ddagger}$ is the Gibbs free energy of activa-

Author contributions: A.d.l.L. and N.S.B. designed research; A.d.l.L. and N.S.B. performed research; J.R. contributed new reagents/analytic tools; A.d.l.L., N.S.B., B.C.S., and D.R.S. analyzed data; and A.d.l.L., N.S.B., B.C.S., and D.R.S. wrote the paper.

The authors declare no conflict of interest.

This article is a PNAS Direct Submission. D.N.B. is a guest editor invited by the Editorial Board.

[1]To whom correspondence should be addressed: dsalahub@ucalgary.ca.

[2]Present address: Laboratoire de Chimie Physique—Centre National de la Recherche Scientifique -Unité Mixte de Recherche 8000, Université Paris-Sud 11, Bâtiment 349, Campus d'Orsay. 15, Rue Georges Clémenceau, 91405 Orsay Cedex, France.

[3]Present address: Institute of Organic Chemistry and Biochemistry, Academy of Sciences of the Czech Republic and Center for Biomolecules and Complex Molecular Systems, Flemingovo náměstí 2, 166 10 Prague 6, Czech Republic.

This article contains supporting information online at www.pnas.org/lookup/suppl/doi:10.1073/pnas.0914457107/-/DCSupplemental.

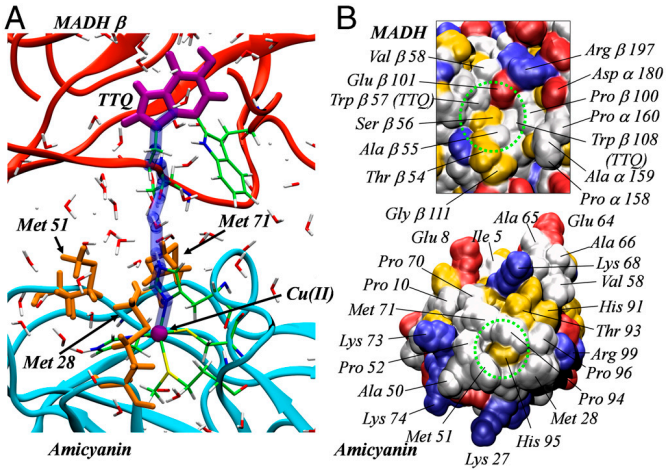

Fig. 1. (*A*) Solvated amicyanin (blue) in contact with MADH subunit β (red). Residues of interest to ET are represented as liquorice. Redox cofactors are shown in purple and surface methionine residues in orange. The dominant pathway A_1 is shown as a transparent blue tube connecting the redox cofactors. (*B*) Direct ("head on") view of interfacial residues represented by their chemical nature: hydrophobic (white), hydrophilic (yellow), positively charged acidic (blue), and negatively charged basic (red). The dotted green circles indicate the ET region on the surface of each protein. The molecular breakwater is visible as a white ring of hydrophobic residues surrounding the amicyanin His 95.

tion, ΔG° is the Gibbs free energy of reaction, λ is the reorganization energy, and T_{DA} is the superexchange matrix element that couples the donor and acceptor electronic states quantum mechanically.

The experimental trends reported by Ma et al. (15) strongly suggest the existence of a correlation between protein motion and ET activity in the MADH-amicyanin complex. While most numerical studies have addressed nanosecond time scales or shorter, we investigated longer time scales (40 ns) that are less well understood, thereby obtaining statistics for vibrational modes spanning several temporal orders of magnitude. In addition to the wild-type complex, we consider four amicyanin mutants: M51A, M51L, M51K, and M51C. The first three mutations correspond to those reported by Ma et al. (15), whereas M51C was added to investigate the impact of a thiol replacing the original thioether. We employed molecular dynamics (MD) simulations to generate the configurations within the transient ET complex along with an ET pathway analysis to characterize each configuration's intrinsic ET activity (see *Methods*). This computationally intensive investigation has allowed us to identify important solvent-stabilizing functions of interprotein surface residues. Because of this solvent-stabilizing effect, the most ET-active wild-type conformations are also the most statistically favored ones, an effect that is lost in the mutant complexes.

Results

We obtained 400,000 molecular configurations from 40 ns of MD simulations of the wild-type complex and each mutant. We employed the semiempirical pathway model originally developed by Beratan, Onuchic, and Hopfield (19) to determine the tunneling pathway with the largest electronic coupling matrix element T_{DA} for each configuration. Although this model does not provide an absolute value for the superexchange coupling matrix element T_{DA} and does not account for interferences between multiple pathways, it can be used to estimate the total electronic coupling decay factor ε_{tot}, where $T_{DA} \approx H_{DA} \cdot \varepsilon_{tot}$ and H_{DA} is the theoretical "close-contact" coupling matrix element (20, 21). Despite its simplicity, the pathway model has previously demonstrated excellent predictive power when comparing different molecular configurations (8, 22, 23). We recorded the pathway with the largest decay factor ε_{tot} for each configuration and labeled it by the surface residue through which the electron exits the MADH. We found that in the vast majority of pathways (>99%), the electron leaves the MADH through one of Ser β 56, Trp β 57, Val β 58, or Trp β 108 before tunneling through one or more water molecules and entering the amicyanin through His 95. Adopting the terminology already in use (21), it is convenient to define four distinct collections of similar pathways, or "pathway tubes," labeled by the letters A (Ser β 56), B (Trp β 57), C (Val β 58), and D (Trp β 108) (Fig. 2 and Fig. S1). All the remaining excess pathways (labeled E) afford comparatively weak electronic coupling (Table S1).

Pathway tube A is of particular interest due to its large coupling strength and high frequency of occurrence (~60%, Table 1). For this reason, we further divided it into three subcategories: A_1 represents a single pathway with a hydrogen-bonded bridge from the Ser β 56 O carbonyl oxygen through a single water molecule to the His 95 HE2 proton, A_2 represents all the remaining completely hydrogen-bonded water bridges between Ser β 56 and His 95, and A_3 represents all the partially broken (i.e., van der Waals coupled) pathways from Ser β 56 to His 95. In a previous pathway analysis performed on the crystal structure of the MADH-amicyanin dimer (24), Brooks et al. found that the strongest pathway required a through-vacuum jump from MADH Trp β 108 to amicyanin Pro 94 (25). In contrast, in our solvated system we find that pathways involving a direct jump from Trp 108 to Pro 94 make up less than 0.01% of our data and are on average one-tenth as strong as the completely hydrogen-bonded A_1 pathway. In another analysis performed on the MADH-amicyanin-cytochrome ternary crystal structure, Chen et al. concluded that the strongest pathway involved a trapped interfacial water molecule, even though its efficiency depended "critically on the presence of the water molecule which may not always be occupied" (26). Chen et al.'s water-mediated pathway is identifiable as our A_1 pathway, assuming a hydrogen-bonded arrangement for the hydrogen atoms that were not resolved. Thus, our computational study strongly supports Chen et al.'s water-bridge hypothesis and moreover stresses the importance of the dynamical behavior of the ET pathways; very frequent switches between the pathways are obtained in the course of the simulations (Fig. S2) but pathway A_1 was favored *only* in the wild-type complex.

Configurations associated with pathway tube A_1 depend critically on the probability P_{hb} of a water molecule forming two simultaneous hydrogen bonds with atoms Ser β 56 O and His 95 HE2. The wild-type complex's statistical affinity for pathway A_1 depends on this high probability ($P_{hb} > 50\%$) compared with those of the mutants ($P_{hb} < 20\%$) (Table 1). In turn, the presence of this water bridge is linked to the discrepancy in the average number of water molecules found at the interface between the proteins. The consistent presence of the water molecule joining Ser β 56 and His 95 in the wild type, its corresponding absence in the mutants, and the resulting reduction in the mutant coupling strength indicate that solvent organization is vital to this reaction. Any destabilization of the A_1 water bridge results in a statistical shift toward less efficient pathways (Table 1).

The A_1 pathway is disrupted when other water molecules jostle or compete with the bridging water molecule (Fig. 2 A_1). To determine the impact of surrounding water molecules on the A_1 bridge, we computed the number of water molecules within the "ET region," which we define to be a sphere of radius R centered between the MADH Ser β 56 O and amicyanin His 95 HE2 atoms. Even for large radii ($R = 5$ Å), an average of only 2.5 water molecules are present within the wild-type ET region, compared with mutant averages ranging from 4.7 to 6.3 (Fig. 3). Comparatively few water molecules are exchanged between the wild-type ET region and the surrounding bath. The mutant ET regions are much more turbulent, as evidenced by the larger number of water molecules present, the lower probability of

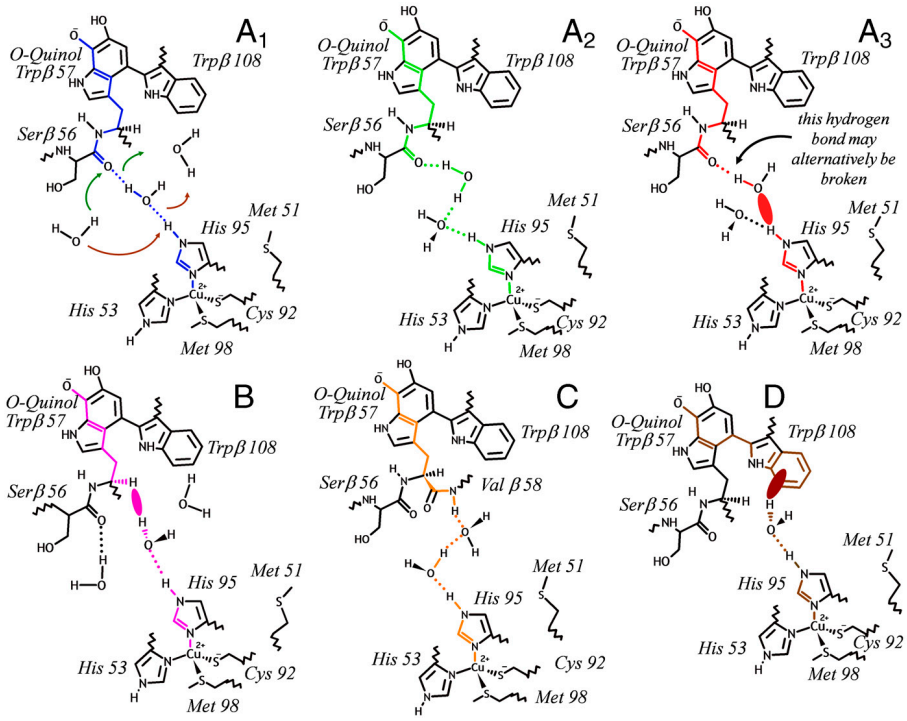

Fig. 2. Representative pathways for each pathway tube in colors corresponding to those in Fig. 3. Hydrogen bonds are represented by dotted lines and through-space jumps by solid ovals. The arrows on A_1 illustrate perturbations to the hydrogen-bond network caused by another nearby water molecule.

hydrogen-bonded bridge formation P_{hb}, and the higher rate of turnover τ between the individual water molecules involved in forming the A_1 bridge (Table 1). These results indicate that the dynamical organization of the intervening solvent is crucial to the formation of the most efficient ET configurations.

A comparison of mutant-to-wild-type ratios of the calculated decay factors $r_\varepsilon^{mut} = \langle \varepsilon_{tot}^2 \rangle^{mut} / \langle \varepsilon_{tot}^2 \rangle^{wt}$ and the experimental rates $r_k^{mut} = k_{ET}^{mut} / k_{ET}^{wt}$ provides insight about the impact of the Met 51 mutation on experimental rates through modifications of the electronic coupling term. Our results are in overall qualitative agreement with experiment, as the decreases in the mutant decay factors are of comparable size to the experimentally observed decreases in the ET rate constants (Table 1). There is, however, a discrepancy between the ordering of the experimentally determined mutant rates ($1 > r_k^{M51L} > r_k^{M51K} > r_k^{M51A}$) and the pathway model decay factors ($1 > r_\varepsilon^{M51A} > r_\varepsilon^{M51K} > r_\varepsilon^{M51L}$), discussed below. We find that the packing density model (27) produces decay factors similar to those of the pathway model for the M51L and M51K mutants, but predicts the M51A and M51C mutants to be at least as kinetically competent as the wild type.

Discussion

It is remarkable that a single strongly coupled pathway should dominate the thermal statistics of the wild-type complex alone (>50%, Fig. 3*A*). There is no a priori correlation between the binding affinity of the complex and ET activity: Maxwell-Boltzmann statistics govern the probability of occurrence of a given configuration, whereas the nonadiabatic Marcus expression (Eq. **1**) independently determines the ET rate constant k_{ET} for that configuration. It is apparent that the protein structure at the wild-type interface is specifically suited to favor conformations most amenable to ET. On the other hand, configurations associated with lower efficiency pathways become more statistically prominent in the mutant distributions, thereby decreasing the average decay factor $\langle \varepsilon_{tot} \rangle$ (Table 1). This statistical change also carries implications for the overall reaction kinetics.

In order to relate solvent dynamics directly to the mutation, it is necessary to consider interactions between the amicyanin 51 residue and other protein or solvent molecules. Previously, when performing a P52G mutation upon amicyanin, Ma et al. attributed the resulting reduction in k_{ET} to a loss of interactions between the amicyanin Met 51 residue and the MADH Val 58 (28). This

Table 1. Expectation values for $\langle \varepsilon_{tot} \rangle$ and the ratios $r_\varepsilon^{mut} = \langle \varepsilon_{tot}^2 \rangle^{mut} / \langle \varepsilon_{tot}^2 \rangle^{wt}$ and $r_k^{mut} = k_{ET}^{mut} / k_{ET}^{wt}$ obtained from packing density and pathway analyses*

		Wild type	M51L	M51K	M51A	M51C
r_k^{mut}	(Experiment)	1.0	0.68	0.49	0.13	—
$\langle \varepsilon_{tot} \rangle \times 10^3$	(Pathway analysis)	0.90 ± 0.03	0.47 ± 0.03	0.61 ± 0.02	0.65 ± 0.02	0.73 ± 0.02
r_ε^{mut}	(Pathway analysis)	1.0	0.36 ± 0.04	0.52 ± 0.04	0.57 ± 0.04	0.76 ± 0.05
$\varepsilon_{tot} \times 10^3$	(Packing density)	0.70 ± 0.03	0.42 ± 0.04	0.51 ± 0.03	0.62 ± 0.05	1.03 ± 0.05
r_ε^{mut}	(Packing density)	1.0	0.56 ± 0.09	0.76 ± 0.07	0.89 ± 0.15	2.29 ± 0.26
P_{hb}		0.53	0.15	0.19	0.18	0.16
τ (ns^{-1})		0.40	0.57	0.60	0.65	0.68

*The uncertainties account for the sampling errors of the computational protocol (see *SI Text*). Experimental rates k_{ET} were obtained from k_3 (at 30 °C) in table 3 of ref. 15 (M51C was not reported). P_{hb} is the unit-normalized likelihood that a water molecule is simultaneously hydrogen bonded to both the MADH Ser β 56 O and amicyanin His 95 HE2 atoms during our simulations. The turnover τ of the bridging water molecule is defined as the number of different water molecules that participate in pathway A_1 divided by the length of the simulation in nanoseconds.

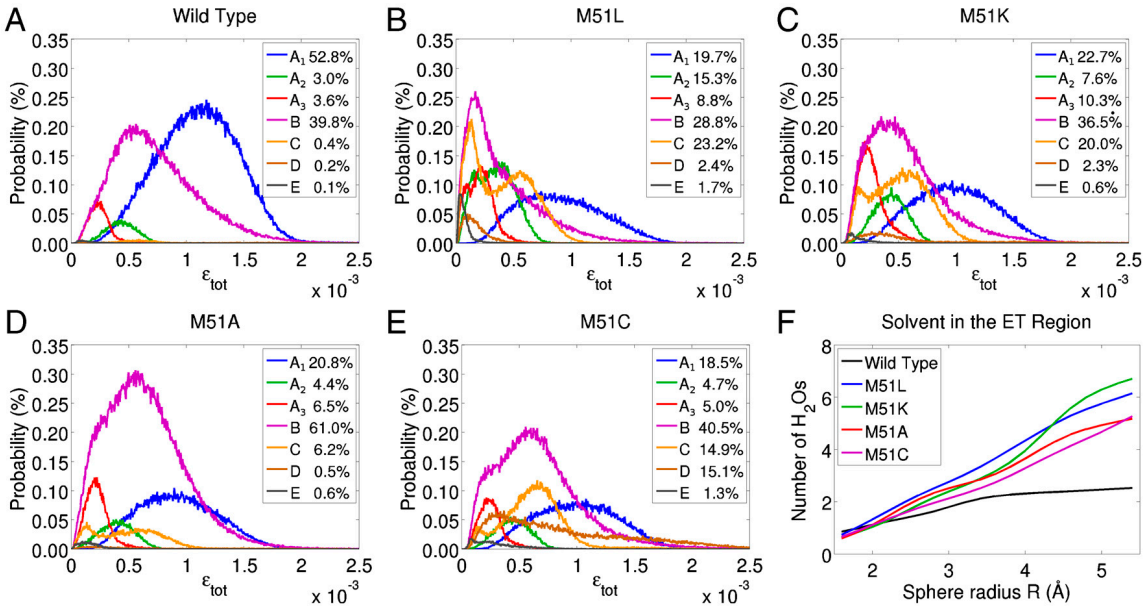

Fig. 3. Normalized distributions of sampled pathway tubes (*A–E*) and the average number of water molecules (*F*) within the ET region defined by a sphere of radius *R* (sphere shown in Fig. 4).

conclusion is compatible with our simulation results, which show that conformational variations in the amicyanin M51K and M51L residues allow an increased number of water molecules to "sneak" into the ET region (Fig. S3). Intuitively, one expects the replacement of Met 51 by a smaller (alanine) or hydrophilic (lysine) residue to allow more water molecules to enter the ET region. The cases of cysteine and leucine are less straightforward to analyze, as both residues are hydrophobic and similar in size to methionine. Many complex interactions influence the dynamics of these residues, and a future analysis will have to examine a variety of chemical effects (e.g., methionine is a Lewis base whereas leucine is more acidic). In this regard, our study highlights the importance of subtle interprotein surface dynamics to the formation of efficient ET pathways.

Ma et al. (28) used the "true, gated, and coupled ET" (17) framework to rationalize the decrease in the ET rates in terms of protein motion at the interface. Based on large increases in the inferred values of T_{DA} and λ, as well as observed changes to the rate-limiting reaction kinetics for the *N*-quinol TTQ form of MADH (15, 28), Ma et al. inferred that the rate constants k_{ET} measured for the M51A and M51K mutants were not those of the true ET reaction, as is the case for the wild-type system. Rather, they proposed that the M51A and M51K reactions were "gated" by an unidentified, separate, slower pre-ET step x that imposed its rate k_x over that of the actual ET event (15). On the other hand, experimental data for the M51L mutant is similar to that of the true wild-type reaction and is not consistent with conformationally gated ET for which $k_{ET} > k_x$. For the M51L mutant, Ma et al. concluded that either $k_x \sim k_{ET}$ or that the ET reaction is kinetically "coupled" to a rapid but unfavorable conformational rearrangement with equilibrium constant K_x, so that the observed rate is actually $k_{ET} \times K_x$ (15). This kinetically coupled picture (29) is compatible with the "dynamic docking" framework in which "a large ensemble of weakly bound protein-protein configurations contribute to binding, but only a few are reactive" (30). It is not clear why the mutation of the MADH Met 51 residue would lead to gated ET ($k_{ET} > k_x$) in the M51A and M51K mutants, but coupled ET ($k_{ET} < k_x$) in the M51L mutant.

Our numerical analysis is consistent with the viewpoint that ET is modulated by rapid interconversion within an ensemble of configurations of varying ET reactivity. The configurations produced by our simulations exhibit a continuum of ET affinities, whereas the kinetically coupled and dynamic docking models assume a simple active/inactive model of ET activity (29, 30). This active/inactive dichotomy fails to capture the variation in intermediate coupling strengths revealed by our pathway analysis (Fig. 3). ET rate reductions comparable to the experimental ones are obtained by summing the contributions to T_{DA} arising from the various accessible molecular configurations within the transient ET complex, without assuming a distinct preorganization step. Because each configuration is associated with an intrinsic ET coupling strength, it is enough to modulate the ET rate simply by modifying each configuration's respective statistical weight. We propose the hypothesis that the increased amount of water at the ET interface dynamically modulates the ET rate in the mutants, akin to kinetically coupled ET as described above.

Further work will be required to reproduce the exact experimental trend in the mutant rate constants (Table 1). Variations in relevant parameters such as $\Delta G°$ and λ contribute to the experimental rate k_{ET}, but given that the wild-type ET rate is $k_{ET} = 10\ s^{-1}$, 40 ns of MD simulation may not fully account for these parameters. Furthermore, although the use of Langevin dynamics improves the sampling of the configuration space, the artificial noise inherent to this method can also become a source of error. The pathway model itself is limited by its inability to account for complex-valued interferences between tunneling pathways. It successfully estimates the electronic coupling for molecular configurations with a single dominant tunneling-pathway or a few constructively interfering pathways, but its accuracy is limited for configurations with multiple destructively interfering pathways (7). Because pathway "tube" A_1 represents only one strongly coupled pathway and because very few water molecules are present at the wild-type interface, the pathway model is expected to provide a good coupling estimate for the statistically favored wild-type A_1 configurations. The increased number of water molecules at the mutant interfaces makes inter- and intratube destructive interference more likely in the mutant complexes, and the pathway model may overestimate the coupling strengths for these configurations. The question of multiple interferences accentuates the potential importance of solvent control to create one dominant strongly coupled pathway at the protein interface.

Conclusions

Earlier studies on both inter- and intraprotein ET revealed the possibility of water-mediated ET pathways in biological ET (6, 31), as well as the specific role of protein residues stabilizing well-defined ET pathways (8, 32). Our study, however, provides compelling evidence that several protein surface residues can act together in concert to organize bridging water molecules, enhancing electron transfer between proteins. Our numerical simulations indicate that MADH Ser β 56 and amicyanin His 95 work together to form a solvent-linked bridge between donor and acceptor, while the surrounding hydrophobic residues act as a "molecular breakwater" to support the stability of this bridge (Fig. 1*B*). Comparisons of the solvent organization in the wild-type and mutant complexes show that the amicyanin Met 51 residue plays an essential role, repelling bulk water molecules from the ET region (Fig. 4). Any modification of the steric or electrostatic interactions at the Met 51 site—by either replacement (15) or repositioning (28)—may disrupt this solvent-repelling mechanism. In this respect, we believe that site-directed mutagenesis studies of the nearby amicyanin Met 28 and Met 71 residues (Fig. 1) would also be of great interest. If Met 28 and Met 71 function in the same manner as Met 51, mutations to these residues will produce reductions in k_{ET} similar to those found for Met 51.

More generally, our proposed solvent-repelling mechanism depends on a patch of hydrophobic surface residues surrounding the acceptor site, a characteristic shared by other blue copper proteins (12). So far, this surface characteristic was believed to ensure a weak binding affinity of the redox partners, allowing fast association and dissociation processes. Our study reveals another possible role for a blue copper protein's hydrophobic surface (Fig. 1*B*). It may enhance the ET activity of the redox complex, controlling solvent dynamics to significantly improve the strength and stability of water-mediated ET pathways.

Methods

Molecular Dynamics Simulations. We carried out molecular mechanics computations using the CHARMM 33a package (33). We selected the ternary MADH-amicyanin-cytochrome-c551i complex resolved to 1.9 Å by X-ray crystallography (Protein Data Bank ID code 2GC4). This is a reasonable starting structure for simulations because crystalline MADH has been demonstrated to be catalytically competent to transfer electrons to amicyanin (34, 35). After deleting the cytochrome-c551i from the ternary complex, hydrogen atoms were added with the HBUILD routine (as implemented in CHARMM), and the proteins were solvated in a TIP3P (36) water box of dimensions $115 \times 80 \times 80$ Å^3. Approximately 40 Na^+ ions were added to ensure electrical neutrality (depending on the mutant). Histidine residues, including His 53 and His 95 were monoprotonated consistent with the experimental pH of 7.5 (15). The mutant complexes were generated from this structure *in silico* using Molden (37). The amicyanin cupric center was treated using the force field parameters developed by Comba and Remeny for blue copper proteins (38). The Lennard-Jones parameters for the copper ion were $\varepsilon = 0.05$ kJ/mol and $\sigma = 2.13$ Å (39). The wild-type and mutant structures were first geometrically optimized by 500 steps of steepest descent algorithm and subsequent 1,500 steps of adopted basis Newton–Raphson optimizer. This was followed by 1 ns of Langevin dynamics to ensure equilibration and a further 40 ns from which conformations were sampled every 100 fs. The Shake algorithm was employed to constrain hydrogenated bonds at their equilibrium bond lengths. A friction coefficient of 15 ps^{-1} and a bath temperature of 298 K were used to propagate the equations of motion within the Langevin approach. Periodic boundary conditions were applied to simulate a continuous medium. Finally, a shift function was used to compute electrostatic interactions between distant pairs of atoms, with a 12-Å cutoff. A switch function was applied for van der Waals interactions (starting from 10 Å and set to zero at 12 Å). This is the recommended (default) scheme in CHARMM to compute nonbonded terms.

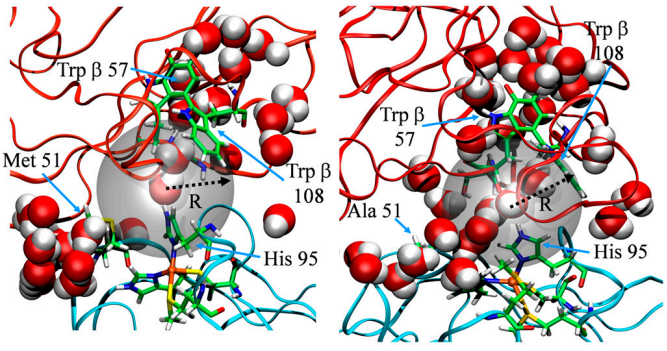

Fig. 4. Representative snapshots of the wild-type (*Left*) and M51A (*Right*) interfaces, revealing the breach in the molecular breakwater due to the mutation (other mutants shown in Fig. S3). The gray sphere represents the ET region for radius $R = 5.5$ Å. Water molecules are shown in the van der Waals representation.

Choice of Donor and Acceptor. We defined the donor based on the density functional theory (DFT) highest occupied molecular orbital of the TTQ cofactor. For these computations we used the deMon2k code (40) with the Perdew–Burke–Ernzerhof functional (41) and the double-zeta-valence plus polarization–generalized gradient approximation basis sets. The catecholate ring represents 63% of the donor molecular orbital, whereas the full MADH Trp β 57 aromatic ring represents almost 73%. There is very little orbital delocalization onto the MADH Trp β 108 residue (less than 15% spread over its aromatic ring), and as such it cannot be considered part of the donor group. We therefore restrict our definition of the donor to the Trp β 57 catecholate ring, assigning a decay factor of 1 between the Trp β 57 atoms. Consequently, the best pathway for a given configuration does not depend on the choice of the starting atom within the MADH Trp β 57 catecholate ring. We note that our DFT-based definition of the donor orbital is different from the one chosen in a previous pathway analysis where the electron density was assumed to be delocalized across both cycles of the TTQ group and the Trp β 108 residue was therefore taken as part of the donor group (25). The copper atom was taken as the acceptor because the beta lowest unoccupied molecular orbital essentially consists of the copper d_{xy} orbital (some contributions are found on the Cys 92 residue but do not extend farther than the sulfur atom 3*p* orbital).

ET Analysis. We chose the empirical pathway model originally developed by Beratan et al. (20) to estimate ε_{tot} for the huge number of sampled molecular configurations. The pathway model allowed us to classify the configurations in terms of distinct geometric motifs, directly relating conformational fluctuations to variations in the coupling strength. The pathway model assumes that the electron can tunnel from atom to atom along a given pathway, each interatomic step *i* contributing a coupling decay factor ε_i. Individual covalently bonded, hydrogen-bonded, and through-vacuum decay factors (denoted ε_c, ε_{hb}, ε_v, respectively) were calculated based on semiempirical formulae (Eqs. **3**–**6**). T_{DA} is the product of the first order close-contact matrix coupling element H_{DA} and the total semiempirical decay factor ε_{tot} (Eq. **3**), where ε_{tot} is the product of N individual decay factors ($N = N_c + N_{hb} + N_v$, respectively). To improve the accuracy of ε_{tot}, we used refined parameters derived recently from constrained DFT (42, 43) for the ε_{hb} term, which depends on the hydrogen-bond angle ϕ and the atom-to-atom distance *R*. We employed Dijkstra's algorithm (44) to find the pathway with the largest coupling for each configuration. To make the search tractable, each protein complex was pruned to about 300 atoms at the ET interface belonging to the following residues: amicyanin Met 28, Met 51, Pro 52, His 53, Met 71, Cys 92, Pro 94, His 95, Met 98, Cu(II); MADH Ala β 55, Ser β 56, Trp β 57, Val β 58, Pro β 100, Glu β 101, Trp β 108; and all water molecules within 7 Å of the amicyanin 95 HE2 or MADH 108 CD2 atoms.

$$T_{DA} = H_{DA} \cdot \varepsilon_{tot}, \qquad [2]$$

$$\varepsilon_{tot} = \prod_{i=1}^{N_c} \varepsilon_c^i \cdot \prod_{j=1}^{N_{hb}} \varepsilon_{hb}^i \cdot \prod_{k=1}^{N_v} \varepsilon_v^k \qquad \text{[pathway model]}, \qquad [3]$$

$$\varepsilon_c = 0.6, \qquad [4]$$

$$\varepsilon_{hb} = 0.36 \cdot e^{-0.64(R-2.01)} \cdot e^{-2.23(\cos\phi+1)} \cdot e^{-1.83(R-2.01)(\cos\phi+1)}, \qquad [5]$$

$$\varepsilon_v = 0.6 \cdot e^{-1.7(R-1.4)}. \qquad [6]$$

For comparison with the pathway model, the packing density (27) approach was also tested. In this case, ε_{tot} is written as a product of two

exponential decay factors that involve the fraction of filled space (i.e., space within the atoms' van der Waals radii), the complementary fraction of vacuum space, and the donor-acceptor separation R_{DA} (Eq. **7**). The associated decay factor parameters β_{fill} (0.45 Å^{-1}) and β_{vac} (1.4 Å^{-1}) were taken from Page et al. (27). To evaluate the fraction of filled space f_{fill} we defined 200 points regularly spaced along the donor-acceptor axis and determined for each of them the presence of any surrounding atom within their van der Waals radius.

$$\varepsilon_{tot} = e^{-f_{fill}\beta_{fill}R_{DA}} \cdot e^{-(1-f_{fill})\beta_{vac}R_{DA}} \quad \text{[packing density model].} \quad \textbf{[7]}$$

Figures. Molecular graphics were prepared with VMD (version 1.8.6) (45).

ACKNOWLEDGMENTS. The authors wish to thank Sergei Noskov (University of Calgary, Canada) and Pascal Permot (Université Paris-Sud 11—CNRS, France) for helpful discussions. This work was supported by the Natural Sciences and Engineering Research Council of Canada, the Canadian Institute for Advanced Research (CIFAR), the Informatics Circle of Research Excellence, and the Alberta Ingenuity Fund. Computational resources were provided by WestGrid. B.C.S. is a CIFAR Fellow.

1. Lane N (2006) *Power, Sex, Suicide: Mitochondria and the Meaning of Life* (Oxford Univ Press, New York).
2. Ball P (2008) Water as an active constituent in cell biology. *Chem Rev* 108:74–108.
3. Tezcan FA, Crane BR, Winkler JR, Gray HB (2001) Electron tunneling in protein crystals. *Proc Natl Acad Sci USA* 98:5002–5006.
4. van Amsterdam IMC, et al. (2002) Dramatic modulation of electron transfer in protein complexes by crosslinking. *Nat Struct Biol* 9:48–52.
5. Francisco WA, Wille G, Smith AJ, Merkler DJ, Klinman JP (2004) Investigation of the pathway for inter-copper electron transfer in peptidyclycine α-amidating monooxygenase. *J Am Chem Soc* 126:13168–13169.
6. Miyashita O, Okamura MY, Onuchic JN (2005) Interprotein electron transfer from cytochrome c_2 to photosynthetic reaction center: Tunneling across an aqueous interface. *Proc Natl Acad Sci* 102:3558–3563.
7. Lin J, Balabin IA, Beratan DN (2005) The nature of aqueous tunneling pathways between electron-transfer proteins. *Science* 310:1311–1313.
8. de la Lande A, Martí S, Parisel O, Moliner V (2007) Long distance electron-transfer mechanism in peptidylglycine α-hydroxylating monooxygenase: A perfect fitting for a water bridge. *J Am Chem Soc* 129:11700–11707.
9. Balabin IA, Beratan DN, Skourtis SS (2008) Persistence of structure over fluctuations in biological electron-transfer reactions. *Phys Rev Lett* 101:158102.
10. Beratan DN, et al. (2009) Steering electrons on moving pathways. *Acc Chem Res* 42:1669–1678.
11. de Rienzo F, Gadboulline RR, Wade RC, Sola M, Menziani MC (2004) Computational approaches to structural and functional analysis of plastocyanin and other blue copper proteins. *Cell Mol Life Sci* 61:1123–1142.
12. de Rienzo F, Gabdoulline RR, Menziani MC, Wade RC (2000) Blue copper proteins: A comparative analysis of their molecular interaction properties. *Protein Sci* 9:1439–1454.
13. Harms N, van Spanning RJM (1991) C1 Metabolism in *Paracoccus denitrificans*: Genetics of *Paracoccus denitrificans*. *J Bioenerg Biomembr* 23:187–210.
14. Brooks HB, Davidson VL (1994) Free energy dependence of the electron transfer reaction between methylamine dehydrogenase and amicyanin. *J Am Chem Soc* 116:11201–11202.
15. Ma JK, Wang Y, Carrell CJ, Mathews FS, Davidson VL (2007) A single methionine residue dictates the kinetic mechanism of interprotein electron transfer from methylamine dehydrogenase to amicyanin. *Biochemistry* 46:11137–11146.
16. Leys D, Basran J, Talfournier F, Sutcliffe MJ, Scrutton NS (2003) Extensive conformational sampling in a ternary electron transfer complex. *Nat Struct Biol* 10:219–225.
17. Davidson VL (2008) Protein control of true, gated, and coupled electron transfer reactions. *Acc Chem Res* 41:730–738.
18. Marcus RA, Sutin N (1985) Electron transfers in chemistry and biology. *Biochim Biophys Acta* 811:265–322.
19. Beratan DN, Onuchic JN, Hopfield JJ (1987) Electronic coupling through covalent and noncovaltent pathways in proteins. *J Chem Phys* 86:4488–4498.
20. Beratan DN, Betts JN, Onuchic JN (1991) Protein electron transfer rates set by the bridging secondary and tertiary structure. *Science* 252:1285–1288.
21. Curry WB, et al. (1995) Pathways, pathway tubes, pathway docking, and propagators in electron transfer proteins. *J Bioener Biomembr* 27:285–293.
22. Gray HB, Winkler JR (2003) Electron tunnelling through proteins. *Q Rev Biophys* 36:341–372.
23. Jasaitis A, Johansson MP, Wikström M, Vos MH, Verkhovsky M (2007) Nanosecond electron tunneling between the hemes in cytochrome *bo3*. *Proc Natl Acad Sci USA* 104:20811–20814.
24. Chen L, et al. (1992) Crystal structure of an electron-transfer complex between methylamine dehydrogenase and amicyanin. *Biochemistry* 31:4959–4964.
25. Brooks HB, Davidson VL (1994) Kinetic and thermodynamic analysis of a physiologic intermolecular electron-transfer reaction between methylamine dehydrogenase and amicyanid. *Biochemistry* 33:5696–5701.
26. Chen L, Durley RCE, Mathews FS, Davidson VL (1994) Structure of an electron transfer complex: Methylamine dehydrogenase, amicyanin, and cytochrome c551i. *Science* 264:86–89.
27. Page CC, Moser MC, Chen X, Dutton PL (1999) Natural engineering principles of electron tunnelling in biological oxidation-reduction. *Nature* 402:47–52.
28. Ma JK, Carrell CJ, Mathews FS, Davidson VL (2006) Site-directed mutagenesis of proline 52 to glycine in amicyanin converts a true electron transfer reaction into one that is conformationally gated. *Biochemistry* 45:8284–8293.
29. Davidson VL (2000) Effects of kinetic coupling on experimentally determined electron transfer parameters. *Biochemistry* 39:4924–4928.
30. Liang Z-X, et al. (2004) Dynamic docking and electron-transfer between cytochrome *b5* and a suite of myoglobin surface-charge mutants. Introduction of a functional-docking algorithm for protein-protein complexes. *J Am Chem Soc* 126:2785–2798.
31. Bizzarri AR, Brunori E, Bonanni B, Cannistraro S (2007) Docking and molecular dynamics simulation of the Azurin-Cytochrome c551 electron transfer complex. *J Mol Recognit* 20:122–131.
32. Prytkova TR, Kurnikov IV, Beratan DN (2007) Sensitivity in protein electron transfer coupling coherence distinguishes structure. *Science* 315:622–625.
33. Brooks BR, et al. (1983) CHARMM: A program for macromolecular energy, minimization, and dynamics calculations. *J Comput Chem* 4:187–217.
34. Merli A, et al. (1996) Enzymatic and electron transfer activities in crystalline protein complexes. *J Biol Chem* 271:9177–9180.
35. Ferrari D, et al. (2004) Electron transfer in crystals of the binary and ternary complexes of methylamine dehydrogenase with amicyanin and cytochrome c551i as detected by EPR spectroscopy. *J Biol Inorg Chem* 9:231–237.
36. Jorgensen WL, Chandrasekhar J, Madura JD, Impey RW, Klein ML (1983) Comparison of simple potential functions for simulating liquid water. *J Chem Phys* 79:926–935.
37. Schaftenaar G, Noordik JH (2000) Molden: A pre- and post-processing program for molecular and electronic structures. *J Comput Aided Mol Design* 14:123–124.
38. Comba P, Remeny R (2002) A new molecular mechanics force field for the oxidized form of blue copper proteins. *J Comput Chem* 23:697–705.
39. Buning C, Comba P (2000) protonation of the copper(I) form of the blue copper proteins plastocyanin and amicyanin—A molecular dynamics study. *Eur J Inorg Chem* 2000:1267–1273.
40. Köster AM, et al. (2006) deMon developers. http://www.demon-software.com/public_html/index.html.
41. Perdew JP, Burke K, Ernzerhof M (1996) Generalized gradient approximation made simple. *Phys Rev Lett* 77:3865–3868.
42. Wu Q, van Voorhis T (2006) Extracting electron transfer coupling elements from constrained density functional theory. *J Chem Phys* 125:164105–8.
43. de la Lande A, Salahub DR (2010) Derivation of interpretative models for long range electron transfer from constrained density functional theory. *J Mol Struct Theochem* 943:115–120.
44. Dijkstra EW (1959) A note on two problems with connections with graphs. *Num Math* 1:269–271.
45. Humphrey W, Dalke A, Schulten K (1996) VMD: Visual molecular dynamics. *J Mol Graphics* 14:33–38.

Supporting Information

de la Lande et al. 10.1073/pnas.0914457107

SI Text

Confidence Intervals. The expectation values reported in Table S1 for the electronic coupling factors $\langle \varepsilon_{tot} \rangle$ and the squared decay factors $\langle \varepsilon_{tot}^2 \rangle$ have been estimated from their average values and standard deviations on the ensemble of snapshots extracted from the molecular dynamics (MD) simulations. The confidence interval is then obtained using the formula (in the case of ε)

$$\langle \varepsilon \rangle = \bar{\varepsilon} \pm \frac{\sigma}{\sqrt{n\rho}},$$

where $\bar{\varepsilon}$ is the average value of ε_{tot} taken over n configurations (400,000 for each system) and ρ is the chain statistical efficiency. The latter term accounts for the statistical correlations among the values within the ensemble of snapshots. Because these ensembles are generated from MD simulations (not from purely stochastic simulation methods such as the Monte Carlo approach), such correlations are unavoidable and must be removed to get reliable confidence intervals (1, 2). The value of ρ can be estimated from the analysis of the autocorrelation function (ACF) of ε_{tot}. For example, in the case of a purely exponential decay for the ACF with a characteristic length τ, ρ would be

$$\rho = (1 + 2\tau)^{-1}.$$

In practice, the ACF does not take an easily identifiable form, and the analysis is done by a numerical fitting of the ε_{tot} autocorrelation function. This was done with the coda package (3) implemented in the "R Project for Statistical Computing" program (4).

1. Allen MP, Tildesley DJ, eds (1987) *Computer Simulation of Liquids* (Clarendon Press, Oxford, UK), pp 192–198.
2. Gregory P, ed (2005) *Bayesian Logical Data Analysis for the Physical Sciences* (Cambridge Univ Press, Cambridge, UK), pp 312–351.
3. Plummer M, Best N, Cowles K, Vines K (2009). coda: Output analysis and diagnostics for MCMC. R package version 0.13-4.
4. R Development Core Team (2008). *R: A language and environment for statistical computing. R Foundation for Statistical Computing*, Vienna, Austria. ISBN 3-900051-07-0. Available at http://www.R-project.org.

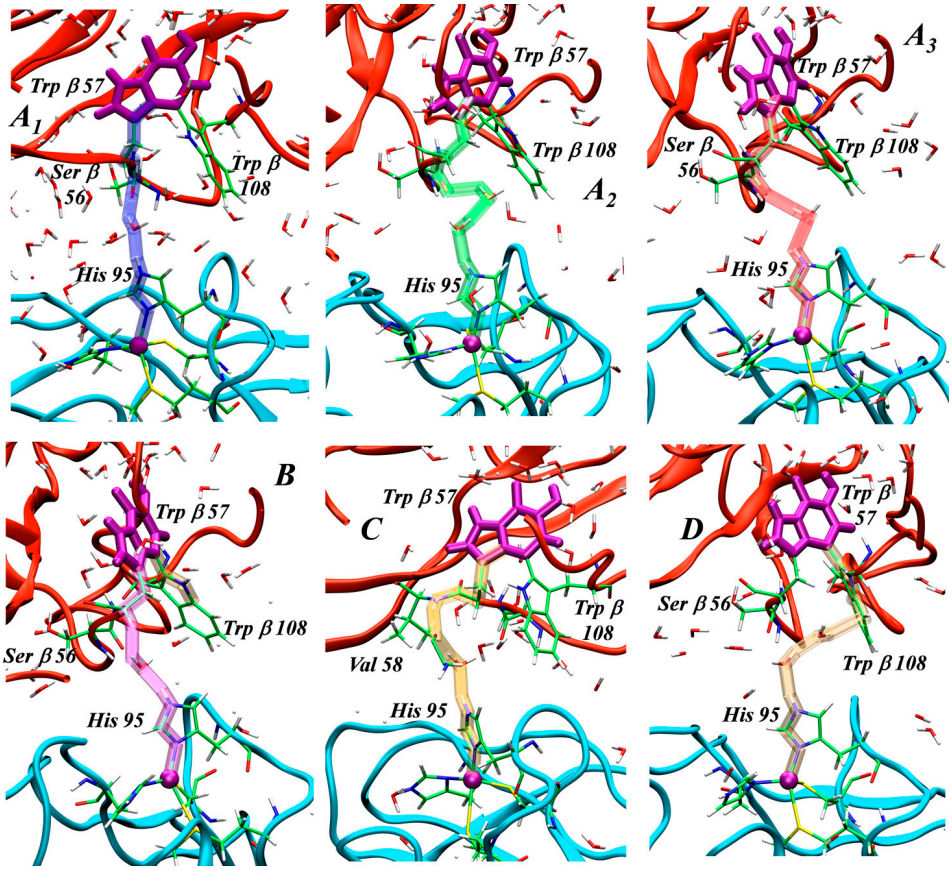

Fig. S1. Representative snapshots of the different configuration types. The colors of the representative ET pathway tubes are the same as shown in Figs. 2 and 3 (A_1, blue; A_2, green; A_3, red; B, purple; C, ochre; and D, brown). The donor and acceptor cofactors are represented in purple.

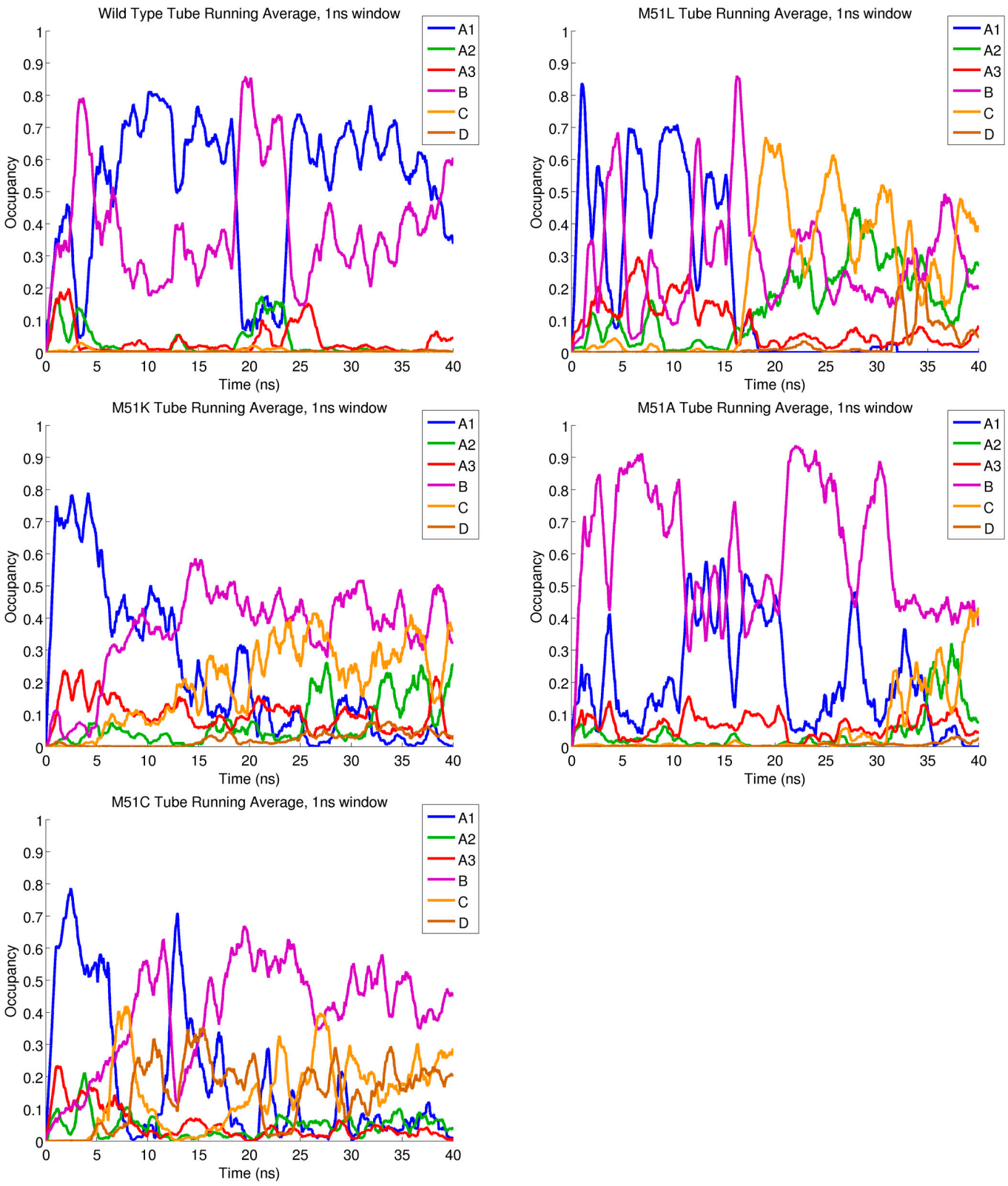

Fig. S2. Running averages showing the percentages of each pathway tube taken over a 1-ns window.

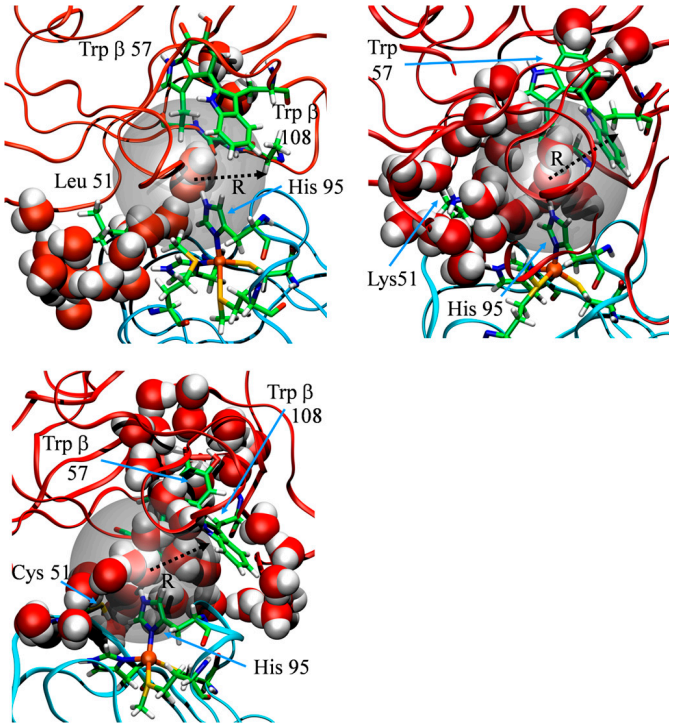

Fig. S3. Representative snapshots of the M51L (*Top Left*), M51K (*Top Right*), and M51C (*Bottom*) interfaces. The gray sphere represents the ET region for $R = 5.5$ Å. Water molecules are shown in the van der Waals representation.

Table S1. Detailed pathway analysis*

	Wild type		M51L		M51K		M51A		M51C	
Tubes	$\bar{\varepsilon}$	%	$\bar{\varepsilon}$	%	$\bar{\varepsilon}$	%	$\bar{\varepsilon}$	%	$\bar{\varepsilon}$	%
A_1	1.10	52.8	0.91	26.2	0.99	29.0	0.94	24.3	1.00	23.0
A_2	0.44	3.0	0.38	13.0	0.43	5.1	0.43	1.9	0.44	4.5
A_3	0.25	3.6	0.23	10.4	0.28	11.1	0.24	6.2	0.26	5.8
B (Trp57β)	0.74	39.8	0.48	29.1	0.60	35.3	0.68	66.1	0.69	39.0
C (Val58)	0.56	0.4	0.48	20.4	0.55	17.4	0.60	0.8	0.61	12.9
D (Trp108)	1.25	0.2	0.23	0.4	0.76	1.4	1.06	0.2	0.96	13.9
E_{wet}	0.32	<0.1	0.09	0.2	0.25	0.1	0.14	<0.1	0.33	0.3
E_{dry}	0.14	0.1	0.06	0.3	0.18	0.5	0.19	0.4	0.30	0.7

*$\bar{\varepsilon}$ is the averaged decay factor obtained for a given pathway tube over 40 ns of simulation time. The ε_{tot} values for the pathway model are scaled by a factor of 10^3. Pathway tube E has been subdivided into E_{wet} and E_{dry}, representing all remaining water-mediated and non-water-mediated pathways, respectively.

Corrections

BIOPHYSICS AND COMPUTATIONAL BIOLOGY

Correction for "Surface residues dynamically organize water bridges to enhance electron transfer between proteins," by Aurélien de la Lande, Nathan S. Babcock, Jan Řezáč, Barry C. Sanders, and Dennis R. Salahub, which appeared in issue 26, June 29, 2010, of *Proc Natl Acad Sci USA* (107:11799–11804; first published June 14, 2010; 10.1073/pnas.0914457107).

The authors note that Table 1 appeared incorrectly. The corrected table appears below.

Additionally, the authors note that on page 11803, right column, first paragraph, lines 7–10, "A friction coefficient of 15 ps^{-1} and a bath temperature of 298 K were used to propagate the equations of motion within the Langevin approach. Periodic boundary conditions were applied to simulate a continuous medium." should instead appear as "A friction coefficient of 10 ps^{-1} and a bath temperature of 298 K were used to propagate the equations of motion within the Langevin approach. No boundary conditions were imposed; the system freely evolved in vacuum."

These errors do not affect the conclusions of the article.

Table 1. Expectation values for $\langle \varepsilon_{tot} \rangle$ and the ratios $r_{\varepsilon}^{mut} = \langle \varepsilon_{tot}^2 \rangle^{mut} / \langle \varepsilon_{tot}^2 \rangle^{wt}$ and $r_k^{mut} = k_{ET}^{mut} / k_{ET}^{wt}$ obtained from packing density and pathway analyses*

		Wild type	M51L	M51K	M51A	M51C
r_k^{mut}	(Experiment)	1.0	0.68	0.49	0.13	—
$\langle \varepsilon_{tot} \rangle \times 10^3$	(Pathway analysis)	0.90 ± 0.03	0.47 ± 0.03	0.61 ± 0.02	0.65 ± 0.02	0.73 ± 0.02
r_{ε}^{mut}	(Pathway analysis)	1.0	0.36 ± 0.04	0.52 ± 0.04	0.57 ± 0.04	0.76 ± 0.05
$\langle \varepsilon_{tot} \rangle \times 10^3$	(Packing density)	0.70 ± 0.03	0.42 ± 0.04	0.51 ± 0.03	0.62 ± 0.05	1.03 ± 0.05
r_{ε}^{mut}	(Packing density)	1.0	0.56 ± 0.09	0.76 ± 0.07	0.89 ± 0.15	2.29 ± 0.26
P_{hb}		0.53	0.15	0.19	0.18	0.16
τ (ns^{-1})		0.23	0.45	1.20	0.50	2.25

*The uncertainties account for the sampling errors of the computational protocol (see *SI Text*). Experimental rates k_{ET} were obtained from k_3 (at 30 °C) in table 3 of ref. 15 (M51C was not reported). P_{hb} is the unit-normalized likelihood that a water molecule is simultaneously hydrogen bonded to both the MADH Ser β 56 O and amicyanin His 95 HE2 atoms during our simulations. The turnover τ of the bridging water molecule is defined as the number of different water molecules that participate in pathway A_1 divided by the length of the simulation in nanoseconds.

www.pnas.org/cgi/doi/10.1073/pnas.1220833110